Conception et contrôle tolérant aux pannes d'une nouvelle machine synchrone multiphasée à flux transversal et à aimant permanent

Wenjing Zhang

HESAM UNIVERSITÉ

Arts et Métiers Sciences et Technologies

ÉCOLE DOCTORALE SCIENCES DES MÉTIERS DE L'INGÉNIEUR
[L2EP – Campus de Lille]

THÈSE

présentée par : **Wenjing ZHANG**

soutenue le : **30 May 2023**

pour obtenir le grade de : **Docteur d'HESAM Université**

préparée à : **École Nationale Supérieure d'Arts et Métiers**

Spécialité : **Génie électrique**

Design and Fault Tolerant Control of a Novel Multiphase Transverse Flux Permanent Magnet Synchronous Machine

THÈSE dirigée par :
[M. Yanliang XU]
[M. Eric SEMAIL]

et co-encadrée par :
[M. Ngac Ky NGUYEN]

Jury

M. Jinji SUN, Professeur des universités, Beihang University	Président, Rapporteur
M. Guillaume Krebs, Maître de conférences HDR, GeePs, Université Paris-Saclay	Rapporteur
M. Guiqing ZHANG, Professeur des universités, Shandong Jianzhu University	Examinateur
M. Xiuhe WANG, Professeur des universités, Shandong University	Examinateur
M. Wenliang ZHAO, Professeur des universités, Shandong University	Examinateur
M. Franck BETIN, Professeur des universités, LTI, Université de Picardie Jules Verne	Examinateur
M. Eric SEMAIL, Professeur des universités, L2EP, Arts et Métiers Sciences et Technologies/ENSAM	Examinateur
M. Ngac Ky NGUYEN, Maître de conférences, L2EP, Arts et Métiers Sciences et Technologies/ENSAM	Examinateur

THÈSE

Acknowledgements

As I come to the end of my doctoral thesis, I would like to take this opportunity to express my heartfelt gratitude to all those who have supported and helped me along this journey.

First and foremost, I would like to thank my esteemed supervisors, Professor. Yanliang Xu from Shandong University, Professor. Eric Semail and Dr. Ngac-Ky Nguyen from ENSAM in France. Their guidance, encouragement, and patience have been invaluable throughout my research, and I am deeply grateful for their unwavering support.

I would also like to extend my appreciation to my colleagues and friends, who have played a significant role in shaping my research and enriching my experience. To my fellow researchers in the Chinese laboratory, Mingxin Sun, Gensheng Li, Peng Zhou, Tianhu Wei, and Yiyang Pan, I express my deepest gratitude for their collaboration, discussions, and encouragement. And to my colleagues at L2EP laboratory in France, Hailong Wu, Haibo Zhang, Youxi Huang, Lei Wang, Duc Tan VU, Lauro Ferreira, and Ryan O. Berriel, I extend my sincere thanks for their invaluable contributions and insights.

I would like to express my sincere gratitude to my reviewers, Professor. Stéphane Clenet and Professor. Giraud Frédéric, for their expert guidance, insightful comments, and valuable suggestions, which have been instrumental in improving the quality of my research.

I would also like to thank the engineers, Jiang Jie from Beijing Guoji Group and Li Shucai from Shandong Jingchuang Group, for their assistance during my experiments. Their expertise and support have been indispensable in making my research successful.

I am also grateful to the School of Electrical Engineering at Shandong University and the L2EP Laboratory in France for providing me with opportunities to study and conduct research. I am grateful for the intellectual freedom and resources that were made available to me, which enabled me to broaden my knowledge and skills.

Lastly, I would like to express my sincere appreciation to my parents, who have been a constant source of encouragement and support throughout my academic journey. Their unwavering love and belief in me have been the driving force behind my success. I would also like to thank my girlfriend for her love, care, and encouragement during the most challenging moments of my research.

In conclusion, my doctoral thesis would not have been possible without the support, guidance, and encouragement of these exceptional individuals and institutions. I am grateful for their unwavering support and encouragement and am honored to have had the opportunity to work with such remarkable people. Thank you for all the support and for helping me achieve my dreams.

Abstract

Transverse flux permanent magnet synchronous machine combines the advantages of intrinsically high torque density, the ability to adjust the electromagnetic load independently, flexible structure design, and simple winding structure, enabling it with significant potential for being used as a servo motor in industrial robot applications to achieve the miniaturization of its electric drive. In addition, multiphase winding structure can be used in transverse flux permanent magnet synchronous machine to obtain advantage of fault tolerant ability, which furtherly improves the functional reliability of the electric drive in industrial robots. However, there are still shortcomings and limitations among the existing research on transverse flux permanent magnet synchronous machine and the research on fault tolerance of multiphase machines, which limit their application in the context of the thesis

The main objective of this doctoral thesis is to propose a novel structure transverse flux permanent magnet synchronous machine to improve the characteristics and performances of the industrial robot.

Firstly, a dual-stator topology transverse flux permanent magnet synchronous machine combined with hybrid stator core and disk-type rotor (DS-HSDR-TFPMSM) is proposed to realize the miniaturization and high dynamics of the electric drives in industrial robots. Its structural and electromagnetic design is proceeded. A fault tolerant design study based on the dual three-phase structure is carried out for the proposed DS-HSDR-TFPMSM to improve its functional reliability.

Considering the complex three-dimensional structure of DS-HSDR-TFPMSM, the calculation method of air-gap magnetic field and performances are investigated based on the Schwarz-Christoffel transformation method. In addition, the optimization design of DS-HSDR-TFPMSM is conducted based on the BP neural network and multi-objective optimization algorithm to improve its torque performance.

Based on the accessible fault tolerant designs of DS-HSDR-TFPMSM, the fault tolerant control method for the dual three-phase permanent magnet synchronous machine is investigated. Firstly, the fault tolerant control method by reconfiguring the reference current in the normal decoupled frame based on the principle of minimum copper loss and maximum torque operation range is proposed. Then, the axial stress on the rotor disk of the dual three-phase DS-HSDR-TFPMSM under different states is analyzed. The synthetic axial force and the axial stress distribution on the rotor disk of the two kinds of dual three-phase DS-HSDR-TFPMSMs are compared. Finally, The fault tolerant control method for dual three-phase permanent magnet electric machine operating under high speed is investigated, in which the harmonic components of the reference current are tracked and controlled under high speed by using a multi-reference frame-based method and a proportional resonant controller-based method.

Eventually, the fabrication technologies and experimental studies are conducted for prototype DS-HSDR-TFPMSM.

Keywords: Transverse flux permanent magnet synchronous machine; dual three-phase permanent magnet synchronous machine; Schwarz-Christoffel transformation method; optimization design of electric machine; fault tolerant control.

Résumé

La machine synchrone à aimant permanent à flux transverse combine les avantages d'une densité de couple intrinsèquement élevée, de la capacité à ajuster la charge électromagnétique de manière indépendante, d'une conception de structure flexible et d'une structure de bobinage simple, ce qui lui confère un potentiel important pour être utilisée comme servomoteur dans les applications de robots industriels afin de parvenir à la miniaturisation de son entraînement électrique. En outre, la structure d'enroulement multiphase peut être utilisée dans une machine synchrone à aimant permanent à flux transverse pour obtenir l'avantage de la capacité de tolérance aux pannes, ce qui améliore encore la fiabilité fonctionnelle de l'entraînement électrique dans les robots industriels. Cependant, les recherches existantes sur les machines synchrones à aimant permanent à flux transverse et les recherches sur la tolérance aux pannes des machines multiphasées présentent encore des lacunes et des limites qui restreignent leur application dans le contexte de la thèse.

L'objectif principal de cette thèse de doctorat est de proposer une machine synchrone à aimant permanent à flux transverse de structure nouvelle pour améliorer les caractéristiques et les performances du robot industriel.

Tout d'abord, une machine synchrone à aimants permanents à flux transverse à topologie bi-statorique combinée avec un noyau de stator hybride et un rotor de type disque (DS-HSDR-TFPMSM) est proposée pour réaliser la miniaturisation et la dynamique élevée des entraînements électriques dans les robots industriels. Sa conception structurelle et électromagnétique est réalisée. Une étude de conception tolérante aux pannes basée sur la structure double-triphasée est réalisée pour le DS-HSDR-TFPMSM proposé afin d'améliorer sa fiabilité fonctionnelle.

Compte tenu de la structure tridimensionnelle complexe du DS-HSDR-TFPMSM, la méthode de calcul du champ magnétique de l'entrefer et les performances sont étudiées sur la base de la méthode de transformation de Schwarz-Christoffel. En outre, la conception de l'optimisation du DS-HSDR-TFPMSM est réalisée sur la base du réseau neuronal BP et de l'algorithme d'optimisation multi-objectifs afin d'améliorer ses performances en termes de couple.

Sur la base des conceptions accessibles de tolérance aux pannes de DS-HSDR-TFPMSM, la méthode de commande tolérante aux pannes pour la machine synchrone double à aimant permanent triphasé est étudiée. Tout d'abord, la méthode de contrôle tolérant aux pannes par reconfiguration du courant de référence dans le repère découplé normal basé sur le principe de la minimisation des pertes cuivre et de l'optimisation de la plage de fonctionnement à couple maximal. Ensuite, la contrainte axiale sur le disque du rotor du DS-HSDR-TFPMSM triphasé double dans différents états est analysée. La force axiale synthétique et la distribution de la contrainte axiale sur le disque du rotor des deux types de DS-HSDR-TFPMSM triphasés doubles sont comparées. Enfin, la méthode de contrôle tolérant aux pannes pour les machines électriques à aimant permanent triphasées fonctionnant à grande vitesse est étudiée, dans laquelle les composantes harmoniques du courant de référence sont suivies et contrôlées à grande vitesse en utilisant une méthode basée sur un repère de travail comprenant plusieurs plans tournants et une méthode basée sur un contrôleur résonant proportionnel.

Enfin, les technologies de fabrication et les études expérimentales sont menées pour le prototype DS-HSDR-TFPMSM.

Mots-clés: Machine synchrone à aimant permanent à flux transverse ; machine synchrone à aimant permanent double-triphasée ; méthode de transformation de Schwarz-Christoffel ; optimisation de la conception de la machine électrique ; contrôle tolérant aux pannes.

Contents

Nomenclature

Abbreviation

AC	Alternating Current
AFM	Axial Flux Machine
ANN	Artificial Neural Network
BP	Back-Propagation
CCS-MPC	Continuous Control Set MPC
DC	Direct Current
DETW	Disconnection of Entire Three-phase Winding
DoF	Degrees of Freedom
DS-HSDR-TFPM	Dual Stator topology Transverse Flux Permanent Magnet Machine topology combined with Hybrid Stator and Disk-type Rotor
DTC	Direct Torque Control
FCS-MPC	Finite Control Set MPC
FEM	Finite Element Method
FOC	Field-Oriented Control
FSCW-PMSM	Fractional-Slot Concentrating-Winding Permanent Magnet Synchronous Machine
FTC	Fault-Tolerant Control
GA	Genetic Algorithm
IPC	Industrial Control Computer
LCM	Least Common Multiple
LPF	Low Pass Filter
MCL	Minimum Copper Loss principle
MMF	Magnetomotive Force
MOPSO	Multi-Objective Particle Swarm Optimization
MPC	Model Predictive Control
MRF	Multiple Reference Frame
MST	Maxwell Stress Tensor
MTOR	Maximum Torque Operation Range

PI	Proportional-Integral
PMSM	Permanent Magnet Synchronous Machine
PR	Proportional-Resonant
RMS	Root Mean Square
RPMSM	Radial flux Permanent Magnet Synchronous Machine
SC	Schwarz-Christoffel
SMC	Soft Magnet Composite
SVPWM	Space Vector Pulse Width Modulation
TFPMSM	Transverse Flux Permanent Magnet Synchronous Machine
THD	Total Harmonic Distortion
TOR	Torque Operation Range
VSD	Vector Space Decomposition
VSI	Voltage Source Inverter

Parameters, variables, matrices, and vectors

T_d	drive torque
T_l	load torque
F_w	friction torque
i_g	gear ratio
m	number of phases
N_{phase}	number of series turns of one phase winding
E	no load back-EMF of the electric machine
U	input phase voltage
k_{w}	winding factor
f	operating fundamental frequency
n	electric machine speed in unit (rpm)
η	efficiency
$\cos\varphi$	power factor
$B_{\delta 2}$	amplitude of the air gap flux density at the position of the inner permanent magnet

k_s	pole-arc coefficient corresponding to the stator core width
γ	stator core diameter ratio
l_b	stator core cross-section height
l_s	stator core total radial height
σ	leakage coefficient
q	number of slots per pole per phase
f_s	Schwarz-Christoffel transformation function
Δx	length along the real axis of the rectangular solution domain in the z-plane
Δy	width along the imaginary axis of the rectangular solution domain in the z-plane
f_c	conformal transformation
φ_g	scalar magnetic potential
$\mathbf{H_g}$	magnetic field intensity vector
υ	learning rate of BP-ANN
ω	inertia weight
P_{id}^k	optimal position of individual particle
P_{gd}^k	global optimal position of the particles in population
δ_e	the phasor shift between the two sets of symmetrical three-phase windings
$\boldsymbol{\Psi}_s$	stator winding flux linkage vector
$\boldsymbol{I}_s$	stator current vector
$\boldsymbol{\Psi}_{PM,s}$	PM flux linkage vector
$\boldsymbol{L}$	stator winding inductance matrix
$\boldsymbol{M}_{fs}(\theta)$	mutual inductance matrix between the equivalent excitation winding of the PM and the stator winding
$\boldsymbol{T}_{\mathrm{VSD}}$	decomposition transformation matrix

List of figures

List of tables

Introduction

Industrial robots are robotic systems specifically designed and utilized in industrial manufacturing processes. Compared with the widely used CNC systems, industrial robots combine the advantages of high versatility, flexible control, and large working space, enabling them a vital part of modern smart factories [1]. In 1961, the world's first industrial robot was created, which was driven by a hydraulic device and put into commercial use in an electric machine manufacturing enterprise[2]. In 1975, the Swiss company ABB successfully developed the first electrically driven industrial robot, which laid the foundation for modern industrial robot systems [2]. Nowadays, electrically driven and microcomputer-controlled industrial robots are widely used in automated factories, especially in the domain of automotive and smart terminal device manufacturing [3], [4].

Industrial robots are composed of several components, including kinematic structures, reducers, electric drives, sensors, control systems, and others [5]. Among them, the kinematic structure determines the motion characteristics of the industrial robot through the different connection patterns between the adjacent robotic arms [6]. The reducer increases the drive torque inputted from the electric machine side through a gear set. The electric drive is a crucial component of industrial robots, comprising servo electric machines, drive circuits (mainly VSI), and corresponding electric machine servo controllers. Its main function is to convert electrical energy into mechanical energy, which drives the robot arm to execute various movements based on control signals. The sensor component of industrial robots captures the position information of both the manipulator and the target object, utilizing various miniature sensing devices, and then sends the signal back to the controller. Besides, the control system is similar to the "brain" of the entire industrial robot system, responsible for sending control signals to each electric drive based on user commands and feedback sensor signals. During system operation, the control system also collects and analyzes various data in real-time.

In summary, research on industrial robot is a complex and multidisciplinary field that requires the collaboration of various areas of expertise. Within the domain of electrical engineering research, the electric drive in industrial robots are a particularly noteworthy area. This component acts as an actuator, providing the power source that drives the robotic arm and enables both power and posture output. As such, the electric machine serves as the core component of industrial robots, and its performance - both good and bad - can significantly impact the performance of the entire robot system. Until to now, most manufacturers and researchers on industrial robot have proposed and applied various issues of electric machines including AC servo electric machines, DC electric machines and stepper electric machines [7]. AC servo electric machines are predominant in the industrial robot electric machine market due to their high torque-to-rotation inertia ratio, high peak output torque, high precision, and wide range of constant torque operation. Among the various types of AC servo electric machines, PMSM (PMSM) are the most promising and widely used due to their high efficiency and high power density [8].

As automated manufacturing continues to develop rapidly, the technical demands placed on industrial robots are also increasing. Consequently, more demanding requirements are placed on their electric drive components, mainly including the need for miniaturization, high dynamics, high functional reliability, and low torque ripple.

(1) Miniaturization

The kinematic joint component of an industrial robot is primarily responsible for providing the driving force (torque) and the degrees of freedom of robot motion, as shown in Fig. 1.

However, this component also suffers from large size and weight, which are key factors leading to industrial robots being regarded as bulky machines. Therefore, optimizing the internal structure of the joint part is the most effective means to achieve miniaturization of industrial robots. A power system is integrated inside the motion joint of the industrial robot, which consists of an electric drive and a reducer, as shown in Fig. 2. In order to minimize the size of the joint part, the drive circuit and electric machine can be combined together to obtain an integrated electric drive system, and this structure is shown in literature [9] and [10] . Alternatively, a more straightforward approach is to separate the electric drive where only the electric machine part is located inside the joint, while the drive circuit (generally referred to as VSI) is located in the controller cabinet. For industrial robot servo electric machines, a brake needs to be installed inside the electric machine to prevent the robot arm from displacement due to motion inertia and sudden power failure. In addition, the encoder is also particularly important for servo electric machine control, so the internal layout of the actual PMSM for industrial robots is shown in Fig. 3, and it can be seen that the overall structure is long due to the combination with the brake and encoder. To make industrial robots even smaller, a new type of electric machine needs to be developed to have a compact design and a high torque density, which will help to decrease the size and weight of the robot's joints.

Fig. 1. Joint of industrial robot

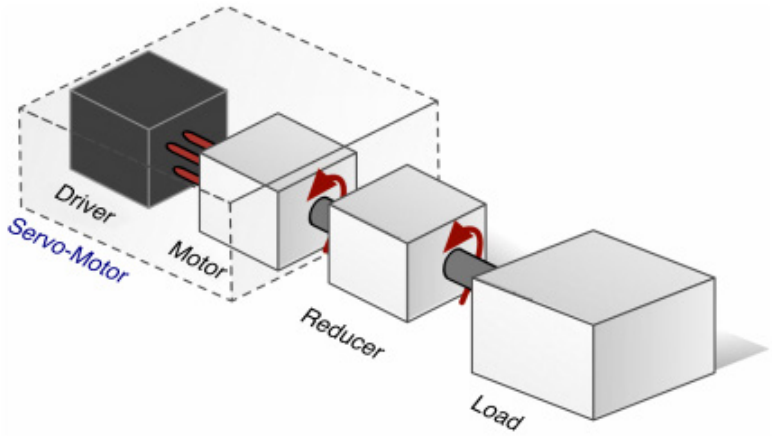

Fig. 2. Power system of industrial robot

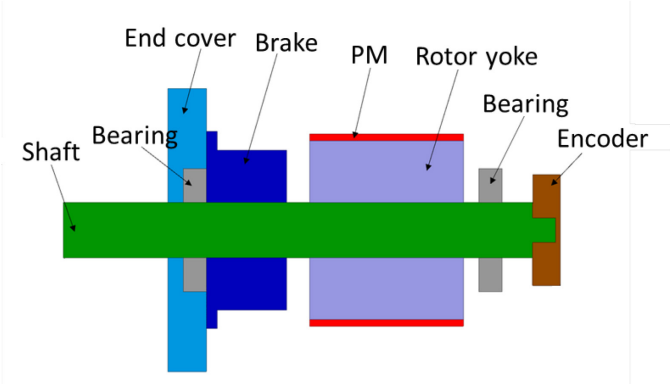

Fig. 3. Internal layout of PMSM applied for industrial robot

(2) High dynamic performance

Industrial robots go through frequent start-stop and acceleration/deceleration processes during operation, so it is especially important to improve their dynamic performance indicators. The dynamic performance of industrial robots is primarily determined by how quickly the system responds to achieve the desired speed or position. A shorter response time indicates better dynamic performance. In terms of electric drive, the dynamic performance of industrial robots is mainly affected by the inertia of the load, drive torque and the inertia of electric machine. Therefore, the dynamic performance can be improved by increasing the output torque of electric machine, however, this approach will bring problems such as high electric machine current rating and large electric machine size. In the domain of servo electric machine, the ratio of moment of inertia between load and electric machine is an important index that needs to be determined in advance [11], if the electric machine inertia is large relative to the load, the electric machine inertia will significantly affect the dynamic performance of the system. In the case of industrial robot applications with gearboxes, the electric machine inertia is scaled up and the total inertia and response time can be calculated using (1)[12]. Therefore, reducing the electric machine inertia is important to improve the dynamic performance of industrial robots [13].

$$t = \int_{\omega_2}^{\omega_1} \frac{\delta}{T_\mathrm{d} - T_\mathrm{l} - T_\mathrm{f}} d\omega$$
$$\delta = I_\mathrm{l} + I_\mathrm{m} \cdot i_\mathrm{g}^2 \cdot \eta_\mathrm{g} \quad , (1)$$

where the symbol T_d is the electric machine output torque, the symbol T_l denotes the load torque, I_l denotes the inertia of the load (robotic arm and object load), I_m is the inertia of the parts connected to the electric machine rotor (mainly including the electric machine rotor and the gear set in the gearbox), i_g indicates the transmission ratio, and η indicates the transmission efficiency of gearbox.

(3) High functional reliability

In an automated manufacturing system, it is crucial to maintain production safety and product quality. However, in the event of an industrial robot failure, the entire manufacturing system may need to be halted, which proves to be an inefficient and uneconomical solution. The reliability and productivity of the manufacturing system can be greatly enhanced by ensuring that the industrial robot continue to work normally in the event of a failure. Regarding

the electric drive, it means that the fault tolerant capability is required which improving the functional reliability of the system. In terms of the fault occurring in the electric drive, it mainly includes the fault of VSI or the fault in the winding of the electric machine. For the fault in VSI, it mainly indicates the damage or communication error of the switching component which can be transformed to an open-circuit fault. And for the fault in the winding of the electric machine, it mainly leaded by the open-circuit of one phase [14], [15].

(4) Low torque ripple

The accuracy of industrial robots can be directly impacted by torque ripple of electric machine. Undesirable actuator jitter may arise when there is significant torque ripple in the electric machine, leading to a negative influence on both the positional and repetitive accuracy of the robot system. Therefore, it is significant to study the weakening of the torque ripple in PMSM. The torque ripple is attributed to both cogging torque and harmonics in the armature magnetic field. The cogging torque is generated by the interaction between the permanent magnets of the PMSM and the stator core cogging, which can be reduced by optimizing the electric machine design parameters[16] or by using other auxiliary issues (e.g. skewing pole[17] , skewing slots[18] , permanent magnets with variable thickness[19] and unequal pole-arc coefficients[20] etc.). The harmonics in the armature field are mainly caused by the interaction between the winding space harmonics and the current time harmonics. However, the reduction of the torque ripple leaded by the armature harmonics is challenging. The research in [21] and [22] introduce the method for reducing the torque ripple through monitoring the speed ripple and producing the reversal compensation, however, it is relatively sophisticated leading to the need for a complex design of the controller. In order to improve the quality of the torque, several research works have been proposed using non-sinusoidal currents [23]–[26] to have a theoretically smooth torque. However, the problem arises when the rotation speed increases because of the limited bandwidth of the current regulator, often of the PI type.

As the crucial component of industrial robots, electric machines play an important role in addressing the requirements for miniaturization, high dynamics, high functional reliability and low torque ripple. Therefore, the promotion of electric machine technology progress can effectively advance the upgrading and development of industrial robot industry technology. To satisfy the high-performance drive requirements of industrial robots, innovative topologies of PMSM are needed. Transverse flux permanent magnet synchronous machine (TFPMSM) combines the advantages of intrinsically high torque density, the ability to adjust the electromagnetic load independently, flexible structure design and simple winding structure [27]. Due to the characteristic of high torque density, the size and weight of the electric machine can be well optimized; in addition, the flexibility of the structural design makes the electric machine structure more diverse allowing the development of compact design solutions for industrial robot applications. At the same time, the flexibility of the rotor structure design will bring forward more design method to reduce the moment of inertia.

Despite the numerous advantages of TFPMSM, its specific structure and principle result in complexity in design and fabrication, which impedes the application and development of TFPMSM in the field of industrial robot electric machines. Therefore, the research on the structure and design of TFPMSM in the context of industrial robot applications is a key technology that needs to be addressed urgently. In addition, in terms of the electromagnetic analysis and calculation of TFPMSM, since its structure is quite different from that of traditional electric machines, the analytical calculation method for traditional electric machines is no longer applicable. So, it is necessary to establish a three-dimensional model of the electric machine of TFPMSM and calculate the magnetic field and main performance parameters of by

FEM. However, the three-dimensional FEM consumes a lot of computing resources and time, which introduce a considerable challenge to the electric machine analysis. Therefore, it is significant to research a fast and efficient analytical calculation method that is applicable to TFPMSM.

However, TFPMSM is difficult to determine the specific design parameters directly due to the lack of guidance from design experience formulas and diagrams. Thus, the optimization methods are generally used to iterate the optimal design rapidly. However, existing optimization design methods for TFPMSM use FEM or equivalent analysis model to calculate optimization objective function values resulting in a time-consuming optimization design process for TFPMSM. Therefore, it is important to study more efficient optimization design methods for TFPMSM to further promote the performance upgrade of TFPMSM.

The study on TFPMSM enables the miniaturization and high dynamics of the electric drive, and the torque ripple of TFPMSM can be reduced by the optimization design method. However, the TFPMSM using the conventional three-phase winding structure is not characterized by fault tolerant ability, which reduces the reliability of industrial robot systems. Multiphase machines are the electric machines with more than three phase winding which are characterized by the advantage of excellent fault tolerant ability. Therefore, high functional reliability can be achieved in industrial robot systems by introducing multiphase machine. Nevertheless, there is no relevant multiphase design cases for TFPMSM until to now. In addition, the control method of multiphase machine is different from that of traditional three-phase electric machine. Especially, the control method of multiphase machine under missing phase fault condition is significant to ensure its fault tolerant ability. Therefore, the research on multiphase design of TFPMSM and fault tolerant control of multiphase machine is important to promote the technological upgrade of industrial robot.

In summary, the advantages of miniaturization and high dynamics can be achieved by using TFPMSM instead of the traditional RPMSM in industrial robot. In addition, the reliability of the industrial robot system can be further improved by introducing multiphase machine. However, the TFPMSM as well as the multiphase machines in the existing research still need to deal with the following challenges that limit its application in industrial robot:

(1) Innovation and design issues of TFPMSM structure. Amounts of inspiring topologies have been proposed based on the research on TFPMSM and been used in various applications. However, the research has never been developed for the application scenario of industrial robots.

(2) Analysis and optimization of TFPMSM. As an electric machine with three-dimensional magnetic circuit, the structure of TFPMSM is more complex than that of traditional RPMSM, which leads to the application of time-consuming three-dimensional finite element analysis of TFPMSM. In addition, the three-dimensional structure of TFPMSM consists of complex design parameters, and its optimization design process is also more complex and time-consuming.

(3) Fault tolerant design and control of TFPMSM. To satisfy the high functional reliability requirements of industrial robot electric drives, fault tolerant design of TFPMSM is needed. However, research on novel topology of multiphase machines, especially with regards to fault tolerant multiphase design of TFPMSM, is still an emerging field. Additionally, the application of this technology in industrial robot electric machines is limited by the complexity of fault tolerant control of multiphase machines.

Based on the above challenges, the following research work was carried out in the thesis.

In chapter 1, the state of the art of the research on the structure of TFPMSM as well as its analysis model, optimization method of novel topology electric machine, the structure and winding design of multiphase machine, and the control method as well as fault tolerant strategy of dual three-phase machine are summarized.

In chapter 2, a dual stator topology transverse flux permanent magnet synchronous machine combined with hybrid stator and disk-type rotor (DS-HSDR-TFPMSM) is proposed

according to the characteristics of electric machines used in industrial robot. The design equations for the main dimensions of DS-HSDR-TFPMSM are derived, and the design as well as analysis of the key electric machine parameters are given. In order to improve the fault tolerant performance of the electric machine, a study on the fault tolerant design of DS-HSDR-TFPMSM is carried out. Firstly, a dual three-phase DS-HSDR-TFPMSM with symmetric stator disk structure was designed based on the 10-pole/12-slot combination. Then, a dual three-phase DS-HSDR-TFPMSM with asymmetric stator disk structure was designed based on the dual stator topology of DS-HSDR-TFPMSM. Finally, the performance of the two types of dual three-phase machines is compared.

In chapter 3, the electromagnetic field analysis and performance calculation method based on Schwarz-Christoffel (SC) transformation is proposed. In order to improve the analysis and calculation speed of DS-HSDR-TFPMSM, its air-gap magnetic field and performance of the electric machine are solved by proposed SC transformation method, and the calculation accuracy are validated using the FEM.

In chapter 4, a novel optimization design method based on BP neural network and multi-objective particle swarm optimization algorithm is proposed. The BP neural network based on genetic algorithm optimization is proposed as a surrogate model, and a multi-objective particle swarm optimization algorithm is used to optimize the electric machine torque performance including output torque average and torque ripple.

In chapter 5, the fault tolerant control technologies for dual three-phase PMSM are researched. Based on the dual three-phase fault tolerant design scheme of DS-HSDR-TFPMSM proposed in Chapter 2, the fault tolerant control technology of dual three-phase PMSM is investigated. Firstly, the mathematical model and vector control method of the dual three-phase machine is derived in detail. Then, the fault tolerant control method based on normal decoupled transformation is proposed for the one phase open-circuit fault of dual three-phase machine. The control model based on the proposed fault tolerant control method is consistent with the model under healthy condition, so it combines the advantage of easy implementation. The reference currents in fault tolerant control method are reconfigured based on the principle of minimum copper loss and maximum torque operation range under the current amplitude constraint. Moreover, two harmonic reference current control methods are introduced: the multi reference frame based harmonic current control method and the PR controller based harmonic current control method. These two methods are introduced to tackle the issue of time-varying reference currents generated due to fault tolerant control method, as well as the difficulty of achieving precise current modulation at high speeds using conventional PI control which results in high torque ripple. The effects of these two methods are compared by the simulation research on dual three-phase DS-HSDR-TFPMSM. Finally, the one-phase open-circuit fault tolerant control method and the harmonic reference current control method are validated by experiments.

In chapter 6, the research on the prototype fabrication and experiments of DS-HSDR-TFPMSM is proceeded. Firstly, the prototype fabrication of DS-HSDR-TFPMSM is studied, including the stator and rotor fabrication process and the overall electric machine assembly process. Then, the structural strengths of the stator and rotor are calibrated. Finally, the experimental platform of DS-HSDR-TFPMSM prototype was built, and experiments under both no load and load condition were carried out. The experimental results are compared with the results measured from a commercial RPMSM products.

Chapter 1. State of the Art

1.1 Superiorities of TFPMSM

The main flux path of the transverse flux structure is perpendicular to the plane where the motion path of the moving components (Movers in linear machine and rotor in rotating machine) is located as shown in Fig. 1.1[28], [29]. Therefore, the electromagnetic load of the transverse flux electric machine can be set independently, which makes the electric machine of this structure benefits from advantages of high torque density and flexible structural design. As a result, transverse flux electric machines have garnered significant attention from scholars[30].

The transverse flux machine was first proposed in 1904, and a patent for the transverse flux machine appeared in Germany in 1934. In the 1970s, Prof. E. R. Laithwaite from the United Kingdom conducted systematic research on the transverse flux linear machine [31]. However, the objects of these studies were limited to induction machines at that time. Since the structural limitations of induction machines, the harmonic content inside the machine was relatively high. It was not until 1986 that German scholar Prof. H. Weh introduced permanent magnets into the transverse flux structure and designed the first TFPMSM[32] , and TFPMSM is really considered by researchers.

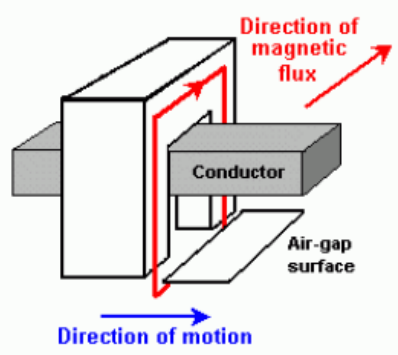

Fig. 1.1. Diagram of the transverse flux structure

Nowadays, with the rapid development of permanent magnet materials and various new magnetically conductive materials, such as soft magnetic composite materials (SMC), Subsequently, a range of TFPMSMs incorporating innovative topologies have begun to emerge, prompting continued exploration of the various potential advantages offered by TFPMSMs. Compared with the conventional RPMSM, the TFPMSM proposed in the existing research combines the advantages of adjusting the electromagnetic load independently, high torque density, flexible structural design, and independence between magnetic circuits of each phase.

(1) The ability to adjust the electromagnetic load independently

The circuit and magnetic circuit of conventional electric machines are constrained to each other, limiting the flexible design of the electric machine stator slots and stator teeth. By using the two types of C-type stator core toroidal winding transverse flux structures as shown in Fig. 1.2, the ability to adjust the electromagnetic load independently is achieved[33][34]. Consequently, the flexibility in the design of the stator tooth and the freedom to increase the number of electric machine poles are accessible.

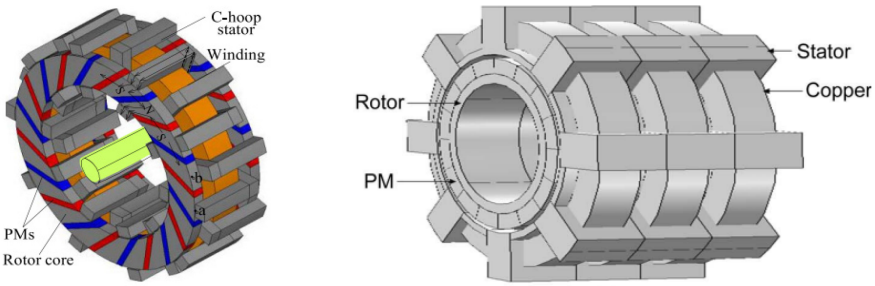

(a) (b)

Fig. 1.2. TFPMSM: (a) The structure proposed in literature [33] (a) The structure proposed in literature; (b) The structure proposed in literature [34]

(2) High torque density

In [35], a double-rotor TFPM with the ring shape winding is proposed, compared with traditional electric machines, it combines the advantages of compactness and smaller volume. In [36], a high-torque flux-concentrating TFPM was applied in aerospace application to meet its requirement for small volume and low weight. In [37], the torque density of TFPM was enhanced by using claw poles. B. Kou et al. proposed a novel dual-consequent-pole TFPM that owns core-tooth-to-magnet types of consequent-pole configuration on both stator and rotor. The no load winding linkage and torque density are greatly enhanced compared with the traditional electric machine through the comparative experiment [38], [39].

(3) Flexible structural design

The structure of TFPM is most abundant among PMSM. Not only its total topology, but also its stator cores can be designed as various types. And it means that the structure of TFPM can be customized according to different application. In [40], a novel TFPM is proposed which uses a flux concentrating structure, and it is used in the limited space of trajectory correction fuze. A. Njeh et al proposed a new configuration of claw pole TFPM with a disk rotor and with a stator which contains teeth in the form of claws and an outer cylindrical part in [41]. The machine can be mounted directly in vehicle wheels or for the applications where electric machine with smaller length in the axial direction is needed. In addition, Y. Yamamoto et al proposed a C-type stator core TFPM of which the winding adopts trapezoidal structure. The manufacturing and assembly method are both simple and can be designed as a multiphase machine conveniently by modulating the slot-pole combination[42].

(4) Independence between magnetic circuits of each phase

In conventional electric machines, a closed magnetic circuit is formed by a common stator yoke and rotor yoke. Nevertheless, not only do the stator yoke and rotor yoke constitute the main magnetic circuit of each phase winding, but they also interconnect between each other, thereby giving rise to mutual coupling among the phase windings. In some TFPMSM structures, the common stator yoke and rotor yoke are eliminated, and the main magnetic circuits of each phase are independent with each other, which simplifies the electric machine control method and improves its fault tolerant ability [43]. At present, three categories of studies concerning the interdependence among TFPMSM phases can be delineated as follows: a) Each phase winding is designed as a separate module and arranged along the axial direction [38]. b) Each phase winding is designed as a separate module and arranged along the circumferential direction [44]. c) Each coil of the electric machine is with a separate magnetic circuit [45].

Based on the advantages of high torque density and flexible structural design of TFPMSM, miniaturization of the electric machines can be realized. However, TFPMSMs for industrial robot applications have never been studied in academia.

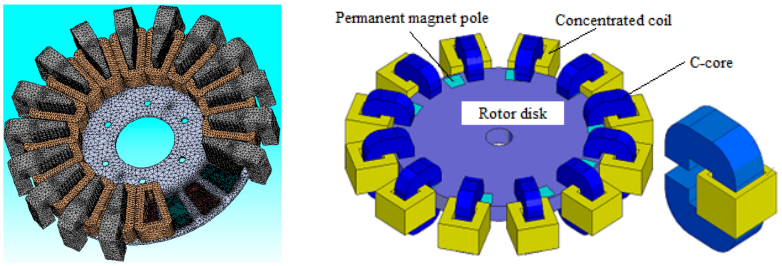

(a) (b)

Fig. 1.3. Disk-type rotor TFPMSM: (a) The structure proposed in literature[42] ; (a) The structure proposed in literature; (b) The structure proposed in literature[46].

In addition, considering the requirement of high dynamic performance in industrial robot applications, the moment of inertia of the TFPMSM needs to be reduced. There are two main approaches to reduce the moment of inertia of the electric machine: the first method is to reduce the weight of the rotor by machining; however, this method will impact the main magnetic circuit of the electric machine[47]. The other method is to reduce the thickness of the rotor core by using the material with high saturation flux density, but this method leads to a significant increase in the cost [48]. In addition to the above methods, disk-type rotors combined with the advantages of small size and low weight can be used. Until to now, disk rotors are mainly used in axial flux electric machines[43], [49], [50]. In [50], an axial flux electric machine with separated stator armature and a dual rotor/single stator topology is proposed, in which permanent magnets are mounted in a disk-type rotor yoke. With the continuous development of TFPMSM, the disk-type rotor structure is also gradually applied to transverse flux electric machines. In [51], a TFPMSM combined with independence between each phase and 72 pairs of poles fixed in a disk-type rotor structure by plastic material is proposed, which benefits from the low moment of inertia. However, the use of this structure requires multiple disk rotors in the axial direction for three-phase or multiphase machines, which increases the difficulty of assembly and manufacturing. To solve this problem, a three-phase TFPMSM with a single yokeless disk-type rotor structure is proposed in [42] and [46], as shown in Fig. 1.3. Compared with the rotor structure in [50], this type of rotor has lower mass and core loss. Compared with the rotor structure in the literature [51], this type of rotor is substantially less difficult to fabricate. However, the TFPMSM structure proposed in [42] and [46] still encounter assembly challenges that impede its suitability for mass production in industry, along with its oversized outer diameter that renders it unsuitable for installation within motion joints of industrial robots.

1.2 Electromagnetic analysis methods of TFPMSM

As mentioned earlier, the transverse flux electric machine is characterized by complex structure with a three-dimensional magnetic circuit. Therefore, its electromagnetic analysis methods are also relatively complex compared with the traditional electric machine. Nowadays, the electromagnetic analysis methods of electric mainly include numerical method and analytical method. However, the electromagnetic analysis using the analytical method is time-consuming and tedious, as it needs derive amounts of equations firstly and is only applicable to solving simplified systems of equations under specific conditions. In addition, some factors

such as the leakage in the electric machine cannot be accurately considered in the analytical formula, which leads to the low calculation accuracy of this method. Thus, the numerical method is generally preferred for achieving high-precision calculation results, with commonly used techniques including the FEM and the equivalent magnetic circuit method [52]. The FEM is the most accurate technique for analyzing electromagnetic performance, but it is also most time-consuming. Hence, for transverse flux electric machines, many researchers prefer to use the equivalent magnetic circuit method, which is faster and more efficient for calculations. In the 1970s, E.M. Freeman was the first to propose using the equivalent magnetic circuit model for analyzing a transverse flux cylindrical linear machine [53]. Since then, there has been a growing number of studies focused on the equivalent circuit model for transverse flux electric machines. In [54], the equivalent magnetic circuit method was used to analyze the magnetic field of a claw-pole transverse flux electric machine, and the results were used to predict the core losses of the electric machine with high computational accuracy. In [55], An improved equivalent magnetic circuit model was developed for claw-pole transverse flux electric machines. This model is based on the three-dimensional magnetic circuit structure, which includes magnetomotive force source and permeance, considering the distribution of the main and leakage flux path. The method also considers the nonlinear characteristics of the core, resulting in more accurate analysis results. In [56], a static field analysis model based on the TFPMSM equivalent magnetic circuit is proposed, which consists of a series-parallel combination of equivalent flux tubes from different parts of the electric machine.

However, the computational accuracy of the equivalent magnetic circuit method cannot fully satisfy the needs of engineering design. Thus, the equivalent magnetic network method, which combines the characteristics of the FEM and the equivalent magnetic circuit method with higher computational accuracy, is proposed and applied to the electromagnetic analysis of TFPMSM. This method divides the magnetic circuit into regular shaped flux tubes according to the flux density distribution in the electric machine, but the number of flux tubes is much smaller than the number of mesh sections in the FEM, so its computational speed is much higher than that of the FEM. In [57], a three-dimensional equivalent magnetic network model is used to analyze the static thrust of a transverse flux permanent magnet linear machine and parameters such as winding flux linkage and inductance. In [46] and [58], [59], the variable reluctance equivalent magnetic network model of the disk-type transverse flux electric machine is established to realize the accurate calculation of the air gap flux density and the winding flux linkage. In [60], a dynamic equivalent magnetic network model was proposed for TFPMSMs, which divides the stator-rotor teeth and air gap within a pair of magnetic poles into eight regions. The sub-network models in different regions are changed according to the relative positions between the stator and rotor during the rotation of electric machine. This approach converts the dynamic analytical model into a static magnetic network analytical model, allowing for the calculation of inductance, no load back EMF based on the solved winding flux linkage.

In addition to the above methods, electromagnetic analysis method based on conformal transformations were proposed by scholars and been used in the field of electric machine [61]–[66]. In [66], an analytical method based on conformal mapping and equivalent magnetic circuit model was proposed to calculate the back EMF and cogging torque waveforms of surface-mounted PMSM, which is more suitable for the analysis of complex structure transverse flux electric machines than the time-consuming FEM due to the short running time and high accuracy. In addition, the Schwarz-Christoffel transformation method, as a special form of conformal transformation, can map complex polygons into another complex-plane by way of conformal transformation to obtain a more regular geometry while keeping the electromagnetic field characteristics unchanged, so it is valuable for the analysis of complex structure electric machines[67]–[71]. In [72], a new type of transverse flux permanent magnet linear machine

(TFPMLM) is proposed, and its magnetic field characteristics are analyzed by the Schwarz-Christoffel transformation method.

1.3 Design optimization of electric machine

Design of electric machine is a complex and systematic task, and if only the electromagnetic design part is considered, the whole workflow can be briefly summarized using Fig. 1.4[73]. For conventional-structured electric machines, parameters design of electric machine can be done more easily by referring to previously summarized empirical coefficients as well as diagrams, and by using the magnetic circuit method for calibration [74]. However, for many electric machines with novel structures, including TFPMSM, there are not enough empirical coefficients and diagrams as design references in the process of design. And the magnetic circuit method is not always able to accurately calculate the performance of the electric machine. As a result, the design cycle for the electric machine is significantly extended.

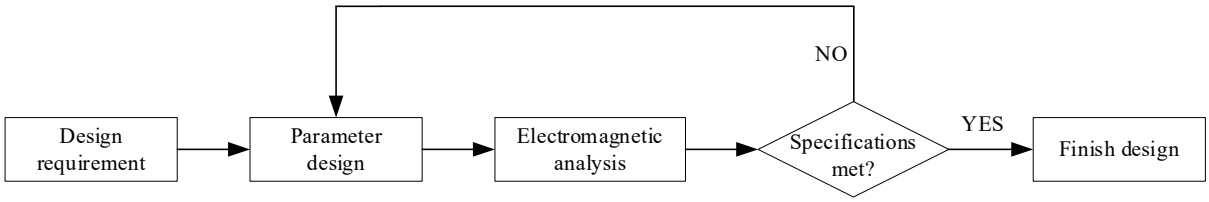

Fig. 1.4. The procedure of electric machine design

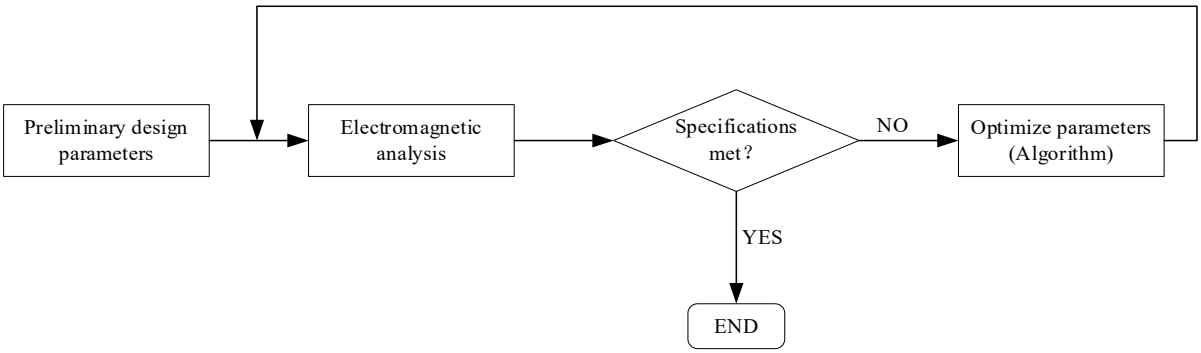

Fig. 1.5. The procedure of optimization design

In recent years, there has been rapid progress in computer technology, leading to the development of a series of intelligent optimization algorithms that possess global optimization capabilities. The intelligent optimization algorithms, such as genetic algorithms, are based on the principles of nature, particularly those observed in the biological world that are then abstracted and used to solve optimization problems[75]. In addition to the genetic algorithm (GA), various intelligent optimization algorithms such as simulated annealing (SA), ant colony optimization (ACO), and particle swarm optimization (PSO) have also been increasingly used in the optimization of electric machine and have demonstrated promising results.

(1) Genetic algorithm

Genetic algorithms are employed to achieve global optimization in the search for solutions to optimization problems by simulating the evolutionary mechanism of superiority and inferiority observed in biology. In [76], the algorithm was used to optimize a three-phase

squirrel-cage induction machine. By optimizing the design parameters of the electric machine, a significant improvement in efficiency was achieved while simultaneously reducing fabrication costs. In addition, some scholars have applied this algorithm to transverse flux electric machines[77] and axial flux electric machines[78].

(2) Simulated annealing algorithm

The simulated annealing algorithm is a global optimization algorithm based on the annealing mechanism of metallic materials, which applies thermodynamic principles from physics to mathematical statistics. In [79], The algorithm was utilized to optimize the design of a DC brushless electric machine and its results were compared with those obtained using the genetic algorithm. The comparison concluded that the optimization search process of the simulated annealing algorithm requires less time, while the genetic algorithm produces a better optimal solution.

(3) Ant colony algorithm

The ant colony algorithm is an optimization algorithm that was inspired by the behavior of ants searching for optimal paths during foraging [80]. In [81], the algorithm is used to optimize the design of a switching reluctance electric machine to maximize its output torque and efficiency.

(4) Particle swarm optimization algorithm

The particle swarm optimization algorithm was originally developed to simulate the unpredictable movement of a flock of birds. Over time, it evolved into the modern optimization algorithm we know today by incorporating concepts such as velocity matching, distance-based acceleration, and inertia weighting factors [82]. In [83], the algorithm was used to optimize the multi-objective design of a transverse flux linear machine to increase its rated thrust while reducing the weight and detent force.

Both the conventional electric machine design process shown in Fig. 1.4 and the optimization design process shown in Fig. 1.5 include the electromagnetic analysis procedure. Due to the high accuracy of the FEM in electromagnetic simulation calculations and the availability of a large number of reliable commercial software packages, such as ANSYS MAXWELL, JMAG, CST STUDIO SUITE from Dassault Aviation, and the open-source code_Carmel developed by L2EP laboratory in France, most researchers and engineers prefer the FEM for electromagnetic simulation calculations [84]. However, the FEM is limited by its computational speed, which leads to a significant extension of the design cycle. To eliminate the reliance on finite element calculations, researchers have proposed alternative methods such as the equivalent magnetic network method, which has fast computational capabilities, and the analysis method based on conformal transformation. For the TFPMSM with a 3D magnetic circuit structure, both the equivalent magnetic network method and the conformal transformation-based analysis method require significant computational time to obtain calculation results that are approximately equivalent to the FEM. When using an optimization algorithm to optimize electric machine, the number of individuals in the sample population and the number of optimization iterations need to be set. For instance, if 50 individuals are in the sample population and 100 iterations are required, it requires 5000 calculations, which consumes a significant amount of time and computational resources. To address this issue, a surrogate model has been proposed as an alternative to electromagnetic simulation, providing accurate results. A surrogate model is a bottom-up mathematical model based on pre-simulation or experimental data, which can be understood as a black box. Commonly used surrogate

modeling methods include support vector machine (SVM), response surface methodology (RSM), and artificial neural network (ANN)[85] .

(1) Support vector machines

Support vector machine (SVM) are supervised learning models used for data analysis in regression analysis and their associated learning algorithms. The use of SVs in regression modeling enables the establishment of a functional relationship between input and output parameters for both linear and non-linear problems [86]. In [86], SVM model is used to accurately fit a function between the design parameters of spherical electric machine and the output torque.

(2) Response surface method

The response surface method aims to estimate multivariate functions by fitting surfaces. For simpler models, regression models can be constructed using first-order polynomial fitting functions, whereas more complex models may require higher-order polynomials to be utilized [87]. In [83], a function between the weight of a transverse flux linear machine and its design parameters was constructed by a second-order response surface model. In [88], the second-order response surface model was used to accurately fit the relationship between design parameters of a double-side linear vernier PMSM and its thrust.

(3) Artificial neural network

Artificial neural network (ANN) is an interdisciplinary field that has gained popularity in recent years. It is an information processing system that is formed by the theoretical abstract, simplification, and simulation of the structure, function, and some basic features of the human brain's physiological neural network. In terms of systematic perspective, ANN is an adaptive, nonlinear dynamic system composed of a large number of neurons with highly interconnected connections. ANN is recognized as superior in recognizing and approximating complex nonlinear systems [89]. It has been widely used in mechanical engineering, distribution network engineering, geotechnical engineering, water conservancy, hydropower engineering, and structural engineering [90]–[93]. In [94], ANN model is developed to accurately fit the mapping relationships between the design parameters and the cost, weight, induced voltage amplitude and harmonic distortion rate of a switching linkage permanent magnet wind turbine.

In summary, in order to shorten design cycle and obtain optimal design, surrogate models and intelligent optimization algorithms should be introduced in electric machine optimization design. Particularly for novel structure electric machine like TFPMSMs, efficient electric machine optimization design methods can significantly reduce the development cycle and compensate for its shortcomings of complex structural parameters.

1.4 Multiphase machines

As mentioned earlier, the functional reliability of industrial robot systems can be effectively improved by using multiphase machines with intrinsic fault tolerant ability. The multiphase electric machine generally indicates a machine with more than three phases. Correspondingly, the characteristic of the electric drive for multiphase machine is that the VSI is consist of more than three legs as shown in Fig. 1.6. Compared with the traditional three-

phase electric machine, the multiphase machine also combines the advantages of low torque ripple and making full use of harmonic resources.

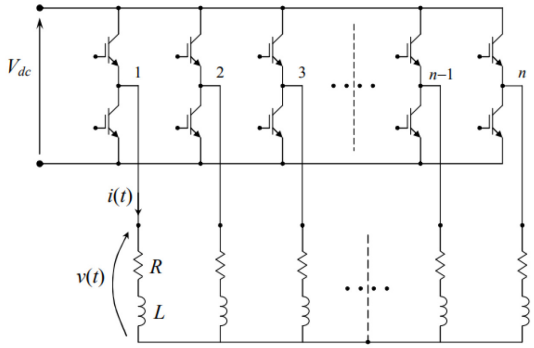

Fig. 1.6. Multiphase driving circuit

(1) Fault tolerant ability

For the traditional three-phase electric machine operating under one-phase open circuit fault condition, the neutral point of three-phase winding must be connected to the neutral point of the DC bus, otherwise it will be degraded to a theoretical single-phase machine and cannot operate normally as well as achieve self-starting. For a multiphase machine, when one or more phase-windings of the stator are open or non-supplied (fault in switching component or the connection between VSI and machine), the machine can still work under a derating state without the need to lead out the neutral line to the DC bus and the interruption maintenance immediately thanks to more than two degrees of freedom (DoF) remaining[95]–[97]. Through adopting an appropriate fault tolerant control strategy, the synthetic rotating magnetomotive force (MMF) trajectory produced by the remaining machine phase-windings is still circular [98], [99], and so the machine can continue to output constant torque. Therefore, the multiphase machine is greatly suitable for the occasions with requirement for high reliability where it is strictly forbidden to stop during operation, such as the automated manufacturing equipped with the industrial robots.

(2) Low torque ripple

As the number of machine phases increases, the order of spatial harmonics also increases, the frequency of torque ripple increases while the amplitude gets down off [100], thereby the noise and vibration of the machine during operation are eliminated [101], [102]. And the main purpose of the early research on multiphase machine is to reduce torque ripple. Although the PWM technology is becoming more and more mature nowadays, low-order harmonics existing in current can be neglected, but there is still torque ripple due that the air-gap harmonic magnetic field generated by nonlinear factors such as slotting of the machine stator interacts with the fundamental component of current. The more phases of the electric machine, the higher the torque ripple frequency generated by the fundamental current. For example, the lowest harmonic orders of torque ripple in 3-phase, 5-phase, and 7-phase electric machine are 6 [103], 10 [104], and 14 [26], respectively. For an asymmetric dual 3-phase machine with 30 degrees phasor shift, the lowest harmonics in torque ripple is twelve [105].

(3) Making full use of harmonic resources

For the multiphase machine, the constant torque can also be generated by the interaction between the harmonic components in current and related components in magnetic field while it is impossible for traditional three-phase machine. Thus, the torque density of the machine can be improved furtherly which is beneficial for the miniaturization of the electric machine. It can also be explained from another point of view by using of the decoupled reference frame. Different with the decoupled of the three-phase machine, the current or MMF vector can be transformed to sets of decoupled reference frames related with fundamental component and harmonic components respectively[106], [107]. The same order harmonics in both current and back-EMF (electromotive force) are transformed to one reference frame. Thereby, the harmonics in the multiphase machine can be controlled to produce constant torque.

Multiphase machine can be divided into two categories according to the connection form of stator windings: one is symmetric winding multiphase machine in which the n-phase windings are connected and the space angle between adjacent two phase-windings is $2\pi/n$, five-phase [108] and seven-phase machines [109] are the typical examples; the other category is asymmetrical winding multiphase machine, which are obtained by spatial displacement of multiple sets of star-connected windings isolated by neutral points that are also called split-phase machines, the most research are concentrated in the asymmetrical six-phase machine or dual three-phase (dual three-phase) machine with a phasor shift of 30° [110], [111].

Among the field of the multiphase machine, the most popular structure is the dual three-phase machine[112], [113] of which the control method is close to that of the conventional three phase machine. The phase band of the asymmetrical dual three-phase machine with the phasor shift of 30° is the same as that of the symmetrical twelve-phase machine, so the spatial distribution of its MMF is also same. Therefore, six times harmonics in torque ripple are eliminated, and the minimum order of torque ripple is up to 12th while it is 6th in traditional three-phase machine. Thus, the asymmetrical dual three-phase machine benefits from the greater advantages in suppressing torque ripple which is the reason why it attracts more attention.

Table 1.1. Different kinds of multiphase machine and its application

Type	Application
Induction machine	5-phase pump machine
FSCW PMSM (Surface mounted PM)	6- and 5-phase in wheel machine for EVs; 6-phase generator for gas turbine engine
FSCW PMSM (Interior PM)	5-phase marine propeller
Brushless PMSM	4- and 5-phase flight control surface actuator
Reluctance machine	5-phase axial flux machines for EVs
Brushless direct current machine	5-phase hydrostatic actuator for aerospace application
Superconducting machine	9- and dual 3-phase synchronous generator

Moreover, with regard to machine topology, a wide variety of multiphase machines have been investigated in existing studies. RPMSM is a commonly used type of multiphase machine, with much of the related research focused on winding design. In [114], P Zheng et al. introduced an alternate-teeth-wound concentrated winding configuration to the multiphase PMSM offering potentials of modular design and fault tolerant capability. In [115], a five-phase fractional-slot concentrating-winding permanent magnet synchronous machine (FSCW-PMSM) is analyzed and compared with a three phase FSCW-PMSM. Aiming at the dual three-phase PMSM, a novel asymmetrical stator winding is proposed of which the phase difference between two sets

of three phase windings is 27.7° (30° is angle used in classical structures). The novel unconventional dual three phase PMSM has an excellent torque quality and a slightly higher torque density level [116]. Recently, the novel topologies of multiphase machines have been gradually attaching more attentions. In reference [117], a novel special hybrid axial–radial flux focusing structure five phase PMSM which combines both radial and axial magnetic path is proposed for a variable speed constant frequency wind power generation application. F. Locment et al. proposed a 7-phase axial-flux double-rotor PMSM characterized by double rotor-single stator topology[118], [119]. F. Barrero et al. studied and summarized the design of multiphase machines and pointed that multiphase machine design moved from the stator winding arrangement and disposition toward novel machine structures with improved reliability and low weight [120]. And some typical examples were given in the thesis and listed as shown in Table 1.1. However, transverse flux permanent magnet machine (TFPM) as a type of high-performance novel structure machines has almost never been designed as a multiphase machine.

1.5 Research status of dual three-phase machine control methods

Similar with traditional three-phase electric machines, the control methods of dual three-phase machine also mainly include field-oriented control (FOC), direct torque control (DTC) and model predictive control (MPC).

(1) *FOC*

From the point of view of the control, it is necessary to convert an AC machine into its equivalent DC counterpart so that independent control of two currents that yields decoupled flux and torque control respectively. The set of control schemes that enable achievement of this objective is usually termed "FOC" or "vector control" methods[121]. If it is supposed that there is no harmonics in magnetic field, the energy conversion from electricity input to mechanical output only occurs in fundamental reference frame $\alpha 1$-$\beta 1$ (*d1-q1*). Thus, it is convenient to achieve the torque and field decoupled control liking the FOC method used for three-phase machine[122]. However, it brings out a new question that the components in harmonic reference frame $\alpha 1$-$\beta 1$ (*d2-q2*) is expected to be eliminated in order to reduce the copper loss[123]. The basic method is just setting the current components in harmonic reference frame $\alpha 1$-$\beta 1$ (*d2-q2*) to 0 [124], [125]. In [124], it is found that the current control in the *d2–q2* reference frame is also responsible for reducing the current harmonics, a notable reduction (fifth harmonic reduces 60% and seventh remains the same) is achieved by using the current control in the *d2–q2* reference frame. This method is easy to achieve, however, two more PI controller are needed compared with the FOC for three-phase machine. The two more PI controllers can be eliminated while the space vector pulse width modulation (SVPWM) is adopted[126], the voltage vector in fundamental reference frame is composed by four state vectors by which the synthesized voltage vector in harmonic reference frame is 0. Nevertheless, it is expected that the current in harmonic reference frame $\alpha 1$-$\beta 1$ (*d2-q2*) can be controlled well to generate the constant torque for a dual three-phase machine with non-sinusoidal back-EMF[127] and suppress the effect of the dead-time[123], [128].

(2) *DTC*

Generally, there is no need for the position of rotor in DTC, so the position sensor can be cancelled. Alternatively, the flux linkage and torque observer are needed to get the state of the machine. The switching signal of VSI is determined by the switching table. Since the

electromechanical energy conversion of dual three-phase machine is only related to the *α1-β1* reference frame, therefore, the stator flux linkage is estimated and partitioned on the *α1-β1* reference frame where the DTC based on the switching table (ST-DTC) of traditional three-phase machine can be directly applied with only small modification[129]–[131]. In [131] and [132], the influence of back EMF harmonics is investigated and a novel ST-DTC method to compensate the back EMF harmonics has proposed, thereby reducing the current harmonics. In [133], a ST with the multiple vector selection is established in which the two adjacent virtual voltage vectors and a null vector are selected in each control period, as a result, the switching sequences can also be generated easily.

Besides, the ST can also be replaced by PWM method by which a constant switching frequency is achieved[134], [135]. In [135], A DTC strategy for dual three-phase induction machine drives is proposed which is based on a predictive algorithm. The advantages include constant inverter switching frequency, superior transient and steady-state performance, and low distortion of machine currents[135].

(3) *MPC*

The MPC method can be seen as an advanced DTC, however, the rotor position is generally needed that is obtained by sensorless position estimator[136]–[139]. MPC method is based on Kalman's theory of the *minimum linear quadratic regulator of quadratic objective function*, in which the objective function is used to describe a more flexible optimization criterion and minimize it[140]. The MPC method is classified under two categories: continuous control set MPC (CCS-MPC) and finite control set MPC (FCS-MPC). The reference voltage in CCS-MPC method is obtained through a prediction model including constraint conditions, and then the predictive reference voltage is output through the PWM modulator[141]. The FCS-MPC method is similar to the DTC method where only a limited number of switching states are considered and the switching state with the smallest objective function is obtained through exhaustive calculation[142].

In [143], an MPC method adding a modulation stage based on a switching pattern with the aim of generating a fixed switching frequency for dual three-phase induction machine is proposed. In [144], a robust MPC scheme is proposed in order to release the parameter dependence of MPC in application of dual three-phase PMSM.

1.6 Fault tolerant control of dual three-phase machine

Being suitable for fault tolerant operation is an important characteristic of dual three-phase machines. The kinds of open-circuit and short-circuit faults occurring in the electric drive can be transformed into phase-winding open-circuit fault through hardware isolation and other measures. Therefore, the fault tolerant control (FTC) strategies for dual three-phase machines mainly focus on the open-circuit fault.

The objective of FTC is to enable the electric machine to operate under fault condition while still generating torque according to the control signal and limiting torque ripple within the allowable range[145]. This objective can be achieved by maintaining the circular rotating magnetic field of the electric machine during the fault condition. For the three-phase electric machine with an isolated neutral point shown in Fig. 1.7(a), the rotating magnetic field cannot continue to be formed using only one remaining degree of freedom when one phase winding is open. For the three-phase electric machine with neutral point connected to the ground shown in Fig. 1.7(b), there are still two degrees of freedom available for control to generate the rotating magnetic field when one phase winding is open, enabling fault tolerant operation under fault

condition[146]–[148]. However, neural point connected with ground of a three-phase electric machine leads to the existence of zero-sequence currents, making it difficult to be utilized for industrial robot.

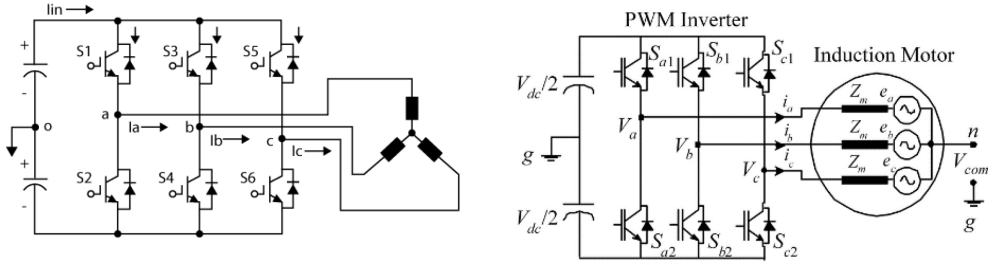

(a) (b)

Fig. 1.7. Three-phase electric machine: (a) Separated neutral point; (b) Neutral point connected with the power supply

In a dual three-phase machine with dual isolated neutral points, the electric drive system (as illustrated in Fig. 1.8) retains three degrees of freedom for control even under one-phase open-circuit fault condition. Thus, it can offer superior fault tolerant control compared to a three-phase electric machine and avoid the negative impacts associated with neutral point connected with ground in three-phase electric machine.

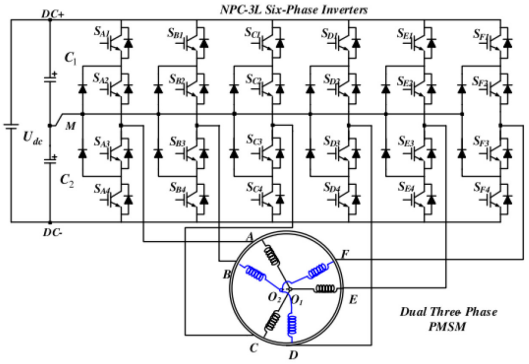

Fig. 1.8. Electric driving unit of dual three-phase machine

The current constraints of the dual three-phase electric machine under fault condition are changed. The use of reference current as in normal operating conditions would result in non-smooth torque output and preclude the attainment of fault tolerant operation under fault condition. As such, it is necessary to reconfigure the reference current based on the current constraints under fault condition[149], [150] . Generally, the reconfiguration of the reference current can be achieved on the natural coordinate system[151], [152]. Nevertheless, the electric machine voltage equations in the natural coordinate system incorporate differential coupling terms that complicate the regulation of stator current using PI controllers. As a result, certain studies have resorted to hysteresis loop current controllers for the control of current [153], [154]. Nonetheless, the fault tolerant control strategy that relies on hysteresis-loop current controller fails to account for the coupling between the two reference coordinate systems (*d1-q1* and *d2-q2*) under fault condition, and as a result, its control performance is suboptimal. To enhance the fault tolerant control performance of the electric machine and realize decoupled control of the current vector, a novel 5x5 transformation matrix has been proposed in previous research. This matrix establishes a reduced-order mathematical model of the dual three-phase machine in a fault condition [155]. Nevertheless, the fault tolerant control approach that utilizes the reduced-

order mathematical model necessitates the frequent adjustment of the decoupled transformation matrix in response to varying neutral connections and specific fault locations, thereby introducing a greater degree of complexity in practical applications [155]. As a result, an increasing number of studies have focused on the use of fault tolerant control methods that rely on the normal decoupled transformation matrix [156]–[158]. This approach simplifies the FTC strategy by employing the same decoupled transformation matrix for both normal and fault conditions of the electric machine.

Furthermore, FTC methods of dual three-phase machine can be classified from two perspectives, based on the various criteria for the reference current reconfiguration under fault condition: 1) the parameters that need to be maintained under fault condition and 2) the optimization objectives of the FTC method.

In terms of the first perspective, FTC methods for dual three-phase machines can be classified into two categories: 1) FTC methods based on constant synthetic magnetomotive force and 2) FTC methods based on constant power. The electromagnetic torque of the electric machine is generated by the interaction between the stator armature magnetic field and the rotor permanent magnetic field. Since the permanent magnetic field remains constant, it is necessary to maintain the synthetic magnetomotive force of the stator armature winding unchanged in order to ensure a smooth output of torque under fault condition[148], [152]. In [159], a method and detailed calculation procedure aiming to keep the synthetic magnetomotive force of the windings constant under open-circuit fault condition of a dual three-phase machine are proposed in which the synthetic magnetomotive force of the remaining five phases are constrained as same as that of normal condition, thus fault tolerant operation of the electric machine can be achieved. The FTC method based on invariant power is to ensure that the active power generated by the remaining healthy phases of the multiphase electric machine under fault condition is consistent with that under healthy condition. When the speed is constant, the electromagnetic torque output by the machine can be guaranteed to remain constant under fault condition. Besides, a more convenient method is to use the torque equation on decoupled reference frame, thereby, the electromagnetic torque can be expressed directly and then the average and ripple components can be controlled[155]. However, the above two methods are developed in the natural coordinate system. In [157], the normal decoupled transformation matrix is used to transform the current under fault condition to the *d1-q1* and *d2-q2* reference frames on which the torque equation is unchanged. Thus, the torque of the dual three-phase machine under fault condition can be calculated, then the torque is controlled unchanged by set the constant component equal to the torque value under healthy condition and ripple component to 0. However, the method proposed in [157] requires the use of an intelligent optimization algorithm to adjust the parameters to be determined in decoupled reference current in real time according to the torque reference value, increasing the difficulty for appliance.

In addition, in terms of the second perspective, the fault tolerant control methods for dual three-phase machine can be divided into the following two categories: FTC methods based on the principle of Minimizing Copper Loss (MCL) and FTC methods based on the principle of Maximizing Torque Operation Range (MTOR). The basic definition of MCL is that the reference current is reconfigured to minimize the copper loss in stator winding while the output torque of the electric machine is kept constant[151], [160]. In [151], a mathematical model of a dual *d-q* reference coordinate system for a dual three-phase PMSM is constructed and an FTC method based on MCL is designed.

However, MTOR-based FTC methods are more complex. By compiling the existing research, the methods can be divided into three categories as follows.

1) Solve the maximum output torque under a given phase current magnitude [156], [157], [161].

2) Output the desired torque while the maximum of the average copper loss in each phase is minimized [151].

3) Output the desired torque while the maximum of the current amplitude in each phase is minimized[162].

For the first category, the algorithms are often used to search the optimal solution [156], [157].

Chapter 2. Design of a novel disk-type transverse flux permanent magnet synchronous machine

The radial flux permanent magnet synchronous machine (RPMSM) is commonly used as a servo electric machine for industrial robots. However, its large axial length poses a challenge to the miniaturization and light weighting of robot motion joints. Moreover, the output torque of the electric machine is typically amplified by a gearbox in industrial robots, leading to an amplification of the moment of inertia of electric machine. Thus, the moment of inertia of electric machine becomes a crucial factor affecting the dynamic performance of industrial robots and needs to be considered during the design and optimization of electric machine using in industrial robots[11]. To address the aforementioned issues, a novel disk-type transverse flux permanent magnet synchronous machine applied for industrial robot applications was proposed in the thesis. The machine adopts a dual-stator single-rotor topology featuring a stator part made of a combined stator core using SMC material and laminated silicon steel sheet, and a yokeless disk-type structure for the rotor part. Thus, the proposed electric machine is named as DS-HSDR-TFPMSM. By design of DS-HSDR-TFPMSM according to the specific characteristics of industrial robot electric machines, the overall structure is more compact, which effectively reduces the size and weight of the electric machine. Additionally, the moment of inertia of DS-HSDR-TFPMSM is significantly reduced by the use of disk-type yokeless rotor, thereby improving its dynamic performance[42], [46]. Above all, the complexity of assembly and manufacturing of the newly proposed DS-HSDR-TFPMSM is reduced, and the magnetic leakage problem is also addressed. However, there are not design case considering the requirements for high functional reliability of industrial robot electric drive. To meet this need, DS-HSDR-TFPMSM can be improved through the introduction of multiphase machine. Among various types of multiphase machines, asymmetrical dual three-phase machines have similar winding structure and control method as conventional three-phase electric machine, while combining the benefits of low torque ripple, making them a more suitable option for application in the electric drive of industrial robot.

This chapter presents the research conducted from the perspective of the structure and parameter design of DS-HSDR-TFPMSM. Firstly, the structure, operation principle, and advantages of DS-HSDR-TFPMSM are analyzed in detail. Then, the basic sizing equation of DS-HSDR-TFPMSM are derived, and the design method as well as analysis process of other key parameters are presented. Finally, a dual three-phase fault tolerant design scheme for DS-HSDR-TFPMSM is proposed and analyzed through electromagnetic analysis.

2.1 Structure and operation principle of DS-HSDR-TFPMSM

2.1.1 Structure of DS-HSDR-TFPMSM

DS-HSDR-TFPMSM proposed in the thesis is obtained through the evolution of the existing disk-type TFPMSM. The evolution from the previous disk-type transverse flux PMSM (Structure 1) to DS-HSDR-TFPMSM proposed in the thesis (Structure 3) is shown in Fig. 2.1 [46]. Fig. 2.1 (a) shows the evolution of the main magnetic circuit of the disk-type TFPMSM. Firstly, the main magnetic circuit of this structure starts from the permanent magnet and enters the stator shoe and the "C-type" stator core in order to form a closed circuit. Then, a stator pole-shoe was added to the "C-type" stator core of Structure 1, resulting in a hybrid stator core structure (Structure 2). This configuration allows the main magnetic circuit to enter the stator shoe from the permanent magnet and then pass through the "C-type" stator core to form a closed

circuit. Finally, the main magnetic circuit of DS-HSDR-TFPMSM (Structure 3) is obtained by dividing the stator core, which is originally in the shape of "C" in Structure 2, into two "U"-shaped cores along the axisymmetric plane. And it can be found that the modification from Structure 2 to Structure 3 creates a new air gap in the main magnetic circuit. To enhance the magnetic field, a permanent magnet is added at the position of the new air gap. The main magnetic circuit of the three structures is extended in the circumferential direction, as depicted in Fig. 2.1 (b) which illustrates the evolution of the electric machine's overall structure. As shown in Fig. 2.1 (b), the modification from structure 1 to structure 2 results in a reduction in the slot open between the two adjacent stator cores, thereby improving the leakage problem of TFPMSM. Furthermore, the progression from structure 2 to structure 3 leads to the implementation of a double-stator single-rotor topology, which simplifies the fabrication and assembly process.

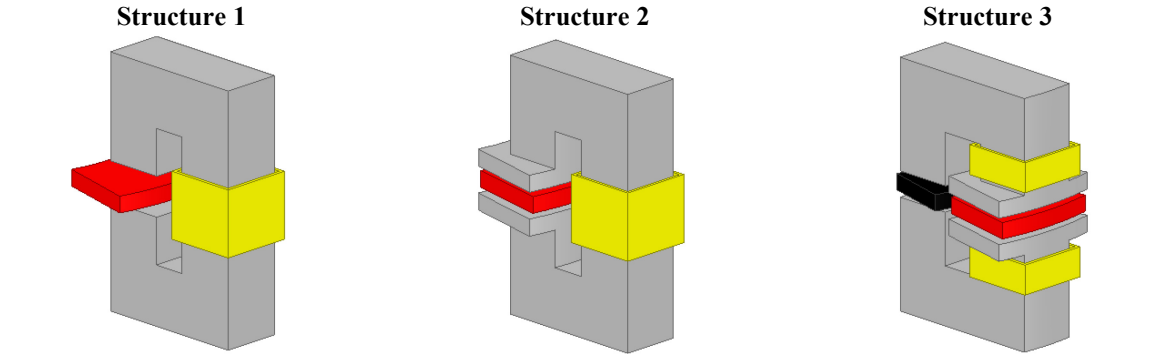

(a) The evolution of the main magnetic circuit

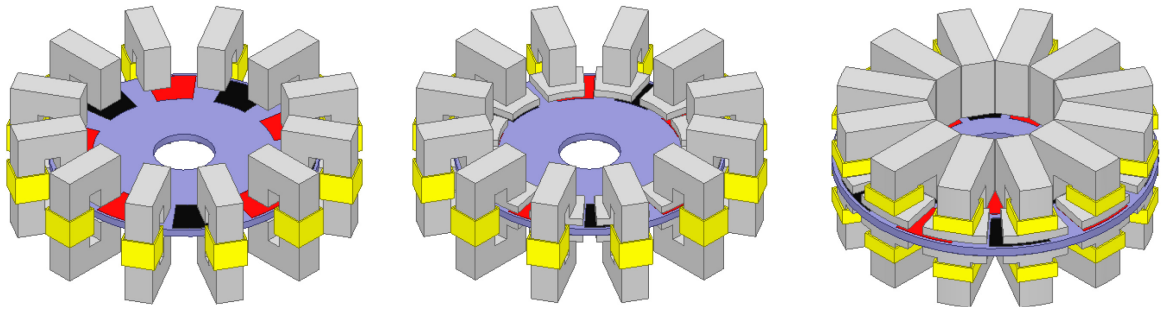

(b) Overall structural evolution process

Fig. 2.1 Evolution of the disk-type TFPMSM

Fig. 2.2 elaborates on the structure of DS-HSDR-TFPMSM. Fig. 2.2 (a) provides a three-dimensional view of the overall structure of the proposed machine, illustrating that two stator disks are symmetrically arranged on either side of the rotor disk. Each stator disk is comprised of separated stator armatures. Fig. 2.2 (b) depicts a single stator armature, demonstrating the use of SMC material for the stator shoe, which reduces the slot open area between adjacent stator cores and effectively decreases magnetic leakage. However, the stator core is still made of laminated silicon steel sheets to reduce stator core loss release saturation under high load condition. Additionally, the armature coil is inserted into the outer arm of the stator core, which connects to the SMC stator shoe, to provide enough space inside the stator disk.

To reduce the size, weight, and loss of the rotor part, a yokeless disk rotor structure is utilized in DS-HSDR-TFPMSM, as shown in Fig. 2.2(c). The rotor permanent magnets are embedded in a non-permeable flanged disk and are divided into two layers along the radial direction, with each layer containing the same number of alternating N and S poles permanent magnets. The polarities of the two adjacent permanent magnets along the radial direction are opposite.

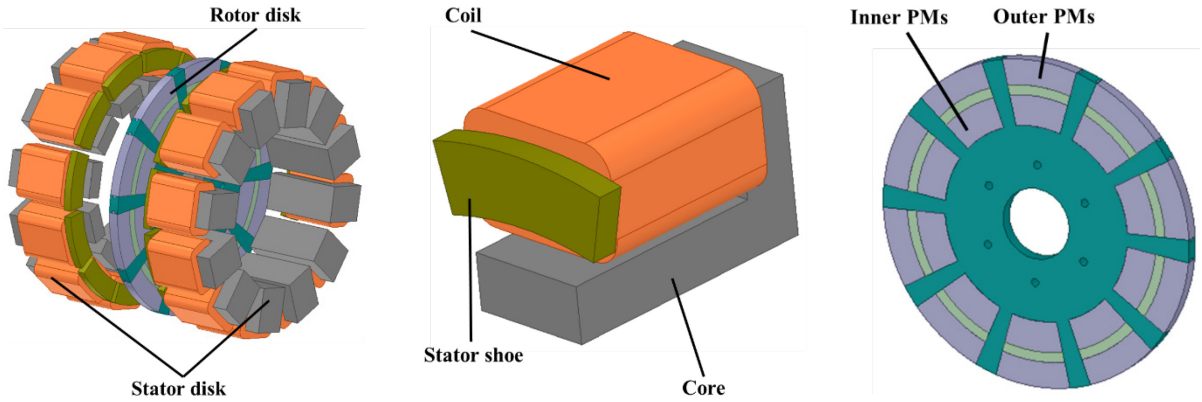

(a) Overall structure (b) Stator armature structure (c) Rotor structure

Fig. 2.2 Structural diagram of DS-HSDR-TFPMSM

2.1.2 Operation principle

According to the classical electromagnetism theory, as the winding flux linkage keeps changing, the electromotive force induced in the winding. If the electric machine adopts $I_d = 0$ control method, then the alternating current with the same phasor of induced electromotive force is input to the winding. As per the law of conservation of energy, the active power generated during operation is converted into electromagnetic torque. The resulting output torque produced by a single phase winding can be represented as a constant value superimposed on the second harmonic component. In the case of a three-phase electric machine, the output torque can be stabilized by superimposing the output torque produced by each of the three phase windings, which cancels out the second harmonic component. Therefore, it can be inferred that the production of alternating flux linkages in the windings, leading to alternating induced electromotive force, is the crucial element to ensure that the electric machine generates electromagnetic torque.

DS-HSDR-TFPMSM is characterized by separated stator armature and yokeless rotor structure and thus it is also characterized by independent magnetic circuits. Thus, the single magnetic circuit of Structure 3 shown in Fig. 2.1(a) is utilized to analyze the alternating flux linkage in the windings. The flux linkages in remaining windings are subsequently derived through the spatial phasor difference.

Fig. 2.3 shows the flux path of the single magnetic circuit of DS-HSDR-TFPMSM. It can be seen that the magnetic circuit consists of the inner and outer air gaps, forming a closed circuit via two symmetrical "U-shaped" cores. As illustrated in Fig. 2.3, the two armature coils are with identical polarity along the axial direction. Consequently, both coils belongs to the same magnetic circuit generate a magnetic field in the same direction when the same current is applied.

The main magnetic circuit of DS-HSDR-TFPMSM comprises two permanent magnets with opposite polarity located inside and outside respectively. In order to simplify the analysis, the magnetic circuit is segmented into two cross-sections along the two permanent magnets, as illustrated in Fig. 2.4 (a). As the rotor permanent magnet moves, the flux through the stator armature core changes continuously. When the rotor permanent magnet reaches positions A and C, the flux interconnected with the stator coil cancels each other. Conversely, when the rotor permanent magnet reaches at positions B and D, the flux interconnected with the stator coil reaches maxima and minima, respectively. Fig. 2.4 (b) shows the flux linkage and electromotive force waveforms induced by a single coil. Due to the three-phase symmetrical

winding structure of DS-HSDR-TFPMSM, a stable output torque can be synthesized eventually, thus driving the electric machine operation.

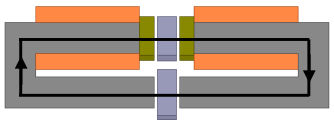

Fig. 2.3. Flux path of main magnetic circuit

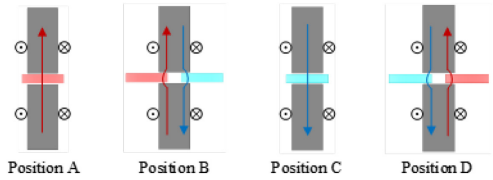

(a) Magnetic flux path diagram at each position

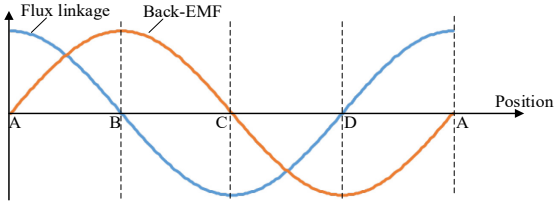

(b) Alternating flux linkage and back-EMF

Fig. 2.4 Operation principle of DS-HSDR-TFPMSM

2.1.3 Superiorities of DS-HSDR-TFPMSM

A servo electric machine is required for each joint of an industrial robot to drive the subsequent robot arm linked to that joint. In case of a power loss, accidents may occur if the servo electric machine lacks a protection device, causing the arm to be displaced by inertia or gravity. To ensure the safety of the system, most industrial robot servo electric machines integrate brakes inside the electric machine to achieve the "holding" function under power failure condition. Traditional RPMSM for industrial application, as shown in Fig. 2.5 (a), usually equips the brake mounted at the front of the electric machine, which increases the axial length of the electric machine. Furthermore, components such as bearings and encoders occupy additional axial space, hindering the miniaturization of industrial robot electric machines.

The application of DS-HSDR-TFPMSM can address the issues mentioned above. As shown in Fig. 2.5(b), the space layout inside the industrial robot electric machine can be reconfigured by DS-HSDR-TFPMSM, which is designed with space reserved inside the stator disk for brakes, bearings, encoders, etc. resulting in a more compact overall structure of the electric machine due to the optimization of the axial length and thus the miniaturization of the industrial robot electric machine can be achieved.

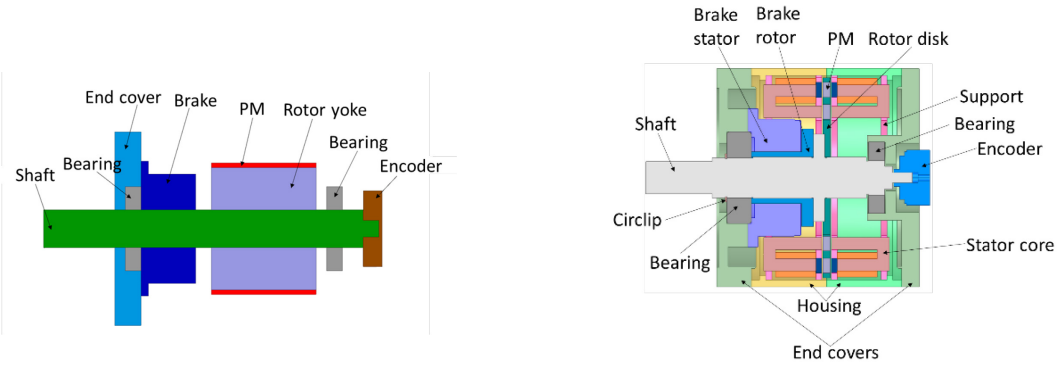

(a) RPMSM (b) DS-HSDR-TFPMSM

Fig. 2.5 The layout of electric machines applied to industrial robot

Besides, the use of DS-HSDR-TFPMSM as an industrial robot electric machine offers the advantage of low moment of inertia due to the disk-type yokeless rotor disk. The moment of inertia is calculated by (2-1), and it can be found that moment of inertia is proportional to mass and the square of the radius. Compared to the RPMSM, DS-HSDR-TFPMSM is characterized by a larger rotor radius, yet significantly lighter and smaller volume. A commercial RPMSM product was selected for a moment of inertia study with DS-HSDR-TFPMSM. And the result of comparison shows that DS-HSDR-TFPMSM exhibited a 54.2% reduction in inertia, thus leading to superior dynamic performance.

$$J = \iiint mr^2 dV \tag{2-1}$$

where V denotes the volume differential element of the rotor disk, m denotes the mass, and r denotes the vertical distance from the center point of the volume differential element to the center of the rotation axis.

In addition to the two advantages mentioned above, DS-HSDR-TFPMSM offers improved fault tolerant ability thanks to its separated stator armature structure which creates magnetic isolation by ensuring that the magnetic circuits in the two adjacent stator cores along the circumferential direction are independent from each other. As a result, a better fault tolerant ability can be achieved.[43]

2.2 Design method of DS-HSDR-TFPMSM

2.2.1 Basic sizing equation of DS-HSDR-TFPMSM

Both the traditional electric machine structure and the new DS-HSDR-TFPMSM structure proposed in the thesis require the determination of specific dimensional parameters for each part of the electric machine structure through electromagnetic design, providing a reference for subsequent electric machine simulation and prototype fabrication. The primary research content of the electromagnetic design of an electric machine is the main dimensional design of the electric machine. By deriving the sizing equation of the electric machine, the relationship between the primary performance parameters of the electric machine and its main dimensional parameters can be determined, allowing for the determination of the basic dimensional outline of the electric machine.

Firstly, all dimensional parameters of DS-HSDR-TFPMSM are given, as shown in Fig. 2.6.

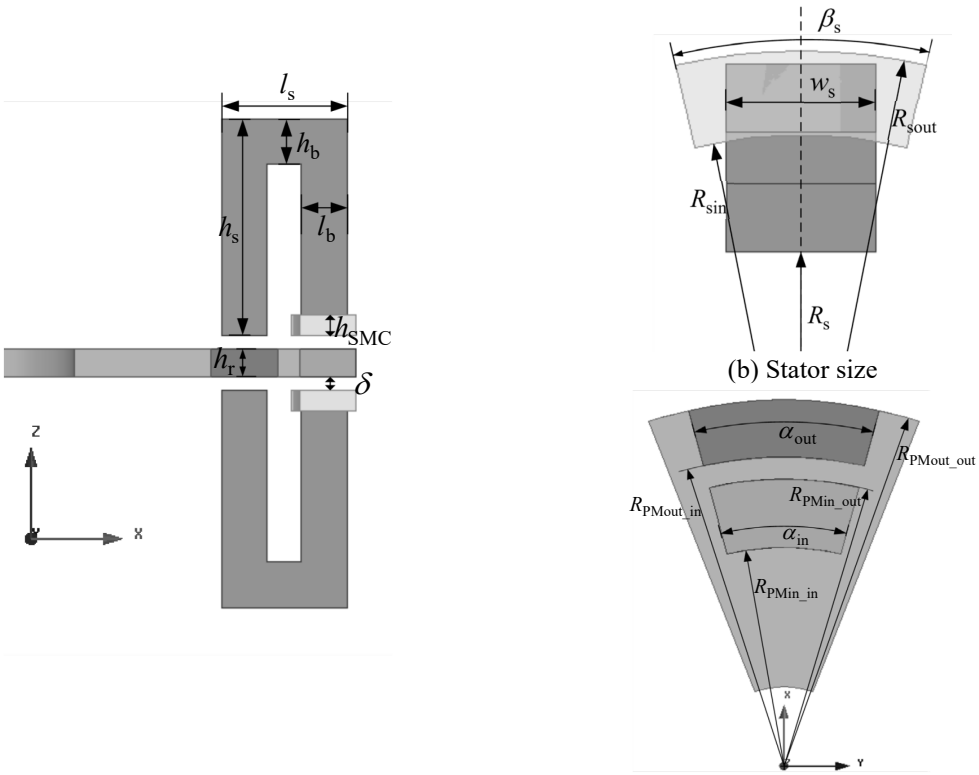

(a) Sectional size (b) Stator size (c) Rotor size

Fig. 2.6 Dimensional diagram of DS-HSDR-TFPMSM

The electrical load is a crucial parameter in determining the main dimensions of the electric machine and is typically defined as the ratio of the algebraic sum of the number of turns of the three-phase winding to the average perimeter of the electric machine armature. However, due to the unique structure and operating principle of DS-HSDR-TFPMSM, its definition of electrical load A differs from that of conventional electric machines. Given the concentrated winding structure of DS-HSDR-TFPMSM, the definition of electrical load A can be modified based on that of the common radial flux concentrated winding electric machine. Finally, the calculation equation for the electrical load A of DS-HSDR-TFPMSM is expressed by combining the definition of electrical load with the specific structural parameters of DS-HSDR-TFPMSM:

$$A = \frac{mN_{\text{phase}}I}{\pi(R_s + l_s - \frac{l_b}{2})} \tag{2-2}$$

where,

I - electric machine phase current.

m - number of phases.

N_{phase} - the number of series turns of one phase winding.

The voltage factor k_u is defined as

$$k_u = \frac{E}{U} \tag{2-3}$$

where,

E – No load back-EMF of the electric machine.

U - Input phase voltage.

If we consider only the fundamental component of the magnetic field in DS-HSDR-TFPMSM, the back-EMF E can be expressed as:

$$E = 2\pi f \Phi N_{\text{phase}} k_{\text{w}} / \sqrt{2} \tag{2-4}$$

Where k_{w} denotes the winding factor and f denotes the operating fundamental frequency.

$$f = np / 60 \tag{2-5}$$

Where, n is the electric machine speed in unit (rpm).

When symmetrical three-phase currents are passed into the symmetrical three-phase windings of the electric machine, the output power of the electric machine can be expressed as

$$P = \eta m U I \cos\varphi \tag{2-6}$$

where,

η -- Efficiency;

$\cos\varphi$ -- Power factor.

Combining equation (2-2) - (2-4) into equation (2-6), it can be obtained that:

$$P = \eta \frac{\sqrt{2}\pi^2 f \Phi k_{\text{w}} A(R_{\text{s}} + l_{\text{s}} - \frac{l_{\text{b}}}{2})}{k_{\text{u}}} \cos\varphi \tag{2-7}$$

Since the magnetic circuits of adjacent stator cores along the circumferential direction of DS-HSDR-TFPMSM are independent from each other, the magnetic flux of DS-HSDR-TFPMSM can be determined by analyzing the magnetic circuit of individual stator core. Ignoring the leakage of electric machine and using the air gap flux density at the inner permanent magnet position to calculate the main flux, the expression for the main flux of DS-HSDR-TFPMSM Φ can be obtained as:

$$\Phi = B_{\delta 2} S_2 = B_{\delta 2} w_{\text{s}} l_{\text{b}} \tag{2-8}$$

Where, $B_{\delta 2}$ is the amplitude of the air gap flux density at the position of the inner permanent magnet.

The width of stator core w_s can be expressed as:

$$w_{\text{s}} \approx k_{\text{s}} \frac{\pi R_{\text{s}}}{6} \tag{2-9}$$

Where, k_{s} is the pole-arc coefficient corresponding to the stator core width.

Define the stator core diameter ratio γ as the ratio of stator core's outer diameter to inner diameter:

$$\gamma = \frac{R_{\text{s}} + l_{\text{s}}}{R_{\text{s}}} \tag{2-10}$$

γ is an important factor in the design process of disk-type machine. When the inner diameter or outer diameter of the disk-type machine is given, the maximum output power can be obtained by optimizing γ. Regarding DS-HSDR-TFPMSM, when the value of γ is set small, the winding space of the electric machine is limited, resulting in densely packed windings and overload issues that can lead to significant temperature rise of electric machine. In contrast, if γ is set large, the overall size of the electric machine may exceed the standard, or the inner

diameter space will be insufficient to accommodate bearings, brakes, and other accessories. In addition, a large value of γ also increases the weight of electric machine. Typically, for small to medium-sized disk-type machines, the value of γ is set between 1.5 and 1.7. In the initial design of DS-HSDR-TFPMSM, the value of γ = 1.6 was set.

To ensure that the "U-shaped" stator core of the electric machine can provide sufficient space for winding, the radial height of the stator core l_s is set as follows

$$l_s = 3l_b \tag{2-11}$$

Combining equation (2-8) - (2-11) into equation (2-7), it can be obtained that:

$$P = \eta \frac{\sqrt{2}\pi^3 n B_{\delta 2} k_s k_w A R_s^3}{240 k_u} \cos\varphi \tag{2-12}$$

Ultimately, the basic sizing equations for DS-HSDR-TFPMSM is as follow:

$$R_s = \frac{1}{\pi} \sqrt[3]{\frac{240 k_u P}{\sqrt{2}\eta n B_{\delta 2} k_s k_w A \cos\varphi}} \tag{2-13}$$

By the basic sizing equation (2-13), it is possible to initially determine the position of the stator core along the radial direction R_s, a parameter that is proportional to the electromagnetic power and inversely proportional to the speed, the magnetic load, the electrical load and the stator core width. Then, by means of (2-10) and (2-11), the stator core cross-section height l_b and the total radial height l_s can be further calculated. The axial length dimensions of stator core will be finally determined by the winding design parameters.

2.2.2 Design based on equivalent magnetic circuit

Among the design of electric machines, the working point of permanent magnets reflects the utilization rate of permanent magnets and helps designers to establish a magnetic field with maximum magnetic energy product in the air gap of electric machine using a limited volume of permanent magnets. Thus, the calculation of the working point of permanent magnets is of great importance.

The equivalent magnetic circuit method is usually used to calculate the operating point of the permanent magnet. For the equivalent magnetic circuit of DS-HSDR-TFPMSM, the equivalent MMF as well as internal permeability of the permanent magnet, the main and leakage permeabilities are the most important components of the equivalent magnetic circuit, as shown Fig. 2.7.

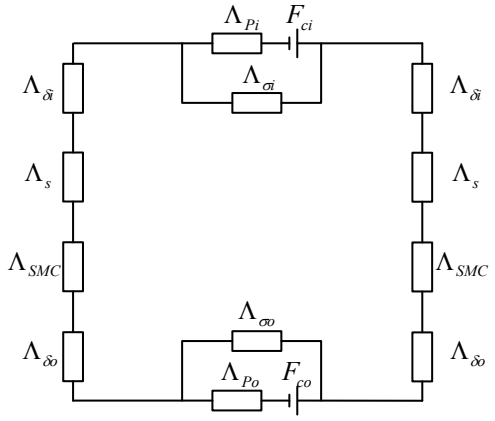

Fig. 2.7 Equivalent magnetic circuit diagram of DS-HSDR-TFPMSM

The main flux as well as the leakage flux of electric machine can be roughly estimated using the equivalent magnetic circuit given in Fig. 2.7. Then, the leakage coefficient of the electric machine σ can be derived. Finally, the no load operating point of the permanent magnets is calculated as:

$$b_{\mathrm{mo}} = \frac{\sigma}{\sigma + \mu_{\mathrm{r}} \delta / h_{\mathrm{r}}} \tag{2-14}$$

where μ_{r} denotes the relative permeability of the permanent magnets.

From equation (2-14) it can be seen that the working point of the permanent magnet is closely related to the length of the air gap as well as the thickness of the permanent magnet. In addition, the calculation of the leakage coefficient σ also depends on the above two parameters. Therefore, the air gap length and the thickness of the permanent magnet need to be reasonably designed to reach the best working point. Besides, the actual machining technology of electric machine must be taken into account. For example, the thickness of the permanent magnet needs to consider the structural strength of the rotor; the design of air gap length needs to consider the assembly process and the potential axial displacement of the rotor disk.

In addition, the radial dimensions of the permanent magnets also have an impact on the working point of the permanent magnets, mainly by affecting the leakage coefficient σ . The permanent magnet structure of DS-HSDR-TFPMSM is shown in Fig. 2.6, two sizes of permanent magnets are used. In the initial design, the radial height of the outer permanent magnet and the stator shoe are kept at the same height:

$$R_{\mathrm{PMout\_out}} - R_{\mathrm{PMout\_in}} = R_{\mathrm{s\_out}} - R_{\mathrm{s\_in}} \tag{2-15}$$

The radial height of the inner PM in the initial design needs to be slightly larger than the radial height of the outer PM in order to make permeability values of both inner and outer PMs as similar as possible, and then the equivalent MMF sources of the inner and outer PMs are similar under the condition of the same thickness, contributing to the similar working points pf both outer and inner PMs. In addition, the effective flux area of the air gap can be increased by increasing the radial height of the permanent magnet, but it also results in a larger magnetic leakage coefficient. Thus, the radial height of the PMs needs to be determined according to specific practical requirements.

2.2.3 Slot/pole combinations choice for DS-HSDR-TFPMSM

DS-HSDR-TFPMSM features a separated stator armature topology, which makes it particularly suitable for concentrated winding. The concentrated winding structure can be further categorized as either integral slot concentrated winding or fractional slot concentrated winding. The integral slot concentrated winding electric machine is characterized by number of slots per pole per phase q=1, while the fractional slot concentrated winding is characterized by number of slots per pole per phase q that is less than 1. Due to the advantages of integral slot concentrated winding to significantly reduce torque ripple when compared to the integral slot concentrated winding electric machine, most studies prefer the fractional slot concentrated winding. In [163], a systematic comparison and summary of above two slot/pole combinations of electric machines is reviewed, and it is concluded that the fractional slot concentrated winding electric machine benefits from significant advantages including low torque ripple and large speed range under flux-weakening condition.

Table 2.1 summarizes the commonly used slot/pole combinations for fractional slot concentrated windings. The selection of slot/pole combinations significantly influence performances of electric machine, therefore the performance indexes for each combination are

compared in Table 2.1, including the winding factor k_w and the least common multiple (LCM) between the number of slots and poles. According to the basic design theory of electric machine, increasing the winding coefficient can improve electric machine torque density, while increasing the LCM can reduce peak-to-peak value of cogging torque.[164] Therefore, it is necessary to choose the slot/pole combination with large winding coefficient and LCM.

Table 2.1 Commonly used fractional slot concentrated winding combination

combination	q	k_w	LCM
9/6	1/2	0.866	18
6/8	1/4	0.866	24
9/8	3/8	0.945	72
12/8	1/2	0.866	24
9/10	3/10	0.945	90
12/10	2/5	0.933 or 0.9659	60
15/10	1/2	0.866	30
9/12	1/4	0.866	36
18/12	1/2	0.866	36

Note: The combination is expressed in the form of (amount of slots/number of poles)

For DS-HSDR-TFPMSM, the number of stator slots is also the number of stator armatures in one stator disk. Thus, the increase of the number of stator slots will make the manufacture of electric machine difficult, especially for DS-HSDR-TFPMSM with low to medium power and small outer diameter. Therefore, the number of stator slots needs to be controlled within a reasonable range. In addition, in order to improve the reliability of the electric drive of industrial robots, DS-HSDR-TFPMSM proposed in the thesis needs to be designed considering the modification to a fault tolerant multiphase machine. Thus, the chosen slot/pole combinations need to be appropriately adapted to a multiphase machine winding structure. Based on the review on multiphase machines, DS-HSDR-TFPMSM with an asymmetric dual three-phase winding structure is deemed more suitable for industrial robots. This type of electric machine achieves fault tolerant ability while further reducing torque ripple, and its control method is similar to that of traditional three-phase electric machines. Hence, DS-HSDR-TFPMSM is selected with a 10-pole/12-slot combination. Specifically, each stator disk of the electric machine consists of 12 separated stator armatures, and the inner and outer layers of the rotor disk both contain 10 permanent magnets with alternating polarity arrangements.

2.2.4 Design of stator core

According to the basic sizing equation (2-13), the relationship between the radial position of the stator core R_s and the stator core width w_s can be determined. In order to reduce the radial dimension of DS-HSDR-TFPMSM, the value of R_s can be taken with reference to the maximum outside diameter of the brake, and then the stator core width w_s can be determined. And the axial length of the stator core need to be designed according to the electrical load A, the current density J and the slot fill factor K_{fill}.

Due to the special structure of DS-HSDR-TFPMSM, the slot fill factor K_{fill} is calculated from two perspectives: K_{fill1}, the slot fill factor between two adjacent stator cores along the circumference; K_{fill2}, the slot fill factor for a single "U-shaped" stator core. The both slot fill factors are shown in Fig. 2.8. According to Fig. 2.8 (a) and Fig. 2.8 (b), the slot fill factors can be expressed as:

$$K_{fill1} = \frac{2w_c}{w_{t1}} \tag{2-16}$$

$$K_{\text{fill2}} = \frac{w_{\text{c}}}{w_{\text{t2}}} \tag{2-17}$$

In the design of electric machine, it is necessary to ensure that the thickness w_{c} can make both K_{fill1} and K_{fill2} smaller than the design threshold.

After determining the coil thickness w_{c}, the axial length of the armature coil can be calculated from the electrical load A and the current density J, which furtherly determines the axial length of the stator core:

$$l_{\text{c}} = \frac{\pi A \cdot (R_{\text{s}} + l_{\text{s}} - l_{\text{b}}/2)}{2QJw_{\text{c}}} \tag{2-18}$$

where Q denotes the number of stator armatures in a single stator disk.

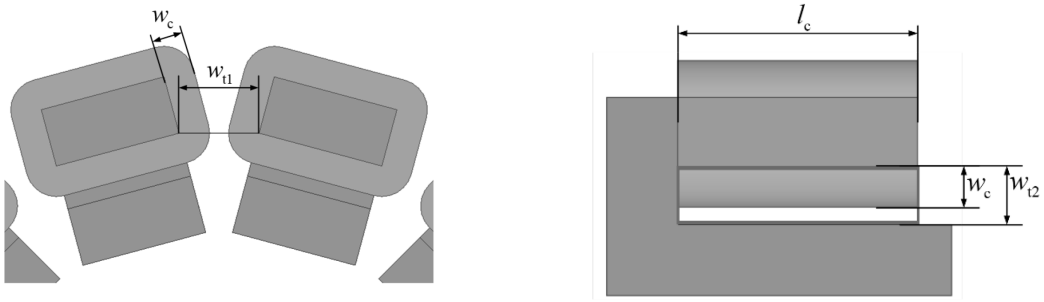

(a) K_{fill1} (b) K_{fill2}

Fig. 2.8 Slot fill factor of DS-HSDR-TFPMSM

2.2.5 Preliminary design parameters

The main objective of this research is to design a DS-HSDR-TFPMSM with 5.4kW rated power and 17.2Nm rated torque. the main performance requirements of the electric machine are shown in Table 2.2 The main performance requirements of the electric machine are listed in detail in Table 2.2.

Table 2.2 Performance requirement for DS-HSDR-TFPMSM

Parameters	Unit	Numerical value
Power Rating	kW	5.4
Rated torque	Nm	17.2
Rated current	A	12.5
Rated speed	r/min	3000
Winding structure		Three-phase Y connection
Cooling method		Natural

Through the preliminary design, the dimensional parameters of DS-HSDR-TFPMSM were obtained in Table 2.3.

Based on the electric machine design parameters given in Table 2.3, the electromagnetic analysis model of DS-HSDR-TFPMSM is established using ANSYS MAXWELL, and the electric machine performance under no load condition as well as rated condition is calculated. The finite element calculation results of the electric machine are presented in Fig. 2.9. The no load back-EMF is calculated under the rated speed condition as shown in Fig. 2.9(a). The symmetrical three-phase winding back-EMF can be observed, and the root mean square (RMS) value all are 159 V. The rated output torque waveform of the electric machine is shown in Fig. 2.9(b) which was obtained under the condition of the rated current. The average value of the

rated torque is 17.26 Nm, while the torque ripple is 9.05%. In conclusion, the preliminary design parameters of DS-HSDR-TFPMSM satisfy the requirements specified in Table 2.2.

Table 2.3 Initial design dimensional parameters of DS-HSDR-TFPMSM

Parameters	Symbols	Unit	Numerical value
Number of rotor poles	p		5
Number of stator slots	Q		12
Pole arc coefficient of outer PMs	a_{out}		0.78
Pole arc coefficient of inner PMs	a_{in}		0.78
Outside diameter of outer PM	$R_{\text{PMout\_out}}$	mm	83
Inside diameter of outer PM	$R_{\text{PMout\_in}}$	mm	72
Outside diameter of inner PM	$R_{\text{PMin\_out}}$	mm	62.5
Inside diameter of inner PM	$R_{\text{PMin\_in}}$	mm	49.5
Thickness of PMs	h_{r}	mm	6.5
Pole-arc coefficient of stator shoe	β_{s}		0.9
Thickness of stator shoe	h_{SMC}	mm	5
Section width of stator core	w_{s}	mm	22.8
Section height of stator core	l_{b}	mm	10.5
Axial length of stator core	h_{s}	mm	50.5
Radial position of stator core	R_{s}	mm	51
Single-side air gap length	δ	mm	1.2
Number of turns of coil	N		62

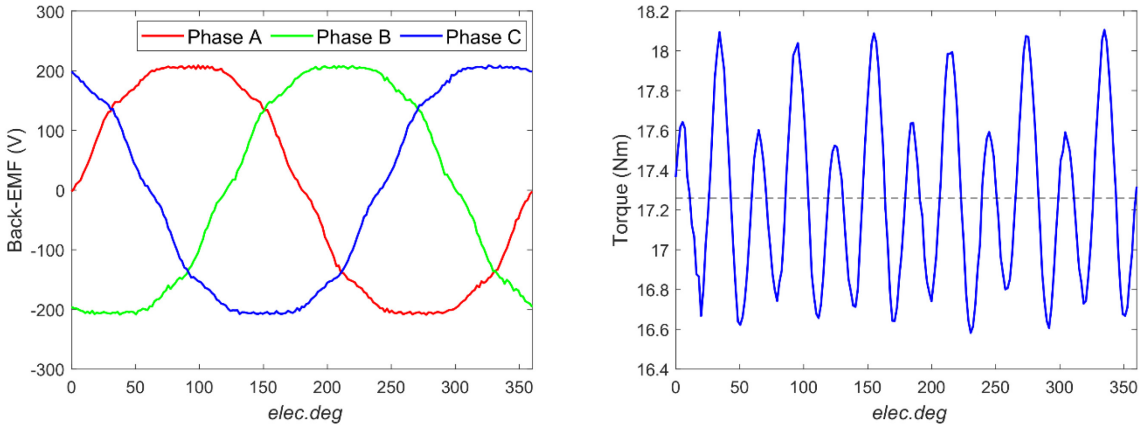

(a) No load back-EMF

(b) Rated torque waveform

Fig. 2.9 FEM results of DS-HSDR-TFPMSM

2.3 Analysis of dimensional parameters

In the preliminary design of the electric machine, a set of design parameters as shown in Table 2.3 satisfying the performance requirements is obtained by the derivation of the basic sizing equation of DS-HSDR-TFPMSM and the design of equivalent magnetic circuit, slot/pole combination, as well as stator core. However, upon the results from the electromagnetic simulation for the preliminary design, it can be found that the torque ripple is high leading to the noise and fluctuation of the machine. Therefore, the further adjustment to the dimensional

parameters is necessary. In the conventional electric machine structure, the size of stator tooth and the pole-arc coefficient of PMs are the primary parameters affecting the cogging torque of the machine. Thus, it is crucial to investigate and adjust the pole-arc coefficient of PMs and dimensional parameters of stator shoe to improve the torque performance, especially the torque ripple.

2.3.1 Parametric analysis of pole-arc coefficient of PMs

DS-HSDR-TFPMSM is a novel structure machine of which the rotor disk consists of outer and inner layers PMs. Variations in the pole-arc coefficient of both layers impact the effective flux area of the air gap, resulting in the influence on the torque.

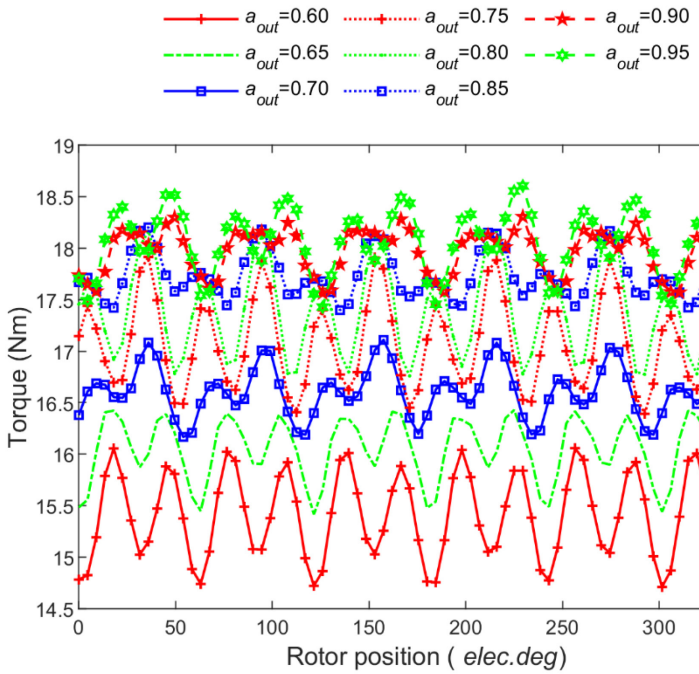

(a) Torque waveform

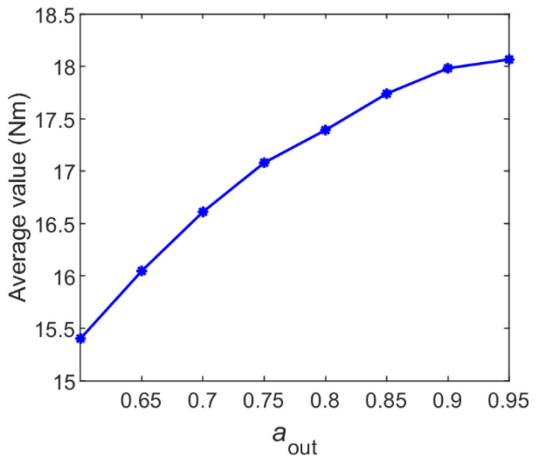

(b) Variance of average value

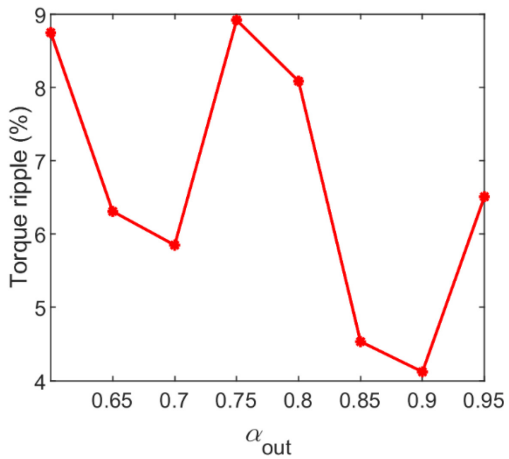

(c) Torque ripple

Fig. 2.10 The influence of the outer PM pole-arc coefficient a_{out} on the output torque

Firstly, the pole-arc coefficient of outer PMs a_{out} is analyzed. The output torque of the electric machine under rated current varies with the change of pole-arc coefficient of outer PMs a_{out} as shown in Fig. 2.10. Fig. 2.10 (a) shows the variation of the torque waveform, and it can be seen that the torque waveform will be displaced upward overall with the increase of a_{out}, and this phenomenon can be more easily seen from Fig. 2.10 (b) in which the variation of the average torque value is given. In addition, it can be found that the average torque value increases from 15.4 Nm to 18 Nm during the change of a_{out} from 0.6 to 0.95, which is mainly due to the increase of the effective flux in the main magnetic circuit as the cross-sectional area of the outer permanent magnet is enlarged with the increase of a_{out}. However, the increasing process of torque is not linear, but gradually slows down with the increase of a_{out}. In addition, the variation of average torque starts to level off when a_{out} reaches 0.9. The torque ripple of the electric machine varies as a_{out} is shown in Fig. 2.10 (c). It can be found that the torque ripple shows a "W-shaped" variation pattern with the increase of a_{out}. When a_{out} reaches 0.7, the torque ripple reaches the first minimal point and then rises rapidly. The minimal value of 4.1% is achieved when a_{out} reaches 0.9. In summary, it is preferred to select values between 0.85 and 0.9 for a_{out}.

The effect of the pole-arc factor of inner PMs a_{in} on the torque is shown in Fig. 2.11. As shown in Fig. 2.11 (a), the output torque waveform is gradually shifted upward with the increase of a_{in}. The average value of torque varies with a_{in} as shown in Fig. 2.11(b) and it can be seen that the average torque value increases from 16.9Nm to 17.5Nm while a_{in} changes from 0.6 to 0.95. Therefore, the ability to improve the average torque value by adjusting a_{in} is limited compared to the variation of the average torque value with a_{out} as shown in with the Fig. 2.10(b). The variation of torque ripple is analyzed in Fig. 2.11(c), and it can be seen that the torque ripple reaches the maximal value when a_{in} is 0.8, and the torque ripple is 9.1% at this point. In summary, the value of a_{in} should be greater than 0.8 to obtain a larger output torque and a lower torque ripple.

From the study of the effect of the pole-arc coefficient of PMs on the torque performance of DS-HSDR-TFPMSM, it can be concluded it is preferred to select a higher design value for both a_{in} and a_{out}. However, DS-HSDR-TFPMSM proposed in the thesis combined with a yokeless disk rotor structure, and a large value of the pole-arc factor of the PMs will lead to a small spacing between two adjacent PMs along the circumferential direction, which makes the rotor non-conductive flange more difficult to fabricate and easily deformed, besides, the overall strength of the rotor disk will not be guaranteed. Therefore, it is necessary to strictly limit the values of a_{in} and a_{out}.

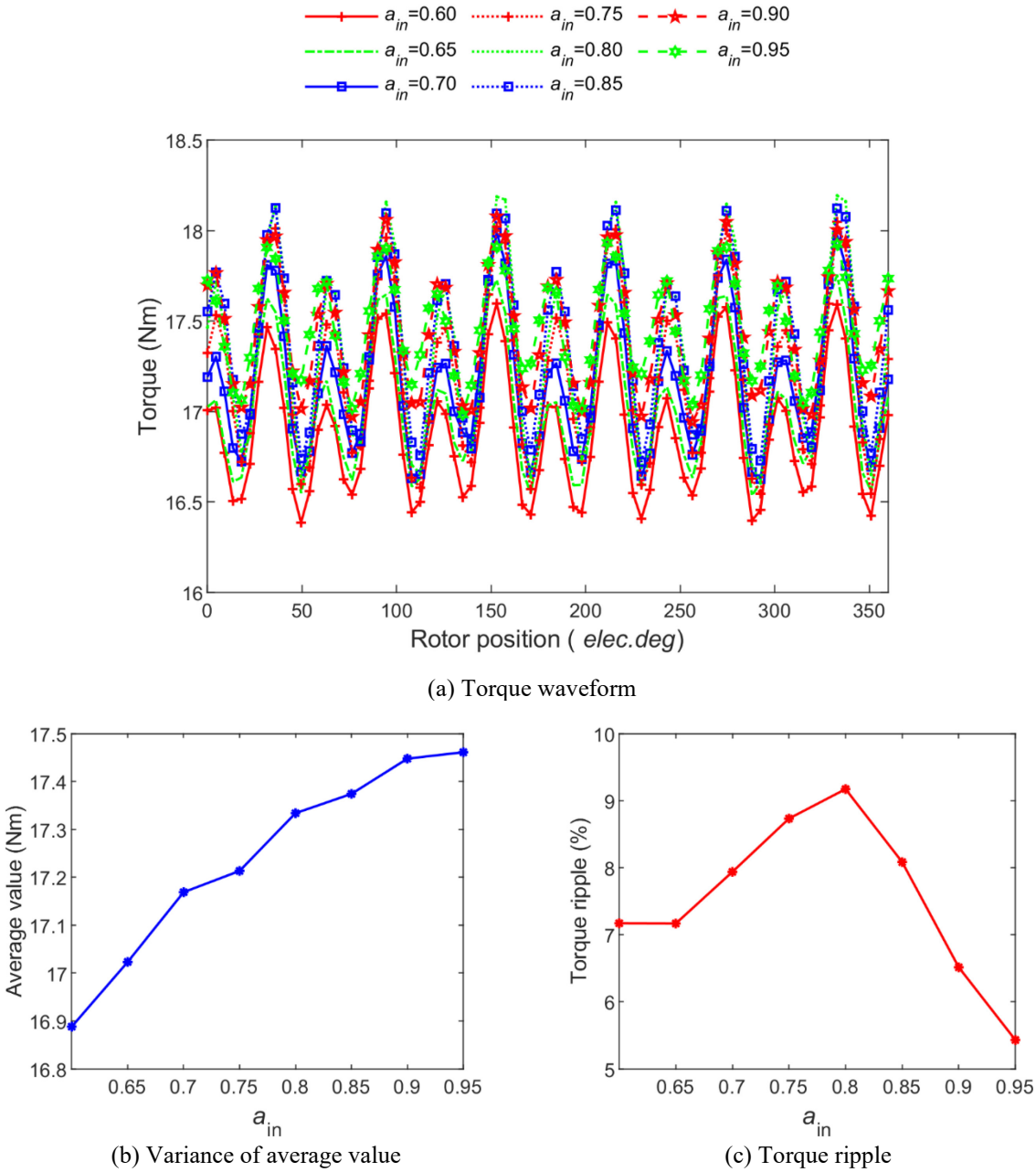

(a) Torque waveform

(b) Variance of average value

(c) Torque ripple

Fig. 2.11 The influence of the inner PM pole-arc coefficient a_{in} on the output torque

2.3.2 Parametric analysis of stator shoe

Another feature of DS-HSDR-TFPMSM is the use of a hybrid stator core structure, which reduces the leakage by adding a stator shoe made of SMC material to the stator core. DS-HSDR-TFPMSM is characterized by a sector-shaped stator shoe with the main dimensional parameters including the pole-arc factor b_s and the thickness h_{SMC}.

Firstly, the effect of the pole-arc factor b_s on the torque under the condition of rated current is investigated. The variation of the torque waveform with b_s is shown in Fig. 2.12(a). Through the analysis on the variance of torque average with the change of b_s as shown in Fig. 2.12(b), it can be found that the average value of the output torque fluctuates with b_s indicating

a trend of initial growth followed by a decrease, and the reason leading to the decrease is that the open between the two adjacent stator shoes decreases with the further increase of b_s, then the magnetic leakage increases and effective flux of the main magnetic circuit decreases. The maximal average value is achieved when b_s is 0.8, and the average value of torque is 17.6Nm at this point. The torque ripple of the electric machine changes as shown in Fig. 2.12 (c) and it can be seen that the torque ripple shows an approximate "M-shaped" variant trend with the increase of b_s, and the minimal value of torque ripple is achieved when b_s is 0.7. Then, the torque ripple increases rapidly and rises to 11% when b_s reaches 0.8. In summary, to ensure that DS-HSDR-TFPMSM achieves the torque performance requirement with low torque ripple, the value of b_s should be within the range from 0.7 to 0.75.

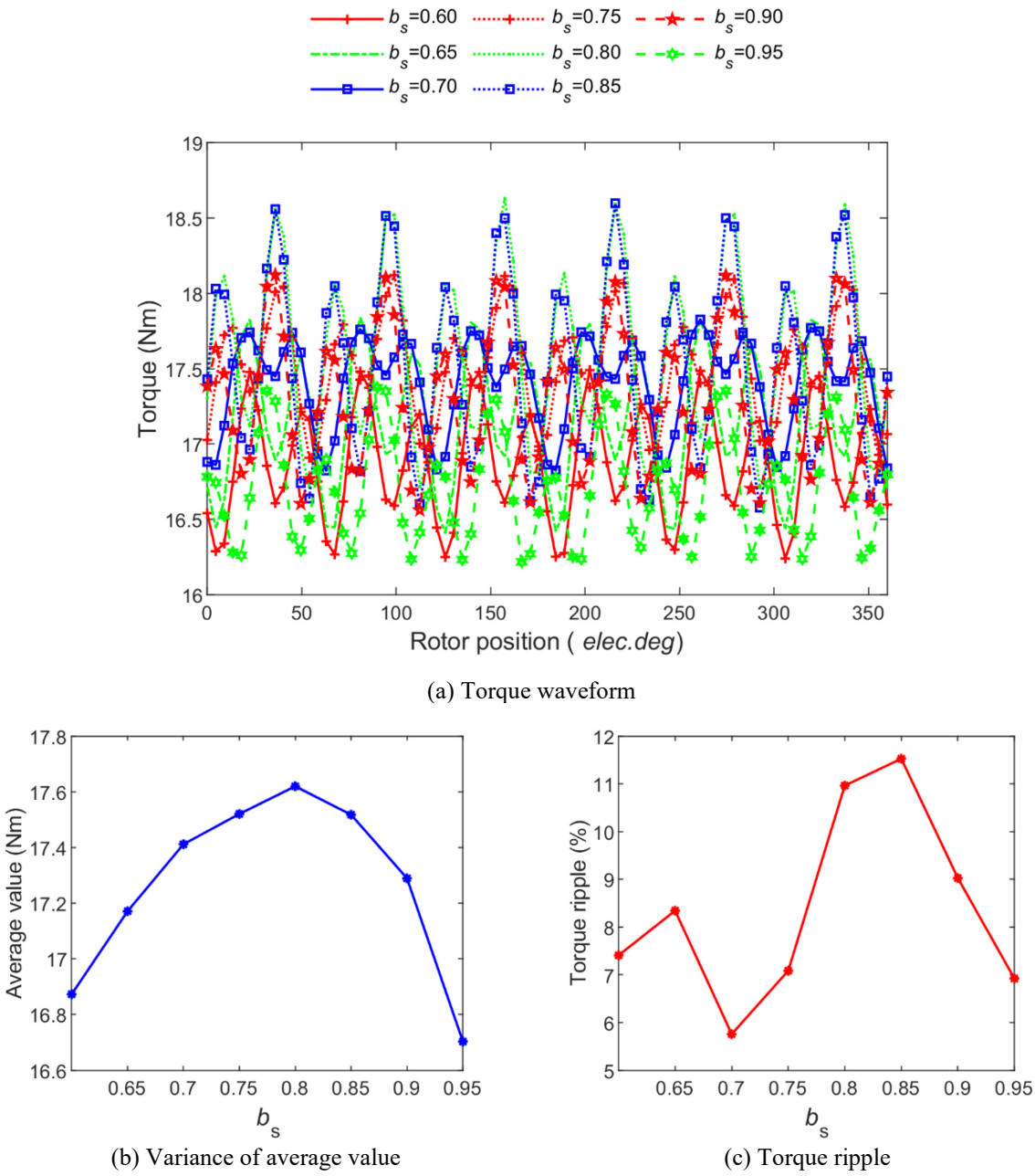

(a) Torque waveform

(b) Variance of average value

(c) Torque ripple

Fig. 2.12 The influence of the pole-arc coefficient b_s on the output torque

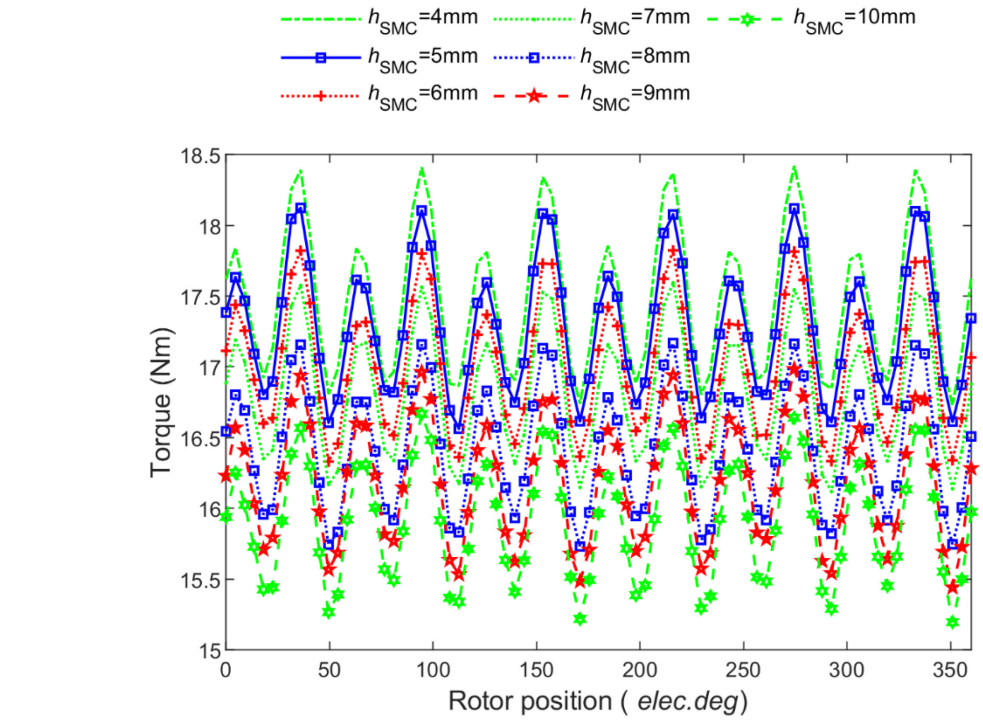

(a) Torque waveform

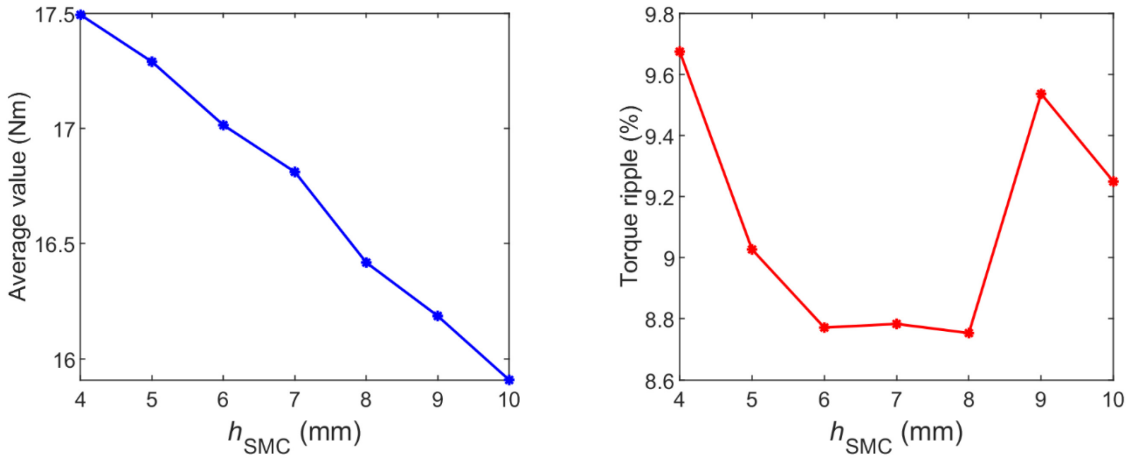

(b) Variance of average value (c) Torque ripple

Fig. 2.13 The influence of the thickness of the stator shoe h_{SMC} on the output torque (b_s =0.9)

In the preliminary design of DS-HSDR-TFPMSM, the pole-arc coefficient of stator shoe $b_s = 0.9$. Under this condition, the effect of the variation of the thickness of stator shoe on the torque is shown in Fig. 2.13. It should be noticed that h_{SMC} should be greater than 4mm due to the molding process of SMC material, otherwise the strength of stator shoe is much low and thus prone to fracture. It can be seen from Fig. 2.13(a) that the variation of h_{SMC} has a significant effect on the torque waveform, and the torque waveform is gradually displaced downward as h_{SMC} increases. The variation of the average torque value with h_{SMC} is shown in Fig. 2.13(b). It can be seen that the average torque value gradually decreases with the increase of h_{SMC}, and the decreasing rate tends to increase. The torque average decreases from 17.5Nm to 15.9Nm during the increase of h_{SMC} from 4mm to 10mm. The primary reason for the issue mentioned above is

that when h_{SMC} increases, the equivalent air gap area between the two adjacent stator shoes increases, which consequently raises the leakage between the two adjacent stator cores, ultimately causing a decline in the output torque of the machine. The variation of torque ripple with h_{SMC} is shown in Fig. 2.13(c) in which it can be seen that the variance of torque ripple with the increase of h_{SMC} presents a trend as "U-shaped", the torque ripple gradually decreases and starts to stabilize when h_{SMC} reaches 6mm, and then gradually increases when h_{SMC} reaches 8mm.

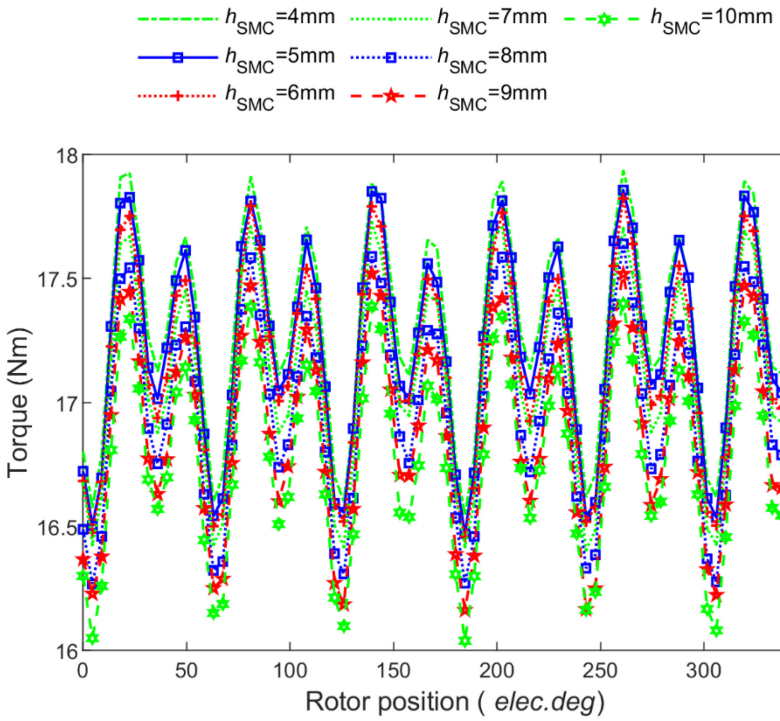

(a) Torque waveform

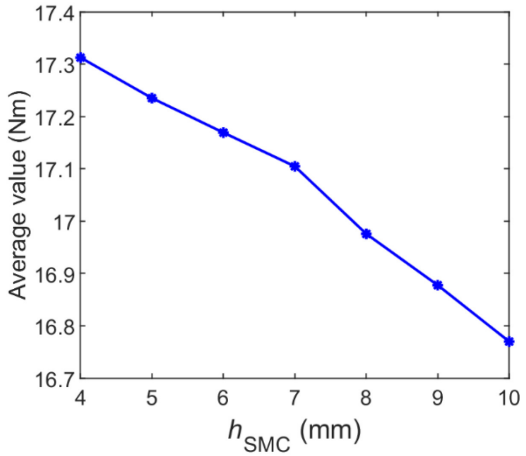

(b) Variance of average value of torque

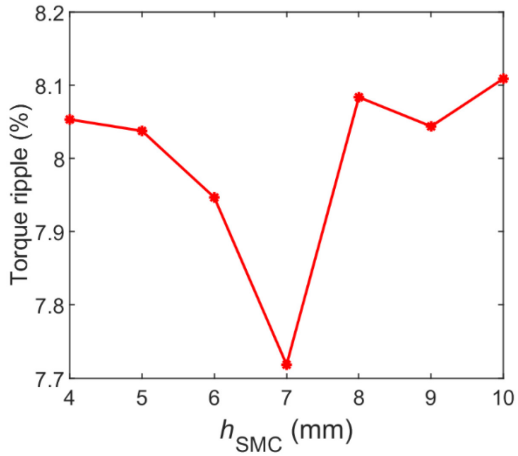

(c) Torque ripple

Fig. 2.14 The influence of the thickness of the stator shoe h_{SMC} on the output torque (b_s =0.67)

The issue of declining average torque with increasing h_{SMC} can be efficiently alleviated by reducing b_s. The analysis of the effect of h_{SMC} on the output torque under the condition of b_s = 0.67 is shown in Fig. 2.14. It can be seen from Fig. 2.14(b) that the average output torque still decreases monotonically with h_{SMC}, but the amplitude is significantly lower compared the

results under the condition of b_s = 0.9. The average torque decreases from 17.4Nm to 16.8Nm as h_{SMC} increases from 4mm to 10mm. The variation of torque ripple with h_{SMC} under the condition of b_s = 0.67 is shown in Fig. 2.14(c). It can be seen that the variant trend of torque ripple is approximately "V-shaped" and reaches the minimal value at h_{SMC} = 7mm.

In summary, it can be concluded that the variation of torque with h_{SMC} is influenced by b_s. If only prefer to increase the average torque of DS-HSDR-TFPMSM, the value of h_{SMC} should be 4mm.

2.4 Fault tolerant design of DS-HSDR-TFPMSM

To improve the reliability of industrial robot, the fault tolerant ability is required for electric machine, which enables machine to continue operate smoothly in the event of a open- or short-circuit fault. The most promising approach for achieving a fault tolerant electric machines is to use multiphase machine structure, which provides the machine with more degrees of freedom for control. Thus, it can be guaranteed that there is enough control margin remaining even after the loss of one or more degrees of freedom.

Dual three-phase machine is predominant type among multiphase machine due to its low torque ripple, of which the lowest harmonic component is 12th. Additionally, its decoupled transformation matrix and control method are similar to traditional three-phase electric machine, which simplifies the control complexity of multiphase machine. DS-HSDR-TFPMSM proposed in the thesis features a 10-pole/12-slot combination and a double stator structure, making it suitable for studying fault tolerant designs based on the dual three-phase structure.

2.4.1 Structure and coil configuration of dual three-phase DS-HSDR-TFPMSM

To achieve the transition from the three-phase DS-HSDR-TFPMSM to the dual three-phase structure, the change in terms of the machine design primarily focuses on adjusting the coil configuration of the stator disk. Therefore, it is necessary to first mark all stator coils of DS-HSDR-TFPMSM, as demonstrated in Fig. 2.15, in order to facilitate subsequent adjustments to the coil configuration for the dual three-phase configuration.

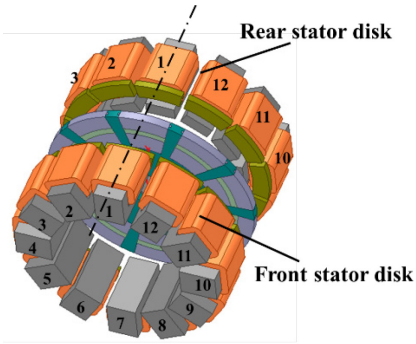

Fig. 2.15 Serial number indication of the stator winding of DS-HSDR-TFPMSM

Based on the 10-pole/12-slot combination, the three-phase DS-HSDR-TFPMSM adopts the three-phase short-pitch concentrated winding structure (W1) as shown in Fig. 2.16. In the winding structure W1, the coil configuration of the single stator disk is shown in Fig. 2.16(a), with "A+" and "A-" indicating two coils belonging to the same A-phase winding but with opposite polarity. The coil space vector diagram corresponding to the W1 configuration is further shown in Fig. 2.16(b), where the synthetic vector of one phase winding is obtained by multiplying the algebraic sum of all coil vectors belonging to the same phase by a diskount factor, namely the short-pitch factor of the winding.

The front and rear stator disks of the three-phase DS-HSDR-TFPMSM are symmetrical in structure and adopt the same winding structure W1, so that the spatial phasor relationship between the windings of the front and rear stator disks can be obtained as shown in Fig. 2.17. In addition, the coils belonging to the same phase in the two stator disks are connected in a series connection.

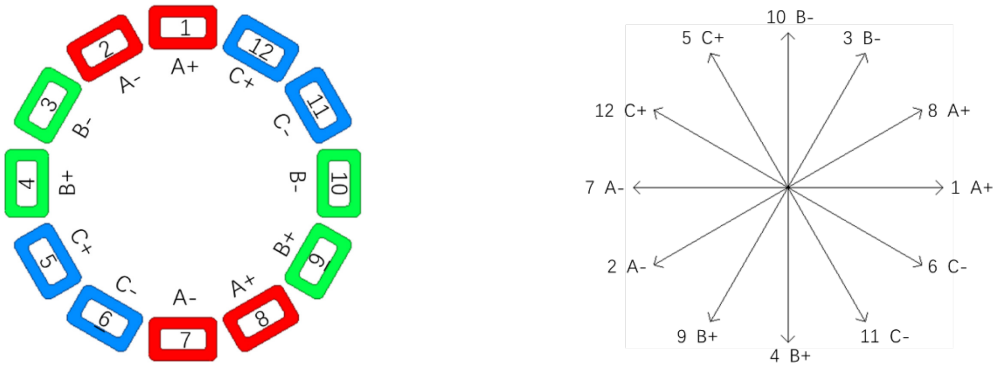

(a) Coil configuration (b) Coil space vector diagram

Fig. 2.16 Three-phase short-pitch concentrated winding (W1)

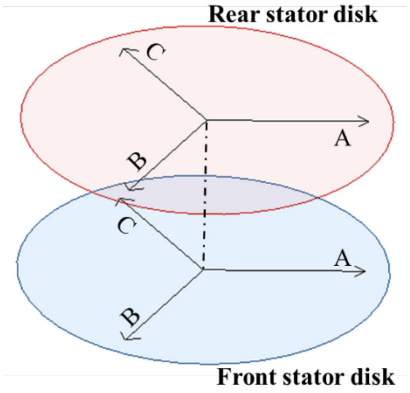

Fig. 2.17 The phasor distribution of three-phase DS-HSDR-TFPMSM

Based on the analysis on the winding of the three-phase DS-HSDR-TFPMSM, adjustments can be made from two perspectives: the coil configuration and phasor distribution of the stator disks, as shown in Figure 2.16(a) and Figure 2.17, respectively. By applying these adjustments, two structures of the dual three-phase DS-HSDR-TFPMSM can be obtained, including the symmetrical stator disk structure and the asymmetrical stator disk structure.

(1) Dual three-phase DS-HSDR-TFPMSM with symmetrical structure

On the basis of the 10-pole/12-slot combination, a dual three-phase full-pitch concentrated winding structure (W2) can be obtained directly, as shown in Fig. 2.18. The coil configuration of a single stator disk is shown in Fig. 2.18 (a). Fig. 2.18 (b) further gives the coil space vector diagram corresponding to the W2 configuration. It can be seen that, unlike the structure W1, the synthesis vector of one phase winding in W2 is the algebraic sum of all the coil vectors belonging to the same phase, so that a higher no load back-EMF and a larger output torque. Eventually, a dual three-phase DS-HSDR-TFPMSM with symmetrical stator disk structure is obtained based on the structure W2 of which the same winding structure W2 is used for both front and rear stator disks, so that the spatial phasor relationship between the windings of the

front and rear stator disks can be obtained as shown in Fig. 2.19. In addition, the coils belonging to the same phase winding in both two stator disks are connected in a series.

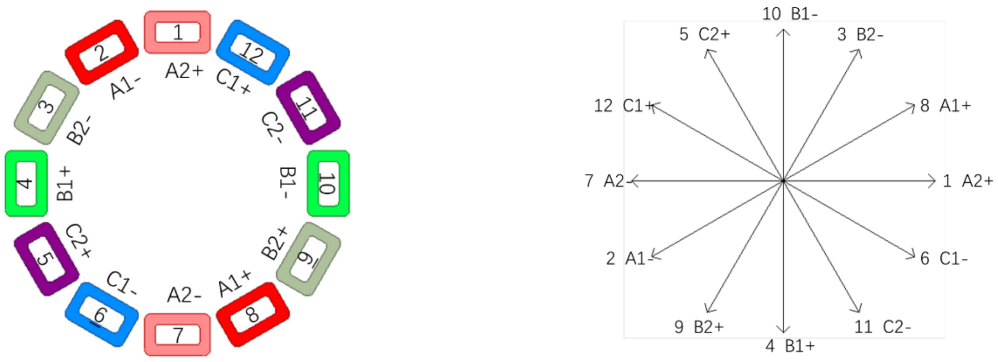

(a) Coil configuration (b) Coil space vector diagram

Fig. 2.18 Dual three-phase full-pitch concentrated winding (W2)

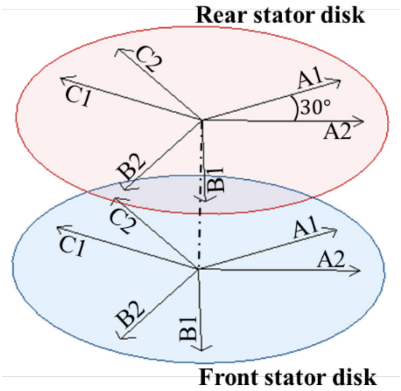

Fig. 2.19 The phasor distribution of dual three-phase DS-HSDR-TFPMSM with symmetrical structure

(2) Dual three-phase DS-HSDR-TFPMSM with asymmetrical structure

In the dual three-phase DS-HSDR-TFPMSM with symmetrical stator disk structure, the coils belonging to the same phase winding in both front and rear stator disks are connected in series, leading to an electrical connection between the two stator disks. In order to eliminate the electrical connection between the two stator disks, a simpler fault tolerant design scheme of DS-HSDR-TFPMSM is proposed, as shown in Fig. 2.20. In this scheme, the front and rear stator disks are no longer symmetrical, and the rear stator disk is rotated by a mechanical angle δ_m. In addition, the front and rear stator disks adopt the winding structure W1. The spatial phasor relationship between the windings of the front and rear stator disks is shown in Fig. 2.21. It can be seen that there is a δ_e phasor difference between the respective three-phase windings on the front and rear stator disks.

$$\delta_e = 5\delta_m \tag{2-19}$$

When the rotation angle δ_m is 6 mechanical degrees (30 electrical degrees), then the same dual three-phase winding structure as in Fig. 2.19 can be obtained.

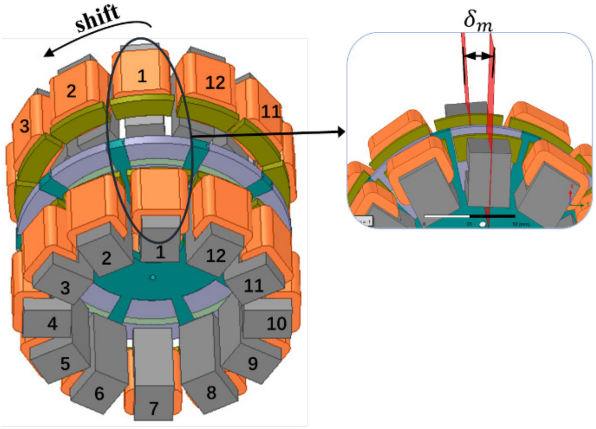

Fig. 2.20 Dual three-phase DS-HSDR-TFPMSM with asymmetrical structure

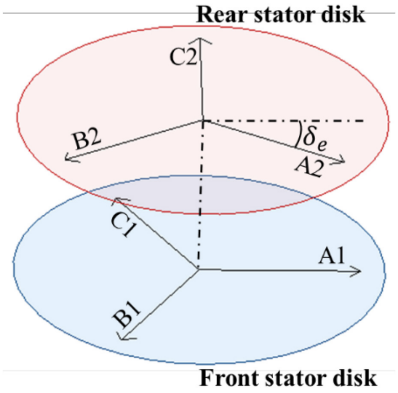

Fig. 2.21 Phasor distribution of dual three-phase DS-HSDR-TFPMSM with asymmetrical structure

Both above proposed structures adopt dual isolated neutral points to eliminate the effect of zero sequence current.

2.4.2 Electromagnetic analysis of dual three-phase DS-HSDR-TFPMSMs

Based on the dimensional parameters of DS-HSDR-TFPMSM given in Table 2.3 and the adjustments made to the structure as well as coil configuration to obtain dual three-phase DS-HSDR-TFPMSMs, analysis models of the two kinds of dual three-phase DS-HSDR-TFPMSMs were obtained. The electromagnetic simulations are performed using the FEM to further analyze and compare the performance of the two structures of dual three-phase DS-HSDR-TFPMSMs.

The back-EMF waveforms of the two structures at rated speed are shown in Fig. 2.22. It is observed that the back-EMF waveforms of the two structures are basically the same, but the analysis results reveal differences in their RMS values. The RMS value of the no load back-EMF is 79.5 V for the asymmetrical structure and 82.4 V for the symmetrical structure. In addition, the Fourier analysis of the no load back-EMF of the two structures in Fig. 2.22 is further conducted to compare the harmonic components, as shown in Fig. 2.23. The total harmonic distortion (THD%) of back-EMF waveform of the dual three-phase machine with asymmetrical structure is 8.4%, while for the dual three-phase machine with symmetrical structure, the THD% is 11.1%. Therefore, it can be concluded that the dual three-phase DS-HSDR-TFPMSM with symmetrical structure combines the advantage of higher RMS value of no load back-EMF and a higher amplitude of the fundamental component, which is conducive

to generating a larger machine output torque. However, the symmetrical structure also suffers from the disadvantage of a relatively high harmonic content. The difference in no load back-EMF between the two structures is mainly due to the use of different winding structures. For the symmetrical structure, the winding coefficient is 1 due to the use of the full-pitch concentrated winding W2, while for the asymmetrical structure, the winding coefficient is 0.9659 due to the use of the short-pitch concentrated winding W1. In addition, as shown in Fig. 2.23, the main harmonic component of the back EMF waveform is the 3rd harmonic. However, due to the adoption of double isolated neutral point, the 3rd harmonic in windings will be eventually cancelled by each other.

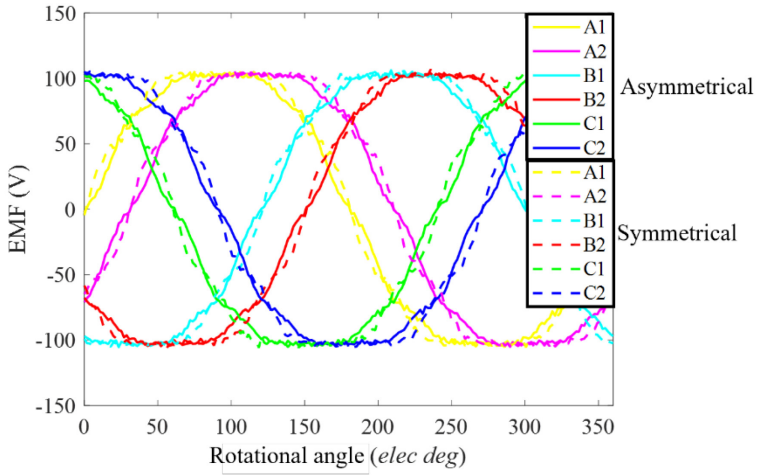

Fig. 2.22 Comparison of back-EMF waveform

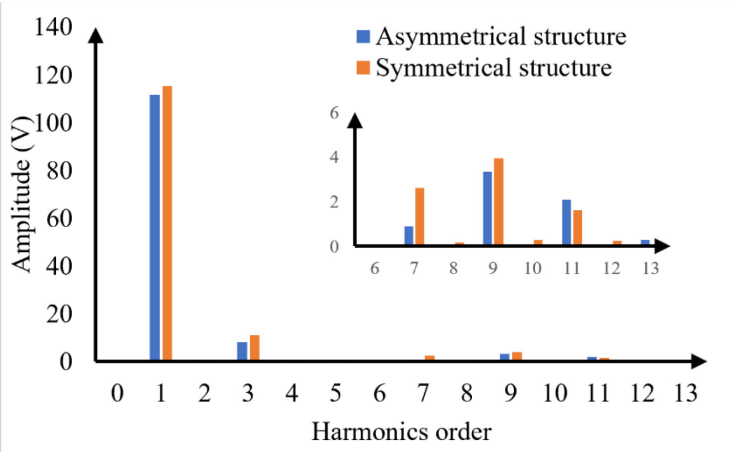

Fig. 2.23 Comparison of the harmonics in back-EMF

The torque performance of the dual three-phase DS-HSDR-TFPMSM is compared as shown in Fig. 2.24. The cogging torque is compared in Fig. 2.24(a), and it can be seen that the cogging torque is basically the same for both structures, with cogging torque peak-peak values of 1052 mN-m and 979 mN-m, respectively. In Fig. 2.24(b), the rated output torque of both structures is compared. It has been concluded that the dual three-phase DS-HSDR-TFPMSM with symmetrical structure is characterized by a higher fundamental content in back-EMF which results in a higher output torque. Nevertheless, the rated output torque of DS-HSDR-TFPMSM with two structures need to be set to 17.2Nm according to the performance requirements in Table 2.2. Under this condition, the rated current of the asymmetrical structure

is kept in 12.5A, while the rated current of the symmetrical structure needs to be adjusted to 12A. Finally, the obtained rated torque waveforms of both structures are shown in Fig. 2.24(b). The torque ripple of the asymmetrical structure is 7.77% and that of the symmetrical structure is 7.39%. Whereas the torque ripple of the three-phase DS-HSDR-TFPMSM in Fig. 2.9(b) is 9.05%. Therefore, the advantage of low torque ripple of the dual three-phase winding structure is further verified.

In conclusion, it can be inferred based on the analysis shown in Table 2.4 that the symmetrical structure combines a lower rated current compared to the asymmetrical structure while rated torque is output and the other performance parameters are similar. However, the winding configuration of the symmetrical structure is slightly intricate due to the need for electrical connection between the front and rear stator disks.

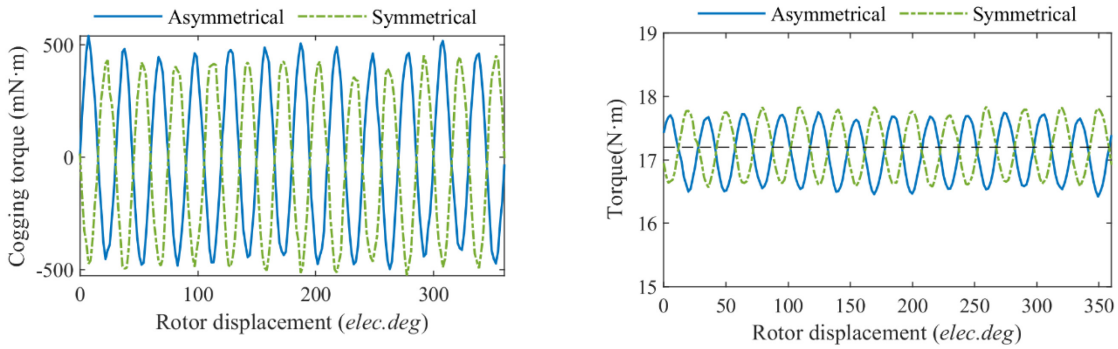

(a) Cogging torque (b) Rated torque

Fig. 2.24 Comparison of torque performance

Table 2.4 Performance comparison of DS-HSDR-TFPMSMs

Parameters	Asymmetrical structure	Symmetrical structure
RMS value of back-EMF	79.5V	82.4V
THD% of Back-EMF	8.4%	11.1%
P2p of cogging torque	1052mN·m	979mN·m
Rated torque	17.2N·m	
Torque ripple	7.77%	7.39%
Rated current	12.5A	12A

2.5 Conclusion

In this chapter, a novel structure of disk-type transverse flux permanent magnet synchronous machine is proposed for the background of industrial robot application. The structure and dimensional design method are investigated, and the main research work and conclusions are as follows.

(1) The evolution process and specific structure of DS-HSDR-TFPMSM are introduced, and the operating principle of DS-HSDR-TFPMSM is analyzed. Based on the application context of industrial robots, and through a comparative analysis with RPMSM, it is concluded that DS-HSDR-TFPMSM has the advantages of compact structure and low moment of inertia, which helps to realize the miniaturization and high dynamics of the electric drives in industrial robots.

(2) The dimensional design method of DS-HSDR-TFPMSM was investigated. Firstly, the basic outline of the machine is determined by deriving the basic sizing equation of DS-HSDR-TFPMSM; then, the preliminary design parameters of the 5.4kW DS-HSDR-TFPMSM are

obtained by investigating the equivalent magnetic circuit design, slot\pole combination design, and stator core design methods; finally, the performance is validated by electromagnetic analysis.

(3) The pole-arc coefficient of PMs and dimensional parameters of stator shoes were analyzed. By studying the effect of the change of the pole-arc coefficient of both outer and inner PMs and the change of the pole-arc coefficient as well as thickness of the stator shoes on the output torque of the machine, the change of both torque average value and torque ripple of DS-HSDR-TFPMSM are obtained for each size parameter, which provides guidance for the reasonable selection of the design value.

(4) The multiphase fault tolerant design method of DS-HSDR-TFPMSM is investigated. Based on the dual stator disk topology and the 10-pole/12-slot coordination of DS-HSDR-TFPMSM, two types of dual three-phase structure DS-HSDR-TFPMSM are obtained respectively. By comparing the main performance of the two structures, it can be concluded that, under the condition that the same rated torque is output and other performance parameters are basically same, the dual three-phase DS-HSDR-TFPMSM with symmetrical structure benefits from a lower rated current, but the electrical connection between the front and rear stator disks resulting in the more complicated winding connection compared to the asymmetrical structure. In addition, a comparative study of the torque ripple of dual three-phase and three-phase DS-HSDR-TFPMSMs is proceeded, and it can be concluded that the dual three-phase DS-HSDR-TFPMSMs combine the advantage of low torque ripple.

Chapter 3. Electromagnetic Analysis Method based on Schwarz-Christoffel Transformation

The electromagnetic analysis method is crucial in the design of DS-HSDR-TFPMSM, among which the FEM (FEM) is widely used in the electromagnetic design of various types of machines because of its advantages of high computational accuracy. However, DS-HSDR-TFPMSM proposed in the thesis characterized by a complex three-dimensional magnetic circuit structure, which is time-consuming to use the FEM and takes up a large amount of computational resources, leading to a longer development cycle of DS-HSDR-TFPMSM. In order to solve the above problems, some researches have realized the fast analysis and calculation of electromagnetic field and performance of TFPMSM by establishing the equivalent magnetic circuit (EMC)[55], [56]. However, the calculation accuracy of this method is not high, and the distribution of the air-gap magnetic field cannot be accurately calculated. In order to overcome the above-mentioned shortcomings of the EMC method, equivalent magnetic network (EMN) method with higher calculation accuracy to analyze the electromagnetic field of TFPMSM were proposed in research, but this method requires the establishment of dynamic magnetic network models according to the rotor position when calculating the machine performance such as back-EMF and torque, which makes its application more difficult[165]. The conformal transformation method is advantageous in the solution of electromagnetic field due to its short computation time and high accuracy, and has become increasingly important in the electromagnetic analysis of machines[65]. The Schwarz-Christoffel transformation is a special type of conformal transform which can simplify the solution domain with complex boundaries into a rectangular solution domain. Therefore, it is particularly suitable for analyzing the electromagnetic fields in complex structured electromagnetic devices, and there is no need to change the machine analysis model along with the movement of rotor when using conformal method for the electromagnetic analysis of electric machines[62], [66], [68], [166]. It is therefore more suitable than the EMN method for the electromagnetic analysis of TFPMSM.

In this chapter, an electromagnetic field analysis method based on Schwarz-Christoffel transformation is proposed for DS-HSDR-TFPMSM. Firstly, the three-dimensional topology of DS-HSDR-TFPMSM is equated in two dimensions, and its simplified analytical model is obtained using the Schwarz-Christoffel transformation. Then, the electromagnetic field analysis and performance calculation method based on the Schwarz-Christoffel transformation method are given. Finally, the computational results are validated using the FEM.

3.1 Fundamental principles of Schwarz-Christoffel transformation

3.1.1 Conformal transformation

The coordinate plane transformation can be used to solve partial differential equation problems with complex boundaries[167]. Its basic principle is to map any point (x,y) in the region D (shown in Fig. 3.1(a)) with complex boundary Γ to a point (u,v) in the region D' (shown in Fig. 3.1(b)) with simple boundary Γ' by the complex variable function f.

The coordinates point (x,y) is any point in the complex-plane z:

$$z = x + jy \tag{3-1}$$

(u,v) corresponds to any point in the complex-plane w:

$$w = u + jv \tag{3-2}$$

The correspondence between coordinate points in two complex-planes can be established using a complex function:

$$w = f(z) = u(x, y) + jv(x, y) \tag{3-3}$$

The function is said to be continuous if equation (3-3) is differentiable everywhere and satisfies the Cauchy-Riemann equations.

$$\begin{cases} \dfrac{\partial u}{\partial x} = \dfrac{\partial v}{\partial y} \\ \dfrac{\partial u}{\partial y} = -\dfrac{\partial v}{\partial x} \end{cases} \tag{3-4}$$

If there exists an analytic solution to equation (3-3), then the mapping of (x,y) to (u,v) is unique and its corresponding inverse function exists, meaning that there is a function that maps a point from (u,v) back to (x,y).

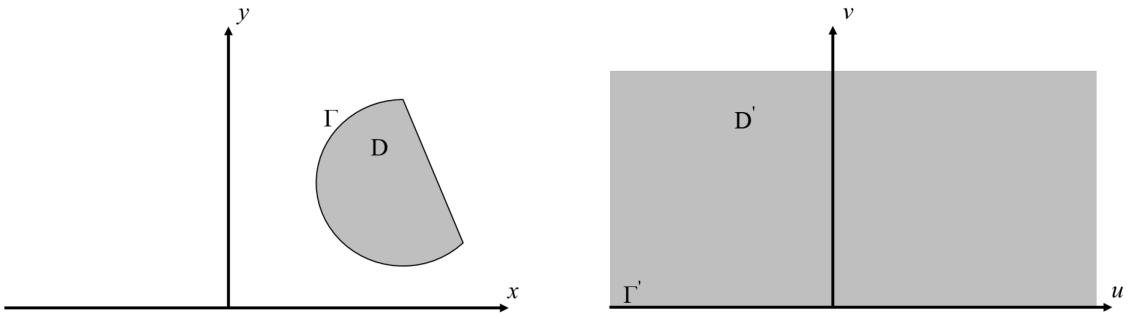

(a) Original plane (b) Mapping plane

Fig. 3.1 Conformal transformation

The coordinate plane transformation described above can have a further geometric representation: all curves intersecting at a point in the original plane z are magnified by the same factor and rotated by the same angle in the image plane w. Therefore, this transformation is also called the conformal transformation.

Conformal transformations typically result in a partial transformation of derivative and differential operators (such as gradient, divergence, and curl). However, the transformed operators in the image plane coordinates maintain a simple correspondence function with the original plane coordinates. As a result, conformal transformations can effectively solve problems involving electric or magnetic field solutions with complex boundary conditions[168].

One of the most typical examples is the use of conformal transformations to solve problems containing Laplace's equations, which are particularly common in the electromagnetic fields of electric machine. By using the conformal transformation, the Laplace's equations in the original plane and the image plane are simply related by the following equation:

$$\nabla_z^2 \varphi = \nabla_w^2 \varphi \cdot \left| f'(z) \right|^2 \tag{3-5}$$

where $f'(z)$ denotes the derivative value of the conformal transform function, which satisfies the Cauchy-Riemann equation (3-4) and whose derivative value is not zero.

3.1.2 Schwarz-Christoffel transformation

Establishing a mapping function between two bounded or infinite regions can be achieved through a complex function, which leads to a conformal transformation between the two planes when the function satisfies the Cauchy-Riemann equation and having nonzero derivatives. However, when the shape of either region changes, the corresponding conformal transformation function must also be modified. In this regard, the Schwarz-Christoffel transformation is a useful tool for determining the relationship between a semi-infinite region (as shown in Figure 3.2(a)) and a polygonal region (as shown in Figure 3.2(b)) in the coordinate plane.

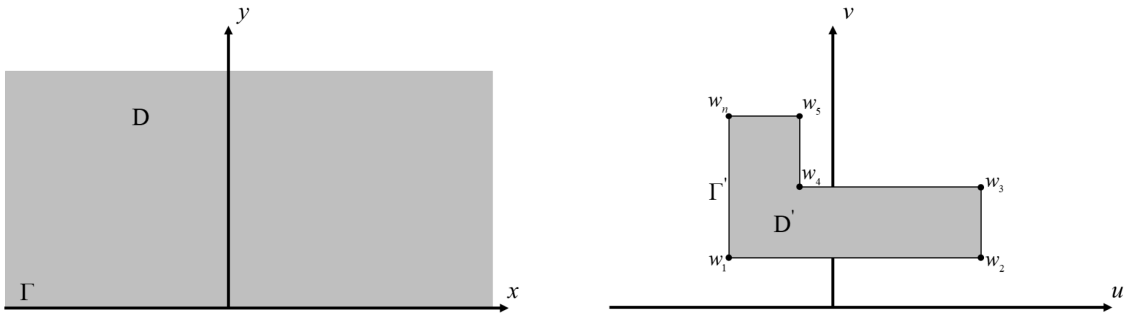

(a) Original plane (b) Mapping plane

Fig. 3.2 Schwarz-Christoffel transformation

The derivative of the Schwarz-Christoffel transformation function can be expressed as[169]:

$$\frac{dw}{dz} = f'(z) = K(z-x_1)^{(\alpha_1/\pi)-1}(z-x_2)^{(\alpha_2/\pi)-1}\ldots(z-x_n)^{(\alpha_n/\pi)-1} \tag{3-6}$$

By the Schwarz-Christoffel transformation, the semi-infinite region D in Fig. 3.2(a) is mapped to the region D' with polygon boundary in Fig. 3.2(b). In (3-6), x_n denotes the value along with the real axis coordinates in the original plane corresponding to the vertex w_n of the polygon region in the image plane, α_n denotes the angle of inflection at the position of the vertex w_n of the polygon region, and K is the scale factor to be determined. Ultimately, the Schwarz-Christoffel transformation function $w = f(z)$ is obtained by the integration of (3-6).

$$w = f(z) = K \cdot \int_{z_0}^{z} \prod_{n=1}^{n} (\chi - x_n)^{(\alpha_n/\pi)-1} d\chi + C \tag{3-7}$$

where C is a complex constant. The Schwarz-Christoffel transformation function equation given in (3-7) can be applied not only to the mapping from the coordinate upper half-plane region to the irregular polygonal region shown in Fig. 3.2, but also to the mapping from the bounded rectangular region to the irregular polygonal region with simple modifications based on (3-7).

3.2 Analytical model of DS-HSDR-TFPMSM based on Schwarz-Christoffel transformation

Due to its complex three-dimensional magnetic circuit structure, DS-HSDR-TFPMSM cannot be analyzed using the Schwarz-Christoffel transformation method directly, which is limited to be used in two-dimensional planes.[72] In particular, there is no precedent for the calculation of electromagnetic field analysis based on the Schwarz-Christoffel transformation

for the rotating TFPMSM. Consequently, to analyze the electromagnetic field of DS-HSDR-TFPMSM using the Schwarz-Christoffel transformation method, it is necessary to first construct a two-dimensional equivalent model based on the machine's design parameters and structural characteristics. Subsequently, the analysis model can be simplified using Schwarz-Christoffel and other conformal transformations to analyze the machine's electromagnetic field in a simpler solution domain.

3.2.1 Two-dimensional equivalent model of DS-HSDR-TFPMSM

DS-HSDR-TFPMSM possesses an axisymmetric structure (as illustrated in Figure 3.3①), and the magnetic field direction in the stator core is perpendicular to its section throughout. This feature allows for the selection of the middle position of the stator core as the equipotential plane (as shown in Figure 3.3③). Leveraging the axisymmetric plane and the equipotential plane, DS-HSDR-TFPMSM can be deformed and expanded to obtain its two-dimensional equivalent model. The two-dimensional equivalent transformation process of DS-HSDR-TFPMSM involves the following three steps and are shown in Figure 3.3.

1) Divide the machine model into two identical semi-structural models along the axisymmetric plane (①--②), where the thickness of the permanent magnet in each semi-structural model is halved from its actual thickness.

(2) Expand the semi-structural model along the circumferential direction and analyze it as an approximate equivalent to a linear machine (②--③).

(3) The linear machine model is separated into two parts along the equipotential plane and further expanded so that it is approximately equivalent to a two-dimensional model (③--④).

In the first step, two identical DS-HSDR-TFPMSM half-models can be obtained directly. However, the approximate equivalence of the models is required during the transformation process in the second and third steps, which mainly involves the adjustment of the transformed model parameters.

In the second step, DS-HSDR-TFPMSM half-model is unfolded into a linear machine along the mean radius position R_{avg}

$$R_{\text{avg}} = \frac{R_{\text{PMout\_out}} + R_{\text{PMin\_in}}}{2} \tag{3-8}$$

The PMs and the stator shoes are expanded into rectangular squares with widths of w_{PM} and w_{shoe}, respectively.

$$\begin{cases} w_{\text{PM}} = \dfrac{\alpha_{\text{out}}}{180}\pi R_{\text{avg}} \\ w_{\text{shoe}} = \dfrac{\beta_{\text{s}}}{180}\pi R_{\text{avg}} \end{cases} \tag{3-9}$$

In the third step, the armature coil on the single stator core is first evenly divided into two parts, each with N/2 turns as shown in Figure 3.3④. In addition, the width of the two parts of the "U-shaped" stator core after separation also needs to be adjusted, and the width of the upper part of the core connected to the stator shoe w_{su} is:

$$w_{\text{su}} = \frac{2w_{\text{s}}R_{\text{avg}}}{R_{\text{PMout\_out}} + R_{\text{PMout\_in}}} \tag{3-10}$$

The width of the lower half of the core w_{sl} is:

$$w_{sl} = \frac{2w_s R_{avg}}{R_{PMin\_out} + R_{PMin\_in}} \quad .(3\text{-}11)$$

Then, the two semi-PMs are combined together into one whole PM during the equivalent process. Finally, the depth of the 2D equivalent model in Figure 3.3④ needs to be set to the radial height of the stator core section l_b.

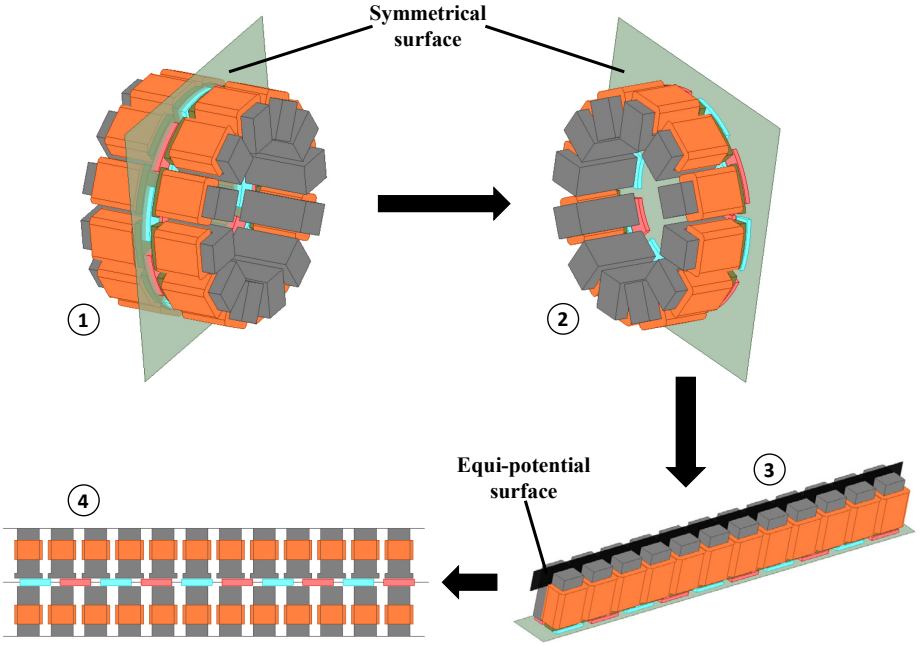

Fig. 3.3 Two-dimensional equivalent transformation of DS-HSDR-TFPMSM

3.2.2 Analytical model in complex-plane of DS-HSDR-TFPMSM

To analyze the electromagnetic field of DS-HSDR-TFPMSM in the two-dimensional coordinate plane, it is necessary to transform the two-dimensional equivalent model obtained in Fig. 3.3 into a complex-plane analytical model. In order to achieve above transformation, certain assumptions must be made.

1) The B-H curve exhibits linearity for both the stator core material made of silicon steel and the stator shoe material made of SMC, with identical permeability for both.

2) The radial leakage of the machine is ignored.

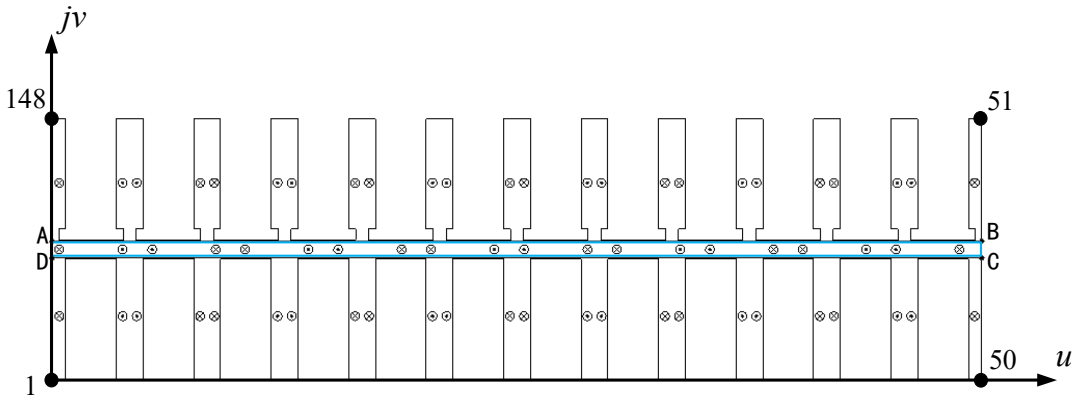

Fig. 3.4 Complex-plane analytical model of DS-HSDR-TFPMSM (w-plane)

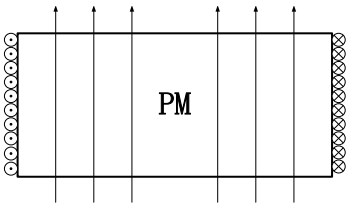

Fig. 3.5 Surface current equivalent model of the PMs

Based on the above assumptions, DS-HSDR-TFPMSM two-dimensional equivalent model is transformed into a complex-plane *w* for analysis, as illustrated in Fig. 3.4. The air gap region which serves as the solution domain is a polygon comprising 148 vertices, with the starting point 1 located at the origin of the *w*-plane coordinate system. In this region, the excitation magnetic field is jointly established by the PMs and the armature coil. The armature coil is represented in the complex-plane analytical model as a pair of current sources with opposite directions and the current amplitude being the phase current multiplied by the number of turns. Moreover, the magnetic field generated by the PMs is simulated by adding equivalent surface currents on its boundary, based on the basic relationship between current and magnetic field. The equivalent surface current is related to the properties and thickness of the PM material. To achieve more precise analysis of the air gap magnetic field, the equivalent surface current of a single PM is divided into 10 turns and distributed uniformly along the direction of magnetization, as depicted in Fig. 3.5. As the relative permeability of the permanent magnet is generally close to 1, the magnitude of the equivalent surface current per turn can be expressed as:

$$I_{\mathrm{e}} = \frac{H_{\mathrm{c}} \cdot h_{\mathrm{r}}}{10} \qquad ,(3\text{-}12)$$

Where, H_{c} is the coercivity of the PM material and h_{r} indicates the thickness of the PM.
In addition, four auxiliary lines AB, BC, CD and DA are added to the complex-plane analytical model as shown in Fig. 3.4 for calculating the air gap flux density and cogging torque.

3.2.3 Simplification of the analysis model in complex-plane based on the Schwarz-Christoffel transformation

The complex-plane analysis model of DS-HSDR-TFPMSM comprises a polygon with 148 vertices, as illustrated in Fig. 3.4. In accordance with the fundamental principle of the Schwarz-Christoffel transformation, the bounded rectangular region in the *z*-plane can be transformed to the polygonal region in the *w*-plane through Schwarz-Christoffel transformation function f_s:

$$w = f_{\mathrm{s}}(z) \qquad (3\text{-}13)$$

The Schwarz-Christoffel transformation function f_s between the two coordinate planes can be calculated by calling the SC Tool toolbox in MATLAB. Subsequently, utilizing the Schwarz-Christoffel transformation function f_s^{-1}, the excitation sources (including armature currents and permanent magnets) in the *w*-plane and the points to be solved (situated on the auxiliary lines AB, BC, CD, and DA) can be mapped to the rectangular region in the *z*-plane, as depicted in Fig. 3.6. Finally, the magnetic field in the rectangular domain can be determined by applying equation of Poisson.

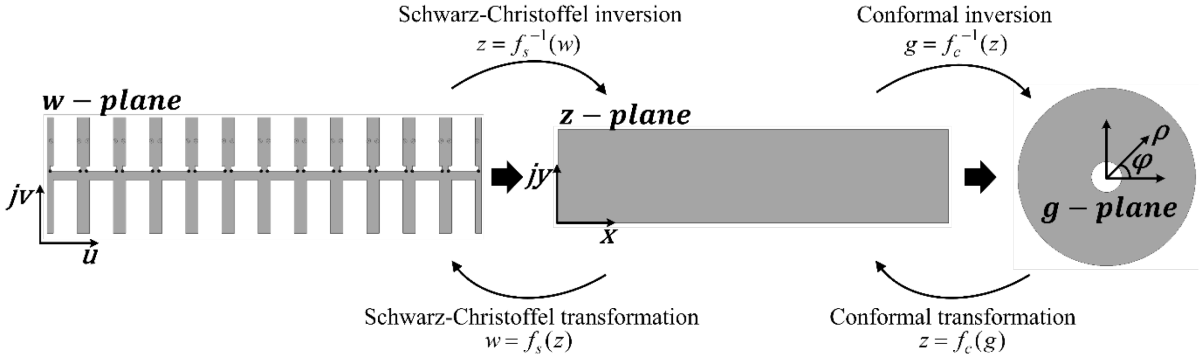

Fig. 3.6 Simplified procedure of complex-plane analytical model

However, as DS-HSDR-TFPMSM is a rotating machine in practical applications, its left and right boundaries of rectangular solution domain should overlap. Hence, to reflect the periodic boundary conditions of the rotating machine, it is necessary to establish a mapping between the rectangular solution domain of DS-HSDR-TFPMSM in the *z*-plane and the circular solution domain in the *g*-plane, as shown in Fig. 3.6. In accordance with the theory of conformal transformation[71], the conformal transformation function for mapping from the circular solution domain to the rectangular solution domain can be derived as:

$$z = f_c(g) = \frac{\Delta x}{2}(1 + j\frac{\log(g)}{\pi}) + j\frac{\Delta y}{2} \quad ,(3\text{-}14)$$

where Δx and Δy denote the length along the real axis and the width along the imaginary axis of the rectangular solution domain in the *z*-plane, respectively.

By using the conformal inversion corresponding to (3-14):

$$g = f_c^{-1}(z) = e^{(\frac{2\pi}{j\Delta x}(z - \frac{j\Delta y}{2}) - \frac{\pi}{j})} \quad ,(3\text{-}15)$$

Afterwards, the excitation sources and the points to be solved can be mapped into the circular solution domain in the g-plane. Ultimately, Equation of Hague, the electromagnetic field in the circular solution domain can be computed through equation of Hague[170] .

3.3 Magnetic field and performance calculation of DS-HSDR-TFPMSM based on Schwarz-Christoffel transformation method

Based on the aforementioned analysis, the circular solution domain of DS-HSDR-TFPMSM is obtained through the two-dimensional equivalent model and simplification of the complex-plane analysis model. The Hague's equations can then be utilized to analyze the electromagnetic field of the machine in circular solution domain. However, it is necessary to map the magnetic field distribution in the circular solution domain to the equivalent complex-plane analysis model of DS-HSDR-TFPMSM through the conformal transformation f_c and the Schwarz-Christoffel transformation f_s since the magnetic field distribution in the circular solution domain does not directly reflect the air-gap magnetic field distribution of the machine.

The calculation of the air-gap magnetic field, including the magnetic field intensity and flux density, is presented firstly. Then, the performances of the machine are further calculated based on the calculated air-gap magnetic field, including the no-load back-EMF, cogging torque, and rated torque. Furthermore, the air-gap magnetic field and performance obtained using the Schwarz-Christoffel transformation method are compared with the results calculated by FEM.

Finally, the proposed Schwarz-Christoffel transformation method is utilized to validate the superiority of the stator shoe.

3.3.1 Air gap magnetic field calculation

In the circular solution domain of the *g*-plane (polar complex-plane), the magnetic field intensity within the air-gap at any point can be expressed as the negative gradient of the scalar magnetic potential φ_{g}:

$$\mathbf{H_g}(r,\theta) = -\nabla \varphi_{\mathrm{g}} \tag{3-16}$$

After the simplification of the complex-plane analysis model as shown in Fig. 3.6, the excitation source and the point to be solved in the *w*-plane are mapped to the circular solution domain in the *g*-plane by the Schwarz-Christoffel inversion and the conformal inversion. The coordinates of the excitation source mapped to the *g*-plane are $g_{\mathrm{I}} = ce^{j\theta_{\mathrm{I}}}$ and the coordinates of the point to be solved are $g_C = re^{j\theta}$. Then equation (3-16) can be further expanded as follows:

$$\begin{aligned}\mathbf{H_g}(r,\theta) = &[-\frac{\partial \varphi_{\mathrm{g}}}{\partial r}\cos\theta + \frac{1}{r}\frac{\partial \varphi_{\mathrm{g}}}{\partial \theta}\sin\theta] \\ &+ j[-\frac{\partial \varphi_{\mathrm{g}}}{\partial r}\sin\theta - \frac{1}{r}\frac{\partial \varphi_{\mathrm{g}}}{\partial \theta}\cos\theta]\end{aligned} \tag{3-17}$$

According to Equation of Hague, the scalar magnetic potential at any point in the circular domain φ_g can be calculated by the following equation:

$$\varphi_{\mathrm{g}} = \begin{cases} \dfrac{I}{2} + \sum\limits_{n=1}^{\infty}((A_n - \dfrac{I}{2\pi n c^n})r^n + B_n r^{-n})\cdot\sin(n\Delta\theta), & r < c \\ \dfrac{I(\Delta\theta+\pi)}{4\pi} + \sum\limits_{n=1}^{\infty}(A_n r^n + B_n r^{-n})\cdot\sin(n\Delta\theta), & r = c \\ \dfrac{I\Delta\theta}{2\pi} + \sum\limits_{n=1}^{\infty}(A_n r^n + (\dfrac{Ic^n}{2\pi n} + B_n)r^{-n})\cdot\sin(n\Delta\theta), & r > c \end{cases} \tag{3-18}$$

where $\Delta\theta = \theta - \theta_I$, A_n and B_n are calculated using the following equations:

$$\begin{cases} A_n == \dfrac{-I(\mu_1-\mu_2)[b^{2n}(\mu_1-\mu_2)+c^{2n}(\mu_1+\mu_2)]}{c^n 2\pi n(-b^{2n}(\mu_1-\mu_2)^2 + a^{2n}(\mu_1+\mu_2)^2)} \\ B_n == \dfrac{b^{2n} I(\mu_1-\mu_2)[c^{2n}(\mu_1-\mu_2)+a^{2n}(\mu_1+\mu_2)]}{c^n 2\pi n(-b^{2n}(\mu_1-\mu_2)^2 + a^{2n}(\mu_1+\mu_2)^2)} \end{cases} \tag{3-19}$$

where μ_1 and μ_2 are the permeability of the stator core and air gap region, respectively, *I* denotes the magnitude of the current in the excitation source, *a* as well as *b* are the outer diameter and inner diameter of the circular solution domain shown in Fig. 3.6, respectively.

Substituting (3-18) into (3-17), the magnetic field intensity vector $\mathbf{H_g}$ at any point in the circular domain can be obtained:

$$
\mathbf{H_g}(r,\theta)=\begin{cases}
\boldsymbol{i}\left\{\begin{array}{l}\cos\theta\left(\sum\limits_{n=1}^{\infty}\left(-\sin(n\Delta\theta)\right)\left[\left(A_n-\dfrac{I}{2\pi nc^n}\right)nr^{n-1}-nr^{-n-1}B_n\right]\right)+\\ \dfrac{1}{r}\sin\theta\left(\sum\limits_{n=1}^{\infty}\left[\left(A_n-\dfrac{I}{2\pi nc^n}\right)r^n+B_nr^{-n}\right]\cdot n\cos(n\Delta\theta)\right)\end{array}\right\}\\
+\boldsymbol{j}\left\{\begin{array}{l}\sin\theta\left(\sum\limits_{n=1}^{\infty}\left(-\sin(n\Delta\theta)\right)\left[\left(A_n-\dfrac{I}{2\pi nc^n}\right)nr^{n-1}-nr^{-n-1}B_n\right]\right)-\\ \dfrac{1}{r}\cos\theta\left(\sum\limits_{n=1}^{\infty}\left[\left(A_n-\dfrac{I}{2\pi nc^n}\right)r^n+B_nr^{-n}\right]\cdot n\cos(n\Delta\theta)\right)\end{array}\right\}, & r<c\\
\boldsymbol{i}\left\{\begin{array}{l}-\cos\theta\left(\sum\limits_{n=1}^{\infty}\left(\sin(n\Delta\theta)\right)\left(nr^{n-1}A_n-nB_nr^{-n-1}\right)\right)+\\ \dfrac{1}{r}\sin\theta\left(\dfrac{I}{4\pi}+\sum\limits_{n=1}^{\infty}\left[\left(A_nr^n+B_nr^{-n}\right)\left(n\cos(n\Delta\theta)\right)\right]\right)\end{array}\right\}\\
+\boldsymbol{j}\left\{\begin{array}{l}-\sin\theta\left(\sum\limits_{n=1}^{\infty}\left(\sin(n\Delta\theta)\right)\left(nr^{n-1}A_n-nB_nr^{-n-1}\right)\right)-\\ \dfrac{1}{r}\cos\theta\left(\dfrac{I}{4\pi}+\sum\limits_{n=1}^{\infty}\left[\left(A_nr^n+B_nr^{-n}\right)\left(n\cos(n\Delta\theta)\right)\right]\right)\end{array}\right\}, & r=c\\
\boldsymbol{i}\left\{\begin{array}{l}\cos\theta\left(\sum\limits_{n=1}^{\infty}\left(-\sin(n\Delta\theta)\right)\left[nA_nr^{n-1}-\left(\dfrac{Ic^n}{2\pi n}+B_n\right)nr^{n-1}\right]\right)+\\ \dfrac{1}{r}\sin\theta\left[\dfrac{I}{2\pi}+\left(\sum\limits_{n=1}^{\infty}\left[A_nr^n+\left(\dfrac{Ic^n}{2\pi n}+B_n\right)r^{-n}\right]\cdot n\cos(n\Delta\theta)\right)\right]\end{array}\right\}\\
+\boldsymbol{j}\left\{\begin{array}{l}\sin\theta\left(\sum\limits_{n=1}^{\infty}\left(-\sin(n\Delta\theta)\right)\left[nA_nr^{n-1}-\left(\dfrac{Ic^n}{2\pi n}+B_n\right)nr^{n-1}\right]\right)-\\ \dfrac{1}{r}\cos\theta\left[\dfrac{I}{2\pi}+\left(\sum\limits_{n=1}^{\infty}\left[A_nr^n+\left(\dfrac{Ic^n}{2\pi n}+B_n\right)r^{-n}\right]\cdot n\cos(n\Delta\theta)\right)\right]\end{array}\right\}, & r>c
\end{cases}
\qquad \text{,(3-20)}
$$

where $\boldsymbol{i}$ and $\boldsymbol{j}$ denote the unit vectors in the complex-plane along the real and imaginary axis directions, respectively. According to (3-23), the flux density vector at any point in the circular domain can be further obtained as:

$$\mathbf{B_g}(r,\theta)=\mu_2\mathbf{H_g}(r,\theta) \tag{3-21}$$

According to the basic principle of conformal transformation, the magnetic field intensity vectors at the corresponding positions in the two solution domains before and after the transformation can be related by a simple functional relationship. Firstly, based on (3-24), the air-gap flux density vector in the z-plane rectangular solution domain can be calculated as

$$\mathbf{B_z}(z)=\frac{\mathbf{B_g}(g)}{(df_c/dg)^*}=\left(\frac{2\pi jg^*}{\Delta x}\right)\mathbf{B_g}(g) \qquad \text{,(3-22)}$$

where the superscript * denotes the conjugate complex of the term. After obtaining $\mathbf{B_z}$ (z), the air-gap flux density vector in the w-plane in the air-gap solution domain can be obtained based on the Schwarz-Christoffel transformation f_s as follows

$$\mathbf{B}_w(z) = \frac{\mathbf{B}_z(z)}{(df_s / dz)^*} \quad .(3\text{-}23)$$

In summary, the air-gap magnetic field distribution of the DS-HSDR-TFPMSM can be determined using the Schwarz-Christoffel transformation (SC) method. Firstly, 417 solution points are uniformly selected along the auxiliary line AB (as shown in Fig. 3.4). Then, Schwarz-Christoffel inversion and conformal inversion is applied to map the location of the equivalent surface current of the PMs and the 417 solution points onto the circular solution domain in the *g*-plane. The Hague's equations are used to calculate the air-gap flux density vector $\mathbf{B_g}$ of the solution points. Finally, (3-22) and (3-23) are employed to obtain $\mathbf{B_w}$, which represents the distribution of the air-gap flux density vector along the auxiliary line AB in the *w*-plane.

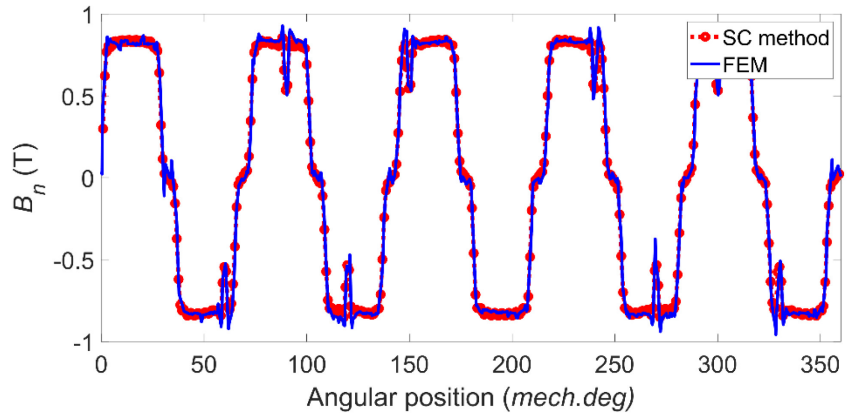

(a) Normal flux density

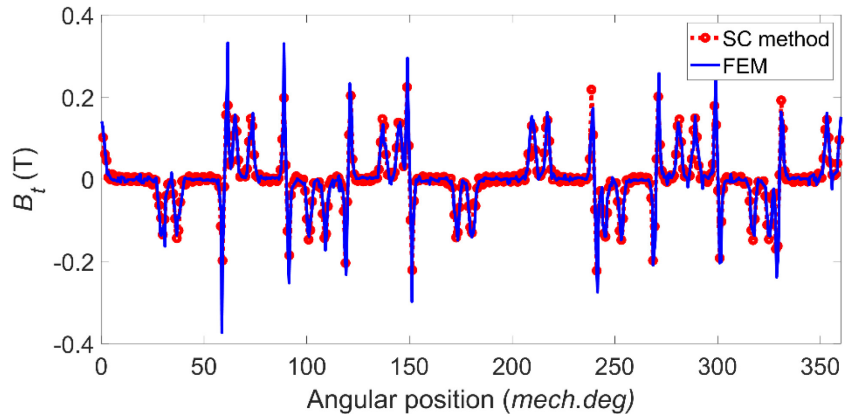

(b) Tangential flux density

Fig. 3.7 Comparison of the air-gap flux density along auxiliary line AB obtained by SC-based analytical method and FEM

The air-gap flux density distribution along the auxiliary line AB is presented in Fig. 3.7, in which both the normal and tangential flux density distribution are given. In terms of DS-HSDR-TFPMSM, the axial direction of the DS-HSDR-TFPMSM is considered as the normal direction, while the circumferential rotation direction is considered as the tangential direction. To validate the accuracy of the Schwarz-Christoffel transformation method, the results obtained by the FEM are also included in Fig 3.7 for comparison. Moreover, the air-gap flux density distribution along the auxiliary line DC using the Schwarz-Christoffel transformation method is calculated, and compared with the results obtained by the FEM, as shown in Fig. 3.8.

By comparing the air gap flux density distributions obtained by the Schwarz-Christoffel transformation method with the results obtained by the FEM, as shown in Fig. 3.7 and 3.8, it can be seen that the results obtained by both methods are consistent. This consistency serves as evidence of the accuracy of the Schwarz-Christoffel transformation method.

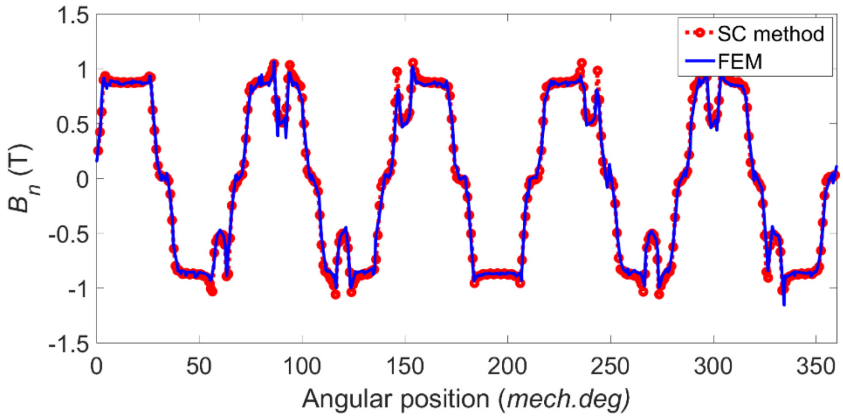

(a) Normal flux density

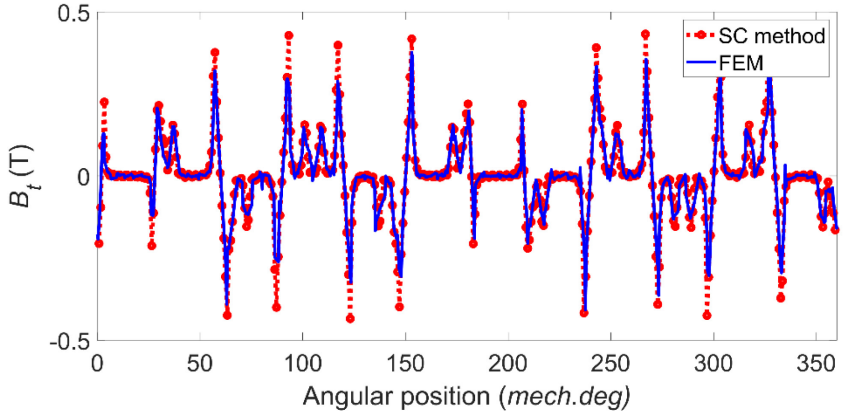

(b) Tangential flux density

Fig. 3.8 Comparison of the air-gap flux density along auxiliary line DC obtained by SC-based analytical method and FEA

3.3.2 Performance Calculations

By integrating the air-gap flux density under the stator core of one phase and multiplying it with the number of turns of each coil, the flux linkage in each phase winding can be determined. To simulate the dynamic process of DS-HSDR-TFPMSM rotor rotation, the position of the rotor permanent magnet equivalent surface current in Fig. 3.4 is linearly shifted, and the flux linkage waveform changing with rotor position is obtained. Finally, the no load back-EMF in one-phase winding can be calculated by the following equation:

$$E_{\text{phase}} = -\frac{d\psi_{\text{phase}}}{dt} = -v_{\text{r}}\frac{d\psi_{\text{phase}}}{du} = -\frac{n_{\text{r}}\pi R_{\text{avg}}}{30}\frac{d\psi_{\text{phase}}}{du} \tag{3-24}$$

Where, v_{r} denotes the linear moving speed of the rotor PMs in the w-plane, n_r denotes the speed of the actual DS-HSDR-TFPMSM model, and u denotes the displacement distance of the rotor PMs in the w-plane.

The no load back-EMF waveforms calculated by the Schwarz-Christoffel transformation method and the FEM are shown in Fig. 3.9. The obtained no-load back-EMF waveforms using both the FEM and the proposed method are in good agreement with each other, as shown in Fig. 3.11 which indicates that the proposed method can accurately predict the no-load

performance of the DS-HSDR-TFPMSM, which is essential for the design and control of the machine. Therefore, the proposed method can be a useful tool for the analysis and design of DS-HSDR-TFPMSM.

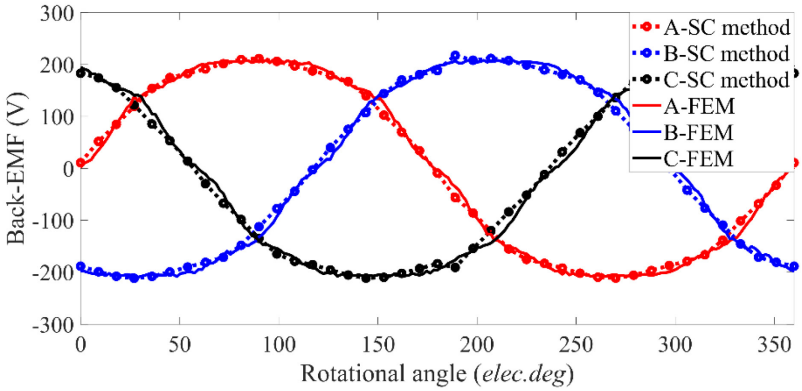

Fig. 3.9 Comparison of no load back-EMF waveforms obtained by SC-based analytical method and FEM

The analysis of the force in magnetic field using the Schwarz-Christoffel transformation method is accomplished through the Maxwell stress tensor method. The cogging force in the machine are obtained by integrating the Maxwell stress tensor over the four auxiliary lines AB, BC, CD, and DA shown in Fig. 3.4. However, considering that the auxiliary lines BC and DA coincide in the actual rotation model of DS-HSDR-TFPMSM, the calculation of the cogging force only requires integrating the Maxwell stress tensor over the auxiliary lines AB and CD as follows:

$$F_{\text{cogging}} = \frac{2l_{\text{b}}}{\mu_2}\left(\int_{AB} B_{\text{n}} B_{\text{t}}\, du - \int_{DC} B_{\text{n}} B_{\text{t}}\, du\right) \quad ,(3\text{-}25)$$

The cogging torque of DS-HSDR-TFPMSM can be obtained by multiplying the cogging force $F_{cogging}$ with the mean radius R_{avg} and a factor of 2, as the complex-plane analytical model in Fig. 3.4 is obtained from the half model of the machine by two-dimensional equivalence. The cogging torque waveforms calculated using the Schwarz-Christoffel transformation method and the FEM method for rotor PMs moving within a slot pitch range are shown in Fig. 3.10. The number of cogging torque periods in a slot pitch range is:

$$N_p = \frac{2p}{GCD(s,2p)} = 5 \quad (3\text{-}26)$$

where $GCD(s,2p)$ denotes the greatest common divisor between the number of stator slots s and the number of PM poles $2p$. It can be seen that the number of periods calculated by the Schwarz-Christoffel transformation method complying with (3-26) and overlaps with the results of obtained by FEM.

The above analysis was performed under no load conditions, and only the equivalent surface current of PM was considered for the excitation source in the analytical model, while the armature current was ignored. In order to calculate the electromagnetic torque of DS-HSDR-TFPMSM under the condition of rated current (I_{N} =12.5A), an armature current excitation source with amplitude $NI_{\text{N}}/\sqrt{2}$ is added to the analytical model. The armature current varies sinusoidally with the displacement of the rotor PMs. Fig. 3.11 shows the waveforms of the electromagnetic torque calculated by the Schwarz-Christoffel transformation method and the FEM. It can be seen that the calculation results obtained by both methods are in good agreement.

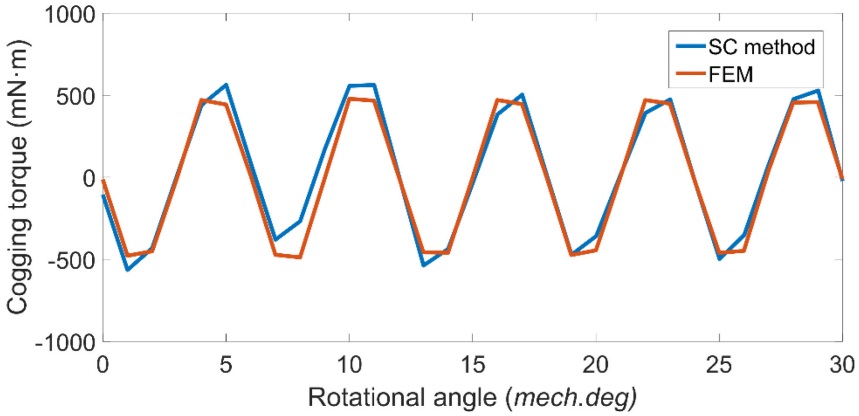

Fig. 3.10 Comparison of cogging torque waveforms obtained by SC-based analytical method and FEA

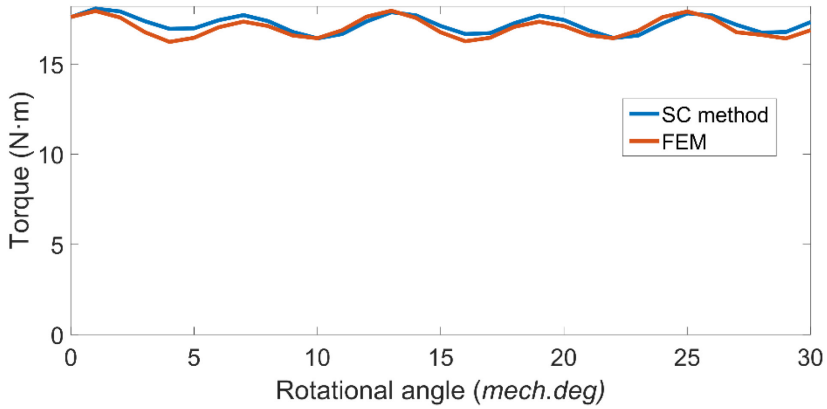

Fig. 3.11 Comparison of electromagnetic torque waveforms obtained by SC-based analytical method and FEA

The above analysis demonstrates the high calculation accuracy of the Schwarz-Christoffel transformation method. Moreover, its major advantage lies in its efficiency in the electromagnetic field analysis and performance calculation of DS-HSDR-TFPMSM. The computational resources used for calculating the rated electromagnetic torque waveform in Fig. 3.11 using the Schwarz-Christoffel transformation method and FEM are compared in Table 3.1. It can be concluded that the Schwarz-Christoffel transformation method saves 90.9% of the computational time and 88.4% of the computational resources compared to FEM. In summary, the Schwarz-Christoffel transformation method can effectively shorten the electromagnetic analysis process of DS-HSDR-TFPMSM due to its superior characteristics of high accuracy and efficient solution.

Table 3.1 Comparison of computing resource usage

	Calculation time consuming	Memory resource consumption
FEM	11160s	4.3GB
SC method	1020s	511MB

3.3.3 Superiority validation of stator shoes

DS-HSDR-TFPMSM proposed in the thesis adopts hybrid stator core structure of which a stator shoe made of SMC material is used to improve the problem of large magnetic leakage coefficient that commonly exists in TFPMSM. In order to validate the effect of the SMC stator shoe on the performance improving of TFPMSM, an analytical model of the TFPMSM with a stator core made of only laminated silicon steel sheets is developed in the thesis for comparative

study. It should be noted that in the shoeless structure TFPMSM, the stator core of the machine needs to be extended by the thickness of stator shoe to obtain the same air gap length as DS-HSDR-TFPMSM.

The electromagnetic characteristics of the shoeless structure motor are calculated by SC-based method and compared with the HSDR-TFPM. The comparison of electromagnetic performance is shown in Fig. 3.12. From the normal air-gap flux density distribution shown in Fig. 3.12 (a), the depression on the curve of the shoeless structure motor can be clearly observed. And this phenomenon is greatly improved after adopting SMC shoes, so the effective magnetic flux through into the main magnetic circuit increases, the motor back EMF and the output torque under rated current is improved furtherly, as shown in Fig. 3.12 (b) and (d). After adopting the SMC shoes, the slot width of the motor is reduced, and the cogging torque and torque ripple are reduced as shown in Fig. 3.12 (c) and (d).

The harmonics of air-gap flux density have a crucial influence on the mechanical, electromagnetic and thermal characteristics of the motor, especially for the servo motors mentioned in this article, the air-gap flux density harmonics would affect the control effect of a drive that uses the space vector control strategy [171]. In addition, it is beneficial for reducing the iron loss and the eddy current loss in the permanent magnet by decreasing the harmonic content of the air-gap flux density. The air gap flux density shown in Fig. 3.12 (a) is decomposed using the Fourier analysis method, and the comparison of the harmonic content is shown in Fig. 3.13. The harmonics are mainly concentrated below the 11th. Except for the 7th and the 11th harmonic, the harmonic content of the HSDR-TFPM is lower than that of the shoeless structure motor. The total harmonic distortion rate (THD%) of air-gap flux density is calculated by (3-27). THD% in HSDR-TFPM is 27.35% while it is 50.83% in shoeless structure motor. It can be concluded that the harmonic content of the air gap flux density is effectively weakened by adopting SMC shoes.

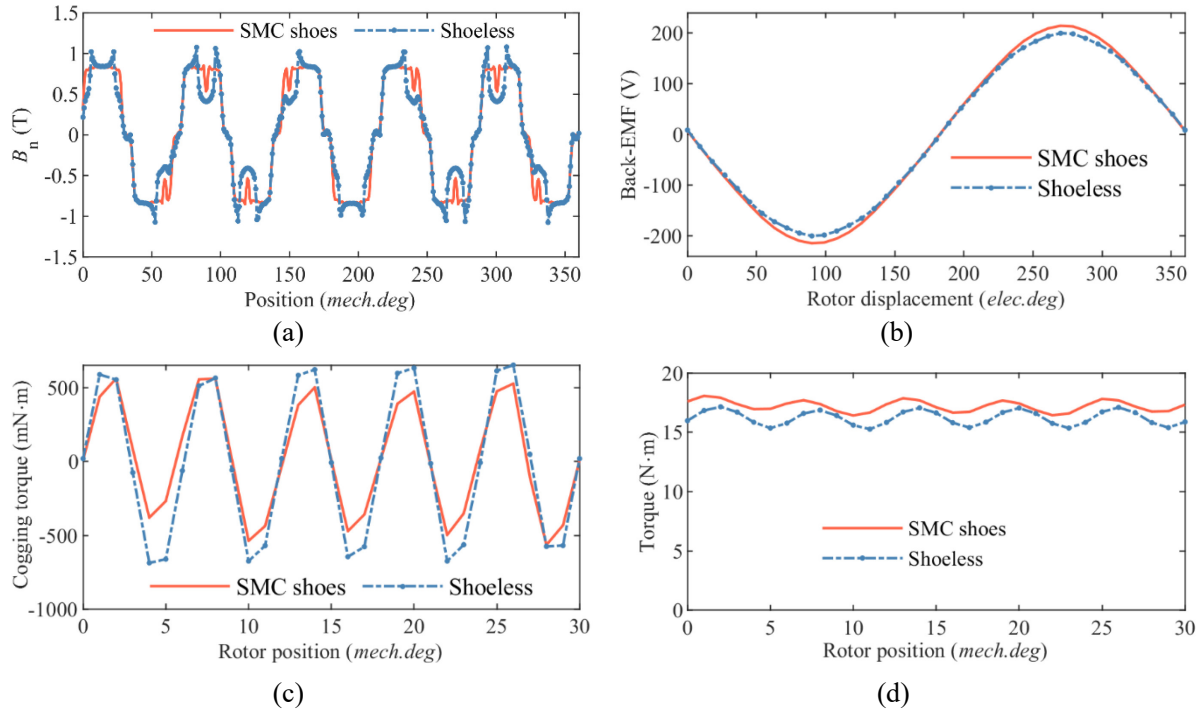

Fig. 3.12 Comparison of performance between the machines with/without stator shoe

$$THD\% = \sqrt{\sum_{n=2}^{H}\left(\frac{G_n}{G_1}\right)^2} \times 100\% \tag{3-27}$$

where G_1 is the RMS value of the fundamental component, G_n is the RMS value of the n_{th} harmonic component, and H is the highest harmonic number.

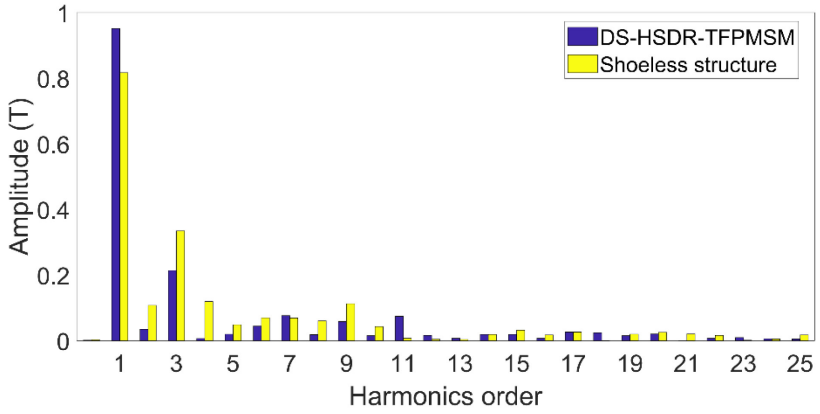

Fig. 3.13 Comparison of the harmonic contents in air-gap flux density between with/without stator shoe

3.4 Conclusion

In this chapter, the research on the air-gap magnetic field and performance analysis of DS-HSDR-TFPMSM using the Schwarz-Christoffel transformation method is proceeded. The research work and main conclusions can be summarized as follows:

(1) The fundamental principle of conformal transformation and Schwarz-Christoffel transformation are introduced. The properties of the electric and magnetic fields (gradient, divergence, and curl) remain unchanged before and after the conformal transformation of the coordinate plane. Thus, it can be concluded that the process of solving field problems with complex boundary can be simplified by using the conformal transformation.

(2) The DS-HSDR-TFPMSM analytical model is simplified using the Schwarz-Christoffel transformation method. Firstly, the two-dimensional equivalent analytical model is obtained based on the axisymmetric and equipotential planes of DS-HSDR-TFPMSM. Then, it is simplified into a polygonal solution domain in the complex-plane analytical model. Finally, the polygonal solution domain is further mapped to the circular solution domain by the Schwarz-Christoffel inversion and conformal inversion.

(3) The air-gap magnetic field and performance of DS-HSDR-TFPMSM are calculated based on the Schwarz-Christoffel transformation method. The Hague's equations are used to calculate the magnetic field intensity vector at any point in the circular solution domain, and the magnetic field distribution in the equivalent polygon solution domain of DS-HSDR-TFPMSM is derived by inverse transformation. The performance such as no load back-EMF, cogging torque, and rated torque are further solved based on the calculation results of the air-gap magnetic field distribution. The accuracy of the Schwarz-Christoffel transformation method is validated by comparing the air-gap magnetic field distribution and performance calculated by the method with the FEM, in which a high agreement is proven. The comparison of the consumption computational resource between the two methods reveals that the Schwarz-Christoffel transformation method can save 90.9% of computational time and 88.4% of computational resources proving the efficiency of the Schwarz-Christoffel transformation method.

In conclusion, the Schwarz-Christoffel transformation method is important for shortening the electromagnetic design process of DS-HSDR-TFPMSM, as it simplifies the analytical model and reduces computational time and resources. The accuracy of the method is verified, and the results show high agreement with FEM. The study contributes to the advancement of the electromagnetic analysis method for DS-HSDR-TFPMSM.

Chapter 4. Optimal Machine Design Based on BP Neural Network and Multi-objective Particle Swarm Optimization Algorithm

Machine design is the process of determining the dimensional parameters of each part of the machine based on specific design requirements. For conventional construction machines, such as RPMSM, the design process is largely fixed, while a large number of empirical formulas and diagrams are available to help the researcher determine the best design solution[74]. However, DS-HSDR-TFPMSM proposed in the thesis is characterized by a complex three-dimensional magnetic circuit structure, and the existing machine design methods are not applicable to DS-HSDR-TFPMSM. To address the challenge to determine the dimensional parameters of the machine with complex structure, optimization methods are commonly employed to efficiently generate the best design solution. With the rapid development of computer science, intelligent optimization algorithms, such as genetic algorithms, have been increasingly applied to the optimal design of machines and have demonstrated significant success in this field[86], [172]. To satisfy the requirements for miniaturization and low torque ripple in industrial robots, the torque performance of DS-HSDR-TFPMSM was identified as the optimization objective, which includes: 1) maximizing the average output torque to improve the machine torque density and thus promote machine miniaturization; 2) minimizing the machine torque pulsation. To obtain optimal design parameters for DS-HSDR-TFPMSM, a multi-objective optimization design approach was deemed necessary. As the optimal design problem of DS-HSDR-TFPMSM does not involve complex constraints, the particle swarm optimization algorithm is chosen over the genetic algorithm to improve optimization efficiency while ensuring the optimization effect[173]. Therefore, a multi-objective particle swarm optimization algorithm to optimize the torque performance of DS-HSDR-TFPMSM is utilized in the thesis. However, the optimization process of the intelligent algorithm requires repeated iterative evolution of a certain number of sample populations to obtain the optimal solution. Furthermore, the new sample populations need to obtain the corresponding optimization objective values after each evolution through electromagnetic analysis method. Unfortunately, for DS-HSDR-TFPMSM with a complex three-dimensional structure, the computational process using either the FEM or the Schwarz-Christoffel transformation method proposed in the thesis would be extremely time-consuming. To address this issue, the thesis proposes using an artificial neural network as a surrogate model to predict the torque performance of the electric machine. An artificial neural network is an adaptive nonlinear dynamic system that simulates the connection of neurons in the human brain[174]. BP neural network (BPNN) are commonly used in engineering fields due to its superior ability in the fitting of function and ease of implementation. Compared with other types of artificial neural networks, BPNN is characterized by significant advantages in identifying and fitting complex nonlinear systems[94]. However, BP neural network also suffers from poor global search capability and lack of appropriate guidance theory for the selection of initial network training values[175]. Therefore, genetic algorithm is introduced to optimize the training of BP neural network in the thesis.

In this chapter, an optimization design method for electric machine based on BP neural network and multi-objective particle swarm optimization algorithm is proposed and applied to the optimization design of DS-HSDR-TFPMSM. Firstly, the optimization design method is described step-by-step in detail, and the flow chart of the algorithm is presented. Then, the torque performance of DS-HSDR-TFPMSM is optimized using the proposed method, which involves the procedures of training the mapping network between optimization variables and objectives using BP neural network optimized by genetic algorithm and obtaining the Pareto

front using multi-objective particle swarm optimization algorithm. Finally, the optimal design obtained from the optimized design is validated using FEM.

4.1 Theoretical basis of optimization design method

4.1.1 Basic principle of BP neural network

BP neural network is a type of feedforward neural network, which consists of unidirectional multilayer. A typical two-input, two-output BP neural network is shown in Fig. 4.1. The topology of BP neural network in Fig. 4.1 is furtherly divided into three layers, including the input layer, the hidden layer and the output layer. Firstly, the input layer variables x_1 and x_2 are weighted to obtain the input values of the hidden layer.

$$\begin{cases} x_{\mathrm{h1}} = w_1 \cdot x_1 + w_2 \cdot x_2 \\ x_{\mathrm{h2}} = w_3 \cdot x_3 + w_4 \cdot x_4 \\ x_{\mathrm{h3}} = w_5 \cdot x_5 + w_6 \cdot x_6 \end{cases} \tag{4-1}$$

For the neurons in hidden and output layer, the inputs x_χ and the outputs y_χ of one neuron are connected by the transfer function f_{BP}.

$$y_\chi = f_{\mathrm{BP}}(x_\chi) + b_\chi \tag{4-2}$$

where χ can be either nodes h1, h2, h3 of the hidden layer or nodes o1, o2 of the output layer. b_χ are the threshold values of different neurons in the hidden layer as well as in the output layer.

In the neurons of the hidden layer of a BP neural network, the transfer function f_{BP} generally adopts the *Sigmoid* function[176]:

$$f_{\mathrm{BP}}(x) = \frac{1}{1+e^{-x}} \tag{4-3}$$

And in the neurons of the output layer of BP neural network, the transfer function is usually expressed directly using a linear function[177], [178]:

$$f_{\mathrm{BP}}(x) = x \tag{4-4}$$

Ultimately, the output values of the hidden layer are weighted to obtain the output values of the BP neural network directly:

$$\begin{cases} y_{\mathrm{o1}} = w_7 \cdot y_{\mathrm{h1}} + w_8 \cdot y_{\mathrm{h2}} + w_9 \cdot y_{\mathrm{h3}} \\ y_{\mathrm{o2}} = w_{10} \cdot y_{\mathrm{h1}} + w_{11} \cdot y_{\mathrm{h2}} + w_{12} \cdot y_{\mathrm{h3}} \end{cases} \tag{4-5}$$

The training process of BP neural network is essentially the process of updating its weights and thresholds. The basic idea of updating the weights and thresholds is to minimize the error *Err* between the desired output value and the actual output value of the BP neural network, so that the neural network can achieve the effect of function approximation. The Widrow-Hoff learning rule based on Least Mean Square (LMS) is usually used to update the weights and thresholds[179]. The update equation for the weights can be simply expressed as:

$$w(n+1) = w(n) + \upsilon\left(-\frac{\partial Err}{\partial w}\right) \tag{4-6}$$

where *Err* is the error function and υ denotes the learning rate, which usually ranges from 0.01 to 0.8.

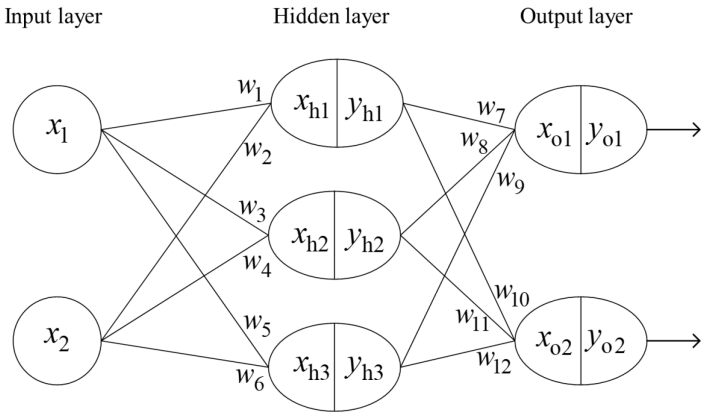

Fig. 4.1 Topology diagram of BP neural network

4.1.2 Basic principles of multi-objective particle swarm optimization algorithm

Particle Swarm Optimization (PSO) is described mathematically as follows: In a D-dimensional searching domain consisting of *m* particles, each particle moves with a certain velocity. In the k_{th} iteration, the position of the i_{th} particle is $X_i^k = (X_{i1}^k, X_{i2}^k, X_{i3}^k, \ldots X_{im}^k)$ and its velocity vector is $V_i^k = (V_{i1}^k, V_{i2}^k, V_{i3}^k, \ldots V_{im}^k)$. Through the iteration, the velocity of the particle in the $(k+1)_{\text{th}}$ generation is calculated as[75]:

$$V_i^{k+1} = \omega V_i^k + c_1 r_1 (P_{\text{id}}^k - X_i^k) + c_2 r_2 (P_{\text{gd}}^k - X_i^k) \quad ;.(4\text{-}7)$$

The iterative calculation equation of position is:

$$X_i^{k+1} = X_i^k + V_i^{k+1} \quad .(4\text{-}8)$$

Where ω is the inertia weight; r_1 and r_2 are random numbers distributed in the interval [0,1]; P_{id}^k is the optimal position of individual particle, and P_{gd}^k is the global optimal position of the particles in population; c_1 and c_2 are constant coefficients to be determined.

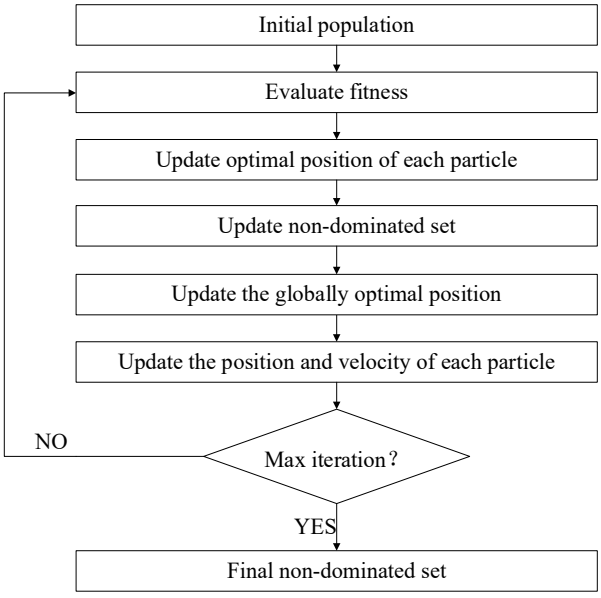

Fig. 4.2 Algorithm procedure of MOPSO

The specific flow of the multi-objectives particle swarm optimization algorithm (MOPSO) is shown in Fig. 4.2. To apply this algorithm, the first step involves initializing the population of particles by randomly generating their initial positions X_i^k and velocities V_i^k. Then, the fitness value of the particles in the population is calculated and furtherly compared with the fitness value of the previous generation of particles to determine the optimal position of an individual particle P_{id}^k. Subsequently, all particles are added to the non-inferior solution set of MOPSO. The dominant relationship between the particles is compared based on the fitness value and the dominant particles are eliminated. One of the particles is randomly selected from the non-inferior set, and its corresponding position is considered as the global optimal position P_{gd}^k. Finally, the particle velocity and position are updated according to P_{id}^k and P_{gd}^k, and the particle population is updated[180], [181].

4.2 Flow of the optimization design method

A novel machine optimization design method that combines the advantages of the BP neural network including accurate nonlinear mapping ability and stable as well as reliable training algorithm, with MOPSO which benefits from easy implementation, high accuracy, and fast convergence is proposed in the thesis[182]. In this method, the BP neural network is used as a surrogate model to efficiently calculate the optimization objective values for different combinations of design variables, while MOPSO is used to iteratively derives the optimal design based on the initial random particle population.

However, the training results of the BP neural network are influenced by the initial weights and thresholds, which means that the random selection of initial weights and thresholds for the BP neural network will negatively impact its function approximation, thus rendering the entire optimization design process ineffective. To address above issues, genetic algorithm which is characterized by excellent effect of global optimization is introduced to optimize the training process of the BP neural network. The resulting genetic algorithm based back-propagation neural network (GA-BPNN) is then applied to optimize the design of the machine.

In summary, an optimization design method based on GA-BPNN and MOPSO is proposed, as illustrated by the algorithm flowchart shown in Fig. 4.3. It can be seen that MOPSO is the main part of the proposed optimization design method, while GA-BPNN serves as a surrogate model that is integrated into MOPSO as an objective function. GA-BPNN is used to calculate the fitness value of particles in population. The detailed procedure to adopt proposed optimization method is as follow:

(1) The orthogonal experiment design method is used to obtain the training sample space for the construction of BP neural network, and the values of optimization objective corresponding to each group of optimization variables in the sample space are calculated.

(2) The GA-BPNN is trained based on training sample space, so as to achieve the fitting of the functional by which the relationship between the optimization variables and the optimization objective can be predicted.

(3) The Pareto optimal solution of the optimal design problem is obtained by the MOPSO algorithm. The Pareto optimal solution is actually a non-dominated set of solutions, so the best design solution is eventually needed to be selected according to the specific design requirements.

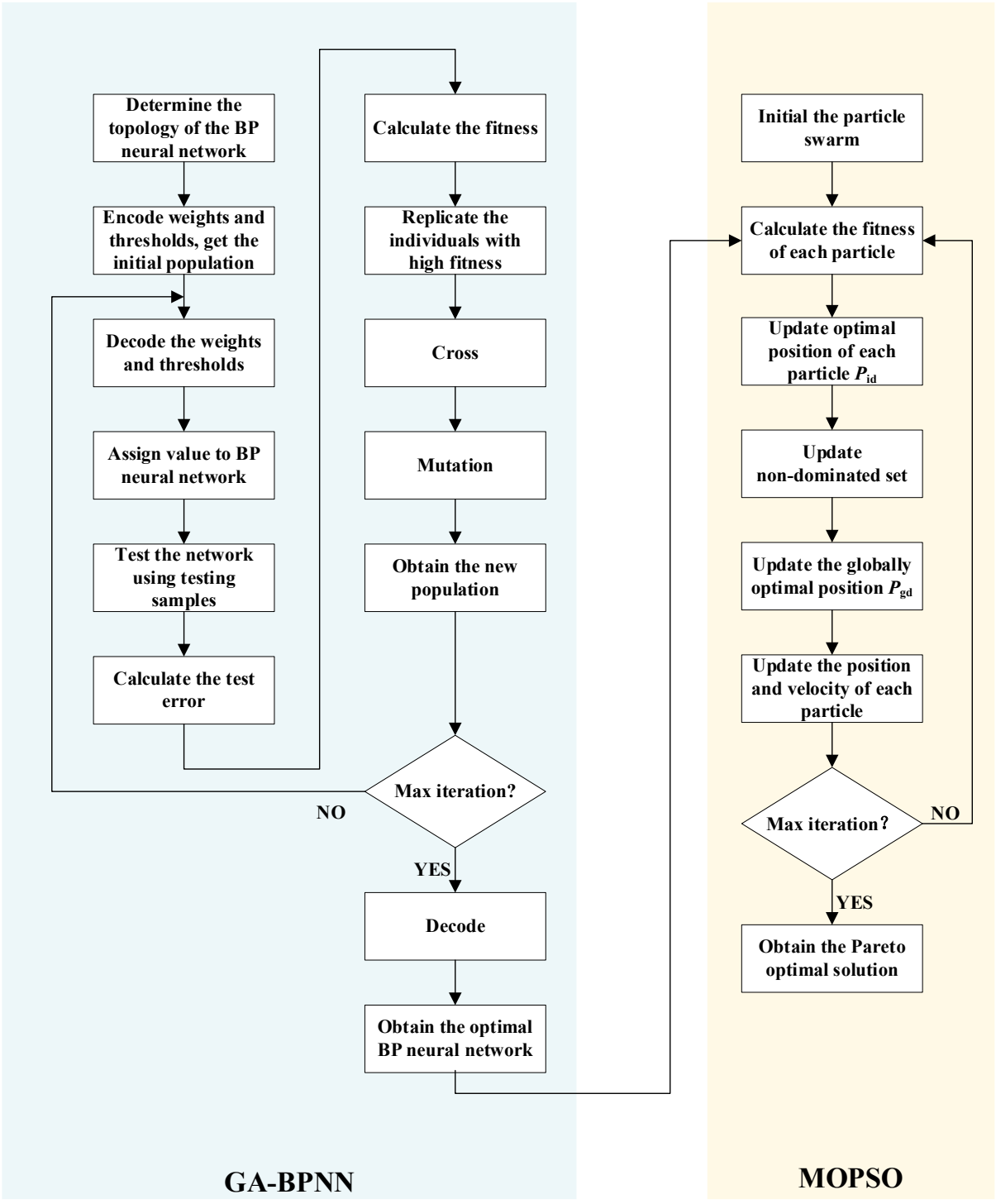

Fig. 4.3 Flow chart of novel optimization design method

4.3 Optimal design of DS-HSDR-TFPMSM

4.3.1 Optimization problem description

In the thesis, the average value of output torque T_{avg} and torque ripple ε_{ripple} of DS-HSDR-TFPMSM at rated current are selected as the optimization objectives to satisfy the requirements of industrial robot for low torque ripple and further improve the torque density of the machine.

Based on the parametric analysis in Chapter 2, the central angle of outer PM α_{out}, the central angle of inner PM α_{in}, the central angle of stator shoe β_{s} and its thickness h_{SMC} are identified as optimization variables and represented by the parameter vector $\boldsymbol{X}$ as follows:

$$\boldsymbol{X} = \left[\alpha_{\text{out}} \quad \alpha_{\text{in}} \quad \beta_{\text{s}} \quad h_{\text{SMC}}\right] \tag{4-9}$$

Considering the fabrication process and structural strength of the rotor disk and stator shoe, the range of the parameter vector $\boldsymbol{X}$ to be optimized is determined in advance. The upper boundary $\boldsymbol{X}_{\text{up}}$ of the parameter vector is:

$$\boldsymbol{X}_{\text{up}} = \left[32° \quad 32° \quad 28° \quad 8\text{mm}\right] \tag{4-10}$$

The lower bound $\boldsymbol{X}_{\text{down}}$ is:

$$\boldsymbol{X}_{\text{up}} = \left[32° \quad 32° \quad 28° \quad 8\text{mm}\right] \tag{4-11}$$

In summary, the multi-objective optimal design problem of DS-HSDR-TFPMSM can be formulated as the following equation:

$$\begin{aligned} &\max\left(T_{\text{avg}}\left(\boldsymbol{X}\right)\right) \qquad \min\left(\varepsilon_{\text{ripple}}\left(\boldsymbol{X}\right)\right) \\ &s.t. \quad \boldsymbol{X}_{\text{down}} \le \boldsymbol{X} \le \boldsymbol{X}_{\text{up}} \end{aligned} \tag{4-12}$$

4.3.2 Design of sample space

Given its function approximation capabilities, the BP neural network can be employed to fit the relationship between optimization objectives and variables. In advance to the construction of the network, it is necessary to design the sample space and collect optimization objective values within it.

The four-factor, five-level table shown in Table 4.1 is used to design the training sample according to the range of values of the optimization variables. To ensure the accuracy of the BP neural network, the output torque performance of DS-HSDR-TFPMSM at rated current for each group of training samples is calculated through FEM.

Table 4.1 The table of four factors and five levels

	1	2	3	4	5
α_{out} /°	24	26	28	30	32
α_{in} /°	24	26	28	30	32
β_{s} /°	20	22	24	26	28
h_{SMC} /mm	4	5	6	7	8

According to the four-factor five-level table shown in Table 4.1, the total number of samples is $5^4 = 625$, which means the whole process for collecting the training samples is time-consuming and occupies too much computational resources. In order to shorten the time required for sample collection, the orthogonal experimental design method is adopted. Table 4.2 shows the training samples of BP neural network obtained by L25 orthogonal experimental table, and the optimization objective values for each sample are. It can be found that the sample

numbered 24 in Table 4.2 possesses the highest average output torque and the lowest torque ripple, so this sample point is taken as the best point in the sample space of the L25 orthogonal experimental design.

Table 4.2 L25 orthogonal experimental design table

Serial number	α_{out} (*mech.deg*)	α_{in} (*mech.deg*)	β_s (*mech.deg*)	h_{SMC} (mm)	Rated torque I=12.5A (Nm)	Torque ripple (%)
1	24	24	20	4	16.06	8.61
2	24	26	22	5	16.41	7.45
3	24	28	24	6	16.43	7.26
4	24	30	26	7	16.13	5.06
5	24	32	28	8	15.07	3.52
6	26	24	22	6	16.77	7.71
7	26	26	24	7	16.73	5.78
8	26	28	26	8	16.33	7.35
9	26	30	28	4	16.83	7.77
10	26	32	20	5	16.92	6.93
11	28	24	24	8	16.88	8.20
12	28	26	26	4	17.52	10.34
13	28	28	28	5	16.94	7.27
14	28	30	20	6	17.26	7.70
15	28	32	22	7	17.41	4.12
16	30	24	26	5	17.59	5.52
17	30	26	28	6	16.88	4.69
18	30	28	20	7	17.43	4.99
19	30	30	22	8	17.54	5.44
20	30	32	24	4	18.20	6.20
21	32	24	28	7	16.66	5.50
22	32	26	20	8	17.49	3.15
23	32	28	22	4	18.22	3.32
24	32	30	24	5	18.25	2.48
25	32	32	26	6	17.97	4.91

4.3.3 BP neural network optimized by genetic algorithm

To establish a BP neural network, there are two main steps are involved. The first step is to determine the topology of the neural network, which includes the number of network layers and neurons in the hidden layer. The second step is to update the values of weight and threshold iteratively through backpropagation (BP) of the error for achieving accurate approximation of the neural network.

Based on the description of optimization problem previously, the input layer of the proposed BP neural network consists of 4 parameters and the output layer includes 2 neurons. Generally, a BP neural network with one hidden layer is sufficient to solve most problems of nonlinear mapping, so the number of hidden layers is set to 1 to alleviate complexity of the network. The number of neurons in the hidden layer should be less than twice the number of input parameters based on existing experience, thus the final decision is to have 7 neurons in the hidden layer. Additionally, the activation function in the neurons of hidden layer can be used to better fit the nonlinear mapping relationship. The most commonly used *Sigmoid* activation function, besides the form given in (4-3), can also be used in the following form [183]:

$$f_{\mathrm{BP}}(x)=\frac{2}{1+e^{-2x}}-1 \qquad ,(4\text{-}13)$$

The two forms given in (4-3) and (4-13) are named *logsig* as well as *tansig*, respectively.

Once the topology of the neural network has been established, the next step is to train the network. In this study, the training samples presented in Table 4.2 are used, and the weights and thresholds are updated iteratively based on the Widrow-Hoff learning rule to achieve the function approximation effect.

Table 4.3 The data of test samples

Serial number	α_{out} (*mech.deg*)	α_{in} (*mech.deg*)	β_{s} (*mech.deg*)	h_{SMC} (mm)	Rated torque I=12.5A (Nm)	Torque ripple (%)
1	30.5	29	24	5	18.06	7.16
2	28.5	28.5	25	6	17.49	11.37
3	27	27	23	7.5	16.99	7.22
4	26.8	24.5	22.8	4.3	17.23	5.39
5	29.3	27.3	26.4	5.2	17.57	7.61

Ultimately, the established BP neural network can be used to approximate the mapping relationship between the optimization variables of DS-HSDR-TFPMSM and its optimization objectives. To evaluate the approximation performance of the BP neural network, additional test sample space is required, as shown in Table 4.3. Firstly, the optimization variables in each set of test sample are input into the BP neural network for computation and compared with the results obtained by FEM. Then, the computational error of the BP neural network is quantified using Euclidean norm.

$$\|err\|_2 = \sqrt{\sum_{n=1}^{5}\left(\left(\hat{X}_n - X_n^*\right)^2 + \left(\hat{Y}_n - Y_n^*\right)^2\right)} \tag{4-14}$$

Where X_n^* and Y_n^* represent the rated torque and torque ripple values of the n_{th} test sample in Table 4.3, respectively, $\hat{X}_n$ and $\hat{Y}_n$ represent the predicted values of rated torque and torque ripple of the n_{th} test sample obtained by BP neural network.

The BP neural network was constructed using two different activation functions, *logsig* and *tansig*, for the hidden layer. The network was trained 1000 times with a learning rate of 0.01 and initial weights and thresholds randomly selected from the range [-0.5 0.5]. The BP neural network after training was tested using the samples in Table 4.3, and the errors were calculated for both activation functions. The computational errors are shown in Table 4.4, and it can be observed that the BP neural network constructed using the *tansig* function has a better approximation effect. Therefore, the *tansig* function was chosen as the activation function for the neurons in the hidden layer.

Table 4.4 Calculation error of BPNN using different activation function

	logsig	***tansig***
$\|err\|_2$	10.7086	1.1948

The initial values of the weight and threshold of the BP neural network can greatly impact its approximating effect. However, there is currently no established theory to guide the selection of initial values. To address this issue, a genetic algorithm characterized by global optimization effect is utilized in the thesis to optimize the initial values of the BP neural network to improve the accuracy of approximation.

The basic principle of the optimization of the BP neural network using genetic algorithms is as follows. Firstly, an evolutionary population indicating the initial values of BP neural network is randomly generated and used to train the BP neural network. Then, the computational error of the neural network is evaluated using test samples, and the fitness value of each set of initial values in the population is calculated. Finally, basic genetic operations such as selection, crossover, mutation, and reinsertion are performed on the population to select the initial value of BP neural network with the highest fitness value by which the smallest computational error of the BP neural network can be obtained.

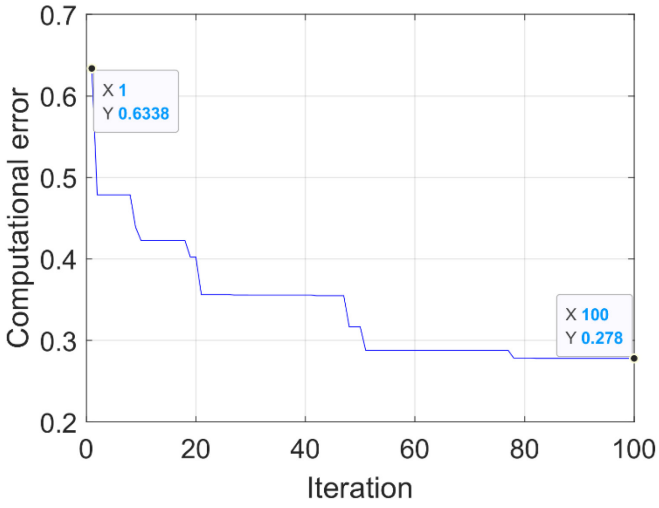

Fig. 4.4 Evolutionary curve of calculation error

The evolutionary curve of the computational error during the optimization process is shown in Fig. 4.4. In the thesis, the number of population individuals for the genetic algorithm is set to 60, and a total of 100 iterations are performed. It can be seen that the final computational error is reduced from the initial value of 0.634 to 0.278, demonstrating the effectiveness of the genetic algorithm in optimization of BP neural network.

4.3.4 Pareto front of MOPSO

The optimized BP neural network is used in conjunction with the MOPSO algorithm to obtain the Pareto optimal solution, in which positions of all non-dominated particles in the are included. In the optimal design of DS-HSDR-TFPMSM, the particle positions are represented by the parameter vector $\boldsymbol{X}$ in equation (4-9). The Pareto optimal solution is then substituted into the BP neural network to calculate the values of optimal objectives, which is then mapped into the objective space to form the Pareto front. In this study, the MOPSO algorithm is implemented with a population of 5000 particles and a maximum iteration number of 100. The resulting Pareto front for the optimization design of DS-HSDR-TFPMSM is shown in Fig. 4.5. The average torque shown in Pareto front is distributed between 17.9Nm and 18.2Nm, while the torque ripple is distributed between 1.5% and 3.5%. And the particles are mainly concentrated around 2.5% as shown in Fig. 4.5. Given that the variation of the average torque value in the Pareto front is only 0.3Nm, the particle located in the red dashed box in Fig. 4.5 is selected as the optimal solution, as it has the smallest torque ripple. The objective values of selected point are average output torque of 17.89Nm and torque ripple of 1.50% while its corresponding optimization parameter vector is $\boldsymbol{X}$= [31.9° 23.0° 21.5° 4.2mm].

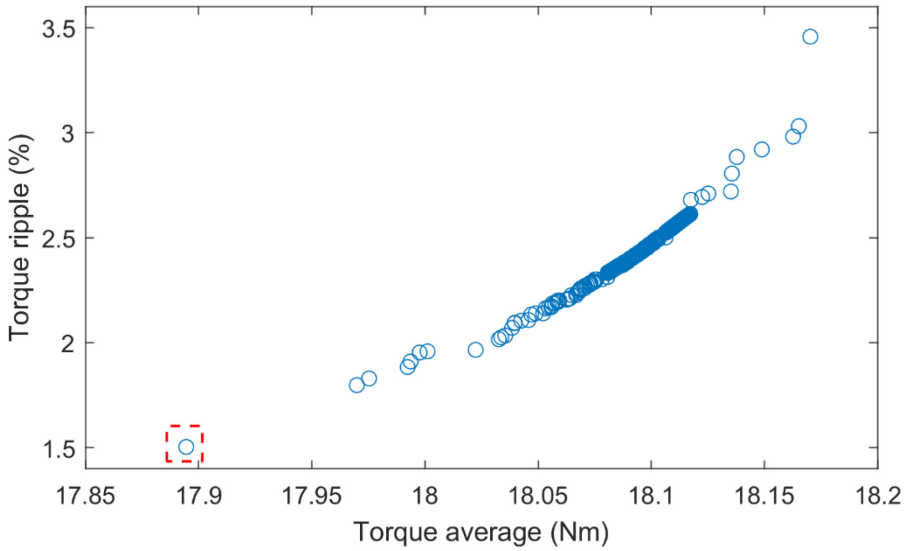

Fig. 4.5 Pareto front

4.4 Validation of optimization results

An electromagnetic analysis model for FEM was constructed based on the optimal solution obtained from the optimization design, and its torque performance was calculated. The simulation results of the preliminary design solution presented in Chapter 2, the simulation results of the optimal point of the training sample in Table 4.2, and the simulation results of the optimal solution obtained by optimization design are compared. The comparison of the output torque waveform under the rated current (I_N =12.5A) is shown in Figure 4.6 shows. It can be concluded through the comparative analysis of the simulation results of both the initial design

solution and the optimal solution of the optimization design that the average output torque of the DS-HSDR-TFPMSM increases from 17.26Nm in the preliminary design to 17.83Nm in optimal solution, while the torque ripple decreases from 9.05% to 1.47%. The simulation results of the optimal point in the training samples were also analyzed of which the average output torque is 18.25Nm and the torque ripple is 2.48%. Although the average torque of the optimal solution was slightly lower than that of optimal point in the training samples, the torque ripple was much better. Comparing the results of the optimal solution using FEM with the results approximated by BP neural network, it can be concluded that the results obtained by the two methods were basically the same. Eventually, the proposed optimization design method is proved to be effective and trustworthy.

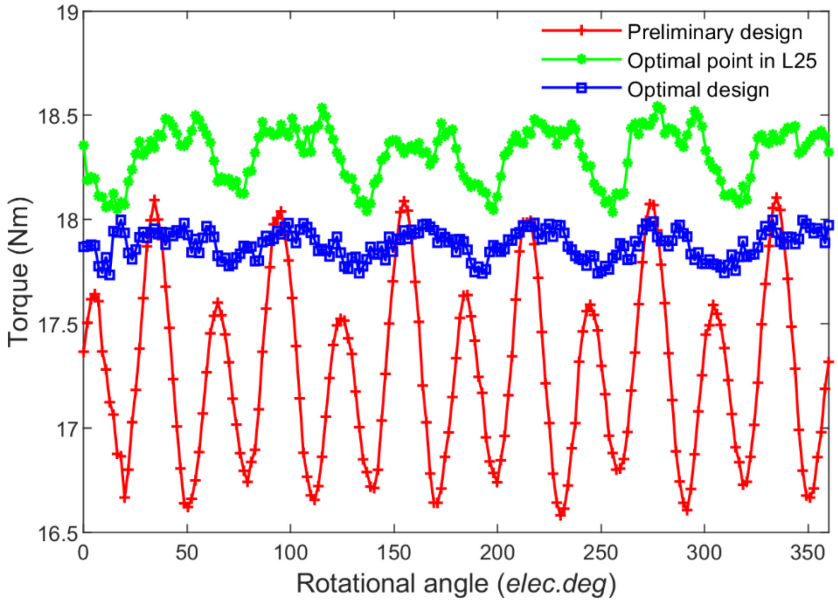

Fig. 4.6 Comparison of torque waveform under rated current

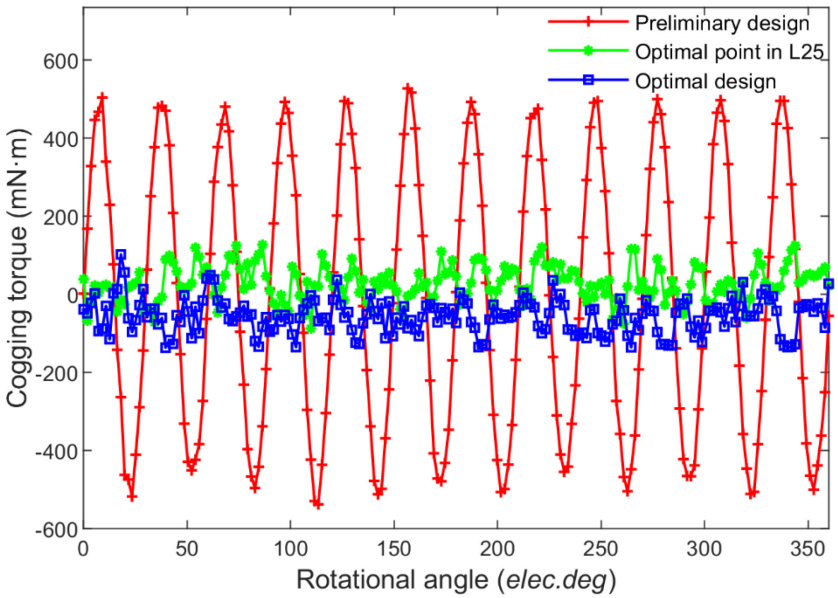

Fig. 4.7 Comparison of cogging torque waveform

In addition, it can be found that the torque ripple of the preliminary design in Fig. 4.6 exhibits clear periodicity that corresponds to the cogging torque that the cogging torque periodically varies 12 times in one electrical cycle for a 10-pole/12-slot PMSM. However, the periodicity of the cogging torque is no longer evident in the simulation results of the optimal point of the training sample and the optimal design. The main reason is due to the significant reduction of the cogging torque resulting from the optimal design, as shown in Fig.4.7, leading the torque ripple mainly influenced by the armature field.

4.5 Conclusion

In this chapter, an optimization design method based on BP neural network and MOPSO is proposed to obtain the optimal design solution of DS-HSDR-TFPMSM. The main research work and conclusions of this chapter are as follows.

(1) A novel optimization design method based on BPNN and MOPSO is proposed, that combines the advantages of the BP neural network including accurate nonlinear mapping ability and stable as well as reliable training algorithm, with MOPSO which benefits from easy implementation, high accuracy, and fast convergence. The mapping relationship between optimization objective and optimization variables are first approximated by BPNN, and the optimal design solution of the machine is then solved by the MOPSO algorithm.

(2) The multi-objective optimization design was conducted for the DS-HSDR-TFPMSM. Firstly, the functional relationship between the optimization variables and the output torque performance of the DS-HSDR-TFPMSM was approximated using BP neural network. However, due to the disadvantage of the BP neural network falling into local optima during the training process, a genetic algorithm was used to optimize it. By comparing the computational error of the neural network before and after the optimization, the effectiveness of the genetic algorithm in optimizing the BP neural network was confirmed. Subsequently, the BP neural network was substituted into the MOPSO algorithm to obtain the Pareto optimal solution set and Pareto front of the multi-objective optimization design of DS-HSDR-TFPMSM. The proposed optimization design method was validated by comparing the output torque calculation results of the optimal solution obtained from the FEM with the results of initial design. The results show that the average value of the motor output torque increases from 17.26Nm to 17.83Nm, and the torque ripple decreases from 9.05% to 1.47%, which verifies the effectiveness of the proposed optimization design method. In addition, the accuracy of the BP neural network is verified by comparing the BP neural network approximating results of the optimal solution with the results obtained by FEM.

Chapter 5. FTC methods of dual three-phase PMSM

In order to satisfy the requirements of the electric drive units in industrial robots for high reliability, the multiphase machine with excellent fault tolerant performance is a better choice. In Chapter 2, the dual three-phase fault tolerant designs are proposed for DS-HSDR-TFPMSM based on its topology and slot/pole combination. The control methods of dual three-phase PMSM are similar to those of traditional three-phase machine, mainly including: vector control, direct torque control and model predictive control. The vector control method for dual three-phase machine has been widely used due to the advantages of high control accuracy and easy implementation. However, the fault tolerant operation of dual three-phase PMSM under fault conditions cannot be achieved using above control methods. Therefore, FTC techniques for dual three-phase PMSM need to be studied to improve its reliability. The faults occurring in electric machine mainly include open or short-circuit faults in one phase winding, and open or short-circuit faults caused by communication interruptions or damage of the switching device, however, above faults can eventually be equated to one-phase open-circuit fault by electrical operation. During one-phase open-circuit fault condition, the winding currents of dual three-phase PMSM need to be reconfigured due to the change in current constraints. Thus, the FTC of dual three-phase PMSM is essentially the reconfiguration and control of its winding currents under fault condition. The reconfiguration of winding currents can be carried out in different frames, including the natural frame, the reduced-order decoupled frame, and the normal decoupled frame. However, FTC in the natural frame generally suffers from poor control accuracy. For FTC in the reduced-order decoupled frame, the mathematical model based on the reduced-order decoupled frame needs to be re-established, and the reduced-order machine mathematical models corresponding to different phase winding open circuits are different, which leads to significant complexity in the control model. Therefore, in the thesis, the normal decoupled frame is chosen to reconfigure the winding currents under fault condition, which reduces the complexity of the machine while ensuring its FTC accuracy. The disk rotor of DS-HSDR-TFPMSM is subject to not only tangential stress for generating torque but also axial stress. The asymmetric distribution of axial stress on both sides of the stator disk can impact the operation of machine, resulting in significant vibration and noise, particularly under fault conditions. Therefore, the analysis of the axial stresses in the rotor disk is significantly important. In addition, a common problem in the field of FTC of dual three-phase PMSM is the poor high-speed control performance. Under the fault condition of one-phase open-circuit condition, the FTC method can only output smooth torque at low speed, which directly affects the dynamics industrial robot systems under fault condition. Therefore, it is significantly important to research the FTC method of dual three-phase PMSM under high-speed condition.

In summary, the main focus of this chapter is on the FTC technology of dual three-phase PMSM based on the normal decoupled frame, which includes the reconfiguration of winding currents and the FTC method under high-speed conditions. Firstly, the mathematical model of dual three-phase PMSM is derived, and the mathematical model of dual three-phase PMSM in decoupled frame is given, and the vector control model of dual three-phase PMSM is established based on Energetic Macroscopic Representation (EMR) method. Then, the FTC methods based on the principle of minimum copper loss and the principle of maximum torque operation range are proposed under the condition of one-phase open-circuit fault, and the fault tolerant vector control model is obtained by reconfiguring the reference current on the basis of the normal vector control model. Finally, the simulation analysis of FTC method is conducted based on the above methods for DS-HSDR-TFPMSM with one-phase open-circuit fault. To validate the influence of the axial force on the rotor, a detailed analysis of the axial stresses on the rotor disk of dual three-phase DS-HSDR-TFPMSM is conducted. In addition, the FTC

method of dual three-phase PMSM at high speed is investigated. A multi-reference frame based method and a proportional-resonant controller (PR) based method are both adopted to track and control the harmonic components in the currents under high speed. Ultimately, the proposed FTC technique is experimentally investigated with a dual three-phase surface-mounted PMSM.

5.1 Mathematical model of dual three-phase PMSM

The derivation of the machine mathematical model is a key prerequisite for establishing an accurate machine control model, as the machine mathematical model serves as the basis for the research of machine control methods. The mathematical model of a dual three-phase PMSM in the natural frame of the windings can be directly derived by analyzing the spatial distribution of the windings and applying the basic principles of circuitry and electromagnetism. The mathematical model mainly consists of equations for the magnetic linkage, voltage, and torque. However, the mathematical model established in the natural frame is characterized by significant coupling between the equations of each phase winding, making the design of control methods difficult. In order to improve the control of dual three-phase machine, Vector Space Decomposition (VSD) transformation is generally used to transform the mathematical model under the dual three-phase natural frame to the decoupled frame, thus the coupling between the phases is eliminated.

5.1.1 Mathematical model under natural frame

The mathematical model in natural frame is the basis for deriving the mathematical model in the decoupled frame. In order to obtain the mathematical model of a dual three-phase PMSM in the natural frame, the following hypotheses are proposed:

(1) The waveforms of both stator winding permanent magnet flux linkage and back-EMF are sinusoidal.

(2) Neglecting the saturation situation existing in the magnetic circuit of the machine.

(3) Neglecting the mutual leakage inductance between the stator windings.

(4) Neglecting the impact of the factors such as temperature rise on the control parameters of electric machine during machine operation.

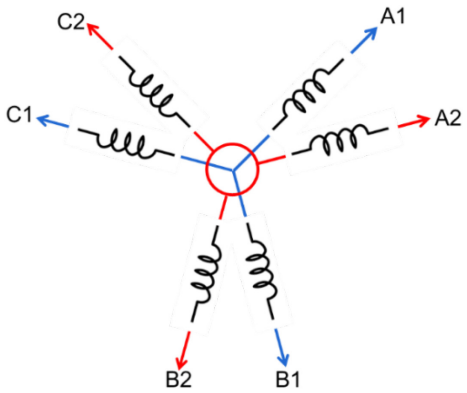

Fig. 5.1 Winding space distribution of dual three-phase permanent magnet machine (separated neutral points)

Based on the above hypotheses, the mathematical model of dual three-phase machine including the equations of magnetic flux linkage, voltage, and torque is derived. The spatial phasor distribution of the windings of dual three-phase PMSM is shown in Fig. 5.1. In order to eliminate the effect of zero-sequence currents, dual symmetrical three-phase winding (A1-B1-C1 and A2-B2-C2) design with isolated neutral point is used; in addition, as previously

described in Chapter 2, the phasor shift between the two sets of symmetrical three-phase windings δ_e is 30°, so that it can be equivalent to a symmetrical half twelve-phase machine.

Combining the assumptions made above and the spatial distribution of the windings shown in Fig. 5.1, the equation of magnetic flux linkage of a dual three-phase PMSM in the natural frame can be expressed as:

$$\boldsymbol{\Psi}_s = \boldsymbol{L}\boldsymbol{I}_s + \boldsymbol{\Psi}_{PM,s} \tag{5-1}$$

Where $\boldsymbol{\Psi}_s$ is the stator winding flux linkage vector, $\boldsymbol{I}_s$ is the stator current vector, and $\boldsymbol{\Psi}_{PM,s}$ is the PM flux linkage vector. Besides, $\boldsymbol{L}$ is the stator winding inductance matrix. The stator winding flux linkage vector and current vector can be expanded as:

$$\begin{aligned} \boldsymbol{\Psi}_s &= [\Psi_{A1} \quad \Psi_{B1} \quad \Psi_{C1} \quad \Psi_{A2} \quad \Psi_{B2} \quad \Psi_{C2}] \\ \boldsymbol{I}_s &= [I_{A1} \quad I_{B1} \quad I_{C1} \quad I_{A2} \quad I_{B2} \quad I_{C2}] \end{aligned} \tag{5-2}$$

The stator winding inductance matrix $\boldsymbol{L}$ in (5-1) can be expanded to the following form:

$$\begin{aligned} \boldsymbol{L} &= \begin{bmatrix} \boldsymbol{L}_s & \boldsymbol{M}_s \\ \boldsymbol{M}_s^T & \boldsymbol{L}_s \end{bmatrix} \\ \boldsymbol{L}_s &= \begin{bmatrix} L_s & M_s & M_s \\ M_s & L_s & M_s \\ M_s & M_s & L_s \end{bmatrix} \quad \boldsymbol{M}_s = \begin{bmatrix} M_1 & M_2 & M_3 \\ M_3 & M_1 & M_2 \\ M_2 & M_3 & M_1 \end{bmatrix} \end{aligned} \tag{5-3}$$

The inductance matrix $\boldsymbol{L}$ further contains the mutual inductance matrix $\boldsymbol{L}_s$ within the same symmetrical three-phase winding and the mutual inductance matrix $\boldsymbol{M}_s$ between the two sets of symmetrical three-phase windings.

The PM flux linkage vector $\boldsymbol{\Psi}_{PM,s}$ in (5-1) is calculated as:

$$\boldsymbol{\Psi}_{PM,s} = \boldsymbol{M}_{fs}(\theta) I_f \tag{5-4}$$

Where, $\boldsymbol{M}_{fs}(\theta)$ denotes the mutual inductance matrix between the equivalent excitation winding of the PM and the stator winding. The mutual inductance between each stator phase winding and the equivalent excitation winding is calculated as:

$$M_{fs}(\theta_i) = \sum_{m=1}^{\infty} M_{fm} \cos(m\theta_i + \phi_m) \tag{5-5}$$

Where θ_i is the spatial phasor difference between the axis of rotor pole and i_{th} phase winding, m is the number of harmonics, M_{fm} is the amplitude of the m_{th} harmonic component, and ϕ_m is the initial phasor of the m_{th} harmonic component. Based on the assumption that only the fundamental PM flux linkage is considered, thus only the term m=1 is included in equation (5-5).

Based on the equation of the magnetic flux linkage, the voltage equation of the dual three-phase PMSM using motor convention as shown in Fig. 5.2 can be obtained as:

$$\boldsymbol{U}_s = R_s \boldsymbol{I}_s + \frac{d\boldsymbol{\Psi}_s}{dt} \tag{5-6}$$

Where, $\boldsymbol{U}_s$ is the voltage vector.

$$\boldsymbol{U}_s = [U_{A1} \quad U_{B1} \quad U_{C1} \quad U_{A2} \quad U_{B2} \quad U_{C2}] \tag{5-7}$$

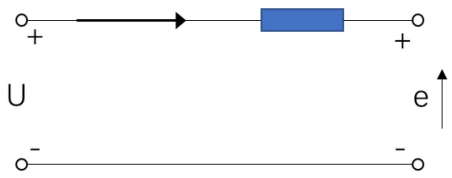

Fig. 5.2 Motor conventions

Based on the equation of the magnetic flux linkage given in (5-1) and the stator current vector $\boldsymbol{I}_s$, then according to the principle of electromechanical energy conversion in the electric machine, the torque equation of the dual three-phase PMSM can be derived as

$$T_{em} = \frac{1}{2} p \frac{\partial(\boldsymbol{I}_s^T \boldsymbol{\Psi}_s)}{\partial \theta} \tag{5-8}$$

where p denotes the number of PM pole pairs and θ is the rotational electrical degrees of the rotor.

5.1.2 Vector space decomposition (VSD) transformation

To simplify the control of dual three-phase PMSM, the equation of state derived in the natural frame need to be transformed into the decoupled frame using VSD transformation [184]. For conventional three-phase machine, the VSD transformation indicates the Clark transformation, through which the equation of state is transformed from the natural frame to the stator $\alpha-\beta$ stationary frame. In addition, to decouple the equation of state from the position of the rotor and eliminate the time-varying characteristic of the equation of state in natural frame, the PARK transformation is further used to transform the equation of state from the $\alpha-\beta$ stationary frame to the $d-q$ rotating frame. There is similarity of winding structure between conventional three-phase winding and dual three-phase winding, so the equation of state of the dual three-phase PMSM in the natural frame can be directly transformed to the rotating $d-q$ frame shown in Fig. 5.3 by using the transformation matrix $\boldsymbol{T}_1$ in (5-9). In Fig. 5.3, the dashed lines indicate the synthetic winding axes of phase A1 and A2, θ indicates the electrical angle between the pole axis of rotor PM where the d-axis is located and the synthetic winding axes, θ_{eh} represents the electrical angle between the synthetic winding axes and the axis of the phase A1. The asymmetric dual three-phase machine with a phasor shift of $\delta_e = 30°$ is researched, thus δ_{eh} is 15°.

$$\boldsymbol{T}_1(\theta) = \begin{bmatrix} \boldsymbol{T}_P(\theta+\delta_{eh}) & \boldsymbol{0}_{2,3} \\ \boldsymbol{0}_{2,3} & \boldsymbol{T}_P(\theta-\delta_{eh}) \end{bmatrix}$$

$$\boldsymbol{T}_P(\chi) = \sqrt{\frac{2}{3}} \begin{bmatrix} \cos(\chi) & \cos(\chi-\frac{2}{3}\pi) & \cos(\chi-\frac{4}{3}\pi) \\ -\sin(\chi) & -\sin(\chi-\frac{2}{3}\pi) & -\sin(\chi-\frac{4}{3}\pi) \end{bmatrix} \tag{5-9}$$

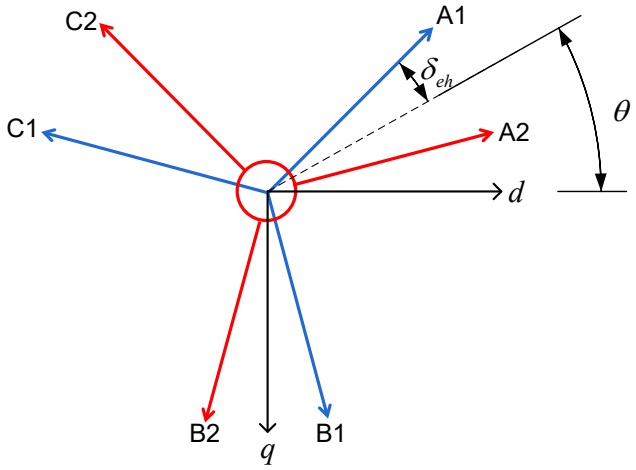

Fig. 5.3 The transformation of winding vector space

However, substituting (5-9) into (5-1) and following equation can be obtained:

$$\boldsymbol{\Psi}_{\mathrm{T1}}=\boldsymbol{T}_1\boldsymbol{\Psi}_{\mathrm{s}}=\boldsymbol{T}_1\boldsymbol{L}\boldsymbol{T}_1^{-1}\left(\boldsymbol{T}_1\boldsymbol{I}_{\mathrm{s}}\right)+\boldsymbol{T}_1\boldsymbol{\Psi}_{\mathrm{PM,s}}=\boldsymbol{L}_{\mathrm{T1}}\boldsymbol{I}_{\mathrm{T1}}+\boldsymbol{\Psi}_{\mathrm{PM,T1}} \tag{5-10}$$

where $\boldsymbol{L}_{\mathrm{T1}}$ is the inductance matrix transformed by $\boldsymbol{T}_1$.

$$\boldsymbol{L}_{\mathrm{T1}}=\begin{bmatrix} L_{\mathrm{d}} & 0 & M_{\mathrm{d}} & M_{\mathrm{q}} \\ 0 & L_{\mathrm{q}} & -M_{\mathrm{q}} & M_{\mathrm{d}} \\ M_{\mathrm{d}} & -M_{\mathrm{q}} & L_{\mathrm{d}} & 0 \\ M_{\mathrm{q}} & M_{\mathrm{d}} & 0 & L_{\mathrm{q}} \end{bmatrix} \tag{5-11}$$

It can be found that there are a large number of non-diagonal elements in (5-11). Therefore, the decoupling of the state equations in the natural frame of the dual three-phase machine cannot be achieved by the transformation matrix $\boldsymbol{T}_1$. In order to make $\boldsymbol{L}_{\mathrm{T1}}$ a diagonal matrix and thus obtain the decoupled equation of state [185], it is necessary to further introduce the transformation matrix $\boldsymbol{T}_2$:

$$\begin{aligned} \boldsymbol{T}_2&=\frac{1}{\sqrt{2}}\begin{bmatrix} \cos\varepsilon & -\sin\varepsilon & \cos\varepsilon & \sin\varepsilon \\ \sin\varepsilon & \cos\varepsilon & -\sin\varepsilon & \cos\varepsilon \\ \sin\varepsilon & \cos\varepsilon & \sin\varepsilon & -\cos\varepsilon \\ -\cos\varepsilon & \sin\varepsilon & \cos\varepsilon & \sin\varepsilon \end{bmatrix} \\ \varepsilon&=\delta_{\mathrm{eh}}-\gamma \\ \gamma&=\frac{1}{2}\sin^{-1}\left(\frac{\sqrt{3}}{2}\frac{M_3-M_2}{M^*}\right) \\ M^*&=\sqrt{M_1^2+M_2^2+M_3^2-M_1M_2-M_2M_3-M_3M_1} \end{aligned} \tag{5-12}$$

For a dual three-phase PMSM with phasor shift $\delta_e=30°$ and symmetrical winding parameters, the transformation matrix $\boldsymbol{T}_2$ can be simplified as:

$$\boldsymbol{T}_2=\frac{1}{\sqrt{2}}\begin{bmatrix} 1 & 0 & 1 & 0 \\ 0 & 1 & 0 & 1 \\ 0 & 1 & 0 & -1 \\ -1 & 0 & 1 & 0 \end{bmatrix} \tag{5-13}$$

Eventually, the decomposition transformation matrix $\boldsymbol{T}_{\mathrm{VSD}}$ of dual three-phase PMSM can be obtained by multiplying the transformation matrix $\boldsymbol{T}_2$ with $\boldsymbol{T}_1$:

$$\boldsymbol{T}_{\mathrm{VSD}}=\frac{1}{\sqrt{3}}\begin{bmatrix}\cos(\theta+\delta_{\mathrm{eh}}) & \cos(\theta+\delta_{\mathrm{eh}}-\frac{2\pi}{3}) & \cos(\theta+\delta_{\mathrm{eh}}+\frac{2\pi}{3}) & \cos(\theta-\delta_{\mathrm{eh}}) & \cos(\theta-\delta_{\mathrm{eh}}-\frac{2\pi}{3}) & \cos(\theta-\delta_{\mathrm{eh}}+\frac{2\pi}{3})\\ -\sin(\theta+\delta_{\mathrm{eh}}) & -\sin(\theta+\delta_{\mathrm{eh}}-\frac{2\pi}{3}) & -\sin(\theta+\delta_{\mathrm{eh}}+\frac{2\pi}{3}) & -\sin(\theta-\delta_{\mathrm{eh}}) & -\sin(\theta-\delta_{\mathrm{eh}}-\frac{2\pi}{3}) & -\sin(\theta-\delta_{\mathrm{eh}}+\frac{2\pi}{3})\\ -\sin(\theta+\delta_{\mathrm{eh}}) & -\sin(\theta+\delta_{\mathrm{eh}}-\frac{2\pi}{3}) & -\sin(\theta+\delta_{\mathrm{eh}}+\frac{2\pi}{3}) & \sin(\theta-\delta_{\mathrm{eh}}) & \sin(\theta-\delta_{\mathrm{eh}}-\frac{2\pi}{3}) & \sin(\theta-\delta_{\mathrm{eh}}+\frac{2\pi}{3})\\ -\cos(\theta+\delta_{\mathrm{eh}}) & -\cos(\theta+\delta_{\mathrm{eh}}-\frac{2\pi}{3}) & -\cos(\theta+\delta_{\mathrm{eh}}+\frac{2\pi}{3}) & \cos(\theta-\delta_{\mathrm{eh}}) & \cos(\theta-\delta_{\mathrm{eh}}-\frac{2\pi}{3}) & \cos(\theta-\delta_{\mathrm{eh}}+\frac{2\pi}{3})\end{bmatrix} \tag{5-14}$$

Since the dual three-phase DS-HSDR-TFPMSM adopts dual isolated neutral points, thus the zero-axis component is not considered in the decomposition transformation matrix.

5.1.3 Mathematical model in decoupled frame

By VSD transformation, the state vector in the natural frame is transformed to the two decoupled frame that consists of two subframes *pd-pq* and *nd-nq*. In the decoupled frame, the state vectors of the dual three-phase PMSM can be expressed as follows:

$$\begin{aligned}\boldsymbol{\Psi}_{\mathrm{VSD}}&=[\Psi_{\mathrm{pd}}\quad \Psi_{\mathrm{pq}}\quad \Psi_{\mathrm{nd}}\quad \Psi_{\mathrm{nq}}]\\ \boldsymbol{I}_{\mathrm{VSD}}&=[I_{\mathrm{pd}}\quad I_{\mathrm{pq}}\quad I_{\mathrm{nd}}\quad I_{\mathrm{nq}}]\\ \boldsymbol{U}_{\mathrm{VSD}}&=[U_{\mathrm{pd}}\quad U_{\mathrm{pq}}\quad U_{\mathrm{nd}}\quad U_{\mathrm{nq}}]\end{aligned} \tag{5-15}$$

The equations of the flux linkage in the decoupled frame can be expressed as:

$$\boldsymbol{\Psi}_{\mathrm{VSD}}=\boldsymbol{L}_{\mathrm{VSD}}\boldsymbol{I}_{\mathrm{VSD}}+\Psi_{\mathrm{M}}\begin{bmatrix}\sqrt{3}\\0\\0\\0\end{bmatrix} \tag{5-16}$$

where Ψ_{M} is the amplitude of the PM flux linkage of one phase winding, and $\boldsymbol{L}_{\mathrm{VSD}}$ is the winding inductance matrix in diagonalized form after the transformation by $\boldsymbol{T}_{\mathrm{VSD}}$:

$$\boldsymbol{L}_{\mathrm{VSD}}=\begin{bmatrix}L_{\mathrm{pd}} & 0 & 0 & 0\\ 0 & L_{\mathrm{pq}} & 0 & 0\\ 0 & 0 & L_{\mathrm{nd}} & 0\\ 0 & 0 & 0 & L_{\mathrm{nq}}\end{bmatrix} \tag{5-17}$$

Substituting (5-14) and (5-16) into (5-6), the voltage equation of the dual three-phase PMSM in decoupled frame can be obtained as:

$$\boldsymbol{U}_{\mathrm{VSD}}=R_{\mathrm{s}}\boldsymbol{I}_{\mathrm{VSD}}+\omega\boldsymbol{L}_{\mathrm{VSD}}\boldsymbol{J}\boldsymbol{I}_{\mathrm{VSD}}+\boldsymbol{L}_{\mathrm{VSD}}\left(\frac{d}{dt}\boldsymbol{I}_{\mathrm{VSD}}\right)+\omega\boldsymbol{J}\Psi_{\mathrm{M}}\begin{bmatrix}\sqrt{3}\\0\\0\\0\end{bmatrix} \tag{5-18}$$

Where, ω denotes the rotational electrical angular velocity and $\boldsymbol{J}$ is the compensation matrix for rotating transformation.

$$\boldsymbol{J}=\begin{bmatrix}0 & -1 & 0 & 0\\ 1 & 0 & 0 & 0\\ 0 & 0 & 0 & -1\\ 0 & 0 & 1 & 0\end{bmatrix} \tag{5-19}$$

Substituting (5-16) into (5-8) and applying the VSD transformation matrix (5-14), the torque equation in decoupled frame is obtained as:

$$T_{\mathrm{em}}=p\left[\sqrt{3}\Psi_{\mathrm{M}}i_{\mathrm{pq}}+\left(L_{\mathrm{pd}}-L_{\mathrm{pq}}\right)i_{\mathrm{pd}}i_{\mathrm{pq}}\right] \tag{5-20}$$

For DS-HSDR-TFPMSM with a yokeless rotor structure, its control can be approximated as a non-salient pole PMSM, so its torque equation can be further simplified as

$$T_{\mathrm{em}}=\sqrt{3}p\Psi_{\mathrm{M}}i_{\mathrm{pq}} \tag{5-21}$$

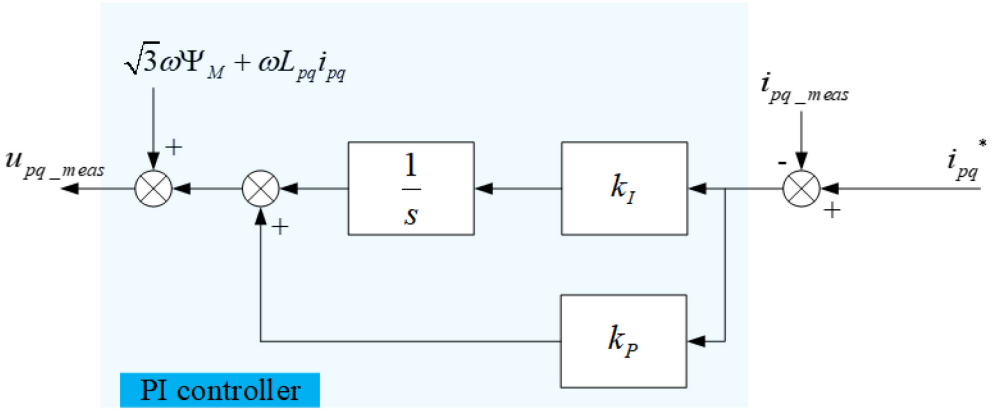

Fig. 5.4 Current PI controller with forward-set compensation

The electromagnetic torque of dual three-phase machine is linearly related to i_{pq} as shown in (5-21). Thus, the output torque can be controlled as a constant through the modulation of i_{pq}. In addition, it can be found that the voltage equations of each phase winding in the decoupled frame are decoupled from each other neglecting the rotational compensation, and the rotational compensation term can be eliminated by adding forward-set compensation to the current controller as shown in Fig. 5.4. An example of current controller for *pq*-axis is shown in Fig. 5.4, where the rotational compensation term is compensated.

In summary, the control complexity of the dual three-phase PMSM can be significantly reduced using the mathematical model under the decoupled frame. Therefore, the vector control model of the dual three-phase PMSM and the FTC model based on the decoupled frame are constructed in the subsequent research.

5.2 Vector control of dual three-phase PMSM

5.2.1 Vector control model

The vector control of the dual three-phase PMSM is realized based on the control of the current in the decoupled frame. According to (5-21), the electromagnetic torque of the dual three-phase DS-HSDR-TFPMSM is only related to the current component i_{pq}, and its vector control is similar to the $i_{\mathrm{d}}=0$ control of the conventional three-phase PMSM under the condition that field weakening is not considered, and i_{pd} is always equal to 0. For the current vector in the *nd-nq* frame, it is always equal to zero based on the assumptions that there is only fundamental

component in flux linkage. to suppress the stator copper loss of the dual three-phase PMSM. Therefore, the reference current in the decoupled frame is given as follows:

$$\begin{cases} i_{\mathrm{pd}} = 0 \\ i_{\mathrm{pq}} = \dfrac{T_{\mathrm{em}}^{\ *}}{\sqrt{3} p \Psi_{\mathrm{M}}} \\ i_{\mathrm{nd}} = 0 \\ i_{\mathrm{nq}} = 0 \end{cases} \tag{5-22}$$

where $T_{\mathrm{em}}^{\ *}$ is the reference value of electromagnetic torque.

The current vector of the dual three-phase PMSM is separated into two decoupled frames: *pd-pq* and *nd-nq* frame. As a result, its control model needs to be redesigned compared to the vector control of a conventional three-phase machine. The control model for dual three-phase PMSM based on Energetic Macroscopic Representation (EMR) is shown in Fig. 5.5, where two adjacent elements of the machine side are linked together by a pair of arrows in opposite directions to represent the action and feedback between the two adjacent elements.

In Fig. 5.5, the energy conversion in the machine side is described using orange elements while the control strategy corresponding to the energy conversion is described using blue elements. The energy conversion occurring in the machine side is described by the actual connection between the devices and the mathematical model of electric machine. In Fig. 5.5, $\boldsymbol{U}_{\mathrm{p}}$, $\boldsymbol{U}_{\mathrm{n}}$, $\boldsymbol{I}_{\mathrm{p}}$, $\boldsymbol{I}_{\mathrm{n}}$, $\boldsymbol{e}_{\mathrm{p}}$ and $\boldsymbol{e}_{\mathrm{n}}$ represent the voltage, current and back-EMF vectors in the decoupled frames *pd-pq* and *nd-nq*, respectively.

$$\begin{aligned} \boldsymbol{U}_{\mathrm{p}} &= \begin{bmatrix} U_{\mathrm{pd}} \\ U_{\mathrm{pq}} \end{bmatrix} \quad \boldsymbol{I}_{\mathrm{p}} = \begin{bmatrix} I_{\mathrm{pd}} \\ I_{\mathrm{pq}} \end{bmatrix} \quad \boldsymbol{e}_{\mathrm{p}} = \begin{bmatrix} e_{\mathrm{pd}} \\ e_{\mathrm{pq}} \end{bmatrix} \\ \boldsymbol{U}_{\mathrm{n}} &= \begin{bmatrix} U_{\mathrm{nd}} \\ U_{\mathrm{nq}} \end{bmatrix} \quad \boldsymbol{I}_{\mathrm{n}} = \begin{bmatrix} I_{\mathrm{nd}} \\ I_{\mathrm{nq}} \end{bmatrix} \quad \boldsymbol{e}_{\mathrm{n}} = \begin{bmatrix} e_{\mathrm{nd}} \\ e_{\mathrm{nq}} \end{bmatrix} \end{aligned} \tag{5-23}$$

T_{p} and T_{n} denote the electromagnetic torque generated within the decoupled frames *pd-pq* and *nd-nq*, respectively. In this research, T_{n} is always 0.

The section of PI controller in Fig. 5.5 can be further expanded as shown in Fig. 5.6 that consists of four separated PI current controllers, and the internal structure of each PI controller can be referred to Fig. 5.4.

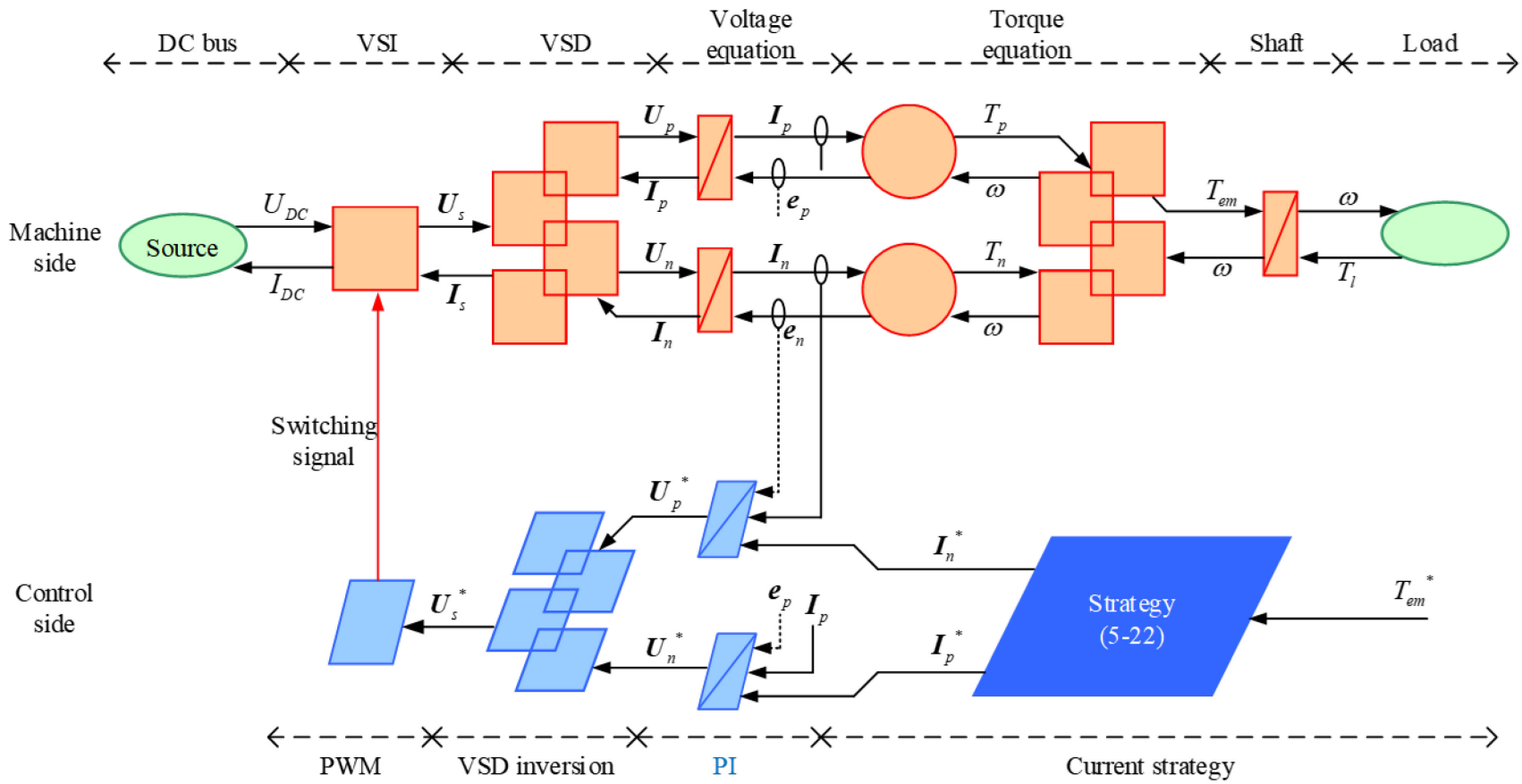

Fig. 5.5 Vector control model of dual three-phase PMSM represented by EMR

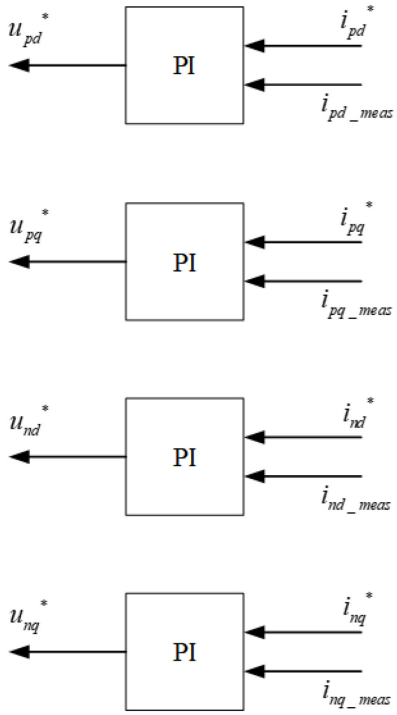

Fig. 5.6 Current controller part of the control model for dual three-phase PM machine

5.2.2 Control parameters of dual three-phase DS-HSDR-TFPMSM

The dual three-phase DS-HSDR-TFPMSM consists of two structures, which are described in Chapter 2. Due to the structural symmetry and different coil configurations of the two machines, there are differences in the control parameters of the machines. Therefore, the performance parameters, such as rated torque, rated current, and no load back-EMF, of the two structures of dual three-phase DS-HSDR-TFPMSM are compared in Chapter 2.

However, in addition to the aforementioned parameters, the winding resistance and inductance parameters are also required based on the voltage equation (5-18). Furthermore, as per the torque equation (5-21), it needs to determine the amplitude of the fundamental component in winding flux linkage. The waveform of the winding flux linkage of the dual three-phase DS-HSDR-TFPMSMs under no load conditions is shown in Fig. 5.7. For the dual three-phase DS-HSDR-TFPMSM with symmetrical structure, the amplitude of the fundamental component in flux linkage is 0.0738 Wb, whereas it is 0.0711 Wb for dual three-phase DS-HSDR-TFPMSM with asymmetrical structure.

The inductance parameters under rated load condition are calculated by the frozen permeabilities method. Firstly, the winding inductance matrix $\boldsymbol{L}_s$ in the natural frame is calculated; then, the diagonalization of $\boldsymbol{L}_s$ is achieved by the VSD transformation matrix:

$$\boldsymbol{L}_{VSD} = \boldsymbol{T}_{VSD}\boldsymbol{L}_s\boldsymbol{T}_{VSD}^{-1} \quad ;(5\text{-}24)$$

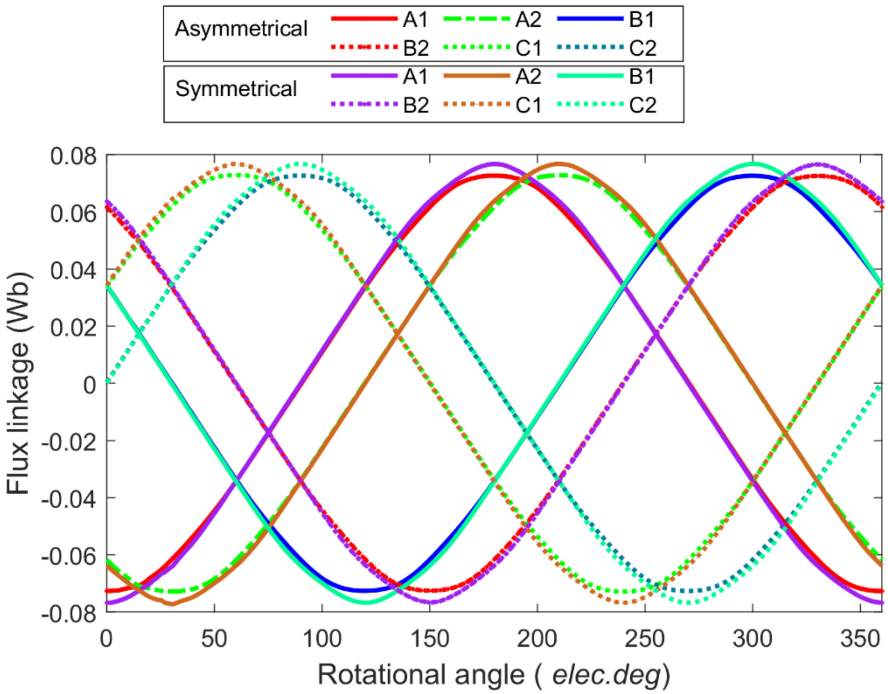

Fig. 5.7 Flux linkage waveforms of dual three-phase DS-HSDR-TFPMSM

Finally, the winding inductance matrix of the dual three-phase DS-HSDR-TFPMSM in the decoupled frame is obtained:

$$\boldsymbol{L}_{\mathrm{VSD\_}sym}=\begin{bmatrix}5.1 & & & \\ & 5.1 & & \\ & & 3.0 & \\ & & & 3.0\end{bmatrix}\mathrm{mH} \tag{5-25}$$

$$\boldsymbol{L}_{\mathrm{VSD\_}asym}=\begin{bmatrix}4.8 & 0 & -0.18 & 0 \\ 0 & 4.8 & 0 & -0.18 \\ -0.18 & 0 & 3.8 & 0 \\ 0 & -0.18 & 0 & 3.8\end{bmatrix}\mathrm{mH} \tag{5-26}$$

The control parameters of the dual three-phase DS-HSDR-TFPMSMs are summarized in Table 5.1.

Table 5.1 Control parameters of dual three-phase DS-HSDR-TFPMSM

	Symmetrical structure	Asymmetric structure
DC bus voltage U_{DC}	350V	
Amplitude of fundamental flux linkage Ψ_{M}	0.0738Wb	0.0711Wb
Winding resistance	0.2 Ω	
pd-axis inductance L_{pd}	5.1	4.8
pq-axis inductance L_{pq}	5.1	4.8
nd-axis inductance L_{nd}	3.0	3.8
nq-axis inductance L_{nq}	3.0	3.8

5.3 One-phase open-circuit FTC method of dual three-phase PMSM

The most commonly occurring fault type in dual three-phase PMSM is one-phase open-circuit fault. Under one-phase open-circuit fault condition, there are changes in the constraints of the machine due to the absence of one-phase winding, leading to the current strategy (5-22) designed for normal condition inapplicable. Therefore, it is crucial to establish an FTC model for the one-phase open-circuit fault condition of dual three-phase PMSM and reconfigure the current strategy.

An FTC method, as shown in Fig. 5.8, can be used for a dual three-phase PMSM with double isolated neutral points to disconnect the entire three-phase winding where the fault is located. However, this method suffers the drawback that the input power of the machine will be concentrated in the other set of three-phase winding without fault, resulting in a considerable increase in copper loss. Therefore, it is essential to investigate an FTC method in which the remaining phase in the fault three-phase winding set still contribute the torque output.

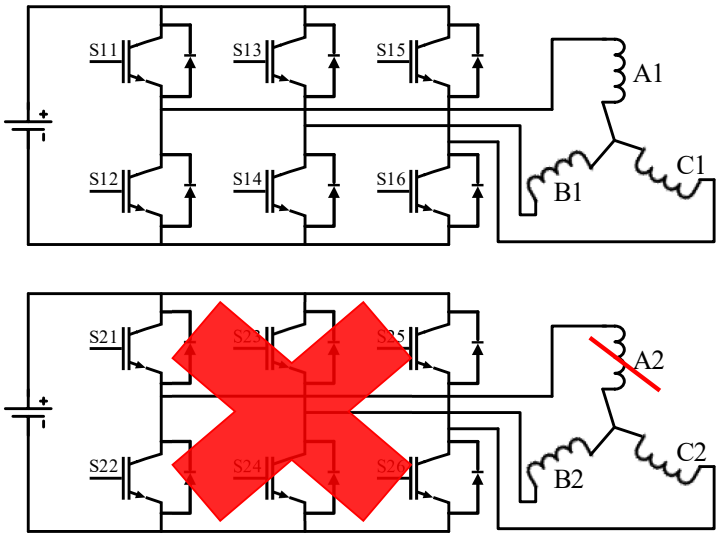

Fig. 5.8 Schematic diagram of FTC method using three-phase winding set cut-off

5.3.1 One-phase open-circuit FTC method based on normal decoupled transformation

As an example, it is assumed that the open-circuit fault occurs in phase A2. Under given fault condition, the current constraint in the normal three-phase winding (A1-B1-C1) remains unchanged, while the current constraint in the three-phase winding (A2-B2-C2), where the fault phase is located, is broken[157]. Utilizing the VSD inversion matrix TVSD-1, Based on the VSD inversion matrix $\boldsymbol{T}_{\mathrm{VSD}}^{-1}$, the current relationship within the normal three-phase winding can be obtained as:

$$\begin{bmatrix} i_{\mathrm{A1}} \\ i_{\mathrm{B1}} \\ i_{\mathrm{C1}} \end{bmatrix} = \begin{bmatrix} \cos(\theta+\delta_{\mathrm{eh}}) & -\sin(\theta+\delta_{\mathrm{eh}}) & -\sin(\theta+\delta_{\mathrm{eh}}) & -\cos(\theta+\delta_{\mathrm{eh}}) \\ \cos(\theta+\delta_{\mathrm{eh}}-\frac{2\pi}{3}) & -\sin(\theta+\delta_{\mathrm{eh}}-\frac{2\pi}{3}) & -\sin(\theta+\delta_{\mathrm{eh}}-\frac{2\pi}{3}) & -\cos(\theta+\delta_{\mathrm{eh}}-\frac{2\pi}{3}) \\ \cos(\theta+\delta_{\mathrm{eh}}+\frac{2\pi}{3}) & -\sin(\theta+\delta_{\mathrm{eh}}+\frac{2\pi}{3}) & -\sin(\theta+\delta_{\mathrm{eh}}+\frac{2\pi}{3}) & -\cos(\theta+\delta_{\mathrm{eh}}+\frac{2\pi}{3}) \end{bmatrix} \begin{bmatrix} i_{\mathrm{pd}} \\ i_{\mathrm{pq}} \\ i_{\mathrm{nd}} \\ i_{\mathrm{pq}} \end{bmatrix} \tag{5-27}$$

However, in the three-phase winding where the fault phase is located, the currents of the remaining phases are with the same amplitude but opposite phasor. Therefore, the winding currents of the dual three-phase PMSM under phase A2 open-circuit condition based on the above analysis can be mathematically expressed as:

$$\begin{cases} i_{\mathrm{A1,f}} = \dfrac{1}{\sqrt{3}}\left[i_{\mathrm{pd}} \cos(\theta+\delta_{\mathrm{eh}}) - i_{\mathrm{pq}} \sin(\theta+\delta_{\mathrm{eh}}) - i_{\mathrm{nd}} \sin(\theta+\delta_{\mathrm{eh}}) - i_{\mathrm{nq}} \cos(\theta+\delta_{\mathrm{eh}}) \right] \\ i_{\mathrm{B1,f}} = \dfrac{1}{\sqrt{3}}\left[i_{\mathrm{pd}} \cos(\theta+\delta_{\mathrm{eh}} - \dfrac{2\pi}{3}) - i_{\mathrm{pq}} \sin(\theta+\delta_{\mathrm{eh}} - \dfrac{2\pi}{3}) - i_{\mathrm{nd}} \sin(\theta+\delta_{\mathrm{eh}} - \dfrac{2\pi}{3}) - i_{\mathrm{nq}} \cos(\theta+\delta_{\mathrm{eh}} - \dfrac{2\pi}{3}) \right] \\ i_{\mathrm{C1,f}} = \dfrac{1}{\sqrt{3}}\left[i_{\mathrm{pd}} \cos(\theta+\delta_{\mathrm{eh}} + \dfrac{2\pi}{3}) - i_{\mathrm{pq}} \sin(\theta+\delta_{\mathrm{eh}} + \dfrac{2\pi}{3}) - i_{\mathrm{nd}} \sin(\theta+\delta_{\mathrm{eh}} + \dfrac{2\pi}{3}) - i_{\mathrm{nq}} \cos(\theta+\delta_{\mathrm{eh}} + \dfrac{2\pi}{3}) \right] \\ i_{\mathrm{A2,f}} = 0 \\ i_{\mathrm{C2,f}} = -i_{\mathrm{B2,f}} \end{cases} \tag{5-28}$$

where i_{pd}, i_{pq}, i_{nd} and i_{nq} are no longer winding currents in the decoupled frame, but coefficients or functional equations used to determine the current relationships.

The winding currents in the decoupled frame under fault condition can be further obtained by multiply (5-28) by (5-14):

$$\begin{bmatrix} i_{\mathrm{pd,f}} \\ i_{\mathrm{pq,f}} \\ i_{\mathrm{nd,f}} \\ i_{\mathrm{nq,f}} \end{bmatrix} = \begin{bmatrix} \dfrac{i_{\mathrm{pd}} - i_{\mathrm{nq}}}{2} + i_{\mathrm{B2,f}} \sin(\theta - \delta_{\mathrm{eh}}) \\ \dfrac{i_{\mathrm{nd}} + i_{\mathrm{pq}}}{2} + i_{\mathrm{B2,f}} \cos(\theta - \delta_{\mathrm{eh}}) \\ \dfrac{i_{\mathrm{nd}} + i_{\mathrm{pq}}}{2} - i_{\mathrm{B2,f}} \cos(\theta - \delta_{\mathrm{eh}}) \\ \dfrac{i_{\mathrm{nq}} - i_{\mathrm{pd}}}{2} + i_{\mathrm{B2,f}} \sin(\theta - \delta_{\mathrm{eh}}) \end{bmatrix} \tag{5-29}$$

Based on the torque equation (5-21) in the decoupled frame, the torque equation under phase A2 open-circuit condition can be obtained as

$$T_{\mathrm{em}} = \sqrt{3} p \Psi_{\mathrm{M}} i_{\mathrm{pq,f}} = \sqrt{3} p \Psi_{\mathrm{M}} \left(\frac{i_{\mathrm{nd}} + i_{\mathrm{pq}}}{2} + i_{\mathrm{B2,f}} \cos(\theta - \delta_{\mathrm{eh}}) \right) \tag{5-30}$$

where $i_{\mathrm{B2,f}}$ needs to be expressed in sinusoidal form without harmonic components in order to reduce copper loss[159].

$$i_{\mathrm{B2,f}} = I_{\mathrm{B2,M}} \cos(\theta - \phi_{\mathrm{B2}}) \tag{5-31}$$

In (5-31), $I_{\mathrm{B2,M}}$ and ϕ_{B2} are the amplitude and the initial phasor of the current in phase B2 under fault condition.

Substituting (5-31) into (5-30), the torque equation under phase A2 open-circuit fault condition is obtained as:

$$T_{\mathrm{em}} = \sqrt{3} p \Psi_{\mathrm{M}} \left(\frac{i_{\mathrm{nd}} + i_{\mathrm{pq}}}{2} + I_{\mathrm{B2,M}} \cos(\theta - \phi_{\mathrm{B2}}) \cos(\theta - \delta_{\mathrm{eh}}) \right) \tag{5-32}$$

The torque expressed in (5-32) can be further decomposed into three components shown in (5-33). It can be seen that the torque components $T_{\mathrm{e0,1}}$ and $T_{\mathrm{e0,2}}$ are mainly used to generate the average torque, while the torque component T_{e2} is the most important source of torque ripple under fault condition.

$$
\begin{aligned}
T_{\mathrm{em}} &= T_{\mathrm{e0,1}} + T_{\mathrm{e0,2}} + T_{\mathrm{e2}} \\
T_{\mathrm{e0,1}} &= \frac{\sqrt{3}}{2} p\Psi_{\mathrm{M}} (i_{\mathrm{nd}} + i_{\mathrm{pq}}) \\
T_{\mathrm{e0,2}} &= \frac{\sqrt{3}}{2} p\Psi_{\mathrm{M}} I_{\mathrm{B2,M}} \cos(\phi_{\mathrm{B2}} - \delta_{\mathrm{eh}}) \\
T_{\mathrm{e2}} &= \frac{\sqrt{3}}{2} p\Psi_{\mathrm{M}} I_{\mathrm{B2,M}} \cos(2\theta - \phi_{\mathrm{B2}} - \delta_{\mathrm{eh}})
\end{aligned}
\tag{5-33}
$$

In addition, it can be concluded through (5-33) that the parameters i_{pd} and i_{nq} in (5-29) devote no contribution to the average torque value. Moreover, it can be found the parameters i_{nd} and i_{pq} can influence the torque component $T_{\mathrm{e0,1}}$, but the relationship between i_{nd} and i_{pq} has no influences on the torque and stator current. In summary, (5-29) can be further simplified by keeping only the parameter i_{pq} and eliminating the parameters i_{pd}, i_{nd} and i_{nq}.

In order to eliminate the torque ripple under fault condition, the second harmonic component in T_{e2} needs to be compensated. Therefore, the second harmonic component is added to the parameter i_{pq} of $T_{\mathrm{e0,1}}$ as follows:

$$
i_{\mathrm{pq}} = I_{\mathrm{pq,0}} + I_{\mathrm{pq,2}} \cos(2\theta - \phi_{\mathrm{q}}) \tag{5-34}
$$

Where, $I_{\mathrm{pq,0}}$ is the DC component, $I_{\mathrm{pq,2}}$ is the amplitude of the second harmonic component, and ϕ_{q} is the initial phasor of the second harmonic component.

When the torque ripple components in $T_{\mathrm{e0,1}}$ and T_{e2} in (5-33) can be compensated by each other as the condition in (5-35) is satisfied, the smooth torque will be output under fault condition.

$$
I_{\mathrm{pq,2}} \cos(2\theta - \phi_{\mathrm{q}}) + I_{\mathrm{B2,M}} \cos(2\theta - \phi_{\mathrm{B2}} - \delta_{\mathrm{eh}}) = 0 \tag{5-35}
$$

In addition, in order to maximize the average value of the output torque provided by the torque component $T_{\mathrm{e0,2}}$, the value of ϕ_{B2} should be taken equal to δ_{eh}. In summary, the values of the parameters to be determined in (5-29) can be obtained as follow:

$$
\begin{cases}
i_{\mathrm{pd}} = i_{\mathrm{nd}} = i_{\mathrm{nq}} = 0 \\
I_{\mathrm{pq,2}} = I_{\mathrm{B2,M}} \\
\phi_{\mathrm{B2}} = \delta_{\mathrm{eh}} = \dfrac{\pi}{12} \\
\phi_{\mathrm{q}} = \phi_{\mathrm{B2}} + \delta_{\mathrm{eh}} - \pi = -\dfrac{5\pi}{6}
\end{cases}
\tag{5-36}
$$

Substituting (5-31), (5-34), and (5-36) into (5-29), the winding currents in the decoupled frame of the dual three-phase PMSM under phase A2 open-circuit condition are obtained as:

$$\begin{cases} i_{\mathrm{pd,f}} = \dfrac{I_{\mathrm{pq,2}}}{2}\sin(2\theta - \dfrac{\pi}{6}) \\ i_{\mathrm{pq,f}} = \dfrac{I_{\mathrm{pq,0}} + I_{\mathrm{pq,2}}}{2} \\ i_{\mathrm{nd,f}} = \dfrac{I_{\mathrm{pq,0}} - I_{\mathrm{pq,2}}}{2} + I_{\mathrm{pq,2}}\cos(2\theta + \dfrac{5\pi}{6}) \\ i_{\mathrm{nq,f}} = \dfrac{I_{\mathrm{pq,2}}}{2}\sin(2\theta - \dfrac{\pi}{6}) \end{cases} \tag{5-37}$$

In addition, the winding currents in the decoupled frame of a dual three-phase PMSM can be derived in the same way while the fault occurs in other phase windings. And it is summarized here by Table 5.2.

However, the parameters $I_{\mathrm{pq},0}$ and $I_{\mathrm{pq},2}$ are still undetermined in (5-37), and the further discussion is required depending on the different optimization objectives for FTC.

Table 5.2 Winding current in the decoupled frames under open-circuit fault condition leaded by arbitrary phase

	Fault in A1-B1-C1 winding			Fault in A2-B2-C2		
	A1 open circuit	B1 open circuit	C1 open circuit	A2 open circuit	B2 open circuit	C2 open circuit
$i_{\mathrm{pd,f}}$	$\frac{I_{\mathrm{pq,2}}}{2}\sin\left(2\theta+\frac{\pi}{6}\right)$	$\frac{I_{\mathrm{pq,2}}}{2}\sin\left(2\theta+\frac{5\pi}{6}\right)$	$-\frac{I_{\mathrm{pq,2}}}{2}\cos(2\theta)$	$\frac{I_{\mathrm{pq,2}}}{2}\sin\left(2\theta-\frac{\pi}{6}\right)$	$\frac{I_{\mathrm{pq,2}}}{2}\cos(2\theta)$	$-\frac{I_{\mathrm{pq,2}}}{2}\sin\left(2\theta+\frac{\pi}{6}\right)$
$i_{\mathrm{pq,f}}$	$\frac{I_{pq,0}+I_{pq,2}}{2}$					
$i_{\mathrm{nd,f}}$	$\frac{I_{\mathrm{pq,2}}-I_{\mathrm{pq,0}}}{2}$ $-I_{\mathrm{pq,2}}\cos\left(2\theta-\frac{5\pi}{6}\right)$	$\frac{I_{\mathrm{pq,2}}-I_{\mathrm{pq,0}}}{2}$ $-I_{\mathrm{pq,2}}\cos\left(2\theta-\frac{\pi}{6}\right)$	$\frac{I_{\mathrm{pq,2}}-I_{\mathrm{pq,0}}}{2}$ $+I_{\mathrm{pq,2}}\sin(2\theta)$	$\frac{I_{\mathrm{pq,0}}-I_{\mathrm{pq,2}}}{2}$ $+I_{\mathrm{pq,2}}\cos\left(2\theta+\frac{5\pi}{6}\right)$	$\frac{I_{\mathrm{pq,0}}-I_{\mathrm{pq,2}}}{2}$ $+I_{\mathrm{pq,2}}\sin(2\theta)$	$\frac{I_{\mathrm{pq,0}}-I_{\mathrm{pq,2}}}{2}$ $+I_{\mathrm{pq,2}}\cos\left(2\theta+\frac{\pi}{6}\right)$
$i_{\mathrm{nq,f}}$	$-\frac{I_{\mathrm{pq,2}}}{2}\sin\left(2\theta+\frac{\pi}{6}\right)$	$-\frac{I_{\mathrm{pq,2}}}{2}\sin\left(2\theta+\frac{5\pi}{6}\right)$	$\frac{I_{\mathrm{pq,2}}}{2}\cos(2\theta)$	$\frac{I_{\mathrm{pq,2}}}{2}\sin\left(2\theta-\frac{\pi}{6}\right)$	$\frac{I_{\mathrm{pq,2}}}{2}\cos(2\theta)$	$-\frac{I_{\mathrm{pq,2}}}{2}\sin\left(2\theta+\frac{\pi}{6}\right)$

5.3.1.1 The principle of minimum copper loss

Firstly, the parameters $I_{\mathrm{pq},0}$ and $I_{\mathrm{pq},2}$ are determined based on the principle of minimum copper loss (MCL) in which the minimization of the copper loss in stator winding is set as the optimization objective of FTC.

The copper loss under fault condition using the FTC method based on normal decoupled transformation is calculated by:

$$p_{\mathrm{Cu}} = R_{\mathrm{s}}[i_{\mathrm{pd,f}}^2 + i_{\mathrm{pq,f}}^2 + i_{\mathrm{nd,f}}^2 + i_{\mathrm{nq,f}}^2] \tag{5-38}$$

Substituting (5-37) into (5-38), the calculation equation of copper loss can be expanded as:

$$p_{\mathrm{Cu}} = R_{\mathrm{s}}\left\{\frac{1}{2}I_{\mathrm{pq,0}}^2 + \frac{1}{2}I_{\mathrm{pq,2}}^2\cos^2(2\theta+\frac{5}{6}\pi) + I_{\mathrm{pq,0}}\cdot I_{\mathrm{pq,2}}\cos(2\theta+\frac{5}{6}\pi) + 2I_{\mathrm{pq,2}}^2\cos^2(\theta-\frac{1}{12}\pi)\right\} \tag{5-39}$$

The relationship between the parameters $I_{\mathrm{pq},0}$ and $I_{\mathrm{pq},2}$ is described by a linear function as:

$$I_{\mathrm{pq},2} = k_1 I_{\mathrm{pq},0} \quad ,(5\text{-}40)$$

Then by substituting (5-36) and (5-40) into (5-33), the torque equation can be obtained as:

$$T_{\mathrm{ec}} = \frac{\sqrt{3}}{2} p \Psi_{\mathrm{M}} I_{\mathrm{pq},0} (1 + k_1) \quad .(5\text{-}41)$$

Substituting (5-40) as well as (5-41) into (5-39), the calculation results of copper loss related to the torque can be obtained as:

$$p_{\mathrm{Cu}} = \frac{T_{\mathrm{ec}}^2 \cdot R_{\mathrm{s}}}{(\frac{\sqrt{3}}{2})^2 p^2 \Psi_{\mathrm{PM}}^2} \left\{ \left[\frac{1}{2} + \frac{1}{2} k_1^2 \cos^2(2\theta + \frac{5}{6}\pi) + k_1 \cos(2\theta + \frac{5}{6}\pi) + 2k_1^2 \cos^2(\theta - \frac{1}{12}\pi) \right] / (1 + k_1)^2 \right\} \quad (5\text{-}42)$$

Normalizing (5-42), the following calculation equation is obtained:

$$p_{\mathrm{Cu}}^* = \frac{p_{\mathrm{Cu}}}{C_{\mathrm{p}}} = \left[\frac{1}{2} + \frac{1}{2} k_1^2 \cos^2(2\theta + \frac{5}{6}\pi) + k_1 \cos(2\theta + \frac{5}{6}\pi) + 2k_1^2 \cos^2(\theta - \frac{1}{12}\pi) \right] / (1 + k_1)^2 \quad .(5\text{-}43)$$

where $C_{\mathrm{p}} = \frac{T_{\mathrm{ec}}^2 \cdot R_{\mathrm{s}}}{(\frac{\sqrt{3}}{2})^2 p^2 \Psi_{\mathrm{PM}}^2}$.

Ultimately, the solution of the winding current parameters under the principle of MCL is transformed into minimizing the average value of p_{Cu}^* over an electrical cycle:

$$\min\left\{ \overline{p}_{\mathrm{Cu}}^* \right\} = \min\left\{ \frac{\frac{5}{4} k_1^2 + \frac{1}{2}}{(1 + k_1)^2} \right\} \quad (5\text{-}44)$$

The optimal solution of (5-44) is $k_1 = 0.4$, which is substituted into (5-40) to obtain the relationship between the parameters $I_{\mathrm{pq},0}$ and $I_{\mathrm{pq},2}$. Substituting (5-40) as well as (5-41) into (5-37), the function between the winding reference current and torque in the decoupled frame is further obtained. Furthermore, the winding current in the natural frame in (5-28) can be expressed as:

$$\begin{cases} i_{\mathrm{A1,f}} = -\frac{I_{\mathrm{pq},0}}{\sqrt{3}} \sin(\theta + \frac{\pi}{12})[1 + 0.4\cos(2\theta + \frac{5\pi}{6})] \\ i_{\mathrm{B1,f}} = -\frac{I_{\mathrm{pq},0}}{\sqrt{3}} \sin(\theta - \frac{7\pi}{12})[1 + 0.4\cos(2\theta + \frac{5\pi}{6})] \\ i_{\mathrm{C1,f}} = -\frac{I_{\mathrm{pq},0}}{\sqrt{3}} \sin(\theta + \frac{3\pi}{4})[1 + 0.4\cos(2\theta + \frac{5\pi}{6})] \\ i_{\mathrm{B2,f}} = 0.4 I_{\mathrm{pq},0} \cos(\theta - \frac{\pi}{12}) \\ i_{\mathrm{C2,f}} = -0.4 I_{\mathrm{pq},0} \cos(\theta - \frac{\pi}{12}) \end{cases} \quad (5\text{-}45)$$

In (5-45), the amplitude of the current in each phase is:

$$\begin{cases} i_{\mathrm{A1,f\_M}} = \dfrac{1.3}{\sqrt{3}} I_{\mathrm{pq,0}} \\ i_{\mathrm{B1,f\_M}} = \dfrac{0.7}{\sqrt{3}} I_{\mathrm{pq,0}} \\ i_{\mathrm{C1,f\_M}} = \dfrac{1.3}{\sqrt{3}} I_{\mathrm{pq,0}} \\ i_{\mathrm{C1,f\_M}} = \dfrac{1.3}{\sqrt{3}} I_{\mathrm{pq,0}} \\ i_{\mathrm{B2,f\_M}} = 0.4 I_{\mathrm{pq,0}} \\ i_{\mathrm{C2,f\_M}} = 0.4 I_{\mathrm{pq,0}} \end{cases} \quad ,(5\text{-}46)$$

It has been observed that the winding current is distorted, and its amplitude significantly increases under open-circuit fault condition in comparison to working under normal condition. Hence, it is imperative to incorporate the constraint for the amplitude of phase current with FTC method, ensuring the protection of not only the winding of electric machine but also the switching devices of the electric drive.

According to (5-41) and (5-46), it can be determined that the torque should satisfy the following equation under the condition of phase current constraint on amplitude I_{m}:

$$T_{\mathrm{ec}} \le \frac{3 p \Psi_{\mathrm{M}} \left(1 + k_1\right) I_{\mathrm{m}}}{2.6} \quad (5\text{-}47)$$

The phase current constraint on amplitude I_{m} of the dual three-phase DS-HSDR-TFPMSM is set to $10\sqrt{2}$ A. Under this condition, the maximum output torque is 8.42Nm for the dual three-phase DS-HSDR-TFPMSM with symmetrical structure and 8.10Nm for the dual three-phase DS-HSDR-TFPMSM with asymmetrical structure.

5.3.1.2 Principle of maximum torque operation range

The principle of maximum torque operation range (MTOR) can be expressed as follows: calculate and minimize the maximum value in the current amplitude of each phase under the condition that the output torque has been determined.

Firstly, the parameters $I_{\mathrm{pq,0}}$ and $I_{\mathrm{pq,2}}$ are related by a linear function:

$$I_{\mathrm{pq,2}} = k_2 I_{\mathrm{pq,0}} \quad ,(5\text{-}48)$$

Referring to (5-41), $I_{\mathrm{pq,0}}$ can be expressed as:

$$I_{\mathrm{pq,0}} = \frac{T_{\mathrm{ec}}}{\frac{\sqrt{3}}{2}(1 + k_2) p \Psi_{\mathrm{M}}} \quad ,(5\text{-}49)$$

Then, by substituting (5-48) and (5-49) into (5-28), the phase currents under fault condition are obtained as:

$$\begin{cases} i_{\mathrm{A1,f}} = -\dfrac{2}{3}\dfrac{T_{\mathrm{ec}}}{p\Psi_{\mathrm{M}}}\left\{\dfrac{\sin(\theta+\dfrac{\pi}{12})}{1+k_2}\left[1+k_2\cos(2\theta+\dfrac{5\pi}{6})\right]\right\} \\ i_{\mathrm{B1,f}} = -\dfrac{2}{3}\dfrac{T_{\mathrm{ec}}}{p\Psi_{\mathrm{M}}}\left\{\dfrac{\sin(\theta-\dfrac{7\pi}{12})}{1+k_2}\left[1+k_2\cos(2\theta+\dfrac{5\pi}{6})\right]\right\} \\ i_{\mathrm{C1,f}} = -\dfrac{2}{3}\dfrac{T_{\mathrm{ec}}}{p\Psi_{\mathrm{M}}}\left\{\dfrac{\sin(\theta+\dfrac{3\pi}{4})}{1+k_2}\left[1+k_2\cos(2\theta+\dfrac{5\pi}{6})\right]\right\} \\ i_{\mathrm{B2,f}} = \dfrac{2}{\sqrt{3}}\dfrac{T_{\mathrm{ec}}}{p\Psi_{\mathrm{M}}}\dfrac{k_2}{1+k_2}\cos(\theta-\dfrac{\pi}{12}) \\ i_{\mathrm{C2,f}} = -\dfrac{2}{\sqrt{3}}\dfrac{T_{\mathrm{ec}}}{p\Psi_{\mathrm{M}}}\dfrac{k_2}{1+k_2}\cos(\theta-\dfrac{\pi}{12}) \end{cases} \tag{5-50}$$

The problem of solving the current parameter under the principle of MTOR is ultimately transformed into minimizing the parameter K in (5-51). And relationship between K and k_2 is shown in Fig. 5.9.

$$\begin{aligned} &\min\{K\} \\ &K = \max\left\{I_{\mathrm{m\_}i} / \left(\frac{T_{\mathrm{ec}}}{p\Psi_{\mathrm{M}}}\right)\right\} \end{aligned} \tag{5-51}$$

where $I_{\mathrm{m\_}i}$ represents the amplitude of phase current in (5-50) in which.

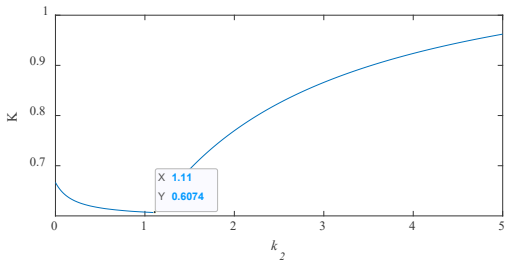

Fig. 5.9 The functional relationship curve between factor K and k_2

Through analysis of Fig. 5.9, it can be concluded that the minimum value of the variable K is obtained when k_2 is equal to 1.1 and the amplitude of the current in each phase at this point is as follow:

$$\begin{cases} i_{\mathrm{A1,f\_M}} = 0.6066\dfrac{T_{\mathrm{ec}}}{p\Psi_{\mathrm{M}}} \\ i_{\mathrm{B1,f\_M}} = 0.2506\dfrac{T_{\mathrm{ec}}}{p\Psi_{\mathrm{M}}} \\ i_{\mathrm{C1,f\_M}} = 0.6066\dfrac{T_{\mathrm{ec}}}{p\Psi_{\mathrm{M}}} \\ i_{\mathrm{B2,f\_M}} = 0.6048\dfrac{T_{\mathrm{ec}}}{p\Psi_{\mathrm{M}}} \\ i_{\mathrm{C2,f\_M}} = 0.6048\dfrac{T_{\mathrm{ec}}}{p\Psi_{\mathrm{M}}} \end{cases} \tag{5-52}$$

Subject to the phase current constraint on amplitude, the maximum value of the output torque is 8.61 Nm for the DS-HSDR-TFPMSM with symmetrical structure and 8.29 Nm for the DS-HSDR-TFPMSM with asymmetrical structure.

5.3.1.3 Performance comparison of FTC methods

FTC methods based on the principle of MCL and MTOR are compared. In addition, the FTC method with disconnection of entire three-phase winding (DETW) shown in Fig. 5.8 is selected as a reference. Under one-phase open-circuit fault condition, a dual three-phase PMSM can be directly simplified to a conventional symmetrical three-phase winding structure PMSM through the implementation of FTC method with DETW. Thus, the output torque and the amplitude of phase current are related as a function of

$$T_{\mathrm{em}} = \frac{3}{2} p \Psi_{\mathrm{M}} I_{\mathrm{M}} \tag{5-53}$$

Where, I_{M} is the amplitude of phase current. And then the maximum output torque of this method can be calculated based on the given phase current constraint on amplitude.

Furthermore, there is no current input in the three-phase winding where the fault phase is located when k1 in (5-40) is set to 0, thus it is equivalent to DETW FTC method. The winding copper loss for the DETW FTC method can be obtained by substituting k1 = 0 into (5-42), while the corresponding loss for the FTC method based on the principle of MTOR can be determined by substituting the coefficient k2 = 1.1 into equation (5-42). The per-unit values of maximum output torque and copper loss on the basis of the calculation results by using DETW FTC method are compared in Tab. 5.

It can be concluded that performance of the DETW FTC method is the worst among the given methods. The limited improvement of the maximum torque under phase current constraints is achieved based on the principles of MCL and MTOR. Besides, the copper loss using the FTC method based on the principle of MCL is reduced by 28.6% compared to the DETW method, thus significantly reducing the power loss during fault tolerant operation of the dual three-phase PMSM.

Table 5.3 Comparison of the performances using different FTC methods

	DETW	MCL	MTOR
Maximum output torque	1	1.077	1.1
Winding copper loss	1	0.714	0.912

5.3.2 Fault tolerant vector control model

The winding currents in the decoupled frame need to be reconfigured according to (5-37) for the FTC method based on normal decoupled transformation proposed in the thesis. Since there is no change in mathematical model of the machine due to the use of normal decoupled transformation, the vector control model shown in Fig. 5.5 can be used as the fault tolerant vector control model continuously, and only the current strategy needs to be reconfigured in the control model according to (5-37). In addition, the current PI controller part is still used as shown in Fig. 5.6, and the PI parameters remain unchanged.

5.3.3 Simulation analysis of one-phase open-circuit FTC method

To validate the effectiveness of the one-phase open-circuit FTC method based on the normal decoupled transformation, a fault tolerant vector control simulation model of the dual three-phase DS-HSDR-TFPMSM is built using MATLAB Simulink in this chapter. The two

FTC methods based on the principle of MCL and the principle of MTOR are validated in the simulation model of dual three-phase DS-HSDR-TFPMSM.

Firstly, the simulation model of dual three-phase DS-HSDR-TFPMSM with asymmetrical structure is used to simulate the dynamic process from normal condition to phase A2 open-circuit fault condition.

The operation speed is set to 120r/min and the torque reference value is set to 8Nm. The machine starts normally, and the open-circuit fault occurs in phase A2 at t=0.3s when the normal current strategy is still used. The torque waveform of the whole dynamic process is shown in Fig. 5.10. It can be found that the output torque of electric machine under normal condition is smooth of which the torque ripple is 0.43%. The average output torque of the machine is still maintained at the reference value of 8Nm under fault condition A2, but the torque ripple increases to 104.65%, causing that electric machine no longer works normally.

In order to reduce the torque ripple under one-phase open-circuit condition shown in Fig. 5.10, the two structures DS-HSDR-TFPMSM are simulated using the FTC method based on the principle of MCL and the principle of MTOR.

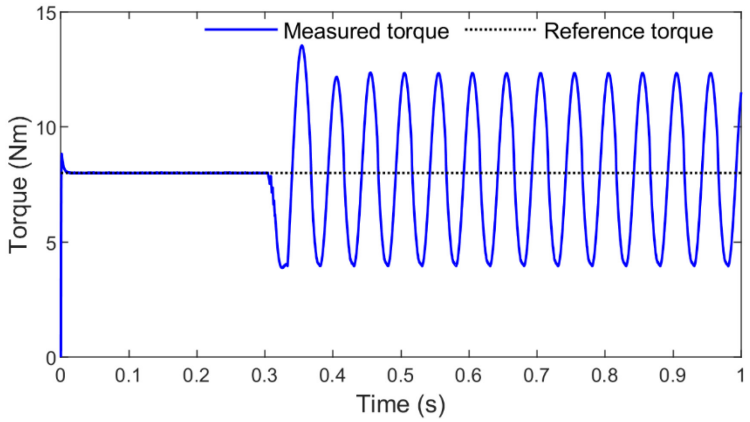

Fig. 5.10 Torque waveform during fault-adding dynamic procedure using different FTC method

Simulation results obtained using the FTC method based on the principle of MCL for dual three-phase DS-HSDR-TFPMSMs under phase A2 open-circuit fault condition are shown in Fig. 5.11. The speed is set to 120 r/min and phase current constraint on amplitude is set to $10\sqrt{2}$ A. The simulation results for both structures of dual three-phase DS-HSDR-TFPMSMs are measured when phase current constraint on amplitude is reached which is marked as the dashed lines in Fig. 5.11(b) and (e). It can be seen that winding currents of phases A1 and C1 of the dual three-phase DS-HSDR-TFPMSMs reach the constrained reference line, and the remaining phase currents are maintained at a low level. As shown in Fig. 5.11(a) and (d), the torque reference values in the figure are the maximum output torque under the phase current constraint on amplitude derived from the analytical calculation, and it can be seen that the measured values in simulation agree well with the reference values, which proves the correctness of the analytical calculation process of the FTC method. The torque ripple is 0.43% for the dual three-phase DS-HSDR-TFPMSM with symmetrical structure, while it is 0.42% for the dual three-phase DS-HSDR-TFPMSM with asymmetrical structure. In addition, the current waveforms in the decoupled frame are given in Fig. 5.11(c) and (f). It can be seen that measured and reference values are in consistency, and i_{pq} approximates a smooth line, thus ensuring that the machine continues to output constant torque under fault condition.

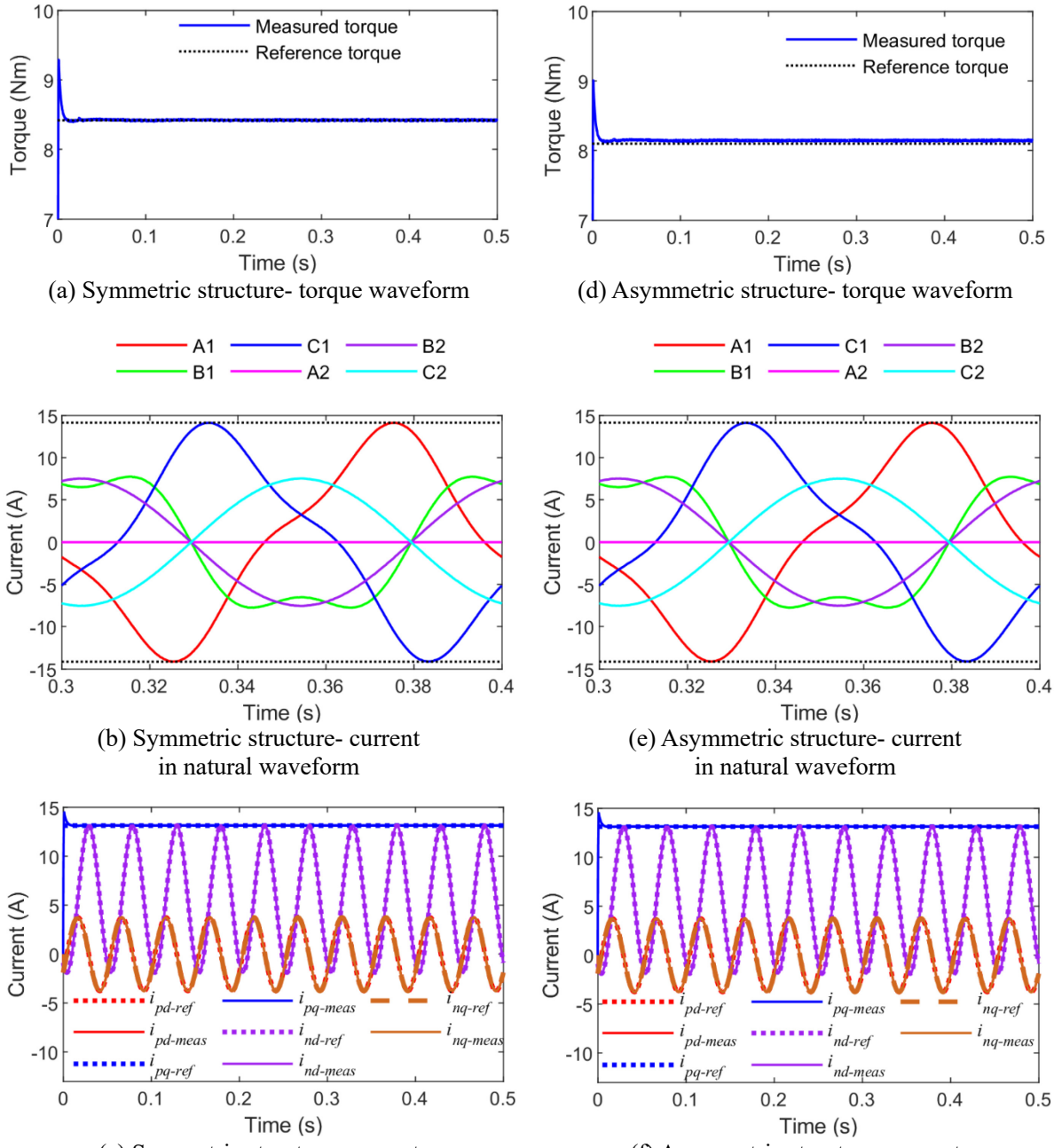

(a) Symmetric structure- torque waveform

(d) Asymmetric structure- torque waveform

(b) Symmetric structure- current in natural waveform

(e) Asymmetric structure- current in natural waveform

(c) Symmetric structure- current in decoupled frame

(f) Asymmetric structure- current in decouple frame

Fig. 5.11 Simulation results of one-phase open circuit FTC method based on MCL principle

Simulation results obtained using the FTC method based on the principle of MTOR for dual three-phase DS-HSDR-TFPMSMs under phase A2 open-circuit fault condition are shown in Fig. 5.12. The speed is set to 120 r/min and the machine simulation results are all measured when phase current constraint on amplitude is reached, as shown in Fig. 5.12 (b) and (e), where the winding currents in phase A1, C1, B2 and C2 of the dual three-phase DS-HSDR-TFPMSMs reach the constrained reference line, and only the winding currents in phase B1 remains at a low level. As shown in Fig. 5.12 (a) and (d), the torque ripple is 0.35% for the dual three-phase DS-HSDR-TFPMSM with symmetrical structure and 0.37% for the dual three-phase DS-HSDR-TFPMSM with asymmetrical structure, proving the effectiveness of proposed MTOL fault tolerant method in suppressing torque ripple. In addition, the winding currents in the decoupled frame are shown in Fig. 5.12 (c) and (f) shows. It can be seen that the simulated

measurements agree well with the calculated reference values, and i_{pq} is approximately a smooth line.

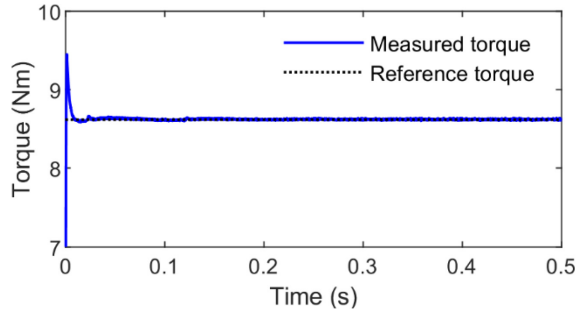

(a) Symmetric structure- torque waveform

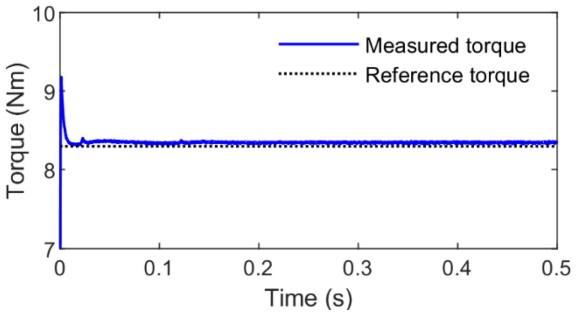

(d) Asymmetric structure- torque waveform

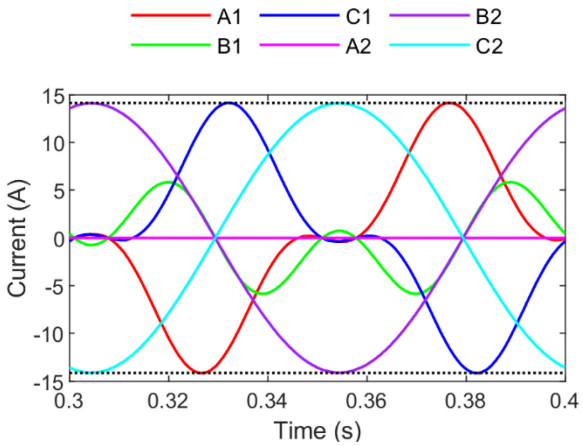

(b) Symmetric structure- current in natural waveform

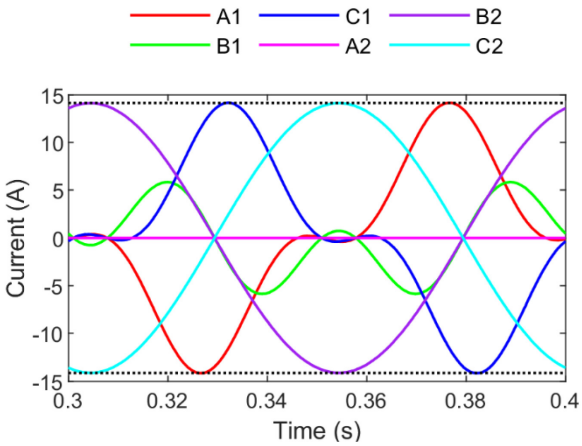

(e) Asymmetric structure- current in natural waveform

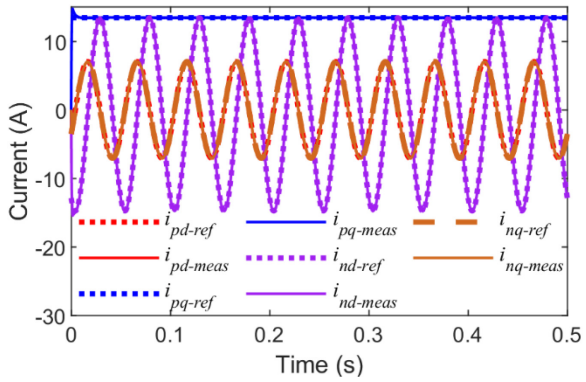

(c) Symmetric structure- current in decoupled frame

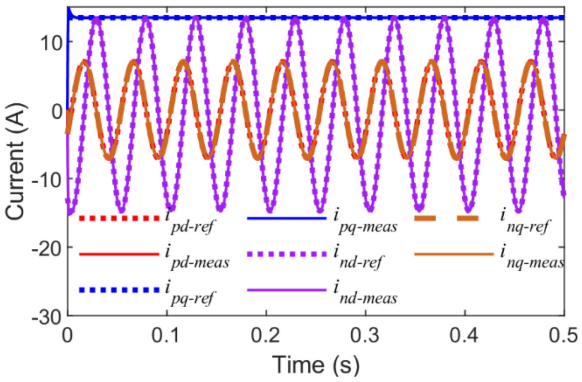

(f) Asymmetric structure- current in decouple frame

Fig. 5.12 Simulation results of one-phase open circuit FTC method based on MTOR principle

The torque performance obtained by using the FTC method based on the principle of MCL and the principle of MTOR for dual three-phase DS-HSDR-TFPMSMs are compared in Table 5.4. It can be concluded that a limited improvement of torque is achieved by using the MTOR method under the phase current constraint on amplitude. Therefore, the FTC method based on the principle of MCL is preferred for dual three-phase PMSM with double isolated neutral points.

Table 5.4 Comparison of torque characteristics of dual three-phase DS-HSDR-TFPMSM under fault condition

	FTC methods	Simulation results		Theoretical reference value
		Average torque	Torque ripple	Average torque
Symmetrical structure	MCL	8.42Nm	0.43%	8.42Nm
	MTOR	8.62Nm	0.35%	8.62Nm
Asymmetrical structure	MCL	8.14Nm	0.42%	8.10Nm
	MTOR	8.35Nm	0.37%	8.30Nm

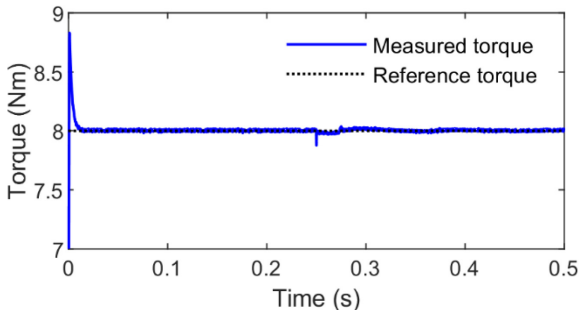

(a) Symmetric structure- torque waveform

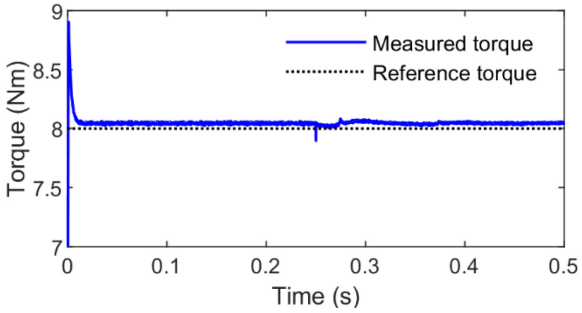

(d) Asymmetric structure- torque waveform

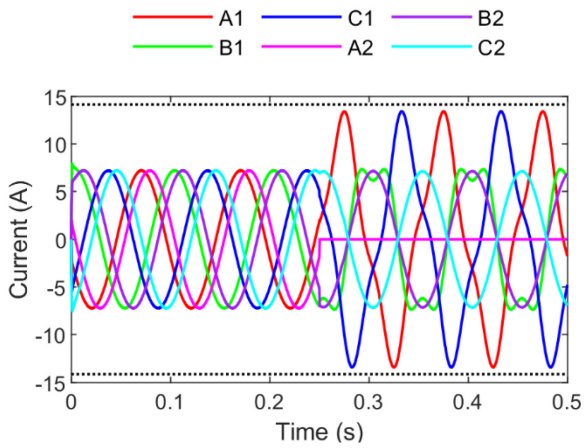

(b) Symmetric structure- current in natural waveform

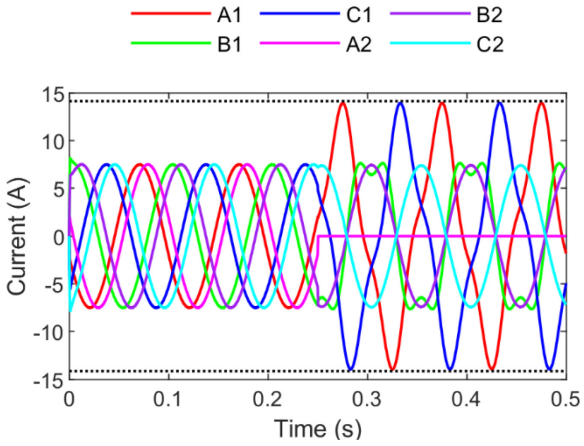

(e) Asymmetric structure- current in natural waveform

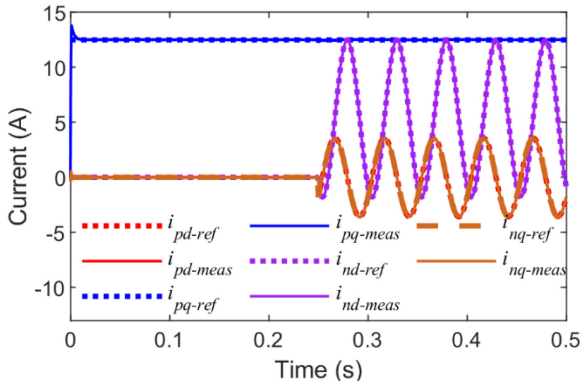

(c) Symmetric structure- current in decoupled frame

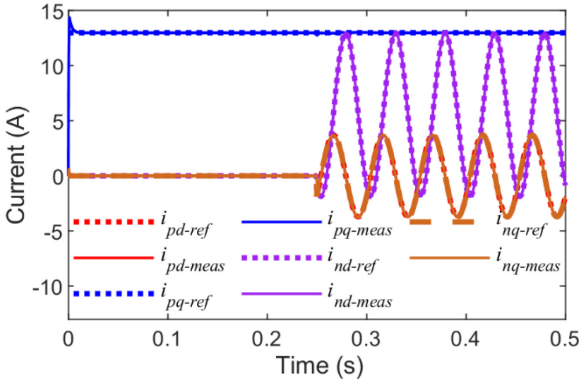

(f) Asymmetric structure- current in decouple frame

Fig. 5.13 Simulation results during fault-adding dynamic procedure

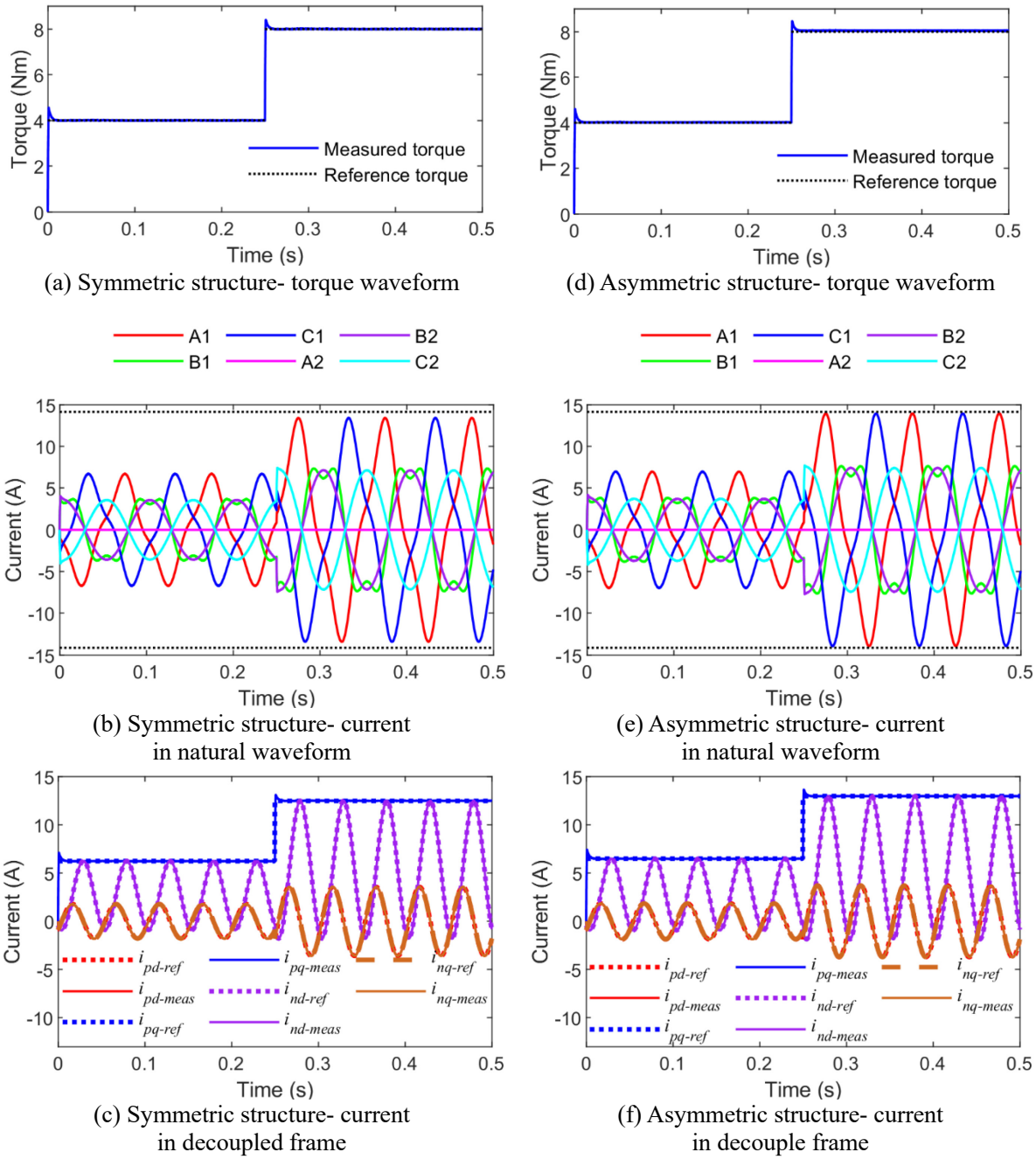

(a) Symmetric structure- torque waveform

(d) Asymmetric structure- torque waveform

(b) Symmetric structure- current in natural waveform

(e) Asymmetric structure- current in natural waveform

(c) Symmetric structure- current in decoupled frame

(f) Asymmetric structure- current in decouple frame

Fig. 5.14 Simulation results of torque changing dynamic procedure under fault condition

The dynamic process of the electric machine transitioning from normal condition to one-phase open-circuit fault condition with a torque reference value of 8Nm is shown in Fig. 5.13. At t=0.25s, the open-circuit fault occurs in phase A2, and the FTC method based on the principle of MCL is utilized to reconfigure the current strategy. The smooth output torque can be achieved rapidly by proposed FTC method while it entering into fault condition as shown in Fig. (a) and (d). However, it can be found that the phase current amplitude amplifies after entering into fault condition as shown in Fig. 5.13(b) and (e). For the dual three-phase DS-HSDR-TFPMSM with a symmetrical structure, the phase current amplitude elevates from 7.3A under normal condition to 13.4A under one-phase open-circuit condition, thereby the necessity of utilizing the phase current constraint on amplitude is proved.

The dynamic process of variant reference torque under open-circuit fault condition is shown in Fig. 5.14, where the initial torque reference value is set to 4Nm and increase subsequently to 8Nm at t=0.25s. As shown in Fig. 5.14(a) and (d), the change in torque reference value is rapidly responded by machine, which rapidly reaches the steady state. The dynamics of the phase current waveform in both natural and decoupled frames are shown in Fig. 5.14(b)(e) and 5.14(c)(f), respectively.

In summary, the proposed FTC method is characterized by excellent dynamic performance and can rapidly respond to the one-phase open-circuit fault and the torque variance under fault condition.

5.4 Axial Stress Analysis and Comparison of DS-HSDR-TFPMSMs

The proposed DS-HSDR-TFPMSM features a yokeless disk rotor structure that improves the dynamic performance of the industrial robot system by reducing the moment of inertia. However, this structure also weakens the structural strength of the rotor, making the DS-HSDR-TFPMSM more sensitive to stress distribution on the rotor. In the rotor of the DS-HSDR-TFPMSM, there are three types of stresses existing according to Maxwell's stress tensor theory: tangential stresses that mainly generate output torque, and radial as well as axial stress that cause vibration and noise. It has been shown in previous research that the radial stress on the rotor is almost negligible compared to the axial stress component[186]. Thus, stress analysis for the DS-HSDR-TFPMSM primarily focuses on its axial stress.

In a disk motor with a single-stator topology, the rotor side is always affected by axial stress, and unevenly distributed axial stresses on the rotor surface will worsen the vibration and noise problems[187]. As a novel machine with a dual-stator topology, DS-HSDR-TFPMSM, combines the advantage of balancing axial stresses on both sides of the rotor. However, the balance will be broken in dual three-phase DS-HSDR-TFPMSM with asymmetric structure due to the asymmetry of the stator disks on both sides of the rotor. The resulting imbalance in the axial stress distribution on both sides of the rotor is further exacerbated by the armature MMF synthesized by the stator disks on both sides, leading to potentially unsafe operation[152]. Therefore, it is necessary to analyze and evaluate the axial stresses on the dual three-phase DS-HSDR-TFPMSM rotor to verify the feasibility of the motor design scheme and ensure safe operation in both normal and fault conditions.

5.4.1 Calculation Method of Synthetic axial stress

According to the Maxwell Stress Tensor (MST) principle, the normal stress on one face can be calculated by following equation:

$$f_z = \frac{1}{2\mu_0}(B_z^2 - B_x^2 - B_y^2) \tag{5-54}$$

in which the symbol μ_0 means the magnetic permeability of the air, B_x, B_y and B_z are given in Fig. 5.15. The symbol B_z is the normal flux density component while the B_x and B_y are a pair of the orthogonal tangential flux density component along the surface of the PM. In the case of the DTP-AFPM, the z-axis in Fig. 5.15 can be seen as the axial axis.

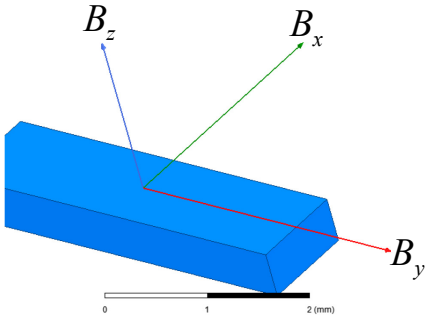

Fig. 5.15 Diagram of the flux density vector components.

The detailed calculating procedure of the synthetic axial stress under both healthy and fault condition is as follows:

1) Calculate the phase current of DTP-AFPM under different conditions;
2) Impose the calculated phase current into the finite element analysis (FEA) model of DTP-AFPM;
3) Solve the flux density distribution in ANSYS MAXWELL, and calculate the axial stress distribution using Fig. 5.16 in which the middle lines locate at the average radius of the PMs. Furtherly, the initial circular area is unfolded to two rectangular area.

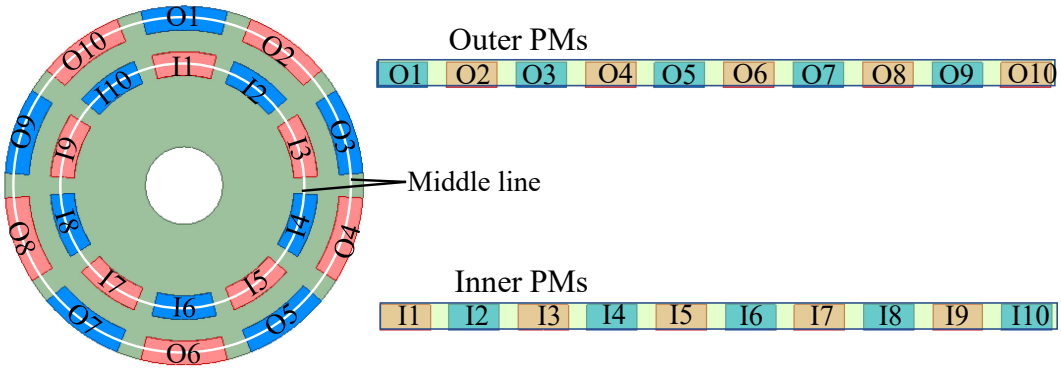

Fig. 5.16 Unfolding procedure from circular area to rectangular area.

5.4.2 Synthetic Axial Stress in the No Shift Model

This paper first calculates the phase currents of the windings of the symmetrical structure dual three-phase DS-HSDR-TFPMSM under various operating states, considering the following three states for axial stress analysis:

State 1: The machine operates under healthy condition;

State 2: The phase A2 is open without any reconfiguration for reference current;

State 3: The phase A2 is open and the reference current is calculated using FTC strategy.

In above descripted 3 stages, the reference torque is set to 8 N.m and the operating speed is 120 RPM. The simulated electromagnetic torque and phase current waveforms in one electrical cycle of symmetrical structure are given in Fig.5.17.

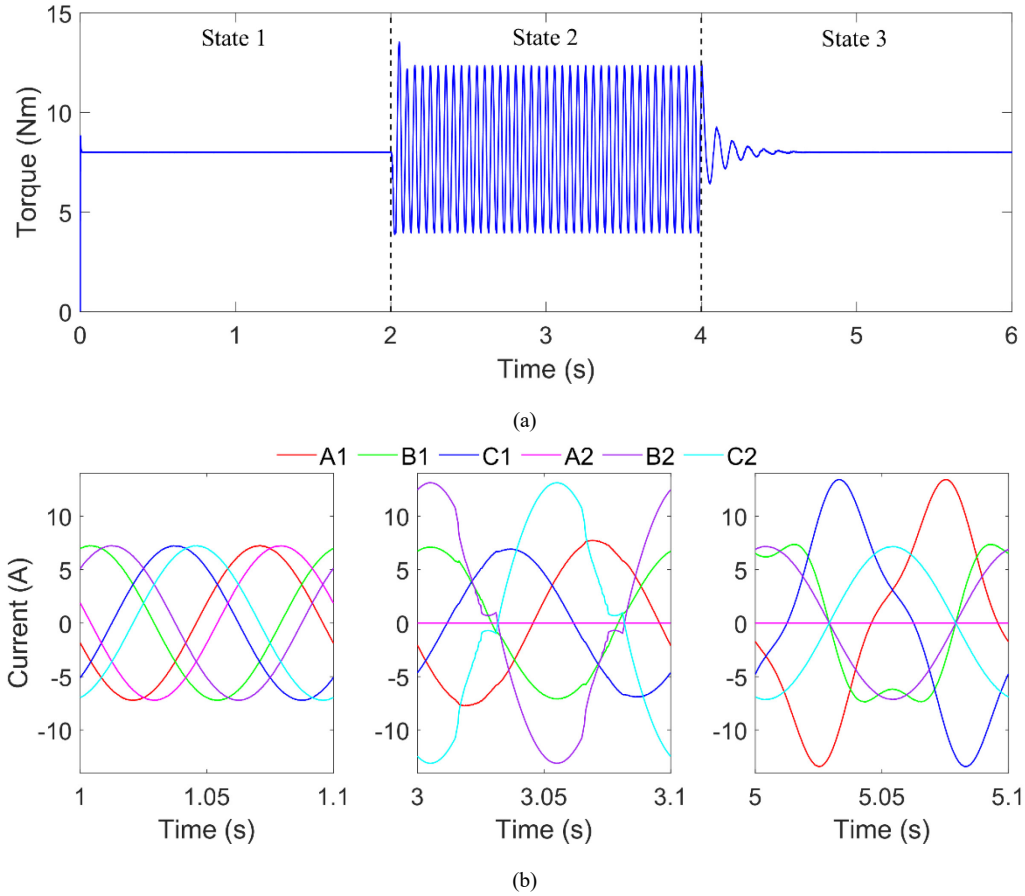

Fig. 5.17 Simulation results of the symmetrical structure: (a) Electromagnetic torque. (b) Phase current.

Firstly, the rotor axial force waveform of the no shift model while the machine operates in different stages is shown in Fig. 5.18 in which the symbol θ indicates the displacement angle of the rotor. It can be seen that all the axial force waveforms fluctuate around 0 N. The synthetic axial stress distributions of the no shift model at the initial moment (θ=0) are shown in Fig. 5.19. Among the six subgraphs in Fig. 5.19, there is no obvious regularity can be found. The peak value of each figure is indicated and the extremum is about 0.1MPa which is most likely due to the calculation errors.

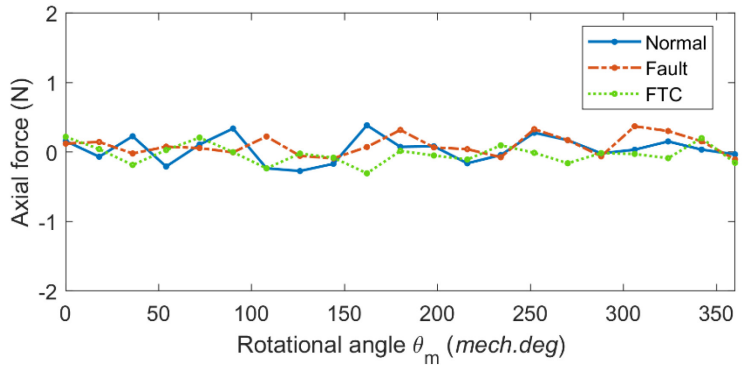

Fig. 5.18 Rotor axial force waveform of the no shift model.

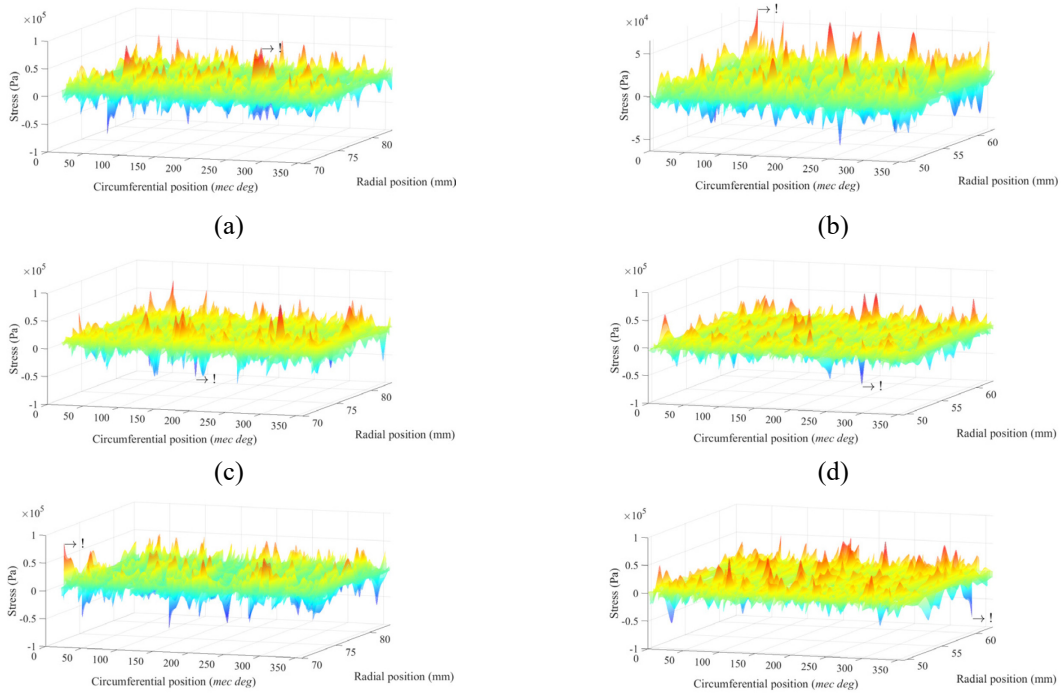

Fig. 5.19 Synthetic axial stress distribution of the no shift model at the initial moment: (a) on the outer PMs area operating under healthy condition, (b) on the inner PMs area operating under healthy condition, (c) on the outer PMs area operating under fault condition, (d) on the inner PMs area operating under fault condition, (e) on the outer PMs area operating under fault condition with FTC, (f) on the inner PMs area operating under fault condition with FTC.

5.4.3 Synthetic Axial Stress in the Shift Model

The simulated electromagnetic torque and phase current waveforms in one electrical cycle of asymmetrical structure are given in Fig. 5.20.

The rotor axial forces of the shift model while the machine operates in different stages are shown in Fig. 5.21. The average value of the rotor axial force in one electrical circle is -2.24N under healthy condition (*stage 1*). It means that the bearing on one side will support the axial force throughout. Under fault condition (*stage 2*), the rotor axial force deteriorate sharply which fluctuates between ±100N. It is bound to cause the serious vibration and noise. Under fault condition with FTC (*stage 3*), the fluctuation of the rotor axial force waveform decreases clearly. However, it is still at a higher level.

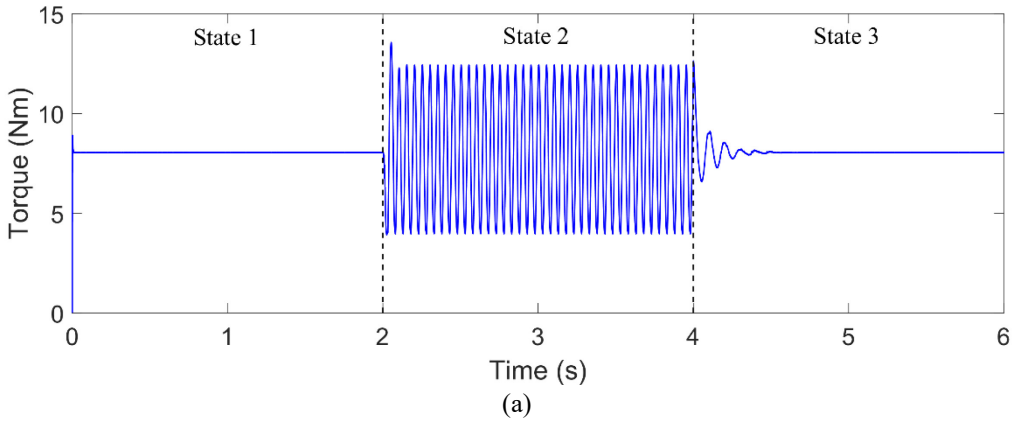

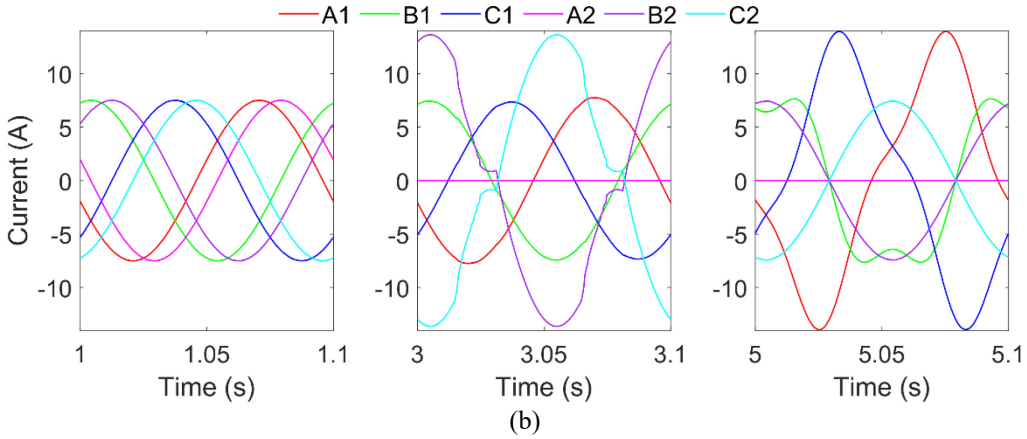

(b)

Fig. 5.20 Simulation results of the asymmetrical structure: (a) Electromagnetic torque. (b) Phase current.

In Fig. 5.21, a special rotor displacement position θ=294° is highlighted where the axial force on the rotor reaches the extremum under fault conditions (*stage 2* and *3*). The synthetic axial stress distribution of the shift model at θ=294° is shown in Fig. 5.22. It can be seen that the synthetic axial stress on PMs of the shift model is variable regularly along the circumferential direction. The peak value of each figure is indicated in Fig. 5.22. The comparison of the peak value of the axial stress between the no shift model and shift model is given in Table.5.5. It can be found that the peak value of the shift model is higher than that of the no shift model. The detailed synthetic axial stress distributions along the middle line shown in Fig. 5.16 are given in Fig. 5.23. The positive or negative fluctuation of the distribution curves shown in Fig. 5.23 is coincide with the position of the slot opens in stator disks. In addition, it can be noticed that the fluctuation of the axial stress on the inner PMs as shown in Fig. 5.23(b) is higher due to the larger slot opens and smaller flux area compared with the outer PMs. It can be predicted that the possibility of the PMs breaking increases greatly compared with the no shift model as the synthetic axial stress on each PM of the shift model is uneven.

Table 5.5 Comparison of the peak value of the axial stress (Unit: MPa)

		No shift	Shift
Healthy	Outer PM	0.0758	-0.31
	Inner PM	0.0663	-0.295
Fault	Outer PM	-0.0973	-0.377
	Inner PM	-0.0803	-0.239
FTC	Outer PM	0.0778	-0.288
	Inner PM	-0.084	-0.349

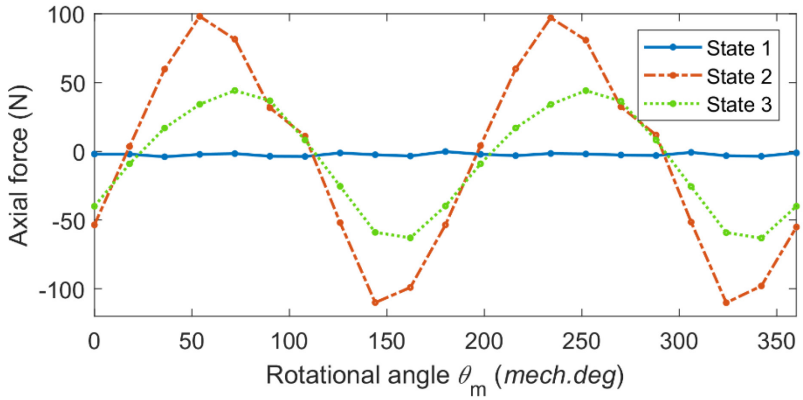

Fig. 5.21 Rotor axial force waveform of the shift model.

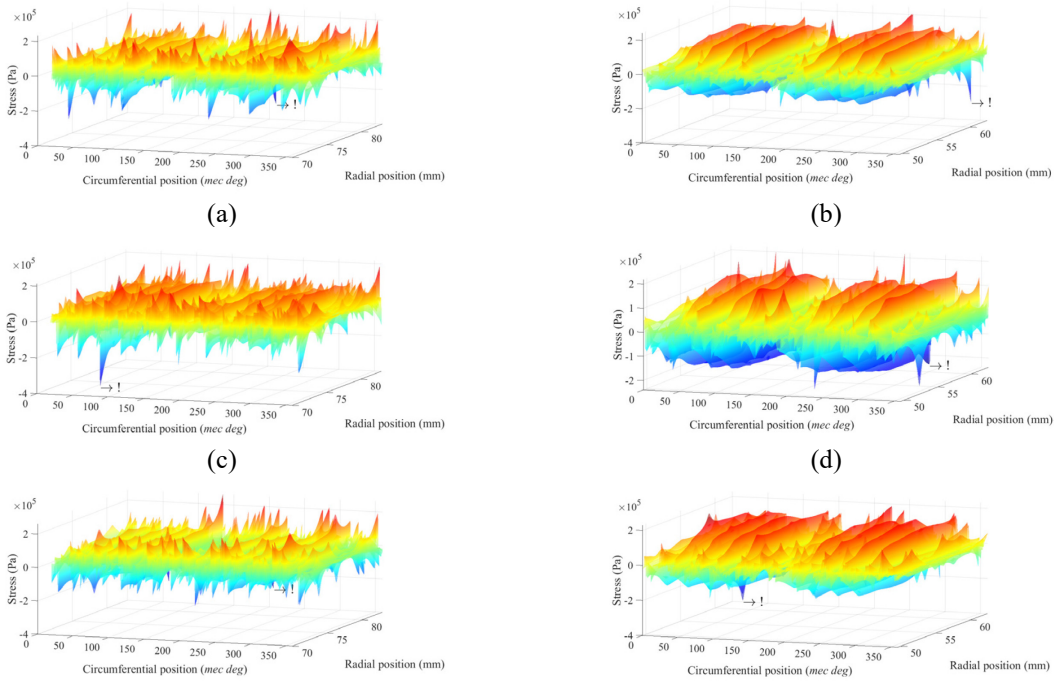

Fig. 5.22 Synthetic axial stress distribution of the shift model (θ=294°): (a) on the outer PMs area operating under healthy condition, (b) on the inner PMs area operating under healthy condition, (c) on the outer PMs area operating under fault condition, (d) on the inner PMs area operating under fault condition, (e) on the outer PMs area operating under fault condition with FTC, (f) on the inner PMs area operating under fault condition with FTC.

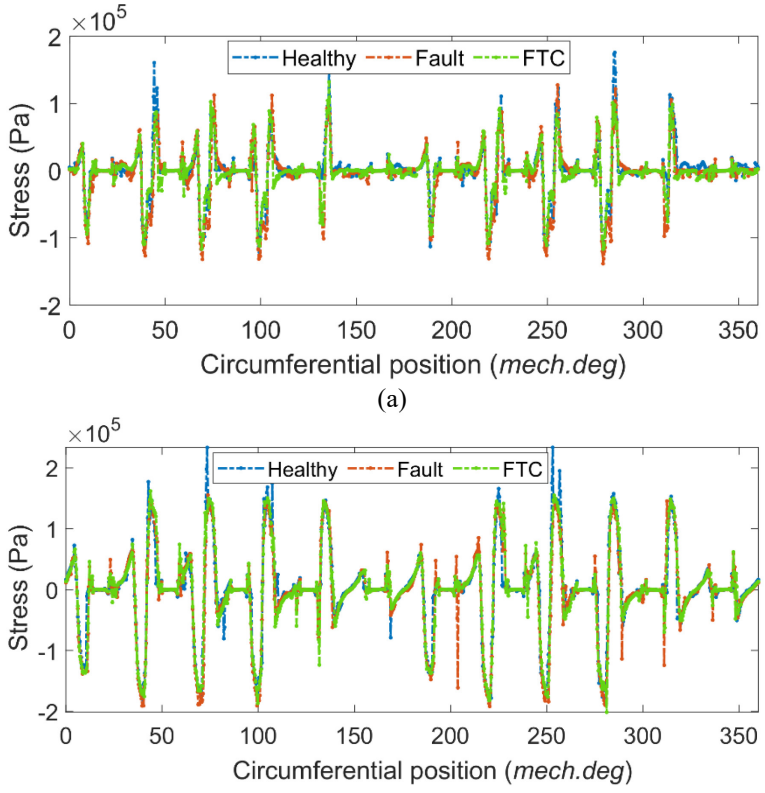

Fig. 5.23 Synthetic axial stress distribution along the middle line given in Fig. 5.16: (a) on the outer PMs area, (b) on the inner PMs area.

5.5 Control of harmonic reference currents in FTC method

As previously mentioned, the current strategy needs to be reconfigured when the electric machine operates under open-circuit fault condition. And the reference current in reconfigured current strategy becomes an alternating variable that changes with the rotor position. Although the traditional PI controller generally combines a tracking ability for the AC component to some content, it inevitably generates phasor delay. This issue can be ignored while the machine operates under low speed, but it gradually worsens as the speed increases and eventually impacts the smoothness of output torque. Therefore, it is essential to ensure that the electric machine can generate smooth torque under an expanded range of speed under fault condition to guarantee the accuracy of industrial robot system. To achieve above objective, the multi-reference frame (MRF)-based harmonic current control method and proportional-resonant (PR)-based control method is proposed in the thesis for tracking the harmonic reference currents generated by FTC method.

The fault tolerant vector control model of a symmetrical dual three-phase DS-HSDR-TFPMSM under open-circuit fault condition in phase A2 is investigated. The torque reference is set to 8 Nm and the FTC method based on the principle of MCL is adopted.

5.5.1 Restrictions of PI controller

It can be found from (5-37) that the reference current in the decoupled frame contain the second harmonic component, except for i_{pq}. The torque waveforms of electric machine under various speeds are shown in Fig. 5.24 if the PI controller part shown in Fig. 5.6 is still utilized. It is evident that the torque ripple gradually increases as the speed increases, and the torque ripple rises to 26.9% at the rated speed of 3000r/min.

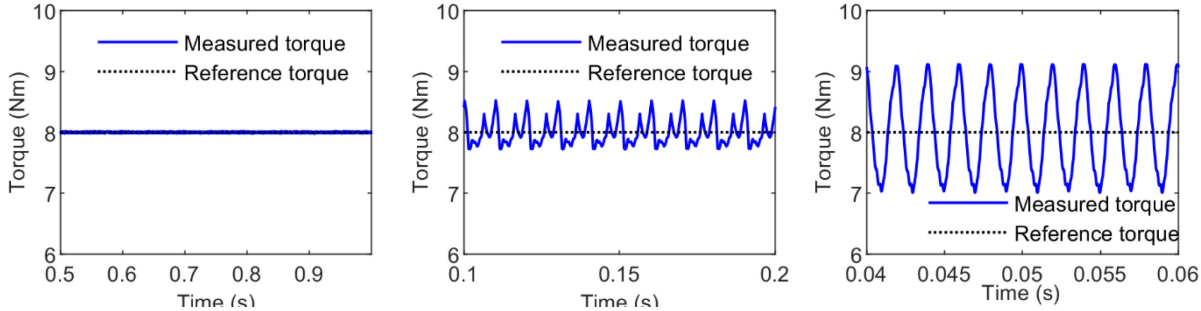

(a) 120r/min (b) 600r/min (c) 3000r/min

Fig. 5.24 Torque waveform under different speed

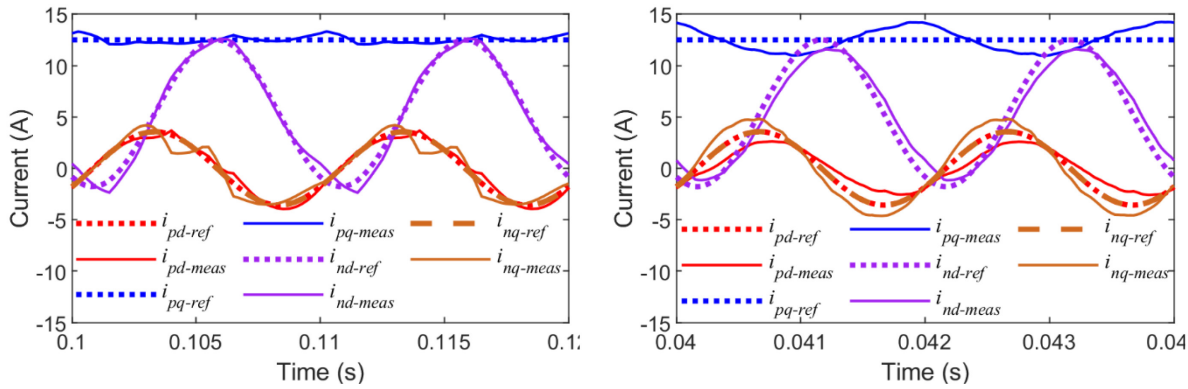

(a) 600r/min (b) 3000r/min

Fig. 5.25 Current in decoupled frame under different speed

The waveforms of the currents in decoupled frame at 600r/min and 3000r/min are shown in Fig. 5.25. It can be found that the reference current value is no longer precisely followed, as shown in Fig. 5.16(a), when compared with the waveform of the current in decoupled frame at 120r/min under fault condition, as shown in Figure 5.11(c). The waveforms of the currents in decoupled frame $i_{\text{pd-meas}}$, $i_{\text{nd-meas}}$ and $i_{\text{nq-meas}}$ display an evident phasor delay concerning the reference current waveform at 3000r/min, and the current amplitude also changes to some extent, resulting in i_{pq} no longer remaining constant and eventually generating the torque ripple displayed in Fig. 5.24(c).

The desynchronization between the measured values of the currents in decoupled frame $i_{\text{pd-meas}}$, $i_{\text{nd-meas}}$ and $i_{\text{nq-meas}}$ and the corresponding reference values $i_{\text{pd-ref}}$, $i_{\text{nd-ref}}$ and $i_{\text{nq-ref}}$ is mainly due to the delayed response of the PI controller to high frequency signals. To address this issue, a common approach is to directly increase the bandwidth of PI controller by increase the value of its proportional or integral coefficients. However, the anti-disturbance ability of the control system will be reduced by improve the bandwidth of PI controller causing the decrease of system stability. Therefore, a method to track harmonic components in reconfigured current strategy without the change of PI controller parameters is proposed.

5.5.2 MRF-based harmonic current control method

Current strategy in decoupled frame under fault condition (5-37) can be further decomposed into DC component and second harmonic component as follows:

$$\begin{cases} i_{pd,0} = 0 \\ i_{pq,0} = \dfrac{I_{pq,0} + I_{pq,2}}{2} \\ i_{nd,0} = \dfrac{I_{pq,0} - I_{pq,2}}{2} \\ i_{nq,0} = 0 \end{cases} \qquad \begin{cases} i_{pd,2} = \dfrac{I_{pq,2}}{2}\sin(2\theta - \dfrac{\pi}{6}) \\ i_{pq,2} = 0 \\ i_{nd,2} = I_{pq,2}\cos(2\theta + \dfrac{5\pi}{6}) \\ i_{nq,2} = \dfrac{I_{pq,2}}{2}\sin(2\theta - \dfrac{\pi}{6}) \end{cases} \tag{5-55}$$

The PI controller can be used to directly regulate the DC component. Furthermore, the MRF method is utilized to transform the second harmonic component in both the *pd-pq* and *nd-nq* frames to the DC component in harmonics decoupled frames for control. In the thesis, the MRF transformation of the second harmonic current vector in the *pd-pq* frame is demonstrated as an example.

A schematic diagram of the MRF transformation in the *pd-pq* frame is shown in Fig. 5.26. $\vec{i}_{p,0}$ is the DC vector consisting of $i_{pd,0}$ and $i_{pq,0}$, $\vec{i}_{p,h2}$ denotes the second harmonic current vector consisting of $i_{pd,2}$ and $i_{pq,2}$, whose component on the pq axis is always zero according to Eq. (5-55). *pAd-pAq* and *pBd-pBq* denote the frames rotated in positive or negative order with respect to the *pd-pq* frame at twice the electrical angular velocity, respectively. Using the *pd*-axis as the real axis and the *pq-axis* as the imaginary axis, $\vec{i}_{p,h2}$ can be further expressed as a composite of the current vector $\vec{i}_{p,A}$ within the *pAd-pAq* frame and the current vector $\vec{i}_{p,B}$ in the *pBd-pBq* frame:

$$\vec{i}_{p,h2} = \vec{i}_{p,A} + \vec{i}_{p,B} = A_p e^{j(2\theta + \varphi_{A_p})} + B_p e^{-j(2\theta + \varphi_{B_p})} \tag{5-56}$$

where A_p and B_p represent the magnitude of $\vec{i}_{p,A}$ and $\vec{i}_{p,B}$, respectively.

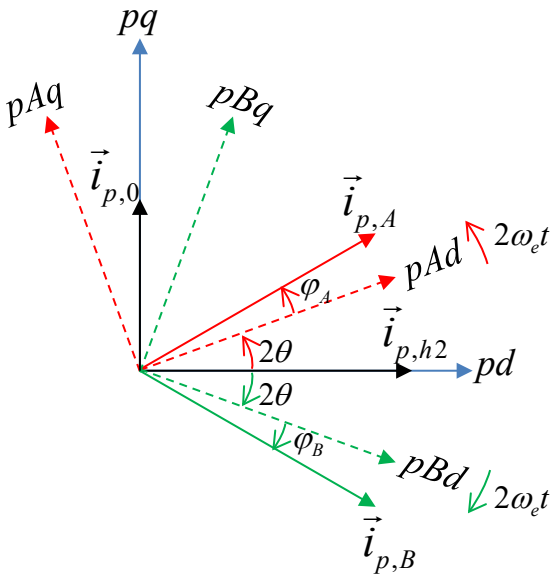

Fig. 5.26 Diagram of MRF transformation

Equation (5-56) can be further expanded to the following form:

$$\vec{i}_{p,h2} = A_p\left[\cos\left(2\theta+\varphi_{A_p}\right)+j\sin\left(2\theta+\varphi_{A_p}\right)\right]+B_p\left[\cos\left(2\theta+\varphi_{B_p}\right)-j\sin\left(2\theta+\varphi_{B_p}\right)\right] \tag{5-57}$$

Comparing (5-57) with the second harmonic components in the *pd-pq* frame in (5-56), the following relationship can be obtained:

$$\begin{cases} A_p\cos\left(2\theta+\varphi_{A_p}\right)+B_p\cos\left(2\theta+\varphi_{B_p}\right)=\dfrac{I_{pq,2}}{2}\sin\left(2\theta-\dfrac{\pi}{6}\right) \\ A_p\sin\left(2\theta+\varphi_{A_p}\right)-B_p\sin\left(2\theta+\varphi_{B_p}\right)=0 \end{cases} \tag{5-58}$$

Solving equation (5-58), it can be obtained that:

$$A_p = B_p = \frac{I_{pq,2}}{4} \qquad \varphi_{A_p} = \varphi_{B_p} = -\frac{2}{3}\pi \tag{5-59}$$

By applying the PARK transformation $e^{-j2\theta}$ and the PARK inverse transformation $e^{j2\theta}$ on basis of 2θ, $\vec{i}_{p,A}$ and $\vec{i}_{p,B}$ can be transformed to the constant vector in the *pAd-pAq* frame and the *pBd-pBq* frame. Finally, the transformation from the second harmonic component to the DC component can be realized.

In the *pAd-pAq* frame, the mathematical model of the machine needs to be re-constructed. Firstly, the voltage equation in the *pAd-pAq* frame is rederived as follow:

$$\begin{bmatrix} u_{pAd} \\ u_{pAq} \end{bmatrix} = R_s\begin{bmatrix} i_{pAd} \\ i_{pAq} \end{bmatrix} + 3\omega_e\begin{bmatrix} 0 & -1 \\ 1 & 0 \end{bmatrix}\begin{bmatrix} L_{pAd} & \\ & L_{pAq} \end{bmatrix}\begin{bmatrix} i_{pAd} \\ i_{pAq} \end{bmatrix} + \begin{bmatrix} L_{pAd} & \\ & L_{pAq} \end{bmatrix}\frac{d}{dt}\begin{bmatrix} i_{pAd} \\ i_{pAq} \end{bmatrix} \tag{5-60}$$

Secondly, the voltage equation in the *pBd-pBq* frame is re-derived:

$$\begin{bmatrix} u_{pBd} \\ u_{pBq} \end{bmatrix} = R_s\begin{bmatrix} i_{pBd} \\ i_{pBq} \end{bmatrix} - \omega_e\begin{bmatrix} 0 & -1 \\ 1 & 0 \end{bmatrix}\begin{bmatrix} L_{pBd} & \\ & L_{pBq} \end{bmatrix}\begin{bmatrix} i_{pBd} \\ i_{pBq} \end{bmatrix} + \begin{bmatrix} L_{pBd} & \\ & L_{pBq} \end{bmatrix}\frac{d}{dt}\begin{bmatrix} i_{pBd} \\ i_{pBq} \end{bmatrix} \tag{5-61}$$

It can be found that, the inductance matrix of for the non-salient PMSM remains unchanged through MRF transformation, that means $L_{pAd}=L_{pAq}=L_{pBd}=L_{pBq}=L_{pd}=L_{pq}$. Thus, there is no requirement for the adjustment of the PI parameters using MRF-based harmonic current control method, and only the forward-set compensation needs to be modified, ensuring the stability of the system.

The MRF transformation of second harmonic current vector $\vec{i}_{n,h2}$ in the *nd-nq* frame can be obtained referring to the above analysis, which can be finally expressed as:

$$\vec{i}_{n,h2}=\vec{i}_{n,A}+\vec{i}_{n,B}=\frac{I_{pq,2}}{4}e^{j(2\theta+\frac{5\pi}{6})}+\frac{3I_{pq,2}}{4}e^{-j(2\theta+\frac{5\pi}{6})} \tag{5-62}$$

The voltage equations in the *nAd-nAq* frame as well as in the *nBd-nBq* frame obtained through MRF transformation are:

$$\begin{bmatrix}u_{nAd}\\u_{nAq}\end{bmatrix}=R_s\begin{bmatrix}i_{nAd}\\i_{nAq}\end{bmatrix}+3\omega_e\begin{bmatrix}0&-1\\1&0\end{bmatrix}\begin{bmatrix}L_{nAd}&\\&L_{nAq}\end{bmatrix}\begin{bmatrix}i_{nAd}\\i_{nAq}\end{bmatrix}+\begin{bmatrix}L_{nAd}&\\&L_{nAq}\end{bmatrix}\frac{d}{dt}\begin{bmatrix}i_{nAd}\\i_{nAq}\end{bmatrix} \tag{5-63}$$

$$\begin{bmatrix}u_{nBd}\\u_{nBq}\end{bmatrix}=R_s\begin{bmatrix}i_{nBd}\\i_{nBq}\end{bmatrix}-\omega_e\begin{bmatrix}0&-1\\1&0\end{bmatrix}\begin{bmatrix}L_{nBd}&\\&L_{nBq}\end{bmatrix}\begin{bmatrix}i_{nBd}\\i_{nBq}\end{bmatrix}+\begin{bmatrix}L_{nBd}&\\&L_{nBq}\end{bmatrix}\frac{d}{dt}\begin{bmatrix}i_{nBd}\\i_{nBq}\end{bmatrix} \tag{5-64}$$

where the inductance matrix also remains unchanged, that means $L_{nAd}=L_{nAq}=L_{nBd}=L_{nBq}=L_{nd}=L_{nq}$.

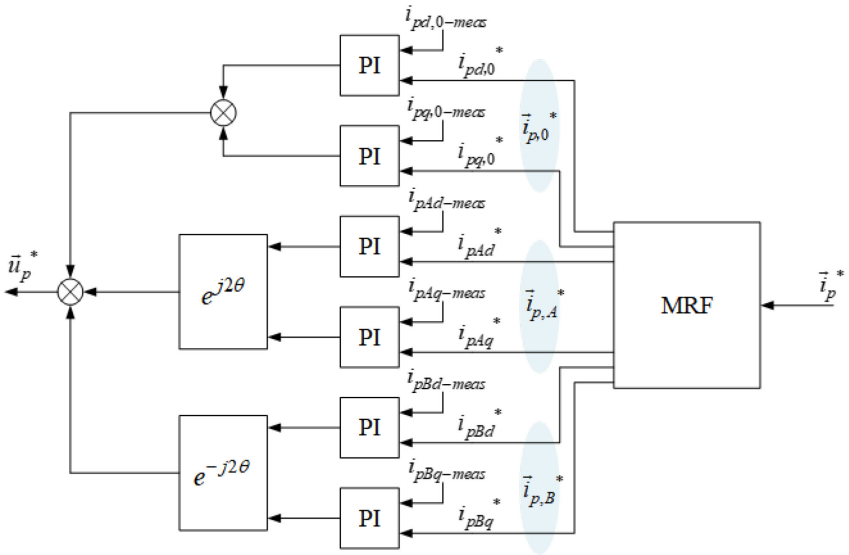

Fig. 5.27 Framework diagram of the PI controller part of the FTC model applying the MRF

In summary, the current vector $\vec{i}_p$ in the *pd-pq* frame under fault condition using fault tolerant method can be decomposed into three vectors by MRF transformation: the constant vector $\vec{i}_{p,0}$, the positive sequence rotation vector $\vec{i}_{p,A}$ and the negative sequence rotation vector $\vec{i}_{p,B}$. The $\vec{i}_{p,0}$ is still controlled in the *pd-pq* frame, while the $\vec{i}_{p,A}$ and $\vec{i}_{p,B}$ are controlled in the *pAd-pAq* and *pBd-pBq* frames, respectively.

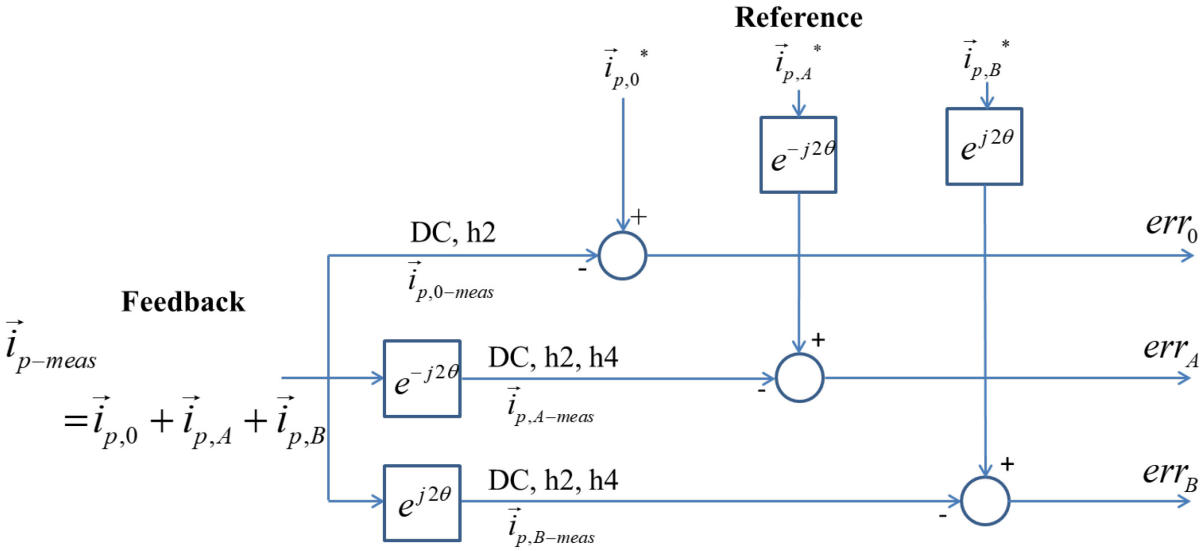

Fig. 5.28 Error calculation of the current imposing the feedback current to the MRF transformation directly

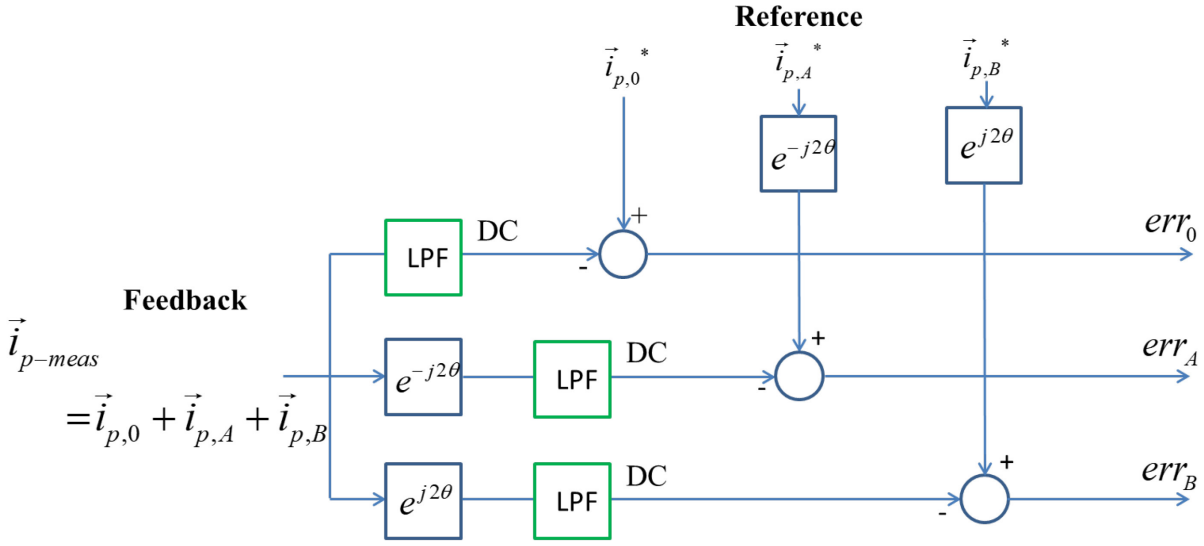

Fig. 5.29 Error calculation of the current adding the LPF to the feedback side

The framework diagram of the PI controller part in the fault tolerant vector control model with MRF transformation in the *pd-pq* frame is shown in Fig. 5.27, while the structure of current controllers in the *nd-nq* frame remains consistent with it. The reference current input to each PI controller can be calculated using (5-55), (5-56), and (5-59). However, the DC component, as well as the positive and negative sequence second harmonic components, cannot be directly separated from the feedback current in decoupled frame. If the MRF transformation is applied directly to the feedback current, the calculation error input to the PI controller is shown in Fig. 5.28 in which the feedback current is superimposed by various harmonic components (h2 indicating the second harmonic component, h4 indicating the fourth harmonic component) on the basis of DC component through MRF transformation, leading to the interference with the input error of PI controller. To eliminate the harmonic components superimposed on the feedback current through MRF transformation, the low-pass filter (LPF) is introduced to the feedback current, as shown in Fig. 5.29.

5.5.3 PR-based harmonic current control method

The MRF harmonic current control method converts the second harmonic component of the reference current into a DC component through the transformation of the coordinate system, effectively solving the problem of substandard tracking performance of AC signals by PI controllers. However, the PI controller part of MRF-based harmonic current control method requires a total of twelve PI current controllers, that increases significantly compared to the use of four PI controllers under normal condition. In order to reduce the number of current controllers, the PR-based harmonic current control method is proposed to control the harmonic component.

In contrast to PI controllers, PR controllers possess a distinctive resonant loop, enabling them to follow high frequency AC signals. The transfer function of the PR controller is as follows:

$$G_{PR} = k_P + \frac{k_r \omega_c s}{s^2 + 2\omega_c s + \omega_{pr}^2} \tag{5-65}$$

Where k_r is the resonant gain, ω_c is the cut-off frequency of the controller, and ω_{pr} is the given electrical angular frequency which is main harmonics frequency to be tracked. And so ω_{pr} needs to be adjusted in real time with the variance of speed.

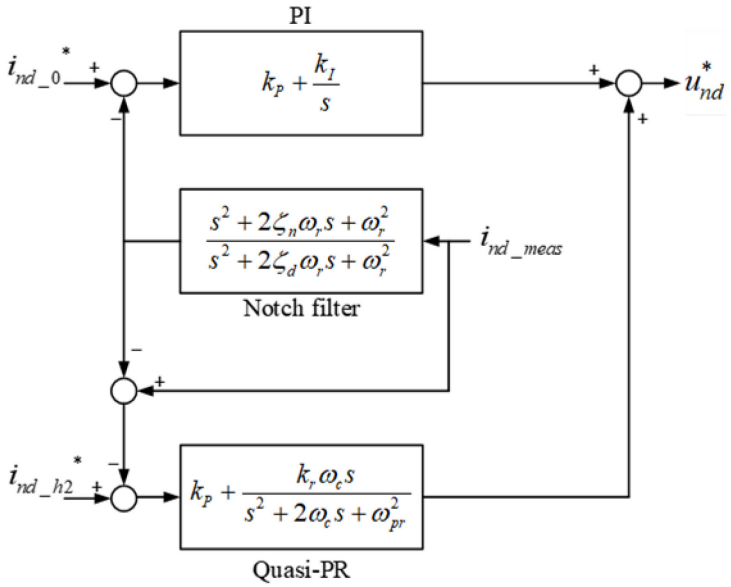

Fig. 5.30 Transfer function diagram of the current controller for $i_{nd,f}$

The introduction of the PR controller allows for direct regulation of harmonic components within the reconfigured current strategy, while DC components is still regulated by PI controllers. According to (5-37), the control of $i_{pq,f}$ is achieved by using PI controller, the control of both $i_{pd,f}$ and $i_{nq,f}$ is achieved by PR controller, besides, the control of $i_{nd,f}$ is slightly more complex, requiring the separate control of its DC component and AC component. The block diagram of transfer function of the $i_{nd,f}$ current controller is illustrated in Fig. 5.30. Similar to the challenges faced in the PI controller part of the MRF-based harmonic current control method, the feedback current $i_{nd,f\text{-}meas}$ also necessitates decomposition into DC and second harmonic components. It is worth to notice that $i_{nd,f\text{-}meas}$ only contains the second harmonic component that can be eliminated using a notch filter.

5.5.4 Simulation results and comparative analysis

Simulation analysis is performed for above two harmonic current control methods.

Firstly, the MRF-based harmonic current control method is researched by simulation. By establishing Simulink simulation model, the dynamic waveforms of torque under four operating states are calculated, as shown in Fig. 5.31, with the speed of 3000 r/min. The specific descriptions of the four operating states are as follows:

(1) State 1: The electric machine operates under normal condition.

(2) State 2: Winding phase A2 is open-circuit, but still using the current strategy.

(3) State 3: Winding phase A2 is open-circuit, reconfiguring the current strategy by FTC method.

(4) State 4: Winding phase A2 is open-circuit, reconfiguring the current strategy by FTC method and using MRF-based harmonic current control method.

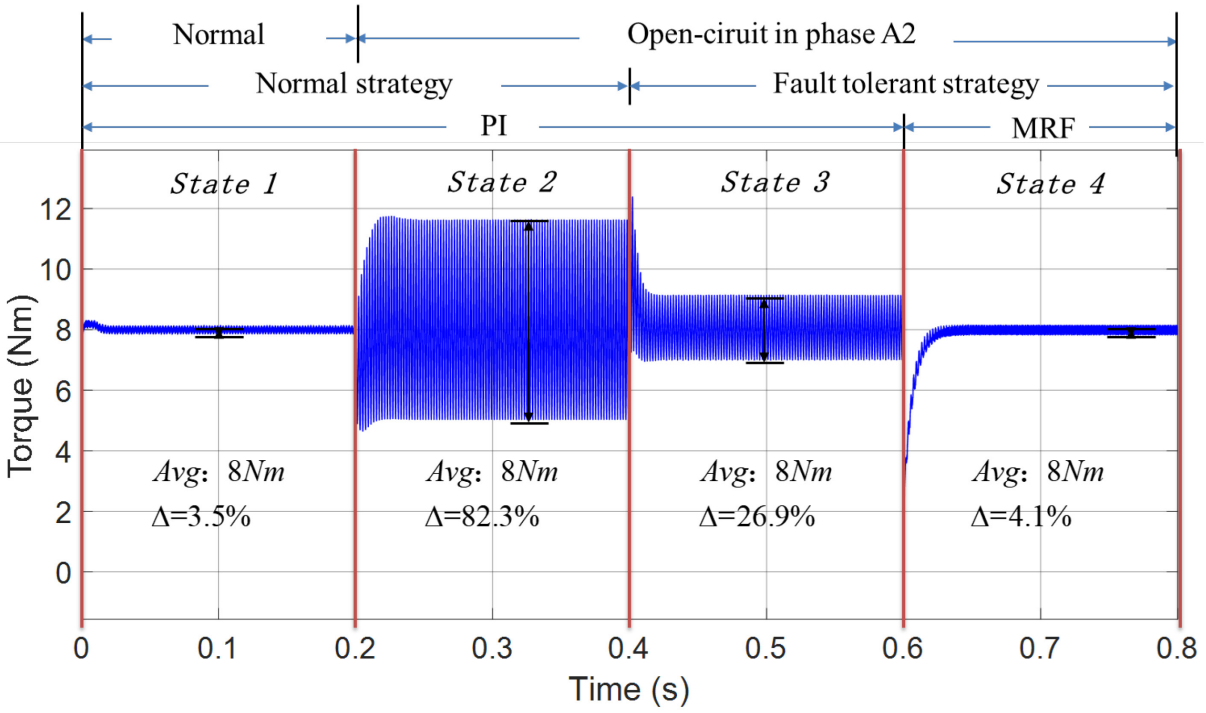

Fig. 5.31 Torque waveform during the dynamic procedure under 3000r/min

It can be seen that the torque ripple increases rapidly when the state transition from normal condition to state 2 as shown in Fig. 5.31. And then the torque ripple decreases to 26.9% when the FTC method is introduced. The torque ripple is furtherly reduced significantly to 4.1% by using MRF-based harmonic current control method in state 4, which is comparable to the torque ripple of 3.5% measured under normal condition, promoting the improvement of the accuracy under high-speed fault condition.

To evaluate the responsiveness of the MRF-based harmonic current control method to torque variation, a dynamic torque variation process is simulated at a speed of 3000r/min. The system is initialized with a starting torque of 4Nm, which is increased to 8Nm at t=0.1s. The torque waveform of the entire dynamic process is shown in Fig. 5.32. The results demonstrate that the system responds to the torque variance with a response time of 0.02s. The torque ripple is 6.34% under reference torque of 4Nm, and 3.69% under reference torque of 8Nm.

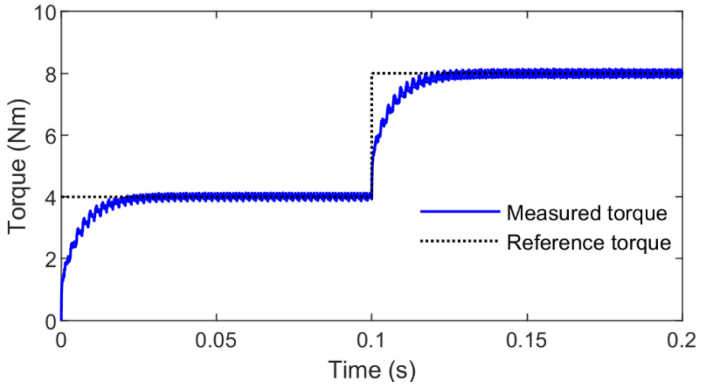

Fig. 5.32 Torque-variant dynamic procedure under 3000r/min

The same Simulink simulation model is established for PR-based harmonic current control method. The dynamic waveforms of the torque are calculated under aforementioned four operating states with the speed of 3000 r/min, as shown in Fig. 5.33. It can be seen that torque reaches the reference value of 8 Nm rapidly while the electric machine operates transitioning from state 3 to state 4. In addition, the torque ripple gradually decreases under state 4, and the torque ripple of the last electric cycle is 11.59%, which is much higher compared with the results obtained by MRF-based harmonic current control method in Fig. 5.31.

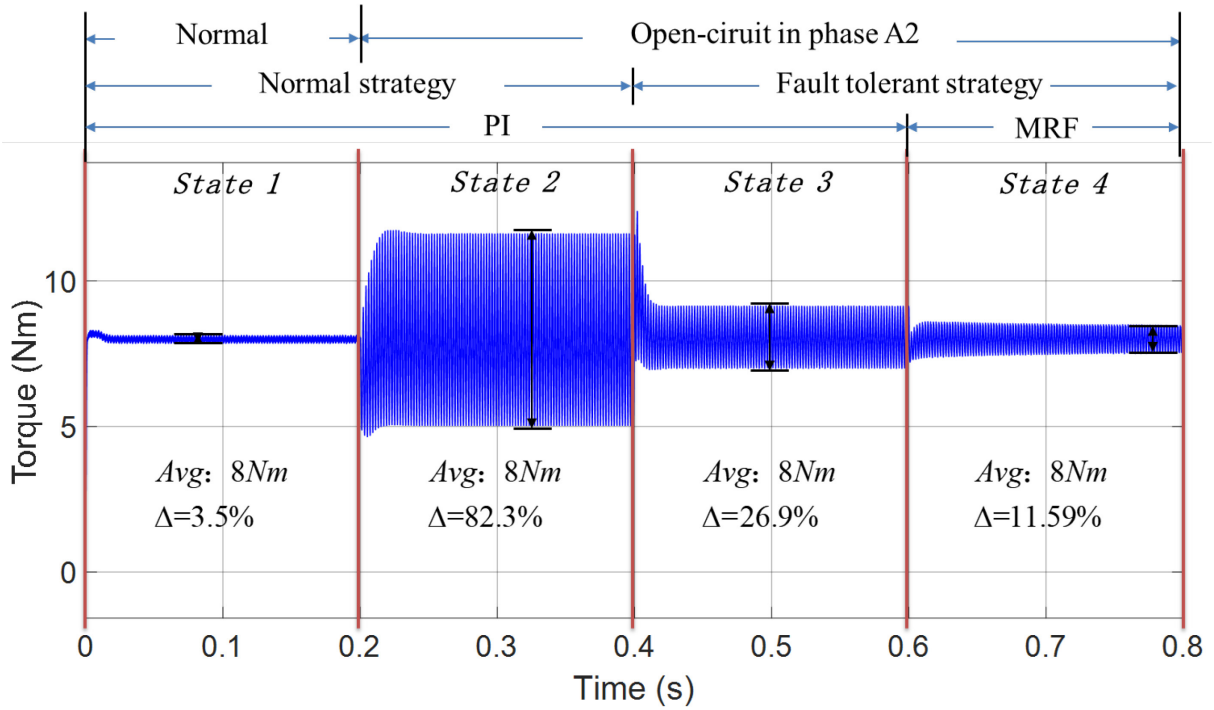

Fig. 5.33 Torque waveform during dynamic procedure under 3000r/min

In addition, to verify the responsiveness of the control system to torque change after using PR-based harmonic current control method, the dynamic process of torque variance is simulated under the speed of 3000 r/min. The system is initialized with a starting torque of 4Nm, which is increased to 8Nm at t=0.1s. The torque waveform of the entire dynamic process is shown in Fig. 5.34. It can be seen that the response time of the system to the torque variance is reduced compared with the MRF harmonic current control method. The machine torque ripple is 19.68% under the reference torque of 4Nm, and 11.93% under the reference torque of 8Nm.

Based on the above analysis, it can be concluded that the responsiveness of PR-based harmonic current control method is better, but its torque ripple under high speed is much higher than that of MRF-based harmonic current control method, which is not conducive to the electric machine to continue to operate stably under high-speed fault condition.

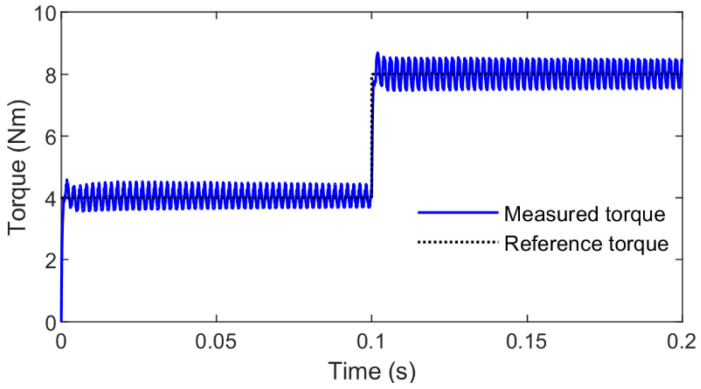

Fig. 5.34 Torque-variant dynamic procedure under 3000r/min

5.6 Experimental validation of FTC techniques

5.6.1 Experimental platform

Table 5.6 Main control parameter of the machine

Parameters	Numerical value
Power Rating	4.3kW
Rated speed	3000r/min
Rated frequency	200Hz
Rated torque	13.6Nm
Rated current	3.87A
Rated voltage	415V

In order to verify the effectiveness of the one-phase open-circuit FTC method based on normal decoupled transformation and the harmonic reference current control method, an experimental platform for a dual three-phase surface-mounted PMSM is constructed based on dSPACE-MicroLabBox, as shown in Fig. 5.35. The main control parameters of the applied dual three-phase surface-mounted PMSM is given in Table 5.6. During the experiment, the load machine operates under the speed mode while the dual three-phase machine operates under the torque mode accordingly. The dSPACE-MicroLabBox package Controldesk software is used to control the dual three-phase surface-mounted PMSM and acquire measured data, of which the real-time interface is shown in Fig. 5.36.

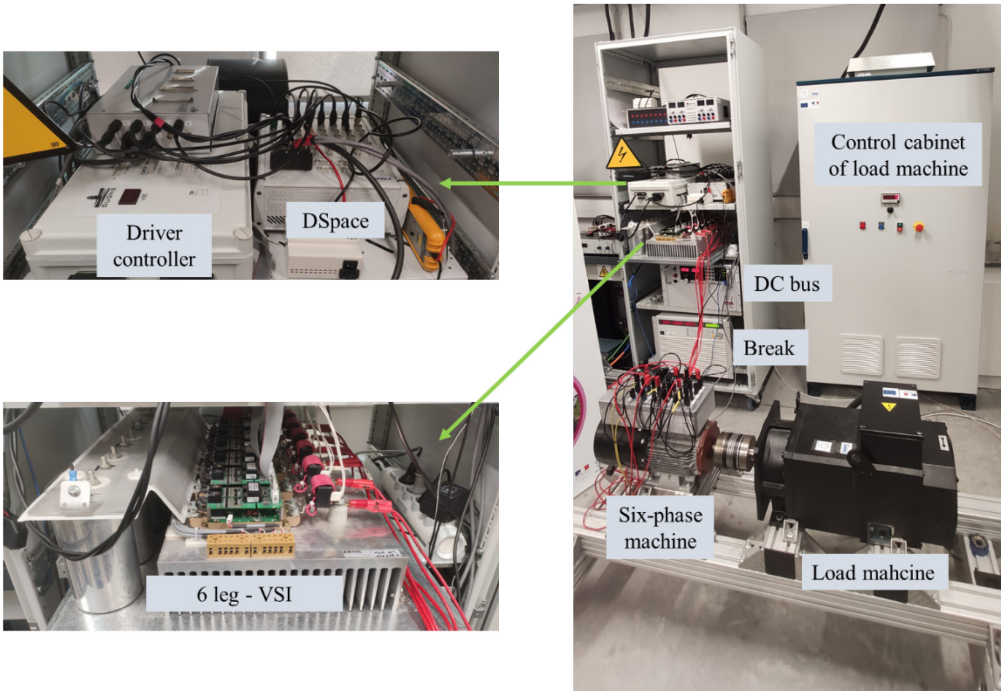

Fig. 5.35 Experimental platform for the dual three-phase surface-type PMSM

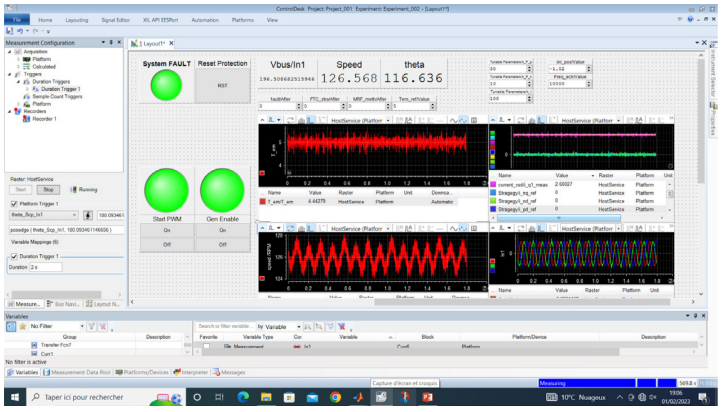

Fig. 5.36 The operation window of Controldesk

5.6.2 Experimental validation of the one-phase open-circuit FTC method

The proposed one-phase open-circuit FTC method based on normal decoupled transformation is first experimentally verified, by which the stable torque output can be achieved by reconfiguring the reference current in the decoupled frame. According to the different optimization objectives of FTC, two reconfiguration strategies of reference current based on the principle of MCL and the principle of MTOR are further obtained, but it has been demonstrated that the principle of MCL is characterized by superior FTC performance through the previous analysis for dual three-phase DS-HSDR-TFPMSM, thus only the FTC method based on the principle of MCL is experimentally verified in this section.

The speed of the load machine was set to 120 r/min and the output torque, machine speed, and the current in decoupled frame were measured during one dynamic cycle. The experimental process of one dynamic cycle was as follows: the dual three-phase machine started with a reference torque of 9.5Nm at t=0s; the corresponding switching device of winding phase A2

was disabled to simulate a one-phase open-circuit fault condition and the current strategy derived under normal operation was applied at t=20s; the FTC method was utilized to reconfigure the reference current at t=40s.

The measured torque waveforms during one dynamic cycle are shown in Fig. 5.37. It can be seen that the torque ripple increases significantly while the machine starts to operate under the fault condition, and then the torque ripple is effectively suppressed by using the FTC method. The torque performance in each stage is compared in Table 5.7. It can be found that the torque ripple under fault condition using reconfigured current strategy is the same as that under the normal condition, and thus the effectiveness of the FTC method is verified.

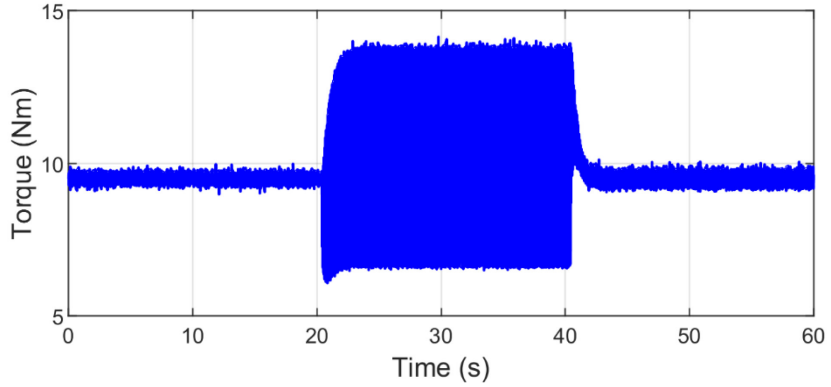

Fig. 5.37 Torque measuring waveform during one dynamic period

Table 5.7 Comparison of the torque characteristics in each status

	Average torque (Nm)	Torque ripple (%)
Normal condition	9.50	10.33
Fault condition	9.50	79.55
Fault tolerant condition	9.50	10.26

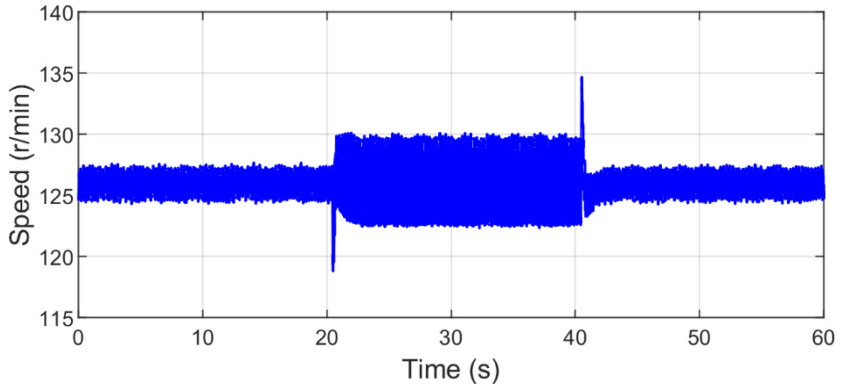

Fig. 5.38 Speed measuring waveform in one dynamic period

The measured speed waveform is shown in Fig. 5.38 during one dynamic cycle. It can be seen that the machine speed is continuously maintained at 126 r/min, and the speed fluctuation increases when the operation transition from normal condition to the fault condition. And then the speed fluctuation is effectively suppressed through the reconfiguration of the reference current using the FTC method. It can be seen that the speed fluctuation of the system under fault condition recovers back as in the normal condition by using FTC method.

Table 5.8 Comparison of the speed characteristics in each status

	Average speed (r/min)	Speed fluctuation (%)
Normal condition	126	2.65
Fault condition	126	6.15
Fault tolerant condition	126	2.53

The measured current waveforms in decoupled frame under different conditions are shown in Fig. 5.39. The measured i_{pq} waveforms remain basically unchanged, thus achieving a smooth torque output; the waveforms of i_{pd} and i_{nq} are consistent with the main component being the second harmonic while the waveform of i_{nd} mainly consists of the DC component and the second harmonic component. It can be concluded that the measured current waveforms in decoupled frame are consistent with the derived calculation results.

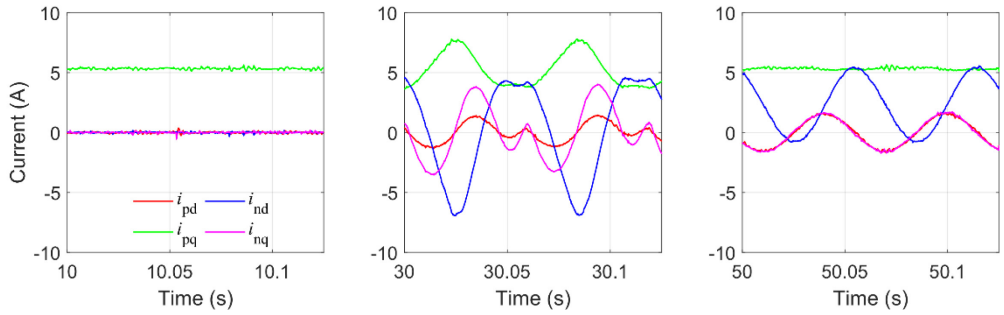

(a) Normal condition (b) Fault condition (c) Fault tolerant condition

Fig. 5.39 Winding current waveform in the decoupled frames under different operation conditions

5.6.3 Experimental validation of harmonic reference current control method

The MRF-based as well as PR-based harmonic current control methods are proposed to achieve the accurate control for the reconfigured reference current of dual three-phase PMSM under high-speed fault condition. Based on aforementioned analysis, it has been concluded that the MRF-based harmonic current control method is characterized by a smaller torque ripple.

Thus, the MRF-based harmonic current control method is experimentally verified. Due to the maximum output voltage constraint of the DC bus power supply, experiments were performed at the speed of 1500r/min. The reference torque of dual three-phase machine is set to 6Nm. The dual three-phase machine was started under one-phase open-circuit condition at t=0s, utilizing the FTC method. The MRF-based harmonic current control method was employed at t=30s. The output torque of the dual three-phase machine and the current in decoupled frame were measured throughout the experiment.

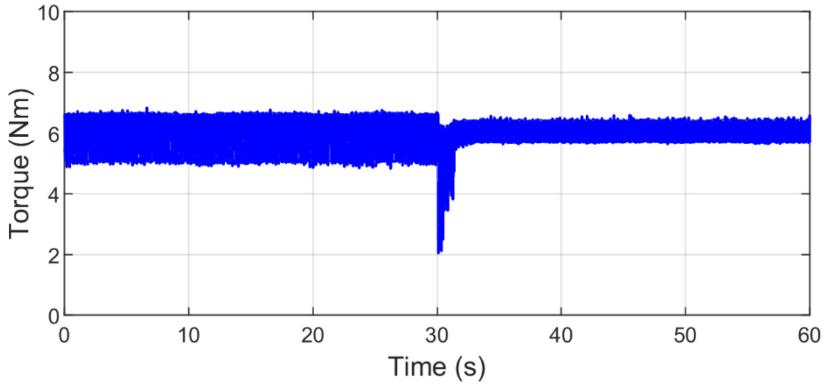

Fig. 5.40 Torque waveform in the validation experiment for the MRF-based method

The measured waveform of output torque is shown in Fig. 5.40. The torque performance before and after using the MRF-based control method are compared in Table 5.9. It can be concluded that the torque ripple under high-speed fault condition of the dual three-phase PMSM can be effectively suppressed using the MRF-based control method.

Table 5.9 Comparison of the torque performance through using MRF-based method

	Average torque (Nm)	Torque ripple (%)
Traditional PI control	6.09	30.75
MRF-based method	6.05	14.22

The tracking condition of the current i_{nd} in the decoupled frame before and after using the MRF-based control method is shown in Fig. 5.41, where the green line is the actual measured waveform while the purple line is the calculated reference waveform. It can be found that the current tracking effect is significantly improved by using the MRF-based control method.

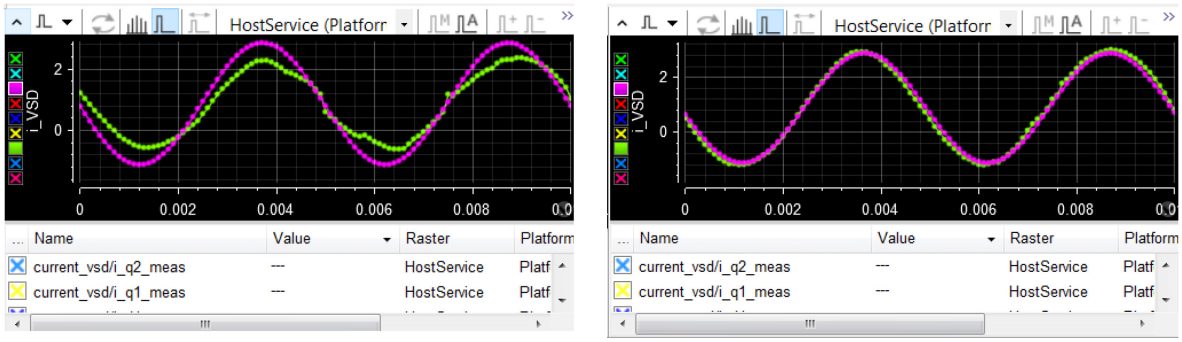

(a) Conventional PI control (b) MRF method

Fig. 5.41 Comparison of the i_{nd} tracking condition in the validation experiment for MRF method

5.7 Conclusion

In this chapter, the FTC technology of dual three-phase PMSM is investigated to satisfy the requirements of industrial robot electric drive for high functional reliability. The main research work and conclusions are as follows:

(1) The mathematical model of the dual three-phase PMSM and the vector control model are investigated. Firstly, the mathematical model of the dual three-phase PMSM in the natural frame is established. Subsequently, the mathematical model in the decoupled frame is obtained by the investigation of the vector space decomposition transformation, which eliminates the coupling between the phase windings and the time-variability of the controlled state vector. Finally, vector control model for the non-salient dual three-phase PMSM is constructed based on EMR method considering the yokeless rotor structure characteristics of the dual three-phase DS-HSDR-TFPMSM.

(2) One-phase open-circuit FTC method based on normal decoupled transformation is investigated. Firstly, the FTC methods based on the principle of MCL and MTOR are proposed under phase current constraint on amplitude according to different FTC optimization objectives. Then, the performance of proposed FTC method is compared with traditional DETW fault tolerant method, and it can be concluded that the advantage of the FTC method based on the principle of MCL is more prominent, by which the copper loss is significantly reduced under fault condition. Finally, the effectiveness of the proposed FTC method is validated through the simulation analysis of the dual three-phase DS-HSDR-TFPMSM under one-phase open-circuit condition.

(3) The harmonic reference current control methods are investigated. The MRF-based and PR-based harmonic reference current control method are investigated to improve the torque performance of the dual three-phase PMSM under high-speed fault condition. By applying the above two harmonic current control methods to the simulation analysis of FTC under high-speed condition of dual three-phase DS-HSDR-TFPMSM, it is concluded that the MRF-based method is characterized by a better suppression effect on the torque ripple.

(4) The fluctuation of the total axial force on the rotor of the shift model is much higher than that of the no shift model, especially operating under the fault condition. Although the FTC strategy can greatly reduce the axial force on the rotor of the shift model, its influence on the vibration and noise still exists. In addition, the breaking possibility of the PMs of the shift model is much higher according to the synthetic axial stress distribution diagram. Considering the axial stress is the crucial indicator for the mechanical safety of the proposed DS-HSDR-TFPMSM, the no shift model is the best choice.

(5) The experimental platform for a surface-mounted dual three-phase PMSM is built, and then the effectiveness of the proposed FTC techniques is verified through experiments.

Chapter 6. Prototype fabrication and experimentation

DS-HSDR-TFPMSM proposed in the thesis combines the advantages of compact structure and low moment of inertia. However, as a new type of structural machine, there is no complete fabrication process for DS-HSDR-TFPMSM, limiting its prototype development and subsequent mass production. Given the above condition, the existing prototype development technologies in axial flux PMSM[50] and separated armature structure TFPMSM is referred to develop the fabrication technologies of DS-HSDR-TFPMSM [46]. In addition, the structural strength of DS-HSDR-TFPMSM is investigated and assessed, and the performance of DS-HSDR-TFPMSM is finally verified through prototype experiments.

6.1 Research on fabrication technologies

To ensure the structural strength and assembly accuracy of DS-HSDR-TFPMSM prototype, the following issues should be considered in the study of its fabrication process.

1) DS-HSDR-TFPMSM also can be seen as an axial flux motor due to its axial magnetic field in the air gaps. Thus, the asymmetry between two air gaps is a critical problem which lead to bearing fatigue, noise and higher mechanical losses. In order to prevent above conditions, the dimension chain of total mechanical structure of DS-HSDR-TFPMSM should be calculated precisely and the bearings with smaller axial clearance should be selected.

2) There are 12 segmented stator cores of each stator disk. A suitable method should be adopted by which these 12 cores can be positioned accurately and fixed together.

3) The rotor of DS-HSDR-TFPMSM adopts yokeless structure and consists of two layers PMs along radial direction. The PMs need to be embedded in rotor disk and positioned not only along circumferential direction but also radial direction.

6.1.1 Fabrication technology of stator

The stator of DS-HSDR-TFPMSM consists of two parts named front and back stator respectively and both of them are assembled in same construction method.

Fig. 6.1 shows the assembly method of single stator core. The Si-steel sheet used to compose stator body is punched to an asymmetric C-shape one end of which is a convex shape. The stator shoe is molded with a rectangular opening by which the stator shoe and body are combined together. Obviously, this combination method is also effective for positioning. Owing to the fact that the stator shoe is made by SMC material whose strength is lower than Si-steel, the opening on the shoe should be slightly larger than the convex of stator body to prevent the breakage of SMC material. Through above method, the combination between these two components is not firm enough and it will be strengthened furtherly through the whole assembly of stator in next step. The single assembled stator core is shown in Fig. 6.2.

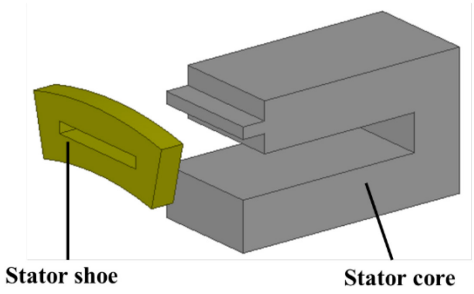

Fig. 6.1 Assembly diagram of single stator armature

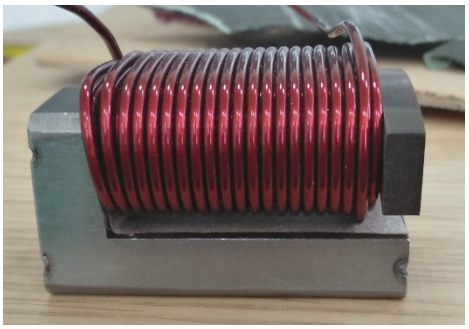

Fig. 6.2 Physical diagram of stator armature

The stator disk of DS-HSDR-TFPMSM is assembled in four parts: the front support plate, the stator disk, the rear support plate and the machine housing. The front support plate is in direct contact with the air gap of the electric machine and is therefore directly affected by the strong magnetic field, so it needs to be made of non-metallic materials to avoid the generation of eddy currents.[50] The front support plate is made of polyether ether ketone (PEEK). In addition, although the rear support plate in Fig. 6.3 is far away from the air gap magnetic field, it is connected to the adjacent stator core. So, the rear support plate should be made of non-permeable material to avoid the magnetic field coupling between the stator cores through it. During the assembly of the stator disk, the assembled stator armatures are firstly inserted into the openings of the front support plate one by one. Then, the rear support plate is pressed on the left terminal of the stator disk. Finally, the assembled stator disk which has been fixed with the support plates is put into the machine housing.

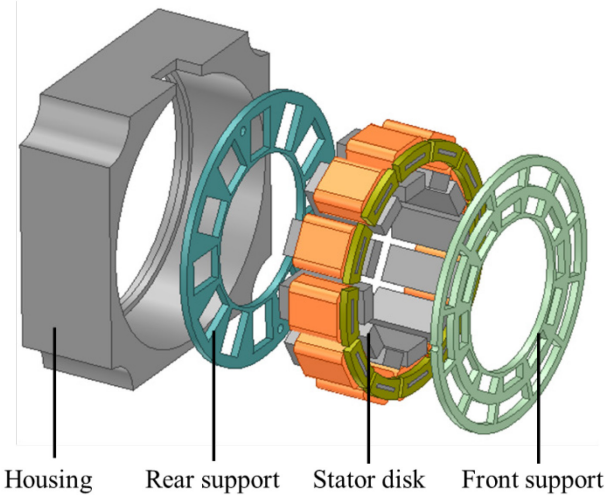

Fig. 6.3 Assembly diagram of stator disk

Nevertheless, it is unreliable to fix the stator disk by using of only two supports. To ensure the structure firmly enough, a gum injecting procedure is applied. This procedure requires corresponding tools by which the whole stator is sealed, and two holes are opened on back support used to inject gum and exhaust respectively. One type of epoxy resin, LORD EP 2000, is selected as the gum injecting material which combines advantages of high strength and well thermal conductivity after curing [50]. Meanwhile, the gum will fill the gap between stator body and stator shoe, so the structure of stator core can be strengthened in this way. Fig. 6.4 shows the stator after assembly, gum injecting and machining.

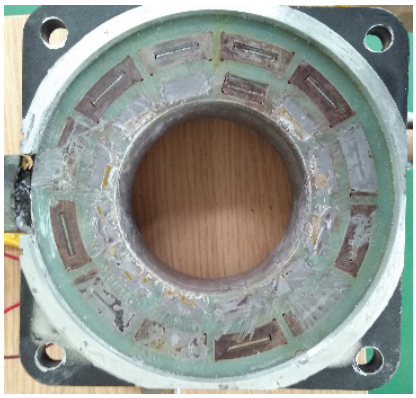

Fig. 6.4 Physical diagram of stator after gluing process

6.1.2 Fabrication technology of rotor

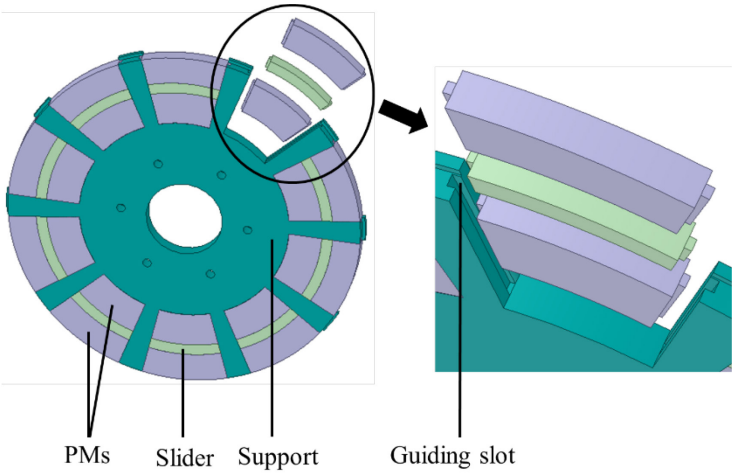

Fig. 6.5 Assembly diagram of rotor disk

Fig. 6.6 Physical diagram of rotor disk

In order to ensure two layers PMs along radial direction fixed firmly and accurately, a construction method is introduced shown in Fig. 6.5. The rotor disk mainly includes PMs, sliders and support, the latter two components are made by aluminum alloy considering its high strength and low weight. The non-magnetic sliders between each adjacent PMs along radial direction aim to separate these two PMs and position the outer PMs. It can be seen that a type

of convex structure is designed on both sides of PMs and sliders by which the PMs and sliders can cooperate with a guide slot. In the assembly process of rotor disk, the inner PM, slider and outer PM are inserted into support in order. And a ferrule made by aluminum alloy is mounted on the outside of support as a final step. Eventually, all PMs are fixed and positioned on support along the axial direction by the guide slots and along radial direction by sliders and ferrule. The assembled rotor disk is shown in Fig. 6.6.

6.1.3 Assembly method

The whole construction of DS-HSDR-TFPMSM is shown in Fig. 6.7. The rotor disk, rotor of break, encoder and two bearings are connected by a shaft. Fig. 6.8 presents a motor opening at the junction of front and back stator. All wires inner motor except encoder are drawn from this opening and integrated into a distribution box. The armature winding of both stators are in series through the connection of terminals belonging to same phase. In addition, the air gap can be utilized to check the size and symmetry of the air gap.

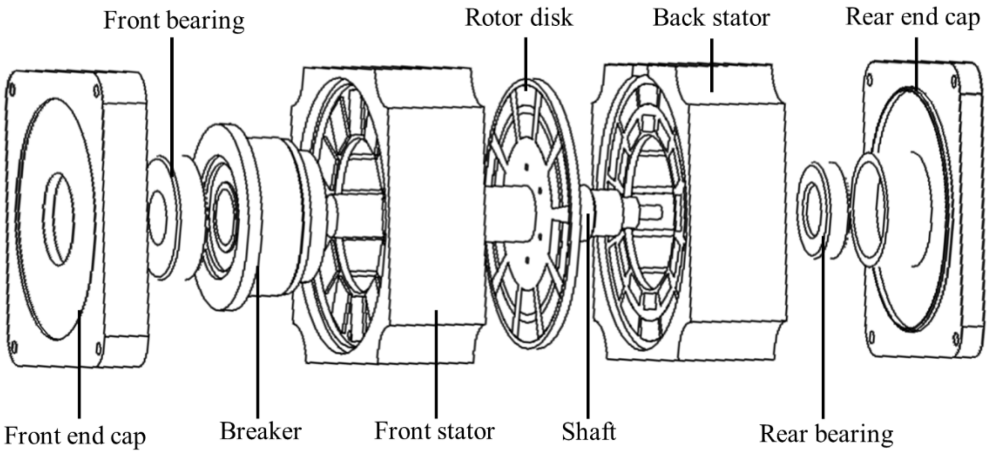

Fig. 6.7 Exploded view of the overall structure of DS-HSDR-TFPMSM

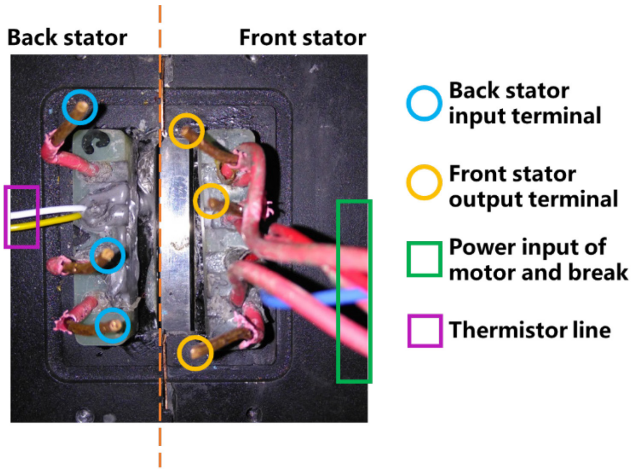

Fig. 6.8 Wiring diagram of DS-HSDR-TFPMSM

6.2 Structural strength assessment

6.2.1 Stator assessment

During the process of motor operation, a large stress will be exerted on stator shoes. In order to prevent SMC material breaking, the strength of SMC material should be validated. Fig. 6.9 shows the stress and strain diagram of stator shoes under double current overload condition. It can be seen from the analysis results that the maximum stress on all 24 stator shoes is 0.524 MPa which is far below the tensile yield strength of SMC material, moreover, the maximum deformation is only 1.14e-4 mm. Thus, it is safe for stator shoes made by SMC material.

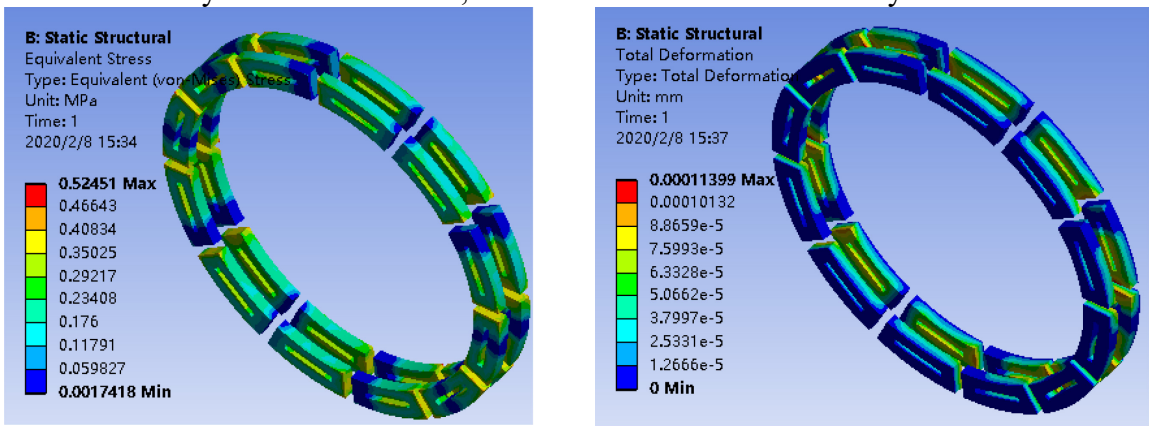

(a) Stress distribution (b) Strain distribution

Fig. 6.9 Stress and strain distribution of stator shoes

6.2.2 Rotor assessment

Under a high rotation speed and load condition, the rotor disk may be deformed to some extent which leads to an asymmetrical air gap and damages the PMs. Therefore, the stress and strain analyses are also crucial for rotor disk. Fig. 6.10 shows the stress and strain diagram of rotor disk under double current overload and 3000 rpm condition. The maximum stress and deformation on rotor disk are 6.553MPa and 1.95e-4 mm that are both safe for operation.

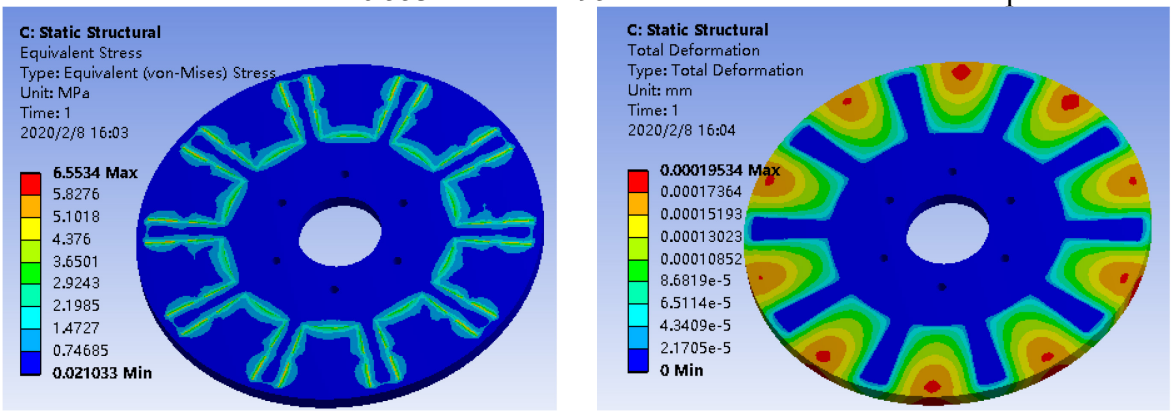

(a) Stress distribution (b) Strain distribution

Fig. 6.10 Stress and strain distribution of rotor disk

6.2.3 Methodologies for preventing axial movement of rotor

The axial movement of rotor is a critical problem that will lead to bearing fatigue, noise and higher mechanical losses. In order to prevent above conditions, the mechanical design shown in Fig. 6.11 is adopted. The front bearing is fixed axially in the closed chamber composed of the end cover and the brake stator, thus the possibility of axial movement of the

bearing is effectively avoided. The brake rotor is connected to the shaft and its front end is located on the surface of the inner ring of the bearing. The circlip is put on the groove of the shaft as shown in the blue box of Fig. 6.11 after the shaft is inserted into the inner ring of the bearing. Finally, the positioning with the front bearing is achieved and the axial movement of the shaft is avoided eventually.

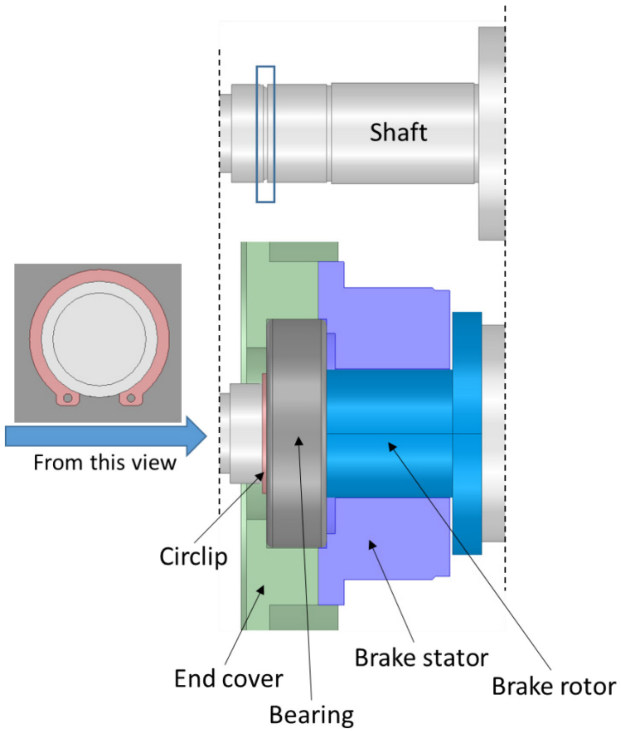

Fig. 6.11 Schematic diagram of shaft positioning

Through the methods as mentioned above, the motor shaft and the inner ring of bearing are fixed together. However, there is generally an axial clearance problem existed in a rolling bearing. While the bearing is subjected to a certain degree of thrust or tension, the inner ring of bearing will be axially displaced relative to the outer ring. Therefore, the impact on the shaft during the installation of the motor should be avoided. At the same time, bearings with smaller axial clearance can be considered for use. The maximum bearing clearance used in this design is 0.2 mm. And the electromagnetic performance of HSDR-TFPM considering 0.2 mm axial displacement of rotor is simulated and it is proved to be consistent with the results obtained while the air-gap is symmetrical.

Large stress is exerted on the stator and whole rotor during the operation. In order to validate the structural strength of the motor, the stress and strain analysis is carried out under the following extreme conditions: the motor is working at rated speed, input 2 times the rated current, and axial displacement of rotor is set to the maximum bearing clearance. Fig. 6.12(a) shows the deformation of the electromagnetic body (including the shaft) of the motor obtained by FEM. The deformation of the motor mainly occurs in the rotor part, and the maximum deformation reaches 0.0216 mm. Thus, the rotor part needs to be furtherly analyzed.

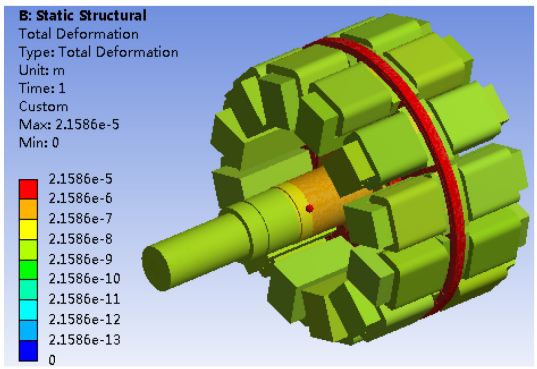

(a) Strain distribution of the electromagnetic part

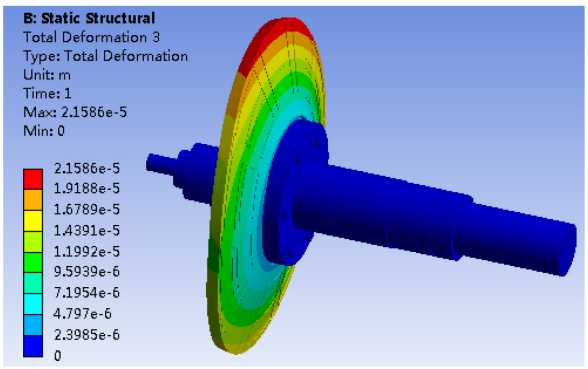

(b) Strain distribution of the rotor

Fig. 6.12 Structural strength validation of DS-HSDR-TFPMSM under the condition of movement of rotor

Fig. 6.12(b) shows the deformation condition of the rotor magnified by 1000 times. It can be seen that the deformation on rotor disk is most apparent, and the rotor is shifted backward along the axial direction. It is not difficult to understand that the distance between the back stator and the rotor disk is smaller than another side after the movement, thus the magnetic field stress on backside of rotor is more significant. Compared with the steel shaft, the strength of aluminum alloy and permanent magnet materials is lower, so it is necessary to validate the strength of the aluminum alloy material and the PMs during extreme condition. The comparison of the maximum stress of each part with the corresponding material strength is given in Table 6.1. It can be concluded that the strength of the rotor structure meets the requirements under extreme conditions.

Table 6.1 Structural strength validation of the rotor under the condition of 0.2mm axial movement

Materials	Maximum stress	Tensile strength	Yield strength
Aluminum alloy	21.3 MPa	205 MPa	228 MPa
PMs (NdFeB)	4.7 MPa	85 MPa	270 MPa

6.3 Prototype experiments

6.3.1 Introduction of experimental platform

DS-HSDR-TFPMSM prototype experimental platform is shown in Fig. 6.13. The eddy current brake is used to generate the load torque during the experiment. The servo driver developed by SINOMACH is used to control and drive the prototype DS-HSDR-TFPMSM. The servo driver communicates with the IPC through Ethernet to receive control signals and feedback internal data of the driver in real time. The torque sensor and power analyzer communicate with the IPC through RS485 to record the measurement data during the experiment.

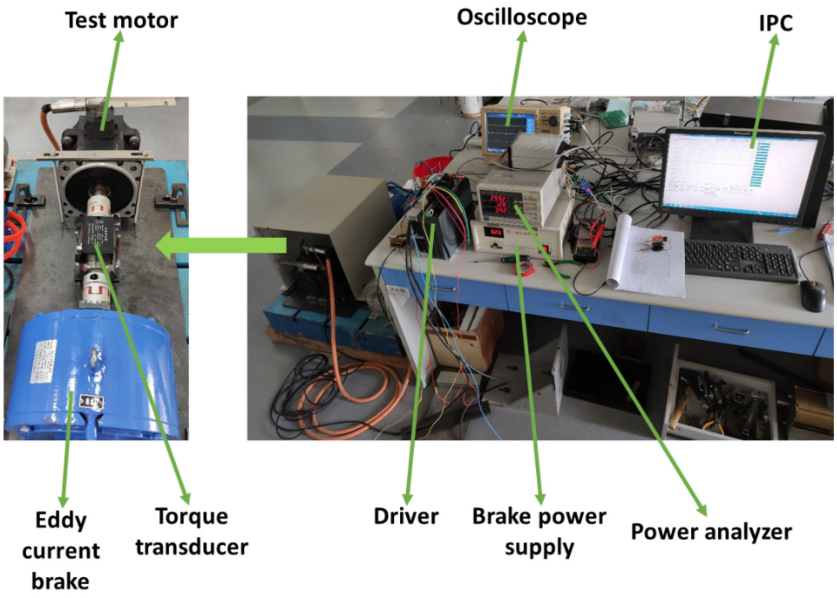

Fig. 6.13 Prototype experimental platform of DS-HSDR-TFPMSM

6.3.2 No load experiment

Firstly, DS-HSDR-TFPMSM prototype was dragged to the rated speed using the prime motor for no load power generation experiment, and the no load back-EMF of the prototype was measured. The measured results were compared with the calculation results of the Schwarz-Christoffel transformation method and the FEM, as shown in Fig. 6.14. It can be seen that the experimental results are consistent with the calculated results of electromagnetic analysis, and the manufacturing of the prototype is certified to meet the design requirements.

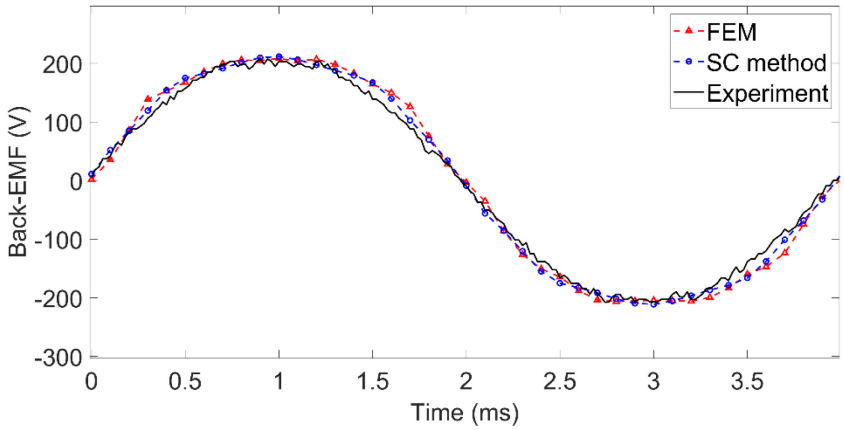

Fig. 6.14 No load back-EMF waveform of DS-HSDR-TFPMSM prototype under rated speed

In order to verify the adaptability of the controller to the DS-HSDR-TFPMSM prototype, the starting and stopping process of the prototype machine under no load condition was tracked and tested, during which the driver controlled the electric machine to accelerate to 3000r/min and then gradually decelerate to stop. The starting and stopping time was set to 2s. Fig. 6.15 shows the speed variant condition and current signal variant curve detected by the IPC. Fig. 6.16 shows the current envelope during dynamic process measured by the oscilloscope. The experimental results show that the servo driver selected can control DS-HSDR-TFPMSM prototype as required.

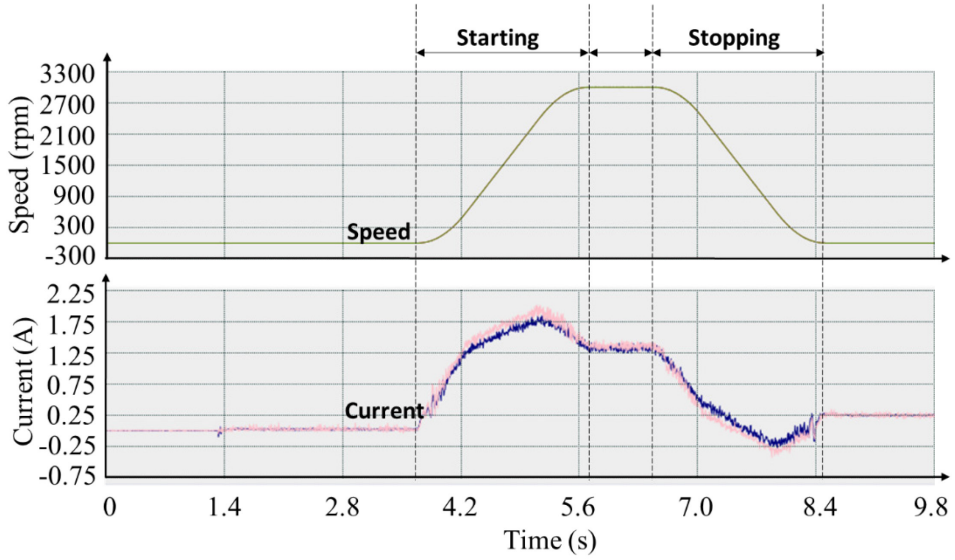

Fig. 6.15 Position and current tracking curves of machine

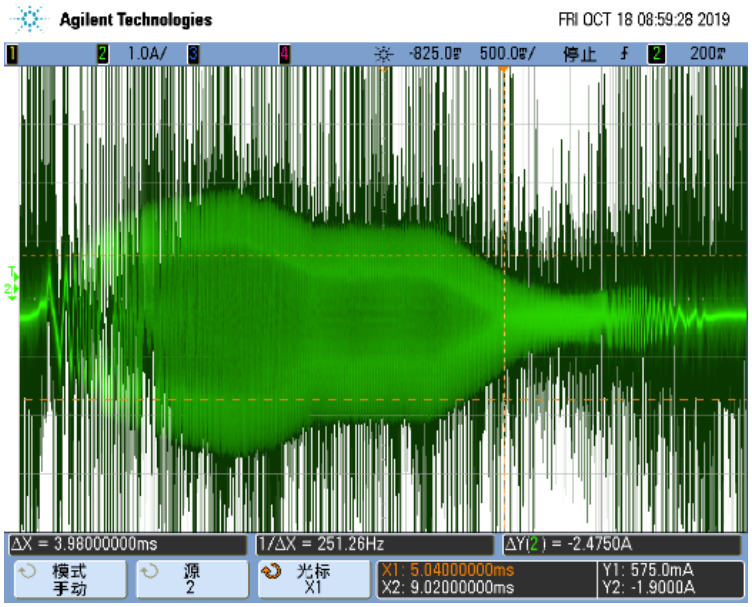

Fig. 6.16 Envelope curve of current

6.3.3 Load experiment

DS-HSDR-TFPMSM prototype was fed with 12.5A rated current at 3000r/min, and the output torque waveform obtained is shown in Fig. 6.17. The average value of output torque is 16.5Nm, and the torque ripple is 9.93%. It can be found that the torque experimental result is slightly lower than the design requirement of 17.2Nm. The error is mainly due to the fact that the calculated torque value obtained during the electromagnetic design and simulation analysis of the machine is the electromagnetic torque, while the electromagnetic torque cannot be measured directly in the prototype experiment, and the measurement results are affected by mechanical losses and various additional losses.

By using the I_d =0 vector control method, the correspondence between the average value of measured output torque and the RMS value of the phase current shown in Fig. 6.18 is obtained. It can be seen that the output torque and input current do not fully comply with the linear relationship. The main reason is that the silicon steel sheet was chamfered to ensure that

the armature coil could be easily nested on the stator core during the prototype fabrication, resulting in a decrease in the core cross-sectional area and an increase of saturation degree in stator core.

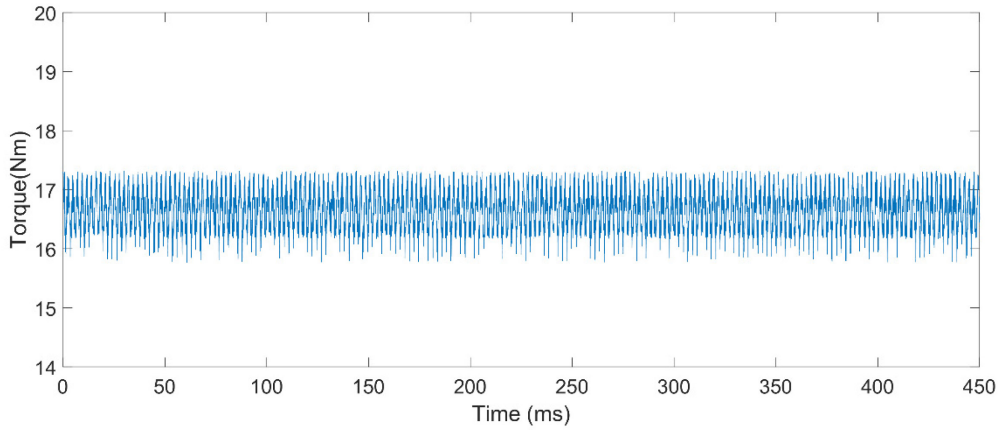

Fig. 6.17 Output torque waveform under rated current

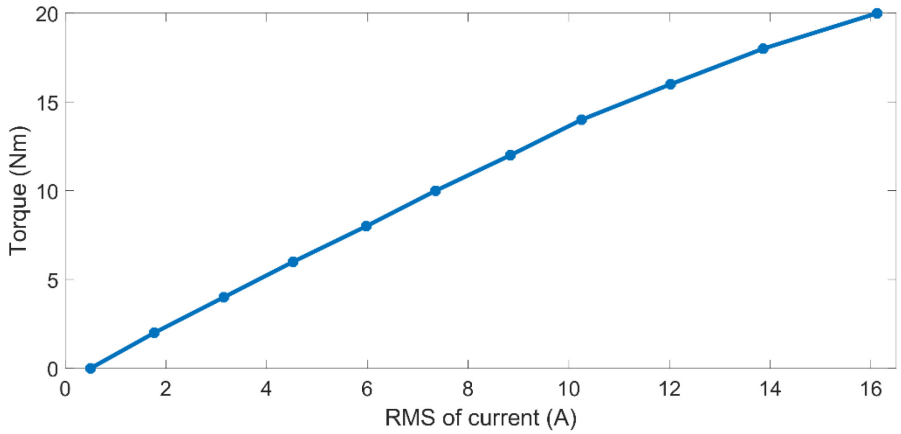

Fig. 6.18 Torque-current curve

6.4 Comparative experimental study

6.4.1 Comparison of basic size and performance

Based on the experimental results of the prototype DS-HSDR-TFPMSM, a same-power commercialized RPMSM is selected for comparative experimental study. Fig. 6.19 shows the comparison of the appearance of the two machines. Table 6.2 further gives the comparison of the basic dimensional and performance parameters of the two machines. It can be seen that DS-HSDR-TFPMSM prototype combines obvious advantages, with a 40.8% reduction in axial length and 21.9% weight reduction, in addition, its moment of inertia is reduced by 54.2%, thus providing better dynamic performance.

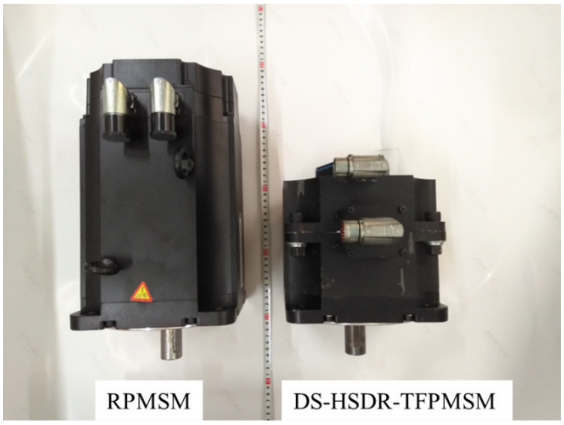

Fig. 6.19 Comparison between DS-HSDR-TFPMSM prototype and commercialized RPMSM

Table 6.2 Comparison of performance and size

	DS-HSDR-TFPMSM	RPMSM
Rated voltage	300V	336V
Rated current	12.5A	10.3A
Rated speed	3000 rpm	
Rated torque	16.5 Nm	
Insulation grade	F	
Cooling method	Natural	
Total axial length	190 mm	308 mm
Outside diameter	190 mm	
Weight	22.8 Kg	28 Kg
Moment of inertia	34.76 Kgcm^2	76 Kgcm^2

6.4.2 Comparison of rated torque

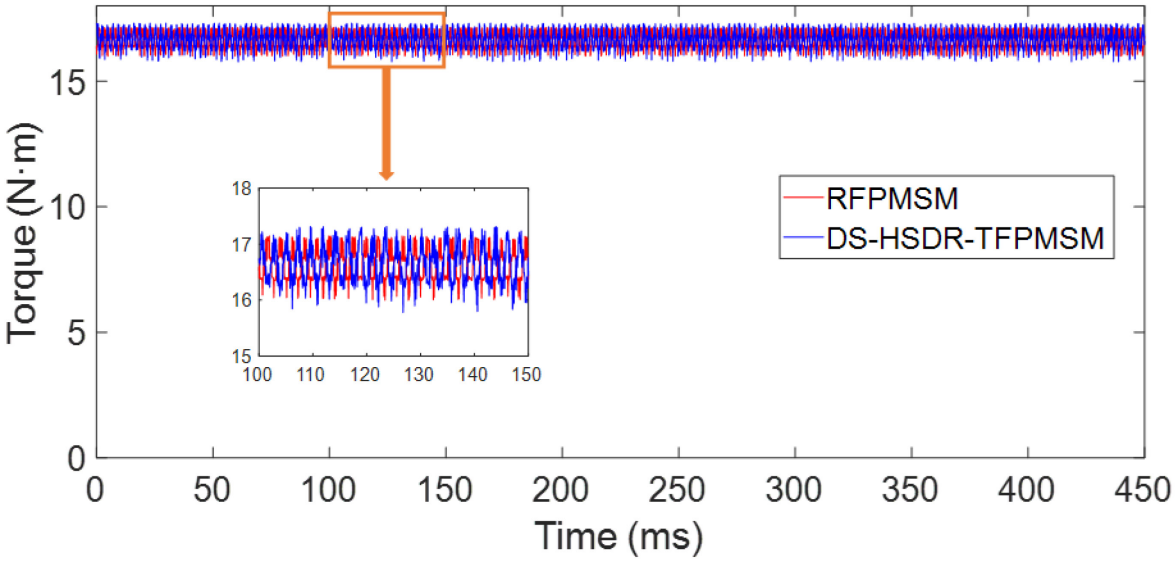

Fig. 6.20 Comparison on the waveforms of rated torque

Fig. 20 shows the comparison of output torque waveforms at rated operating state. As can be seen, the torque average is 16.5Nm of both machine while the torque ripple of HSDR-TFPM is relatively higher than RPMSM. The aforementioned issue can be further addressed by utilizing the design parameters obtained through the optimization design given in Chapter 4.

6.4.3 Comparison of dynamic performance

The dynamic characteristics of both motors are evaluated through the test during one dynamic process. The complete dynamic process is described as follows: the motor starts under no load condition at t=0s; the half load (8.25N·m) is suddenly added at t=10s; the half load is removed at t=20s; the full load (16.5N·m) is suddenly added at t=60s and finally the load is removed at t=80s. The speed and phase current of SPMSM as well as DS-HSDR-TFPM are recorded during the dynamic process, as shown in Fig. 6.21.

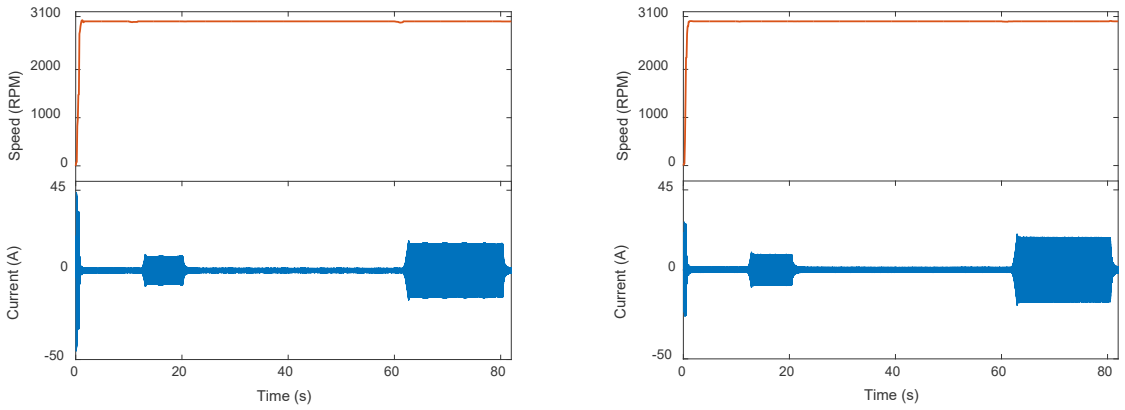

(a) RPMSM (b) DS-HSDR-TFPMSM

Fig. 6.21 Comparison of the total dynamic process

In order to compare the dynamic characteristics of the test motors more clearly, the dynamic waveforms of the starting process and the process of adding full load are extracted, as shown in Fig. 22 and Fig. 23 respectively. The starting time of the two motors is set to the same, and the starting current can be used for comparison. Table 6.3 shows the characteristic parameters of the starting process. It can be concluded that the starting current of DS-HSDR-TFPM is greatly reduced. Thus, the energy consumption of DS-HSDR-TFPM is lower during the starting process, and that is crucial for industrial robots that need to start servo motors frequently during operation. During the process of adding full load shown in Fig. 6.23, DS-HSDR-TFPM takes 1.2s to re-enters the steady-state and its speed dropped to 2993RPM at the lowest, while SPMSM needs 1.5s to re-enters the steady-state and its speed dropped to 2972RPM at the lowest. In summary, it is proved that the dynamic performance of DS-HSDR-TFPM is more superior.

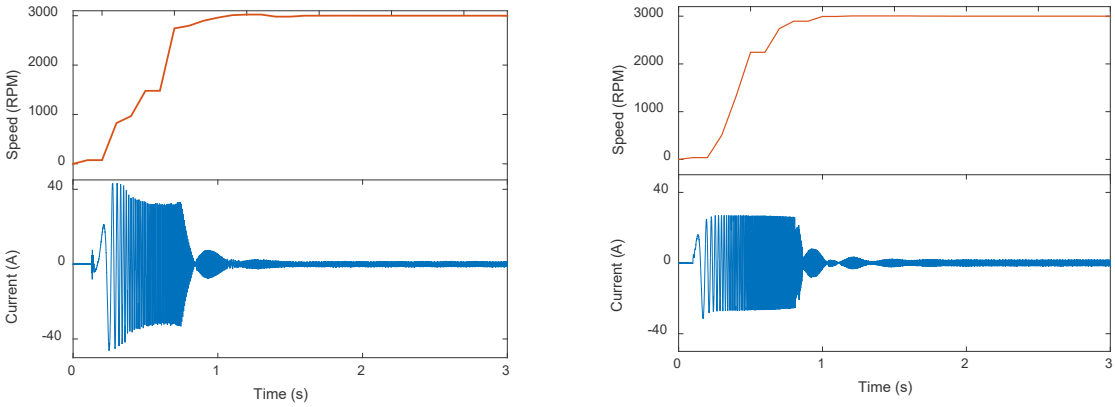

(a) RPMSM (b) DS-HSDR-TFPMSM

Fig. 6.22 Comparison of the starting dynamic process

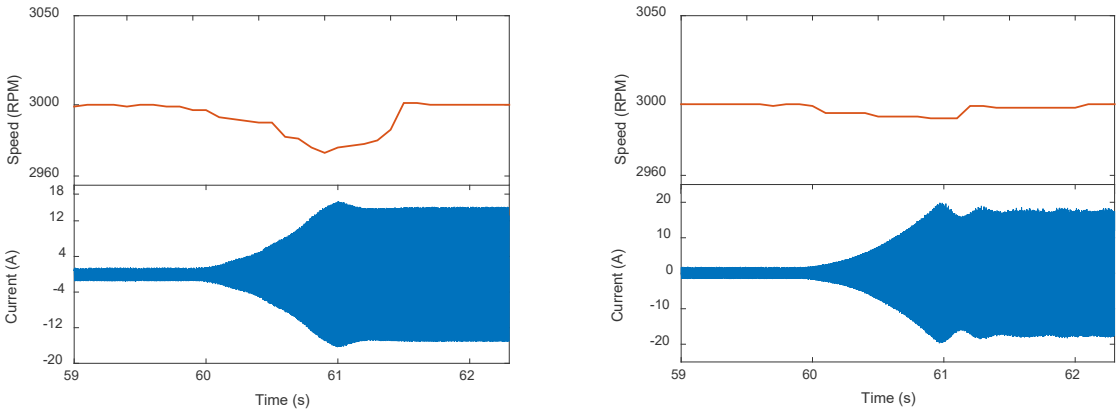

(a) RPMSM (b) DS-HSDR-TFPMSM

Fig. 6.23 Comparison of the dynamic process under adding rated load condition

Table 6.3 Comparison of starting characteristics during starting process

	Start time	Starting current
RPMSM	1.1s	43.6A
DS-HSDR-TFPMSM	1.1s	25.3A

6.4.4 Comparison of efficiency

The efficiency of motors is tested under rated speed as shown in Fig. 6.24. It can be seen that the efficiency of RPMSM is higher than DS-HSDR-TFPM after load torque reaches 10N·m. The efficiency of SPMSM at rated operating state is 92.6% while it is 85.3% in DS-HSDR-TFPM.

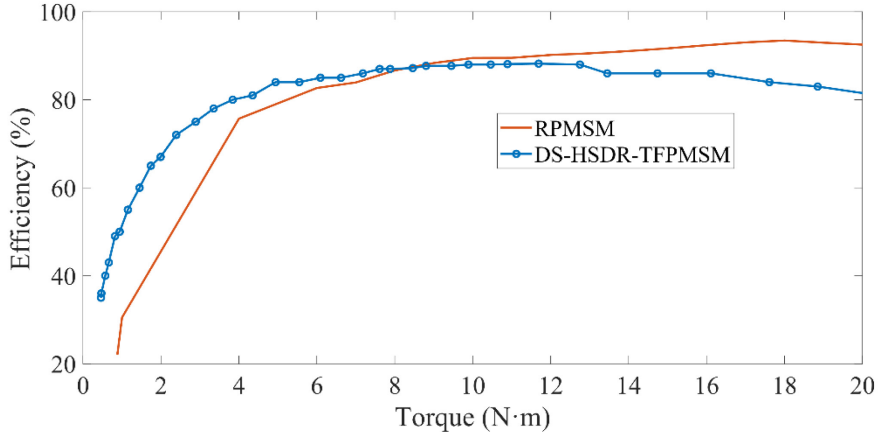

Fig. 6.24 Efficiency under rated speed

6.4.5 Comparison of temperature rise

Fig. 6.25 shows the temperature rise of both motors at rated operating state. It can be seen that the temperature rise in DS-HSDR-TFPM is higher than RPMSM. The main reasons are as follows. The volume of DS-HSDR-TFPM is smaller, so the heat exchange area is reduced compared with RPMSM. In addition, the copper loss of DS-HSDR-TFPM is much higher due to the high rated current density.

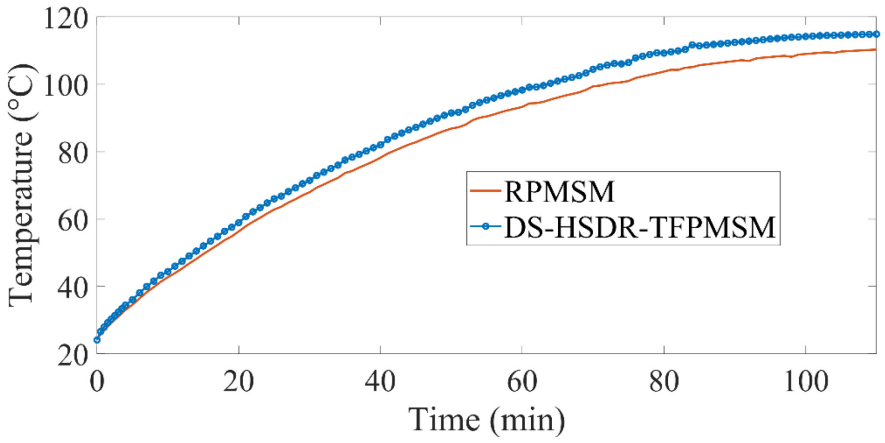

Fig. 6.25 Temperature rise at rated operating state

6.5 Conclusion

In this chapter, the fabrication technologies of DS-HSDR-TFPMSM prototype were investigated and the experimental research was conducted, and the main research work and conclusions are as follows:

(1) The fabrication and assembly process of DS-HSDR-TFPMSM is summarized, and its structural strength is assessed. The stator disk of DS-HSDR-TFPMSM is positioned by the front and rear support plates and its structural strength is enhanced by the glue filling operation. The rotor PMs are positioned and fixed by the "convex" structure and the guiding slot. Finally, the structural strength of DS-HSDR-TFPMSM was validated by assessing the structural strength of the SMC stator shoe and the yokeless disk-type rotor.

(2) The axial movement of rotor and corresponding prevention methodology was investigated. The positioning and fixing of the front bearing as well as the rotor shaft were achieved by using the rotor shaft positioning method. Given that the axial clearance of the rolling bearing will make the air gap on the two sides asymmetric, the stress-strain analysis is conducted for the DS-HSDR-TFPMSM model with axial movement of the rotor to verify. Finally, the structural strength of the machine complies with the requirements under extreme condition.

(3) DS-HSDR-TFPMSM prototype was experimentally studied. Through the measurement of the no-load back-EMF of the prototype and comparison with the results obtained by using the Schwarz-Christoffel transformation method and FEM, it can be concluded that the experimental results are in good agreement with the electromagnetic analysis, demonstrating that the prototype satisfies the design specifications. Furthermore, a commercial RPMSM with same power was chosen for a comparative experimental study. The results of the size and dynamic performance comparisons demonstrate the superior miniaturization and high dynamics of the DS-HSDR-TFPMSM.

General conclusions and Perspectives

General conclusions

As the crucial component of industrial robots, electric machines play an important role in addressing the requirements for miniaturization, high dynamics, high functional reliability and low torque ripple. Transverse flux permanent magnet synchronous machine (TFPMSM) combines the advantages of intrinsically high torque density, the ability to adjust the electromagnetic load independently, flexible structure design and simple winding structure, thus it possesses significant potential to be used as the PMSM in industrial robot. In addition, for transverse flux permanent magnet synchronous machine, a multiphase winding structure can be used to obtain advantage of fault tolerant ability, which furtherly improves the reliability of the electric drive in industrial robots. However, there are still shortcomings and limitations among the existing research on transverse flux permanent magnet synchronous machine and the research on fault tolerant of Multiphase machines, which limit their application in the context of the thesis. Aiming at above issues, the thesis investigates the design, analysis, and optimization of transverse flux permanent magnet synchronous machine for industrial robot applications, as well as its multiphase designs and FTC methods. The main research contents and obtained results are as follows.

1. A novel structure of disk-type transverse flux permanent magnet synchronous machine is proposed for the background of industrial robot application. Through a comparative analysis with RPMSM, it is concluded that DS-HSDR-TFPMSM has the advantages of compact structure and low moment of inertia, which helps to realize the miniaturization and high dynamics of the electric drives in industrial robots. By investigating the basic sizing equation, equivalent magnetic circuit design, slot\pole combination design, and stator core design methods, the preliminary design parameters of the 5.4kW DS-HSDR-TFPMSM are obtained. By studying the effect of the change of the pole-arc coefficient of both outer and inner PMs and the change of the pole-arc coefficient as well as thickness of the stator shoes on the output torque of the machine, the change of both torque average value and torque ripple of DS-HSDR-TFPMSM are obtained for each size parameter, which provides guidance for the reasonable selection of the design value. Based on the dual stator disk topology and the 10-pole/12-slot coordination of DS-HSDR-TFPMSM, two types of dual three-phase structure DS-HSDR-TFPMSM are obtained. By comparing the main performance of the two structures, it can be concluded that, under the condition that the same rated torque is output and other performance parameters are basically same, the dual three-phase DS-HSDR-TFPMSM with symmetrical structure benefits from a lower rated current, but the electrical connection between the front and rear stator disks resulting in the more complicated winding connection compared to the asymmetrical structure. A comparative study of the torque ripple of dual three-phase and three-phase DS-HSDR-TFPMSMs is proceeded, and it can be concluded that the dual three-phase DS-HSDR-TFPMSMs combine the advantage of low torque ripple.

2. The research on the air-gap magnetic field and performance analysis of DS-HSDR-TFPMSM using the Schwarz-Christoffel transformation method is proceeded. Firstly, the two-dimensional equivalent analytical model is obtained based on the axisymmetric and equipotential planes of DS-HSDR-TFPMSM. Then, it is simplified into a polygonal solution domain in the complex-plane analytical model. Finally, the polygonal solution domain is further mapped to the circular solution domain by the Schwarz-Christoffel inversion and conformal inversion. The Hague's equations are used to calculate the magnetic field intensity vector at any point in the circular solution domain, and the magnetic field distribution in the equivalent

polygon solution domain of DS-HSDR-TFPMSM is derived by inverse transformation. The performance such as no load back-EMF, cogging torque, and rated torque are further solved based on the calculation results of the air-gap magnetic field distribution. The accuracy of the Schwarz-Christoffel transformation method is validated by comparing the air-gap magnetic field distribution and performance calculated by the method with the FEM, in which a high agreement is proven. The comparison of the consumption computational resource between the two methods reveals that the Schwarz-Christoffel transformation method can save 90.9% of computational time and 88.4% of computational resources proving the efficiency of the Schwarz-Christoffel transformation method.

3. Optimization design method based on BP neural network and MOPSO is proposed to obtain the optimal design solution of DS-HSDR-TFPMSM. Firstly, the functional relationship between the optimization variables and the output torque performance of the DS-HSDR-TFPMSM was approximated using BP neural network. However, due to the disadvantage of the BP neural network falling into local optima during the training process, a genetic algorithm was used to optimize it. By comparing the computational error of the neural network before and after the optimization, the effectiveness of the genetic algorithm in optimizing the BP neural network was confirmed. Subsequently, the BP neural network is substituted into the MOPSO algorithm to obtain the Pareto optimal solution set and Pareto front of the multi-objective optimization design of DS-HSDR-TFPMSM. The proposed optimization design method was validated by comparing the output torque calculation results of the optimal solution obtained from the FEM with the results of initial design. The results show that the average value of the motor output torque increases from 17.26Nm to 17.83Nm, and the torque ripple decreases from 9.05% to 1.47%, which verifies the effectiveness of the proposed optimization design method. In addition, the accuracy of the BP neural network is verified by comparing the BP neural network approximating results of the optimal solution with the results obtained by FEM.

4. The FTC technology of dual three-phase PMSM is investigated to satisfy the requirements of industrial robot electric drive for high functional reliability. The mathematical model of the dual three-phase PMSM and the vector control model are investigated. Firstly, the mathematical model of the dual three-phase PMSM in the natural frame is established. Subsequently, the mathematical model in the decoupled frame is obtained by the investigation of the vector space decomposition transformation, which eliminates the coupling between the phase windings and the time-variability of the controlled state vector. Finally, vector control model for the non-salient dual three-phase PMSM is constructed based on EMR method considering the yokeless rotor structure characteristics of the dual three-phase DS-HSDR-TFPMSM.

The following research has been carried out on FTC of dual three-phase PMSM:

1) One-phase open-circuit FTC method based on normal decoupled transformation is investigated. Firstly, the FTC methods based on the principle of MCL and MTOR are proposed under phase current constraint on amplitude according to different FTC optimization objectives. Then, the performance of proposed FTC method is compared with traditional DETW fault tolerant method, and it can be concluded that the advantage of the FTC method based on the principle of MCL is more prominent, by which the copper loss is significantly reduced under fault condition. Finally, the effectiveness of the proposed FTC method is validated through the simulation analysis of the dual three-phase DS-HSDR-TFPMSM under one-phase open-circuit condition.

2) The harmonic reference current control methods are investigated. The MRF-based and PR-based harmonic reference current control method are investigated to improve the torque

performance of the dual three-phase PMSM under high-speed fault condition. By applying the above two harmonic current control methods to the simulation analysis of FTC under high-speed condition of dual three-phase DS-HSDR-TFPMSM, it is concluded that the MRF-based method is characterized by a better suppression effect on the torque ripple.

The fluctuation of the total axial force on the rotor of the shift model is much higher than that of the no shift model, especially operating under the fault condition. Although the FTC strategy can greatly reduce the axial force on the rotor of the shift model, its influence on the vibration and noise still exists. In addition, the breaking possibility of the PMs of the shift model is much higher according to the synthetic axial stress distribution diagram. Considering the axial stress is the crucial indicator for the mechanical safety of the proposed DS-HSDR-TFPMSM, the no shift model is the best choice.

Finally, the experimental platform for a surface-mounted dual three-phase PMSM was built, and the effectiveness of the proposed FTC techniques is verified through experiments.

5. The fabrication technologies of DS-HSDR-TFPMSM prototype were investigated and the experimental research was conducted. In terms of the fabrication: Firstly, the fabrication and assembly process of DS-HSDR-TFPMSM is summarized, and its structural strength is assessed. Then, the axial movement of rotor and corresponding prevention methodology was investigated. the positioning and fixing of the front bearing as well as the rotor shaft were achieved by using the rotor shaft positioning method. Finally, the stress-strain analysis was conducted for the DS-HSDR-TFPMSM model with axial movement of the rotor to verify proving that the structural strength of the machine complies with the requirements under extreme condition. In terms of the experiment: Through the measurement of the no-load back-EMF of the prototype and comparison with the results obtained by using the Schwarz-Christoffel transformation method and FEM, it can be concluded that the experimental results are in good agreement with the electromagnetic analysis, demonstrating that the prototype satisfies the design specifications. Furthermore, a commercial RPMSM with same power was chosen for a comparative experimental study. The results of the size and dynamic performance comparisons demonstrate the superior miniaturization and high dynamics of the DS-HSDR-TFPMSM.

Perspectives

The thesis primarily focuses on the design, analysis, and optimization of a new transverse flux PMSM structure, as well as fault-tolerant control technology for dual three-phase PMSMs. Although several innovative results have been achieved, limitations in the author's level and time have resulted in insufficient analysis in certain areas and some defects that must be addressed, as outlined below.

1. DS-HSDR-TFPMSM, as a transverse flux PMSM, combines a serious leakage issue, while partially mitigated by SMC stator shoes, leading to lower power factors and higher bus voltage requirements when compared to traditional RPMSMs. Therefore, methods to improve the power factor of DS-HSDR-TFPMSM need to be researched.

2. The analytical method used in the thesis, based on the Schwarz-Christoffel transformation, neglects the nonlinear saturation of the stator core material in the calculation of the magnetic field and performance of DS-HSDR-TFPMSM. As a result, this method is not suitable for calculating performance parameters under overload conditions, and further research

is needed to establish an efficient computational model considering material nonlinear saturation.

3. The MRF method used to track the harmonic reference current caused by fault-tolerant control in the thesis requires too many current PI controllers, increasing the complexity of the control system. Additionally, the use of a large number of LPFs in this method creates instability in the system. Further exploration is needed to develop a harmonic reference current tracking control method with fewer PI controllers or without LPF.

4. The modular design concept of the stator disk in DS-HSDR-TFPMSM offers the advantage of easy maintenance, making it easier to repair and replace a damaged stator armature core. However, the method used in the thesis requires the entire stator disk to be glued together after positioning and fixing, resulting in all the stator armature cores solidifying into one unit and creating difficulties for subsequent maintenance.

The thesis may contain errors and omissions due to the limitations of the author's abilities and knowledge. Constructive criticism and correction from experts, scholars, teachers, and students are greatly appreciated.

References

[1] J. Wallén, *The history of the industrial robot*. Linköping: Linköping University Electronic Press, 2008.

[2] L. Westerlund, *The extended arm of man: a history of industrial robot*. Stockholm: Informationsförlaget, 2000.

[3] Y.-H. Zhu and J. Jiao, "Automatic Control of Mobile Industrial Robot Based on Multiobjective Optimization Strategy," *Journal of Electrical and Computer Engineering*, vol. 2022, 2022.

[4] L. D. Evjemo, T. Gjerstad, E. I. Grøtli, and G. Sziebig, "Trends in smart manufacturing: Role of humans and industrial robots in smart factories," *Current Robotics Reports*, vol. 1, no. 2, pp. 35–41, 2020.

[5] A.-D. Pham and H.-J. Ahn, "High precision reducers for industrial robots driving 4th industrial revolution: state of arts, analysis, design, performance evaluation and perspective," *International journal of precision engineering and manufacturing-green technology*, vol. 5, no. 4, pp. 519–533, 2018.

[6] T. S. Mruthyunjaya, "Kinematic structure of mechanisms revisited," *Mech Mach Theory*, vol. 38, no. 4, pp. 279–320, 2003.

[7] E. Darie and L. Pîslaru-Dănescu, "Variable Speed Control of the Direct Current Servomotor versus the Stepper Motor by using Arduino UNO Platform," *Electrotehnica, Electronica, Automatica*, vol. 69, no. 3, pp. 14–22, 2021.

[8] M. Ruba and D. Fodorean, "Analysis of fault-tolerant multiphase power converter for a nine-phase permanent magnet synchronous machine," *IEEE Trans Ind Appl*, vol. 48, no. 6, pp. 2092–2101, 2012.

[9] S. M. Lambert, B. C. Mecrow, R. Abebe, G. Vakil, and C. M. Johnson, "Integrated drives for transport-A review of the enabling electronics technology," in *2015 IEEE Vehicle Power and Propulsion Conference (VPPC)*, Montreal, Canada, 2015, pp. 1–6.

[10] A. H. Mohamed, H. Vansompel, and P. Sergeant, "Design of an integrated DC-link structure for reconfigurable integrated modular motor drives," *IEEE Transactions on Industrial Electronics*, vol. 69, no. 3, pp. 2312–2321, 2021.

[11] S. Andersson, "Optimization of a servo motor for an industrial robot application," Lund University, LUND, SWEDEN, 2000.

[12] ABB, *ABB Proposals for Coordination of Protective Devices*, vol. 7. 2004.

[13] H. N. Huynh, H. Assadi, E. Rivière-Lorphèvre, O. Verlinden, and K. Ahmadi, "Modelling the dynamics of industrial robots for milling operations," *Robot Comput Integr Manuf*, vol. 61, pp. 1–16, 2020.

[14] M. Barcaro, N. Bianchi, and F. Magnussen, "Faulty operations of a PM fractional-slot machine with a dual three-phase winding," *IEEE Transactions on Industrial Electronics*, vol. 58, no. 9, pp. 3825–3832, 2010.

[15] A. Gonzalez-Prieto, I. Gonzalez-Prieto, M. J. Duran, and F. Barrero, “Efficient model predictive control with natural fault-tolerance in asymmetrical six-phase induction machines,” *Energies (Basel)*, vol. 12, no. 20, p. 3989, 2019.

[16] W. Zhang, Y. Xu, and M. Sun, “Design of a Novel Claw Pole Transverse Flux Permanent Magnet Motor Based on Hybrid Stator Core,” *IEEE Trans Magn*, vol. 57, no. 6, pp. 1–5, 2021.

[17] M. Aydin and M. Gulec, “Reduction of cogging torque in double-rotor axial-flux permanent-magnet disk motors: A review of cost-effective magnet-skewing techniques with experimental verification,” *IEEE Transactions on Industrial Electronics*, vol. 61, no. 9, pp. 5025–5034, 2013.

[18] Z. Fan, Y. Liao, L. Han, and L. Xie, “No-load voltage waveform optimization and damper bars heat reduction of tubular hydrogenerator by different degree of adjusting damper bar pitch and skewing stator slot,” *IEEE Transactions on Energy Conversion*, vol. 28, no. 3, pp. 461–469, 2013.

[19] Z. Chen, C. Xia, Q. Geng, and Y. Yan, “Modeling and analyzing of surface-mounted permanent-magnet synchronous machines with optimized magnetic pole shape,” *IEEE Trans Magn*, vol. 50, no. 11, pp. 1–4, 2014.

[20] C. Peng, D. Wang, Z. Feng, and B. Wang, “A new segmented rotor to mitigate torque ripple and electromagnetic vibration of interior permanent magnet machine,” *IEEE Transactions on Industrial Electronics*, vol. 69, no. 2, pp. 1367–1377, 2021.

[21] J. Liu, H. Li, and Y. Deng, “Torque ripple minimization of PMSM based on robust ILC via adaptive sliding mode control,” *IEEE Trans Power Electron*, vol. 33, no. 4, pp. 3655–3671, 2017.

[22] G. Feng, C. Lai, and N. C. Kar, “Practical testing solutions to optimal stator harmonic current design for PMSM torque ripple minimization using speed harmonics,” *IEEE Trans Power Electron*, vol. 33, no. 6, pp. 5181–5191, 2017.

[23] L. Parsa and H. A. Toliyat, “Fault-tolerant interior-permanent-magnet machines for hybrid electric vehicle applications,” *IEEE Trans Veh Technol*, vol. 56, no. 4 I, pp. 1546–1552, Jul. 2007, doi: 10.1109/TVT.2007.896978.

[24] P. L. Chapman and S. D. Sudhoff, “A multiple reference frame synchronous estimator/regulator,” *IEEE Transactions on energy conversion*, vol. 15, no. 2, pp. 197–202, 2000.

[25] X. Kestelyn and E. Semail, “A vectorial approach for generation of optimal current references for multiphase permanent-magnet synchronous machines in real time,” *IEEE Transactions on Industrial Electronics*, vol. 58, no. 11, pp. 5057–5065, Nov. 2011, doi: 10.1109/TIE.2011.2119454.

[26] D. T. Vu, N. K. Nguyen, and E. Semail, “Fault-tolerant control for nonsinusoidal multiphase drives with minimum torque ripple,” *IEEE Trans Power Electron*, vol. 37, no. 6, pp. 6290–6304, 2021.

[27] C. Liu, J. Zhu, Y. Wang, G. Lei, and Y. Guo, “Design considerations of PM transverse flux machines with soft magnetic composite cores,” *IEEE Transactions on Applied Superconductivity*, vol. 26, no. 4, pp. 1–5, 2016.

[28] E. R. Laithwaite, J. F. Eastham, H. R. Bolton, and T. G. Fellows, “Linear motors with transverse flux,” *Proceedings of the Institution of Electrical Engineers*, vol. 118, no. 12, pp. 1761–1767, 1971.

[29] J. F. Eastham and J. H. Alwash, “Transverse-flux tubular motors,” *Proceedings of the Institution of Electrical Engineers*, vol. 119, no. 12, pp. 1709–1718, 1972.

[30] 吴迪 and 辜承林, “新型横向磁通永磁电机三维磁路分析,” 中国电机工程学报, no. 33, pp. 90–95, 2010.

[31] T. Meguro and M. Morimoto, “Performance improvement of an induction motor by Soft Magnetic Composite (SMC),” in *2012 15th International Conference on Electrical Machines and Systems (ICEMS)*, Sapporo, Japan, 2012, pp. 1–4.

[32] H. Weh and H. May, “Achievable force densities for permanent magnet excited machines in new configurations,” in *Proc. Int. Conf. Electrical Machines*, 1986, pp. 1107–1111.

[33] Z. Jia, H. Lin, S. Fang, and Y. Huang, “A novel transverse flux permanent magnet generator with double C-hoop stator and flux-concentrated rotor,” *IEEE Trans Magn*, vol. 51, no. 11, pp. 1–4, 2015.

[34] A. Chen, R. Nilssen, and A. Nysveen, “Performance comparisons among radial-flux, multistage axial-flux, and three-phase transverse-flux PM machines for downhole applications,” *IEEE Trans Ind Appl*, vol. 46, no. 2, pp. 779–789, 2010.

[35] M. Wang, P. Zheng, C. Tong, Q. Zhao, and G. Qiao, “Research on a transverse-flux brushless double-rotor machine for hybrid electric vehicles,” *IEEE Transactions on Industrial Electronics*, vol. 66, no. 2, pp. 1032–1043, 2018.

[36] V. Murali, S. A. VT, and C. C. Joseph, “A Comprehensive Study on Transverse Flux Motor for Direct Drive Low-Speed Spacecraft Applications,” *IEEE Transactions on Industrial Electronics*, vol. 68, no. 1, pp. 412–422, 2020.

[37] F. Dreher and N. Parspour, “A novel high-speed permanent magnet claw pole transverse flux machine for use in automation,” in *International Symposium on Power Electronics Power Electronics, Electrical Drives, Automation and Motion*, Sorrento, Italy, 2012, pp. 1240–1245.

[38] X. Yang, B. Kou, J. Luo, and H. Zhang, “A novel dual-consequent-pole transverse flux motor and its analytical modeling,” *IEEE Transactions on Industrial Electronics*, vol. 68, no. 5, pp. 4141–4152, 2020.

[39] X. Yang, B. Kou, J. Luo, and H. Zhang, “Electromagnetic Design of a Dual-Consequent-Pole Transverse Flux Motor,” *IEEE Transactions on Energy Conversion*, vol. 35, no. 3, pp. 1547–1558, 2020.

[40] J. Hui, M. Gao, and Y. Wang, “Design and optimisation of transverse flux machine with passive rotor and flux-concentrating structure,” *IET Electr Power Appl*, vol. 13, no. 7, pp. 922–931, 2019.

[41] A. Njeh and H. Trabelsi, “New design of the claw-pole transverse flux permanent magnet machine,” in *2018 15th International Multi-Conference on Systems, Signals & Devices (SSD)*, Yasmine Hammamet, Tunisia, 2018, pp. 1311–1316.

[42] Y. Yamamoto, R. Watanabe, Y. Takada, T. Koseki, and Y. Aoyama, “Design using simple modeling and experimental study on direct-drive disk-type motor with dense stator configuration,” in *2013 15th European Conference on Power Electronics and Applications (EPE)*, Lille, France, 2013, pp. 1–10.

[43] J. R. Fard and M. Ardebili, “Design and control of a novel yokeless axial flux-switching permanent-magnet motor,” *IEEE Transactions on Energy Conversion*, vol. 34, no. 2, pp. 631–642, 2018.

[44] G. Yang, D. Cheng, H. Zhang, and B. Kou, “Bidirectional cross-linking transverse flux permanent magnet synchronous motor,” *IEEE Trans Magn*, vol. 49, no. 3, pp. 1242–1248, 2012.

[45] J.-H. Oh, J.-H. Lee, S.-I. Kang, K.-S. Shin, and B.-I. Kwon, “Analysis of a novel transverse flux type permanent magnet reluctance generator,” *IEEE Trans Magn*, vol. 50, no. 2, pp. 809–812, 2014.

[46] 宫晓, 徐衍亮, and 冯开杰, “新型盘式横向磁通永磁电机及其空载电动势波形的解析计算,” 电工技术学报, vol. 29, no. 7, pp. 77–82, 2014.

[47] S. Abdi, E. Abdi, and R. McMahon, “A light-weight rotor design for brushless doubly fed machines,” in *2018 XIII International Conference on Electrical Machines (ICEM)*, Alexandroupoli, Greece, 2018, pp. 493–498.

[48] T. Osaka, M. Takai, K. Hayashi, K. Ohashi, M. Saito, and K. Yamada, “A soft magnetic CoNiFe film with high saturation magnetic flux density and low coercivity,” *Nature*, vol. 392, no. 6678, pp. 796–798, 1998.

[49] L. Xu, Y. Xu, and J. Gong, “Analysis and optimization of cogging torque in yokeless and segmented armature axial-flux permanent-magnet machine with soft magnetic composite core,” *IEEE Trans Magn*, vol. 54, no. 11, pp. 1–5, 2018.

[50] B. Zhang, T. Seidler, R. Dierken, and M. Doppelbauer, “Development of a yokeless and segmented armature axial flux machine,” *IEEE Transactions on Industrial Electronics*, vol. 63, no. 4, pp. 2062–2071, 2015.

[51] J. Doering, G. Steinborn, and W. Hofmann, “Torque, power, losses, and heat calculation of a transverse flux reluctance machine with soft magnetic composite materials and disk-shaped rotor,” *IEEE Trans Ind Appl*, vol. 51, no. 2, pp. 1494–1504, 2014.

[52] 徐妲, 赵旭鸣, 林明耀, 付兴贺, 郝立, and 李欣哲, “基于等效磁路法的轴向磁场磁通切换型永磁电机静态特性分析,” 电机与控制应用, vol. 44, no. 11, pp. 79–84, 2017.

[53] E. M. Freeman, “EQUIVALENT CIRCUIT FOR THE TRANSVERSE-FLUX TUBULAR INDUCTION MOTOR.,” 1975.

[54] X. Ba, Y. Guo, J. Zhu, and C. Zhang, “An equivalent circuit model for predicting the core loss in a claw-pole permanent magnet motor with soft magnetic composite core,” *IEEE Trans Magn*, vol. 54, no. 11, pp. 1–6, 2018.

[55] S.-H. Lee, S.-O. Kwon, J.-J. Lee, and J.-P. Hong, “Characteristic analysis of claw-pole machine using improved equivalent magnetic circuit,” *IEEE Trans Magn*, vol. 45, no. 10, pp. 4570–4573, 2009.

[56] M. Zafarani, M. Moallem, and A. Tabesh, “Analytical model for a transverse flux permanent magnet machine using improved magnetic equivalent circuit approach,” in *2011 21st International Conference on Systems Engineering*, Las Vegas, NV, USA, 2011, pp. 96–99.

[57] J.-Y. Lee, J.-P. Hong, and D.-H. Kang, “Analysis of permanent magnet type transverse flux linear motor by coupling 2D finite element method on 3D equivalent magnetic circuit network method,” in *Conference Record of the 2004 IEEE Industry Applications Conference, 2004. 39th IAS Annual Meeting.*, Seattle, WA, USA, 2004, pp. 2092–2098.

[58] 宫晓 and 徐衍亮, “轴向磁场盘式永磁电机等效磁路网络及气隙漏磁的分析计算,” 电机与控制学报, vol. 17, no. 10, pp. 59–64, 2013.

[59] 徐衍亮, 吴巧变, and 宫晓, “新型盘式横向磁通永磁无刷电机的变网络等效磁路模型,” 电工技术学报, vol. 31, no. 17, pp. 147–153, 2016.

[60] 张昌锦, 陈志辉, 梅庆枭, and 段津津, “横向磁通永磁同步电机非线性动态等效磁网络模型分析,” 中国电机工程学报, vol. 39, no. 1, pp. 307–314, 2019.

[61] L. Fang, S.-O. Kwon, P. Zhang, and J.-P. Hong, “Conformal Mapping technique for magnetic saliency analysis of Double-layer Interior Permanent Magnet Motor,” in *2006 12th Biennial IEEE Conference on Electromagnetic Field Computation*, Miami, 2006, pp. 231–231.

[62] B. Rezaeealam and F. Rezaee-Alam, “An improved conformal mapping method for magnetic field analysis in surface mounted permanent magnet motors,” *COMPEL-The international journal for computation and mathematics in electrical and electronic engineering*, vol. 36, no. 4, pp. 892–905, 2017.

[63] D. Zarko, “A systematic approach to optimized design of permanent magnet motors with reduced torque pulsations,” The University of Wisconsin - Madison, Madison, USA, 2004.

[64] L. Fang, S.-O. Kwon, and J.-P. Hong, “Conformal transformation technique for prediction of the magnetic field distribution in an IPM motor,” in *2005 International*

Conference on Electrical Machines and Systems, Nanjing, China, 2005, pp. 2124–2128.

[65] D. Zarko, D. Ban, and T. A. Lipo, "Analytical solution for electromagnetic torque in surface permanent-magnet motors using conformal mapping," *IEEE Trans Magn*, vol. 45, no. 7, pp. 2943–2954, 2009.

[66] A. Hanic, D. Zarko, and Z. Hanic, "A novel method for no-load magnetic field analysis of saturated surface permanent-magnet machines using conformal mapping and magnetic equivalent circuits," *IEEE Transactions on Energy Conversion*, vol. 31, no. 2, pp. 740–749, 2015.

[67] K. Boughrara, D. Zarko, R. Ibtiouen, O. Touhami, and A. Rezzoug, "Magnetic field analysis of inset and surface-mounted permanent-magnet synchronous motors using Schwarz–Christoffel transformation," *IEEE Trans Magn*, vol. 45, no. 8, pp. 3166–3178, 2009.

[68] K. Ramakrishnan, D. Zarko, A. Hanic, and G. Mastinu, "Improved method for field analysis of surface permanent magnet machines using Schwarz–Christoffel transformation," *IET Electr Power Appl*, vol. 11, no. 6, pp. 1067–1075, 2017.

[69] H. Saneie, Z. Nasiri-Gheidari, and F. Tootoonchian, "Design-oriented modelling of axial-flux variable-reluctance resolver based on magnetic equivalent circuits and Schwarz–Christoffel mapping," *IEEE Transactions on Industrial Electronics*, vol. 65, no. 5, pp. 4322–4330, 2017.

[70] L. Zeng, X. Chen, X. Li, W. Jiang, and X. Luo, "A thrust force analysis method for permanent magnet linear motor using Schwarz–Christoffel mapping and considering slotting effect, end effect, and magnet shape," *IEEE Trans Magn*, vol. 51, no. 9, pp. 1–9, 2015.

[71] T. C. O'Connell and P. T. Krein, "A Schwarz–Christoffel-based analytical method for electric machine field analysis," *IEEE Transactions on Energy Conversion*, vol. 24, no. 3, pp. 565–577, 2009.

[72] D. Fu, Y. Xu, F. Gillon, J. Gong, and N. Bracikowski, "Presentation of a novel transverse-flux permanent magnet linear motor and its magnetic field analysis based on Schwarz–Christoffel mapping method," *IEEE Trans Magn*, vol. 54, no. 3, pp. 1–4, 2017.

[73] M. Gulec and M. Aydin, "Implementation of different 2D finite element modelling approaches in axial flux permanent magnet disc machines," *IET Electr Power Appl*, vol. 12, no. 2, pp. 195–202, 2018.

[74] 陈世坤, "电机设计." 北京: 机械工业出版社, 2000.

[75] 郁磊, MATLAB 智能算法 30 个案例分析. 北京航空航天大学出版社, 2015.

[76] S. Mallik *et al.*, "Efficiency and cost optimized design of an induction motor using genetic algorithm," *IEEE Transactions on Industrial Electronics*, vol. 64, no. 12, pp. 9854–9863, 2017.

[77] H. M. Hasanien, A. S. Abd-Rabou, and S. M. Sakr, “Design optimization of transverse flux linear motor for weight reduction and performance improvement using response surface methodology and genetic algorithms,” *IEEE Transactions on Energy Conversion*, vol. 25, no. 3, pp. 598–605, 2010.

[78] A. Mahmoudi, S. Kahourzade, N. Abd Rahim, and W. P. Hew, “Design, analysis, and prototyping of an axial-flux permanent magnet motor based on genetic algorithm and finite-element analysis,” *IEEE Trans Magn*, vol. 49, no. 4, pp. 1479–1492, 2012.

[79] K. S. R. Rao and A. H. Bin Othman, “Design optimization of a BLDC motor by Genetic Algorithm and Simulated Annealing,” in *2007 International Conference on Intelligent and Advanced Systems*, Kuala Lumpur, Malaysia, 2007, pp. 854–858.

[80] M. Dorigo, V. Maniezzo, and A. Colorni, “Ant system: optimization by a colony of cooperating agents,” *IEEE Transactions on Systems, Man, and Cybernetics, Part B (Cybernetics)*, vol. 26, no. 1, pp. 29–41, 1996.

[81] A. YILDIZ, M. POLAT, and M. T. Özdemir, “Design optimization of inverted switched reluctance motor using ant colony optimization algorithm,” in *2018 International Conference on Artificial Intelligence and Data Processing (IDAP)*, Malatya, Turkey, 2018, pp. 1–6.

[82] 杨维 and 李歧强, “粒子群优化算法综述,” 中国工程科学, vol. 6, no. 5, pp. 87–94, 2004.

[83] H. M. Hasanien, “Particle swarm design optimization of transverse flux linear motor for weight reduction and improvement of thrust force,” *IEEE Transactions on Industrial Electronics*, vol. 58, no. 9, pp. 4048–4056, 2010.

[84] H. Taha, Z. Tang, T. Henneron, Y. le Menach, J.-P. Ducreux, and F. Salomez, “Stabilized Gauged Formulation of Darwin Model for FEM Computation of Industrial Applications,” *IEEE Trans Magn*, 2022.

[85] 谢冰川, 张岳, 徐振耀, 张凤阁, and 刘文慧, “基于代理模型的电机多学科优化关键技术综述,” 电工技术学报, vol. 37, no. 20, pp. 5117–5143, 2022.

[86] 鞠鲁峰, “基于支持向量机建模的永磁球形电机的优化设计研究,” 合肥工业大学, 合肥, 2015.

[87] A. I. Khuri and S. Mukhopadhyay, “Response surface methodology,” *Wiley Interdiscip Rev Comput Stat*, vol. 2, no. 2, pp. 128–149, 2010.

[88] W. Zhao, A. Ma, J. Ji, X. Chen, and T. Yao, “Multiobjective optimization of a double-side linear Vernier PM motor using response surface method and differential evolution,” *IEEE Transactions on Industrial Electronics*, vol. 67, no. 1, pp. 80–90, 2019.

[89] T. Chen and H. Chen, “Universal approximation to nonlinear operators by neural networks with arbitrary activation functions and its application to dynamical systems,” *IEEE Trans Neural Netw*, vol. 6, no. 4, pp. 911–917, 1995.

[90] 刘伟达 and 赵波, “小波神经网络及其在机械工程领域中的应用,” 现代制造工程, no. 12, pp. 135–138, 2007.

[91] 杨二静, “人工神经网络和遗传算法在岩土及结构工程中的应用研究,” 广西大学, 桂林, 2007.

[92] J. H. Kim, B. C. Kang, B. Y. Choi, M. C. Kim, S. Kim, and K. Y. Kim, “Phase boundary estimation in electrical resistance tomography with weighted multilayer neural networks,” *IEEE Trans Magn*, vol. 42, no. 4, pp. 1191–1194, 2006.

[93] 陈允平, “人工神经网络及其在控制与系统工程中的应用 第一讲 人工神经网络简介,” 电网技术, no. 1, pp. 56–58, 1993.

[94] S. Meo, A. Zohoori, and A. Vahedi, “Optimal design of permanent magnet flux switching generator for wind applications via artificial neural network and multi-objective particle swarm optimization hybrid approach,” *Energy Convers Manag*, vol. 110, pp. 230–239, 2016.

[95] D. T. Vu, N. K. Nguyen, E. Semail, and T. J. dos Santos Moraes, “Control strategies for non-sinusoidal multiphase PMSM drives in faulty modes under constraints on copper losses and peak phase voltage,” *IET Electr Power Appl*, vol. 13, no. 11, pp. 1743–1752, 2019.

[96] T. D. S. Moraes, N. K. Nguyen, E. Semail, F. Meinguet, and M. Guerin, “Dual-multiphase motor drives for fault-tolerant applications: Power electronic structures and control strategies,” *IEEE Trans Power Electron*, vol. 33, no. 1, pp. 572–580, 2017.

[97] A. Khamitov, W. Gruber, G. Bramerdorfer, and E. L. Severson, “Comparison of Combined Winding Strategies for Radial Nonsalient Bearingless Machines,” *IEEE Trans Ind Appl*, vol. 57, no. 6, pp. 6856–6869, 2021.

[98] V. Ferreira, T. S. de Souza, R. R. Bastos, M. Liserre, and B. Cardoso, “Soft-Unbalance Operation for Power Routing in Multiphase Drives,” *IEEE Trans Ind Appl*, vol. 58, no. 1, pp. 435–443, 2021.

[99] P. Kalaj *et al.*, “Multi-Pole Winding Behavior in Multiphase Motors Under Current Harmonics Operation,” *IEEE Transactions on Energy Conversion*, vol. 37, no. 4, pp. 2546–2555, 2022.

[100] M. Benkhoris, M. Merabtene, and B. Davat, “Approches de modélisation de la Machine Synchrone Double Etoile alimentée par des onduleurs de tension en vue de la commande,” 2003.

[101] K. B. Tawfiq, M. N. Ibrahim, E. E. El-Kholy, and P. Sergeant, “Refurbishing three-phase synchronous reluctance machines to multiphase machines,” *Electrical Engineering*, vol. 103, no. 1, pp. 139–152, 2021.

[102] D. T. Vu, N. K. Nguyen, and E. Semail, “Torque Ripple Eliminations for Multiphase Nonsinusoidal Permanent Magnet Synchronous Machines,” in *2021 International Symposium on Electrical and Electronics Engineering (ISEE)*, Ho Chi Minh, Vietnam, 2021, pp. 178–183.

[103] T. Soeda and H. Haga, “Suppression to Radial Force and Torque Ripple of Concentrated PMSM with Double Independent Three-Phase Windings,” in *2020 23rd International Conference on Electrical Machines and Systems (ICEMS)*, Hamamatsu, Japan, 2020, pp. 509–514.

[104] A. Akay and P. Lefley, “Research on torque ripple under healthy and open-circuit fault-tolerant conditions in a PM multiphase machine,” *CES Transactions on Electrical Machines and Systems*, vol. 4, no. 4, pp. 349–359, 2020.

[105] B. Zheng, J. Zou, Y. Xu, X. Lang, and G. Yu, “Torque ripple suppression based on optimal harmonic current injection in dual three-phase PMSMs under magnetic saturation,” *IEEE Transactions on Industrial Electronics*, vol. 69, no. 6, pp. 5398–5408, 2021.

[106] R. H. Loewenherz, S. A. Koschik, M. Kruse, and R. W. de Doncker, “Transformations of Reference Frames and Model Development for Multi-Phase Machines,” *IEEJ Journal of Industry Applications*, p. 21001412, 2021.

[107] S. Rubino, O. Dordevic, E. Armando, I. R. Bojoi, and E. Levi, “A novel matrix transformation for decoupled control of modular multiphase PMSM drives,” *IEEE Trans Power Electron*, vol. 36, no. 7, pp. 8088–8101, 2020.

[108] E. Semail, E. Levi, A. Bouscayrol, and X. Kestelyn, “Multi-machine modelling of two series connected 5-phase synchronous machines: effect of harmonics on control,” in *2005 European Conference on Power Electronics and Applications*, Dresden, Germany, 2005, pp. 1–10.

[109] G. Yang *et al.*, “Overmodulation strategy for seven-phase induction motors with optimum harmonic voltage injection based on sequential optimization scheme,” *IEEE Trans Power Electron*, vol. 36, no. 12, pp. 14039–14050, 2021.

[110] S. Paul and K. Basu, “Linear PWM Techniques of Asymmetrical Six-phase Machine With Optimal Current Ripple Performance,” *IEEE Transactions on Industrial Electronics*, vol. 70, no. 2, pp. 1298–1309, 2022.

[111] T. Liu, Z. Q. Zhu, X. Wu, Z. Wu, D. A. Stone, and M. P. Foster, “A position error correction method for sensorless control of dual three-phase permanent magnet synchronous machines,” *IEEE Trans Ind Appl*, vol. 58, no. 3, pp. 3589–3601, 2022.

[112] Z. Shen, D. Jiang, J. Zou, Z. Liu, and C. Ma, “Current-balance Mode-based Unified Common-Mode Voltage Elimination Scheme for Dual Three-Phase Motor Drive System,” *IEEE Transactions on Industrial Electronics*, vol. 69, no. 12, pp. 12575–12586, 2022.

[113] Y. Hu, Z.-Q. Zhu, and K. Liu, “Current control for dual three-phase permanent magnet synchronous motors accounting for current unbalance and harmonics,” *IEEE J Emerg Sel Top Power Electron*, vol. 2, no. 2, pp. 272–284, 2014.

[114] P. Zheng, F. Wu, Y. Lei, Y. Sui, and B. Yu, “Investigation of a novel 24-slot/14-pole six-phase fault-tolerant modular permanent-magnet in-wheel motor for electric vehicles,” *Energies (Basel)*, vol. 6, no. 10, pp. 4980–5002, 2013.

[115] L. Zhang, Y. Fan, R. D. Lorenz, A. Nied, and M. Cheng, “Design and comparison of three-phase and five-phase FTFSCW-IPM motor open-end winding drive systems for electric vehicles applications,” *IEEE Trans Veh Technol*, vol. 67, no. 1, pp. 385–396, 2017.

[116] Y. Demir and M. Aydin, “A novel dual three-phase permanent magnet synchronous motor with asymmetric stator winding,” *IEEE Trans Magn*, vol. 52, no. 7, pp. 1–5, 2016.

[117] Y. Liu, S. Niu, and W. N. Fu, “A novel multiphase brushless power-split transmission system for wind power generation,” *IEEE Trans Magn*, vol. 52, no. 2, pp. 1–7, 2015.

[118] F. Locment, E. Semail, and F. Piriou, “Design and study of a multiphase axial-flux machine,” *IEEE Trans Magn*, vol. 42, no. 4, pp. 1427–1430, 2006.

[119] F. Locment, E. Semail, and X. Kestelyn, “Vectorial approach-based control of a seven-phase axial flux machine designed for fault operation,” *IEEE Transactions on Industrial Electronics*, vol. 55, no. 10, pp. 3682–3691, 2008.

[120] F. Barrero and M. J. Duran, “Recent advances in the design, modeling, and control of multiphase machines—Part I,” *IEEE Transactions on Industrial Electronics*, vol. 63, no. 1, pp. 449–458, 2015.

[121] A. Ba-Razzouk, A. Cheriti, G. Olivier, and P. Sicard, “Field-oriented control of induction motors using neural-network decouplers,” *IEEE Trans Power Electron*, vol. 12, no. 4, pp. 752–763, 1997.

[122] X. Sun, C. Hu, G. Lei, Y. Guo, and J. Zhu, “State feedback control for a PM hub motor based on gray wolf optimization algorithm,” *IEEE Trans Power Electron*, vol. 35, no. 1, pp. 1136–1146, 2019.

[123] C. Zhou, G. Yang, and J. Su, “PWM strategy with minimum harmonic distortion for dual three-phase permanent-magnet synchronous motor drives operating in the overmodulation region,” *IEEE Trans Power Electron*, vol. 31, no. 2, pp. 1367–1380, 2015.

[124] J. Karttunen, S. Kallio, P. Peltoniemi, P. Silventoinen, and O. Pyrhönen, “Decoupled vector control scheme for dual three-phase permanent magnet synchronous machines,” *IEEE Transactions on Industrial Electronics*, vol. 61, no. 5, pp. 2185–2196, 2013.

[125] Y. Hu, Z. Q. Zhu, and M. Odavic, “Comparison of two-individual current control and vector space decomposition control for dual three-phase PMSM,” *IEEE Trans Ind Appl*, vol. 53, no. 5, pp. 4483–4492, 2017.

[126] Y. He, Y. Wang, J. Wu, Y. Feng, and J. Liu, “A comparative study of space vector PWM strategy for dual three-phase permanent-magnet synchronous motor drives,” in *2010 Twenty-Fifth Annual IEEE Applied Power Electronics Conference and Exposition (APEC)*, IEEE, 2010, pp. 915–919.

[127] Y. Hu, K. Huang, X. Li, D. Luo, S. Huang, and X. Ma, “Torque enhancement of dual three-phase PMSM by harmonic injection,” *IET Electr Power Appl*, vol. 14, no. 9, pp. 1735–1744, 2020.

[128] Y. Zhu, W. Gu, K. Lu, and Z. Wu, “Vector control of asymmetric dual three-phase PMSM in full modulation range,” *IEEE Access*, vol. 8, pp. 104479–104493, 2020.

[129] J. Xu, M. Odavic, Z.-Q. Zhu, Z.-Y. Wu, and N. Freire, “Switching-table-based direct torque control of dual three-phase PMSMs with closed-loop current harmonics compensation,” *IEEE Trans Power Electron*, vol. 36, no. 9, pp. 10645–10659, 2021.

[130] Y. Ren, Z. Q. Zhu, J. E. Green, Y. Li, S. Zhu, and Z. Li, “Improved duty-ratio-based direct torque control for dual three-phase permanent magnet synchronous machine drives,” *IEEE Trans Ind Appl*, vol. 55, no. 6, pp. 5843–5853, 2019.

[131] B. Shao *et al.*, “Improved direct torque control method for dual-three-phase permanent-magnet synchronous machines with back EMF harmonics,” *IEEE Transactions on Industrial Electronics*, vol. 68, no. 10, pp. 9319–9333, 2020.

[132] B. Shao, Z. Q. Zhu, J. Feng, S. Guo, Y. Li, and W. Liao, “Compensation of current harmonics for switching-table-based direct torque control of dual three-phase PMSM drive,” in *2019 22nd International Conference on Electrical Machines and Systems (ICEMS)*, IEEE, 2019, pp. 1–6.

[133] L. Huang, J. Ji, W. Zhao, H. Tang, T. Tao, and S. Jin, “Direct Torque Control for Dual Three-Phase Permanent Magnet Motor With Improved Torque and Flux,” *IEEE Transactions on Energy Conversion*, 2022.

[134] U. R. Muduli, R. K. Behera, K. Al Hosani, and M. S. El Moursi, “Direct torque control with constant switching frequency for three-to-five phase direct matrix converter fed five-phase induction motor drive,” *IEEE Trans Power Electron*, vol. 37, no. 9, pp. 11019–11033, 2022.

[135] R. Bojoi, F. Farina, G. Griva, F. Profumo, and A. Tenconi, “Direct torque control for dual three-phase induction motor drives,” *IEEE Trans Ind Appl*, vol. 41, no. 6, pp. 1627–1636, 2005.

[136] A. Singh, R. Aashish, and A. Saha, “Control of Jeffcott Rotor Vibrations Using Model Predictive Control,” in *International Conference on Advances in Mechanical Engineering and Material Science*, Singapore, 2022, pp. 11–22.

[137] S. Saberi and B. Rezaie, “Sensorless FCS-MPC-based speed control of a permanent magnet synchronous motor fed by 3-level NPC,” *Journal of Renewable Energy and Environment*, vol. 8, no. 2, pp. 13–20, 2021.

[138] X. Sun, T. Li, Z. Zhu, G. Lei, Y. Guo, and J. Zhu, “Speed sensorless model predictive current control based on finite position set for PMSHM drives,” *IEEE Transactions on Transportation Electrification*, vol. 7, no. 4, pp. 2743–2752, 2021.

[139] S. Batiyah, R. Sharma, S. Abdelwahed, and N. Zohrabi, “An MPC-based power management of standalone DC microgrid with energy storage,” *International Journal of Electrical Power & Energy Systems*, vol. 120, p. 105949, 2020.

[140] C. Loeblein and J. D. Perkins, “Structural design for on-line process optimization: I. Dynamic economics of MPC,” *AIChE Journal*, vol. 45, no. 5, pp. 1018–1029, 1999.

[141] A. A. Ahmed, B. K. Koh, and Y. Il Lee, “A comparison of finite control set and continuous control set model predictive control schemes for speed control of induction motors,” *IEEE Trans Industr Inform*, vol. 14, no. 4, pp. 1334–1346, 2017.

[142] C. S. Lim, E. Levi, M. Jones, N. A. Rahim, and W. P. Hew, “FCS-MPC-based current control of a five-phase induction motor and its comparison with PI-PWM control,” *IEEE Transactions on Industrial Electronics*, vol. 61, no. 1, pp. 149–163, 2013.

[143] O. Gonzalez, M. Ayala, J. Doval-Gandoy, J. Rodas, R. Gregor, and M. Rivera, “Predictive-fixed switching current control strategy applied to six-phase induction machine,” *Energies (Basel)*, vol. 12, no. 12, p. 2294, 2019.

[144] S. Liu and C. Liu, “Virtual-vector-based robust predictive current control for dual three-phase PMSM,” *IEEE Transactions on Industrial Electronics*, vol. 68, no. 3, pp. 2048–2058, 2020.

[145] N. P. Nguyen, N. Xuan Mung, L. N. N. T. Ha, and S. K. Hong, “Fault-Tolerant Control for Hexacopter UAV Using Adaptive Algorithm with Severe Faults,” *Aerospace*, vol. 9, no. 6, p. 304, 2022.

[146] M. Tousizadeh, H. S. Che, J. Selvaraj, N. Abd Rahim, and B.-T. Ooi, “Performance comparison of fault-tolerant three-phase induction motor drives considering current and voltage limits,” *IEEE Transactions on Industrial Electronics*, vol. 66, no. 4, pp. 2639–2648, 2018.

[147] M. Tousizadeh, H. S. Che, J. Selvaraj, N. Abd Rahim, and B.-T. Ooi, “Fault-tolerant field-oriented control of three-phase induction motor based on unified feedforward method,” *IEEE Trans Power Electron*, vol. 34, no. 8, pp. 7172–7183, 2018.

[148] S. Ding, H. Tan, J. Hang, K. Ma, and J. Fan, “Optimized OP-FTC for SPMSM Considering Copper Loss Minimization,” *IEEE Transactions on Energy Conversion*, vol. 37, no. 3, pp. 2138–2146, 2022.

[149] H.-M. Ryu, J.-W. Kim, and S.-K. Sul, “Synchronous-frame current control of multiphase synchronous motor under asymmetric fault condition due to open phases,” *IEEE Trans Ind Appl*, vol. 42, no. 4, pp. 1062–1070, 2006.

[150] M.-A. Shamsi-Nejad, B. Nahid-Mobarakeh, S. Pierfederici, and F. Meibody-Tabar, “Fault tolerant and minimum loss control of double-star synchronous machines under open phase conditions,” *IEEE Transactions on Industrial Electronics*, vol. 55, no. 5, pp. 1956–1965, 2008.

[151] W. Wang, J. Zhang, M. Cheng, and S. Li, “Fault-tolerant control of dual three-phase permanent-magnet synchronous machine drives under open-phase faults,” *IEEE Trans Power Electron*, vol. 32, no. 3, pp. 2052–2063, 2016.

[152] H. Lu, J. Li, R. Qu, D. Ye, and L. Xiao, “Reduction of unbalanced axial magnetic force in postfault operation of a novel six-phase double-stator axial-flux PM machine using model predictive control,” *IEEE Trans Ind Appl*, vol. 53, no. 6, pp. 5461–5469, 2017.

[153] A. N. Tiwari, P. Agarwal, and S. P. Srivastava, “Performance investigation of modified hysteresis current controller with the permanent magnet synchronous motor drive,” *IET Electr Power Appl*, vol. 4, no. 2, pp. 101–108, 2010.

[154] A. Tripathi and P. C. Sen, “Comparative analysis of fixed and sinusoidal band hysteresis current controllers for voltage source inverters,” *IEEE Transactions on Industrial Electronics*, vol. 39, no. 1, pp. 63–73, 1992.

[155] Z. Liang, D. Liang, P. Kou, and S. Jia, “Postfault control and harmonic current suppression for a symmetrical dual three-phase SPMSM drive under single-phase open-circuit fault,” *IEEE Access*, vol. 8, pp. 67674–67686, 2020.

[156] G. Feng, C. Lai, W. Li, Y. Han, and N. C. Kar, “Computation-efficient solution to open-phase fault tolerant control of dual three-phase interior PMSMs with maximized torque and minimized ripple,” *IEEE Trans Power Electron*, vol. 36, no. 4, pp. 4488–4499, 2020.

[157] G. Feng, C. Lai, W. Li, J. Tjong, and N. C. Kar, “Open-phase fault modeling and optimized fault-tolerant control of dual three-phase permanent magnet synchronous machines,” *IEEE Trans Power Electron*, vol. 34, no. 11, pp. 11116–11127, 2019.

[158] 周长攀, 杨贵杰, 苏健勇, and 孙国栋, “基于正常解耦变换的双三相永磁同步电机缺相容错控制策略,” 电工技术学报, vol. 32, no. 3, pp. 86–96, 2017.

[159] J. Xu, Y. Cui, B. Song, T. Chen, and K. Wang, “Simulation Analysis of Fault-tolerant Control for Dual Three-Phase Permanent Magnet Synchronous Motor,” in *Journal of Physics: Conference Series*, 2022.

[160] A. G. Yepes, J. Doval-Gandoy, F. Baneira, and H. Toliyat, “Postfault strategy for dual three-phase machines with minimum loss in the full torque operation range under two open phases,” in *2018 IEEE Energy Conversion Congress and Exposition (ECCE)*, Portland, OR, USA, 2018, pp. 3380–3385.

[161] W. Li, G. Feng, Z. Li, J. Tjong, and N. C. Kar, “Multireference frame based open-phase fault modeling and control for asymmetrical six-phase interior permanent magnet motors,” *IEEE Trans Power Electron*, vol. 36, no. 10, pp. 11712–11725, 2021.

[162] Z. Changpan, Y. Guijie, and S. Jianyong, “The control strategy for dual three-phase PMSM based on normal decoupling transformation under fault condition due to open phases,” *Transactions of China Electrotechnical Society*, vol. 32, no. 3, pp. 86–96, 2017.

[163] G. De Donato, F. G. Capponi, G. A. Rivellini, and F. Caricchi, “Integral-slot versus fractional-slot concentrated-winding axial-flux permanent-magnet machines: Comparative design, FEA, and experimental tests,” *IEEE Trans Ind Appl*, vol. 48, no. 5, pp. 1487–1495, 2012.

[164] E. Carraro, N. Bianchi, S. Zhang, and M. Koch, “Design and Performance Comparison of Fractional Slot Concentrated Winding Spoke Type Synchronous Motors with Different Slot-Pole Combinations,” *IEEE Trans Ind Appl*, vol. 54, no. 3, pp. 2276–2284, May 2018.

[165] 徐衍亮, 吴巧变, and 宫晓, “新型盘式横向磁通永磁无刷电机的变网络等效磁路模型,” 电工技术学报, vol. 31, no. 17, pp. 147–153, 2016.

[166] L. Zeng, X. Chen, X. Li, W. Jiang, and X. Luo, “A thrust force analysis method for permanent magnet linear motor using Schwarz–Christoffel mapping and considering slotting effect, end effect, and magnet shape,” *IEEE Trans Magn*, vol. 51, no. 9, pp. 1–9, 2015.

[167] R. Plonsey and R. E. Collin, *Electromagnetic fields*. New York: McGraw-Hill Book Co, 1961.

[168] 曾理湛, “永磁同步直线电机复杂机电耦合系统分析与控制方法,” 华中科技大学, 武汉, 2011.

[169] T. C. O’Connell, “An investigation of boundary-based field analysis methods for electric machines: The Schwarz-Christoffel and boundary element methods,” University of Illinois at Urbana-Champaign, Champaign, IL, USA, 2008.

[170] B. Hague, *The Principles of Electromagnetism Applied to Electrical Machines:(formerly Titled: Electromagnetic Problems in Electrical Engineering).*, vol. 246. Dover publications, 1962.

[171] A. Souissi, I. Abdennadher, R. di Stefano, A. Masmoudi, and F. Marignetti, “Pole shape-based reduction of the harmonic content of the IPM T-LSM air gap flux density,” *IEEE Transactions on Industrial Electronics*, vol. 65, no. 2, pp. 1429–1438, 2017.

[172] 王晓远 and 高鹏, “基于进化策略的轮毂电机永磁体结构优化设计,” 中国电机工程学报, vol. 35, no. 4, pp. 979–984, 2015.

[173] Y. Duan, R. G. Harley, and T. G. Habetler, “Comparison of particle swarm optimization and genetic algorithm in the design of permanent magnet motors,” in *2009 IEEE 6th international power electronics and motion control conference*, Wuhan, China, 2009, pp. 822–825.

[174] J. Zou, Y. Han, and S.-S. So, “Overview of artificial neural networks,” *Artificial neural networks: methods and applications*, pp. 14–22, 2009.

[175] N. M. Nawi, A. Khan, and M. Z. Rehman, “A new back-propagation neural network optimized with cuckoo search algorithm,” in *Computational Science and Its Applications–ICCSA 2013: 13th International Conference*, Ho Chi Minh City, Vietnam, 2013, pp. 413–426.

[176] W. Wu, J. Wang, M. Cheng, and Z. Li, “Convergence analysis of online gradient method for BP neural networks,” *Neural Networks*, vol. 24, no. 1, pp. 91–98, 2011.

[177] S. Yang, T. O. Ting, K. L. Man, and S.-U. Guan, “Investigation of neural networks for function approximation,” *Procedia Comput Sci*, vol. 17, pp. 586–594, 2013.

[178] L. Liu, J. Chen, and L. Xu, “Realization and application research of BP neural network based on MATLAB,” in *2008 International Seminar on Future BioMedical Information Engineering*, Wuhan, China, 2008, pp. 130–133.

[179] Z.-Q. Wang, M. T. Manry, and J. L. Schiano, “LMS learning algorithms: misconceptions and new results on converence,” *IEEE Trans Neural Netw*, vol. 11, no. 1, pp. 47–56, 2000.

[180] 刘文颖, 谢昶, 文晶, 王佳明, and 王维洲, “基于小生境多目标粒子群算法的输电网检修计划优化,” 中国电机工程学报, vol. 33, no. 4, pp. 141–148, 2013.

[181] N. Ghorbani, A. Kasaeian, A. Toopshekan, L. Bahrami, and A. Maghami, “Optimizing a hybrid wind-PV-battery system using GA-PSO and MOPSO for reducing cost and increasing reliability,” *Energy*, vol. 154, pp. 581–591, 2018.

[182] S. Agrawal, Y. Dashora, M. K. Tiwari, and Y.-J. Son, “Interactive particle swarm: a Pareto-adaptive metaheuristic to multiobjective optimization,” *IEEE Transactions on systems, man, and cybernetics-Part A: Systems and humans*, vol. 38, no. 2, pp. 258–277, 2008.

[183] G. Sun, S. J. Hoff, B. C. Zelle, and M. A. Smith, “Development and comparison of backpropagation and generalized regression neural network models to predict diurnal and seasonal gas and PM10 concentrations and emissions from swine buildings,” in *2008 Providence, Rhode Island, June 29–July 2, 2008*, 2008, p. 1.

[184] E. Levi, “Multiphase AC machines,” in *The industrial electronics handbook: power electronics and motor drives*, CRC Press, 2011.

[185] E. Semail, A. Bouscayrol, and J.-P. Hautier, “Vectorial formalism for analysis and design of polyphase synchronous machines,” *The European physical journal-applied physics*, vol. 22, no. 3, pp. 207–220, 2003.

[186] S. Park, W. Kim, and S.-I. Kim, “A numerical prediction model for vibration and noise of axial flux motors,” *IEEE Transactions on Industrial Electronics*, vol. 61, no. 10, pp. 5757–5762, 2014.

[187] W. Deng and S. Zuo, “Axial force and vibroacoustic analysis of external-rotor axial-flux motors,” *IEEE Transactions on Industrial Electronics*, vol. 65, no. 3, pp. 2018–2030, Mar. 2018, doi: 10.1109/TIE.2017.2739697.

Résumé étendu en Français

Nomenclature

PMSM	Machines synchrone à Aimants Permanents
TFPMSM	Machine Synchone à Flux Transverse à Aimants Permanents
RPMSM	Machines Synchrones à Aimants Permanents à Flux Radial
DS-HSDR-TFPMSM	TFPMSM discoide à double-stator et circuit magnétique statorique hybride
SMC	Soft Magnetic Composite (Poudre de Fer)
MTOR	Stratégie pour Maximisation de la plage de fonctionnement du couple (Maximizing Torque Operation Range)
MCL	Stratégie pour Minimisation des pertes Cuivre à Couple donné (Minimum Copper Loss principle)
MRF	Controle dans des repères tournants multiples (Multiple Reference Frame)

R.1 Exigences relatives à l'entraînement électrique d'un robot industriel

La fabrication automatisée continuant à se développer rapidement induit les exigences techniques imposées aux robots industriels. Par conséquent, leurs composants électriques d'entraînement sont soumis à des exigences plus strictes, notamment en matière de miniaturisation, de dynamique élevée, de fiabilité fonctionnelle et de faible ondulation du couple.

(1) Miniaturisation

L'agencement interne classique de machines synchrones à aimants permanents pour les robots industriels est illustré dans la Fig. R.1. On peut voir que la structure globale est longue en raison de la combinaison avec le frein et l'encodeur. Pour rendre les robots industriels encore plus compacts, un nouveau type de machine électrique doit être développé pour avoir une machine plus courte et avec une densité de couple élevée, ce qui contribuera à réduire la taille et le poids des articulations du robot.

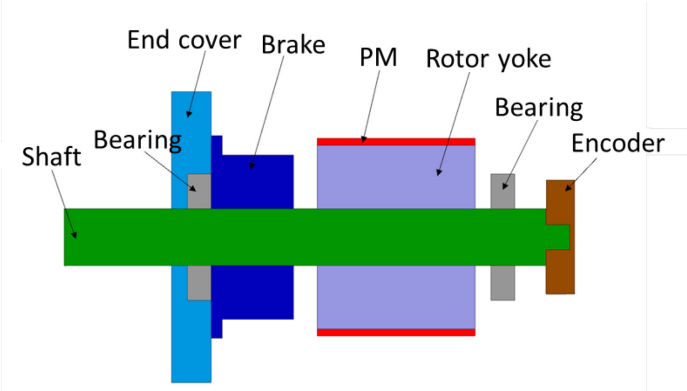

Fig. R.1 Schéma interne d'un PMSM appliqué à un robot industriel

(2) Performance dynamique élevée

Les robots industriels sont fréquemment soumis à des processus de démarrage, d'arrêt et d'accélération/décélération au cours de leur fonctionnement ; il est donc particulièrement important d'améliorer les indicateurs de performance dynamique. Dans le cas des applications de robots industriels avec boîtes de vitesses, l'inertie de la machine électrique est augmentée. Par conséquent, il est important d'avoir un faible moment d'inertie de la machine électrique pour améliorer les performances dynamiques des robots industriels[13].

(3) Haute fiabilité fonctionnelle

En cas de défaillance d'un robot industriel, il peut être nécessaire d'arrêter l'ensemble du système de fabrication, ce qui s'avère être une solution inefficace et peu rentable. La fiabilité et la productivité du système de fabrication peuvent être considérablement améliorées en veillant à ce que le robot industriel continue à fonctionner normalement en cas de défaillance. En ce qui concerne l'entraînement électrique, cela signifie qu'une capacité de tolérance aux pannes est nécessaire pour améliorer la fiabilité fonctionnelle du système.

(4) Faible ondulation du couple

La précision des robots industriels peut être directement affectée par l'ondulation du couple des machines électriques. L'ondulation du couple est attribuée à la fois au couple de détente ainsi qu'au couple lié aux harmoniques dans le champ magnétique de l'induit. Le couple de détente est généré par l'interaction entre les aimants permanents du PMSM et la structure ferromagnétique du stator et peut être réduit en optimisant soit la structure de la machine lors de la conception [16] soit en ajoutant ou modifiant des éléments de structures existantes (par exemple, inclinaison de pôle, encoches inclinées, aimants permanents à épaisseur variable[19] et coefficients inégaux de l'arc polaire[20] etc.). Les harmoniques dans le champ de l'induit sont principalement causés par l'interaction entre les harmoniques d'espace de l'enroulement et les harmoniques de temps du courant. La réduction de l'ondulation du couple provoquée par les harmoniques de l'induit est un défi. En soucis d'améliorer la qualité du couple, plusieurs travaux de recherche ont été proposés en utilisant des courants non sinusoïdaux [23]–[26] pour avoir un couple théoriquement lisse. Cependant, le problème survient quand la vitesse de rotation augmente à cause la bande passante restreinte des correcteurs de courants souvent de type PI.

En tant que composant essentiel des robots industriels, les machines électriques jouent un rôle important pour répondre aux exigences de miniaturisation, de dynamique élevée, de fiabilité fonctionnelle élevée et de faible ondulation du couple. Par conséquent, la promotion des progrès de la technologie des machines électriques peut effectivement faire progresser la modernisation et le développement de la technologie de l'industrie des robots industriels. Pour répondre aux exigences d'entraînement à haute performance des robots industriels, des topologies innovantes de PMSM sont nécessaires.

La machine synchrone à aimant permanent à flux transverse (TFPMSM) combine les avantages d'une densité de couple intrinsèquement élevée, d'une conception de structure flexible et d'une structure d'enroulement simple[27]. En raison de la caractéristique de densité de couple élevée, la taille et le poids de la machine électrique peuvent être bien optimisés ; en outre, la flexibilité de la conception structurelle rend la structure de la machine électrique plus évolutive ce qui permet le développement de solutions de conception compactes pour les applications de robots industriels. En même temps, la flexibilité de la conception de la structure du rotor apportera plus de degrés de liberté permettant aux méthodes de conception de réduire le moment d'inertie.

L'étude sur le TFPMSM permet la miniaturisation et la dynamique élevée de l'entraînement électrique, et l'ondulation du couple du TFPMSM peut être réduite par la méthode d'optimisation de la conception. Cependant, le TFPMSM utilisant la structure conventionnelle de l'enroulement triphasé n'est pas caractérisé par une capacité de tolérance aux pannes, ce qui réduit la fiabilité des systèmes robotiques industriels. Les machines multiphasées sont des machines électriques avec plus de trois phases de bobinage qui se caractérisent par une excellente capacité de tolérance aux pannes. Par conséquent, l'introduction d'une machine multiphasée permet d'obtenir une grande fiabilité fonctionnelle dans les systèmes robotiques industriels.

R.2 État de l'Art

R.2.1 Recherche sur la Machine Synchone à Flux Transverse à Aimants Permanents (TFPMSM)

Par rapport à la RPMSM classique, la TFPMSM proposée dans la recherche existante combine les avantages de densité de couple élevée [35], conception structurelle flexible[40]et l'indépendance entre les circuits magnétiques de chaque phase[43]. Les avantages de la densité de couple élevée et de la conception structurelle flexible du TFPMSM permettent de réaliser la miniaturisation des machines électriques..

Un TFPMSM triphasé avec une structure de rotor unique de type disque sans culasse ferromagnétique est proposé dans [42] et [46] comme le montre la Fig. R.2. Il est donc possible de l'utiliser dans des applications industrielles, avec les avantages d'une masse plus faible et d'une perte dans le noyau ferromagnétique plus faible. Cependant, il se heurte encore à des problèmes d'assemblage qui l'empêchent d'être adapté à la production de masse dans l'industrie, ainsi qu'à son diamètre extérieur surdimensionné qui le rend inadapté à l'installation dans les articulations de mouvement des robots industriels.

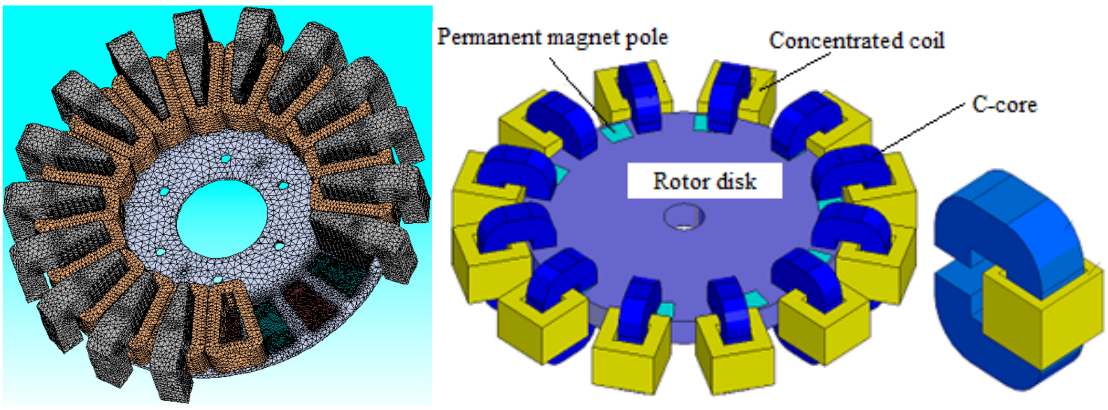

(a) (b)

Fig. R.2 TFPMSM à rotor à disque : (a) La structure proposée dans la littérature[42] ; (b) structure proposée dans la littérature[46].

Comme indiqué précédemment, la machine électrique à flux transverse se caractérise par une structure complexe avec un circuit magnétique tridimensionnel. Par conséquent, ses méthodes d'analyse électromagnétique sont également relativement complexes par rapport à la machine électrique traditionnelle. La méthode des éléments finis est la technique la plus précise pour analyser les performances électromagnétiques, mais c'est aussi celle qui prend le plus de temps. C'est pourquoi, pour les machines électriques à flux transverse, de nombreux chercheurs préfèrent utiliser la méthode du circuit magnétique équivalent, qui est plus rapide et plus

efficace pour les calculs. Dans les années 1970, E.M. Freeman a été le premier à proposer d'utiliser le modèle du circuit magnétique équivalent pour analyser une machine linéaire cylindrique à flux transverse [53]. Cependant, la précision de calcul de la méthode du circuit magnétique équivalent ne peut pas satisfaire pleinement les besoins de la conception technique. C'est pourquoi la méthode du réseau magnétique équivalent, qui combine les caractéristiques de la MEF et de la méthode du circuit magnétique équivalent avec une plus grande précision de calcul, est proposée et appliquée à l'analyse électromagnétique de la TFPMSM[57]. Outre les méthodes susmentionnées, des méthodes d'analyse électromagnétique basées sur des transformations conformes ont été proposées par des chercheurs et utilisées dans le domaine des machines électriques [61]–[66].

R.2.2 Commande tolérante aux défauts d'une machine double-triphasée

Les machines multiphasées peuvent être divisées en deux catégories selon la forme de connexion des enroulements du stator : la première est une machine multiphasée à enroulement symétrique dans laquelle les n enroulements de phase sont connectés et l'angle d'espace entre deux enroulements de phase adjacents est de 2π/n, les machines à cinq et sept phases en sont des exemples typiques [109]L'autre catégorie est celle des machines multiphasées à enroulement asymétrique, qui sont obtenues par le déplacement spatial de plusieurs ensembles d'enroulements connectés en étoile et isolés par des points neutres, qui sont également appelées machines à phase divisée ; la plupart des recherches se concentrent sur les machines asymétriques à six phases dites aussi machines double-triphasée avec un décalage de phase de 30° [110], [111].

Dans le domaine des machines multiphasées, la structure la plus populaire est la machine double-triphasée[112], [113] dont la méthode de contrôle est proche de celle de la machine triphasée conventionnelle. Le déphasage angulaire entre bobines de la machine double-triphasée asymétrique est de 30°, identique à celui de la machine symétrique à 12 phases, de sorte que la distribution spatiale de sa FMM est également la même. Par conséquent, l' harmonique de rang 6 dans l'ondulation du couple est éliminée, et l'ordre minimum de l'ondulation du couple est de rang 12 alors qu'il est de 6 dans la machine triphasée traditionnelle. Ainsi, la machine double-triphasée asymétrique bénéficie d'avantages plus importants dans la suppression de l'ondulation du couple, ce qui explique pourquoi elle attire davantage l'attention.

La tolérance aux pannes est une caractéristique importante des machines double-triphasée. Les types de défauts de circuit ouvert et de court-circuit survenant dans l'entraînement électrique peuvent être transformés en défauts de circuit ouvert de l'enroulement de phase grâce à l'isolation matérielle et à d'autres mesures. Par conséquent, les stratégies de contrôle tolérant aux pannes (FTC) pour les machines double-triphasée se concentrent principalement sur les pannes de circuit ouvert. Dans [157], la matrice de transformation découplée est utilisée pour transformer le courant en cas de défaut de circuit ouvert monophasé dans les repères tournants *d1-q1* et *d2-q2* sur lesquels l'équation du couple est inchangée. Cependant, la méthode proposée dans [157] nécessite l'utilisation d'un algorithme d'optimisation intelligent pour ajuster les paramètres à déterminer dans le courant de référence découplé en temps réel en fonction de la valeur de référence du couple, ce qui augmente la difficulté. En outre, en termes d'objectifs d'optimisation de la méthode FTC, les méthodes FTC pour les machines double-triphasée peuvent être divisées en deux catégories : les méthodes FTC basées sur le principe de minimisation des pertes cuivre (MCL) et les méthodes FTC basées sur le principe de maximisation de la plage de fonctionnement du couple (MTOR). La définition de base de la MCL est que le courant de référence est reconfiguré pour minimiser les pertes cuivre dans l'enroulement du stator tandis que le couple de la machine électrique est maintenu constant[151], [160]. En [151] un modèle mathématique d'un système de coordonnées de référence *d-q double*

pour une machine synchrone double-triphasée à aimants permanents est élaborée et une méthode FTC basée sur le MCL est conçue.

Toutefois, les méthodes FTC basées sur MTOR sont plus complexes. En compilant les recherches existantes, les méthodes peuvent être divisées en trois catégories, comme suit.

1) Déterminer le couple maximum sous une amplitude de courant de phase donnée [156], [157], [161].

(2) Produire le couple désiré tout en minimisant au maximum des pertes Cuivre moyenne dans chaque phase [151].

3) Produire le couple désiré tout en minimisant l'amplitude du courant dans chaque phase [162].

R.3 Objectifs de la thèse

Les avantages de la miniaturisation et de la dynamique élevée peuvent être obtenus en utilisant les TFPMSM au lieu des Machines Synchrones à Aimants Permanents à Flux radial (RPMSM) traditionnel dans le robot industriel. En outre, la fiabilité du système de robot industriel peut être encore améliorée par l'introduction d'une machine multiphasée. Cependant, le TFPMSM ainsi que les machines multiphasées dans la recherche existante doivent encore faire face aux défis suivants qui limitent leur application dans les robots industriels :

(1) Questions relatives à l'innovation et à la conception de la structure du TFPMSM. De nombreuses topologies inspirantes ont été proposées sur la base de la recherche sur le TFPMSM et ont été utilisées dans diverses applications. Cependant, la recherche n'a jamais été développée pour le scénario d'application des robots industriels.

(2) Analyse et optimisation de la TFPMSM. En tant que machine électrique dotée d'un circuit magnétique tridimensionnel, la structure de la TFPMSM est plus complexe que celle de la RPMSM traditionnelle, ce qui entraîne l'utilisation d'une analyse par éléments finis tridimensionnelle de la TFPMSM, qui prend beaucoup de temps. En outre, la structure tridimensionnelle du TFPMSM comprend des paramètres de conception complexes, et son processus d'optimisation est également plus complexe et prend plus de temps.

(3) Conception et contrôle du TFPMSM tolérant aux pannes. Pour répondre aux exigences élevées de fiabilité fonctionnelle des entraînements électriques des robots industriels, il est nécessaire de concevoir des TFPMSM tolérantes aux pannes.

En ce qui concerne les préoccupations susmentionnées, la thèse étudie la conception, l'analyse et l'optimisation d'une machine synchrone à aimant permanent à flux transverse pour les applications robotiques industrielles, ainsi que ses conceptions multiphasées et ses méthodes de contrôle tolérants aux pannes. Les principaux résultats des travaux sont les suivants.

1. Une nouvelle machine synchrone à aimant permanent à flux transverse discoide à deux stators comportant un circuit statorique magnétique hybride (DS-HSDR-TFPMSM) est proposée. Elle exploite pleinement les avantages des tôles d'acier au silicium laminées et des matériaux composites magnétiques doux. Sa conception structurelle et électromagnétique est poursuivie. Tout d'abord, le principe de fonctionnement et la supériorité du DS-HSDR-TFPMSM sont décrits. Ensuite, l'équation de dimensionnement de base est déduite et les paramètres de conception sont analysés. Enfin, une étude de conception tolérante aux pannes basée sur la structure double-triphasée est réalisée pour le DS-HSDR-TFPMSM proposé afin d'améliorer sa fiabilité fonctionnelle.

2. Compte tenu de la structure tridimensionnelle complexe de la DS-HSDR-TFPMSM, la méthode de calcul du champ magnétique de l'entrefer et les performances sont étudiées sur la base de la méthode de transformation de Schwarz-Christoffel. Tout d'abord, un modèle analytique équivalent bidimensionnel de DS-HSDR-TFPMSM est établi. Ensuite, son modèle

analytique simplifié basé sur la transformation de Schwarz-Christoffel est déduit. Enfin, la distribution du champ magnétique de l'entrefer est obtenue à l'aide des équations de Hague, qui sont ensuite utilisées pour calculer les performances du DS-HSDR-TFPMSM. Les résultats ci-dessus sont tous comparés aux résultats de calcul obtenus par FEM pour valider la précision de la méthode de transformation de Schwarz-Christoffel.

3. La conception de l'optimisation du DS-HSDR-TFPMSM est réalisée sur la base du réseau neuronal BP et de l'algorithme d'optimisation multi-objectif. Le DS-HSDR-TFPMSM proposé est optimisé à travers les étapes de la description du problème d'optimisation, de la conception de l'espace d'échantillonnage, de la modélisation du réseau neuronal et de l'optimisation par essaim particulaire multi-objectifs. Enfin, les résultats de la conception de l'optimisation sont validés par la FEM.

4. Sur la base des conceptions accessibles de tolérance aux pannes de la DS-HSDR-TFPMSM, la méthode de commande tolérante aux pannes pour la machine synchrone à aimant permanent double-triphasée est étudiée. Tout d'abord, la méthode de commande tolérante aux pannes par reconfiguration des courants de référence dans le repère découplé basée sur le principe des pertes cuivre minimales et celle sur la plage de fonctionnement du couple maximal est proposée. Ensuite, le modèle de contrôle vectoriel tolérant aux pannes est obtenu en modifiant les courants selon les critères choisis (les pertes par effet Joule égales sur les phases ou le couple maximal). Enfin, la méthode de contrôle tolérant aux pannes pour une machine électrique triphasée à aimant permanent fonctionnant à grande vitesse est étudiée. En effet, l'augmentation de la vitesse conduit à une difficulté à contrôler les courants de référence dans le repère tournant (les harmoniques de courants sont de rang 2). Une deuxième transformation de Park à 2θ a été proposée pour obtenir des consignes de courants constantes. Cette approche a été comparée avec une méthode basée sur un contrôleur résonant proportionnel.

5. Les technologies de fabrication et les études expérimentales sont menées pour le prototype DS-HSDR-TFPMSM. Tout d'abord, l'évaluation de la résistance structurelle, la fabrication et le processus d'assemblage du prototype DS-HSDR-TFPMSM font l'objet de recherches. Ensuite, la plate-forme expérimentale pour le prototype DS-HSDR-TFPMSM et une machine synchrone à aimant permanent à flux radial commercialisée de même puissance est construite pour valider les performances de DS-HSDR-TFPMSM.

R.4 Contenu de la recherche

R.4.1 Conception d'une nouvelle machine synchrone à aimant permanent à flux transverse de type disque

Fig. R.3 décrit la structure du DS-HSDR-TFPMSM. Le matériau SMC est utilisé pour réaliser l'épanouissement polaire du stator, ce qui réduit la zone ouverte entre les noyaux adjacents du stator et diminue efficacement les fuites magnétiques. Le noyau du stator est constitué de tôles d'acier au silicium laminées afin de réduire la saturation et les pertes fer du noyau du stator dans des conditions de charge élevée. Pour réduire la taille, le poids et les pertes fer de la partie rotor, une structure de rotor à disque à aimants sans carcasse ferromagnétique est utilisée, comme le montre la Fig. R.3(c).

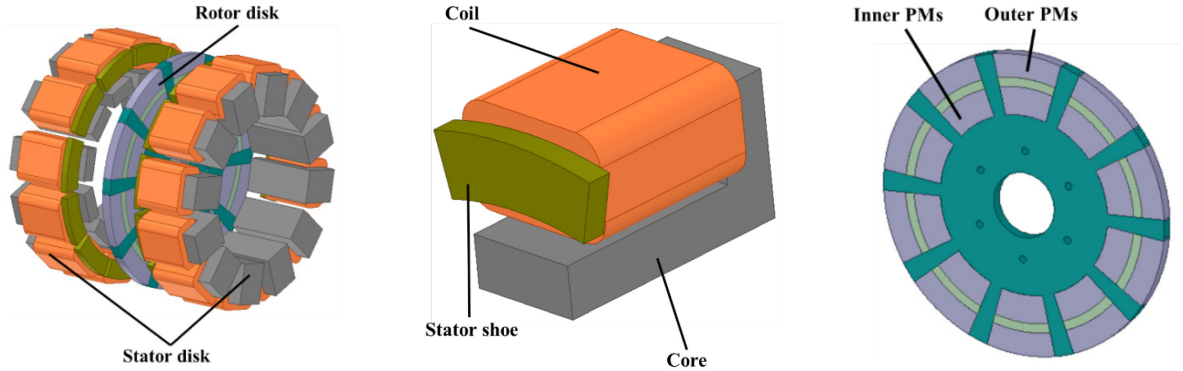

(a) Structure générale (b) Structure de l'induit statorique (c) Structure du rotor

Fig. R.3 Schéma structurel du DS-HSDR-TFPMSM

La disposition des phases des deux disques du stator de la DS-HSDR-TFPMSM est illustrée à la Fig. R.4(a). Sur la base de la combinaison à 10 encoches 12 pôles, il est commode de le transformer en un DS-HSDR-TFPMSM dont l'agencement des phases est illustré dans la figure R.4 (b) grâce à la reconfiguration des bobines. Néanmoins cette approche nécessite de transformer chaque stator triphasé en un stator double-triphasé puis à connecter entre elles les bobines de chaque stator qui appartiennent à une même phase. Pour éviter cela le stator arrière est décalé d'un certain nombre de degrés mécaniques par rapport au stator avant. Ce décalage doit correspondre au décalage électrique désiré de 30° correspondant aux 30° degrés électriques δ_e par rapport au stator avant . On obtient alors deux ensembles d'enroulements triphasés avec un déphasage δ_e comme le montre la Fig. R.4(c). L'ondulation de couple de la structure asymétrique est de 7,77% et celle de la structure symétrique de 7,39%. L'ondulation de couple du DS-HSDR-TFPMSM triphasé est de 9,05 %. Par conséquent, l'avantage d'une faible ondulation du couple de la structure à double enroulement triphasé est encore vérifié.

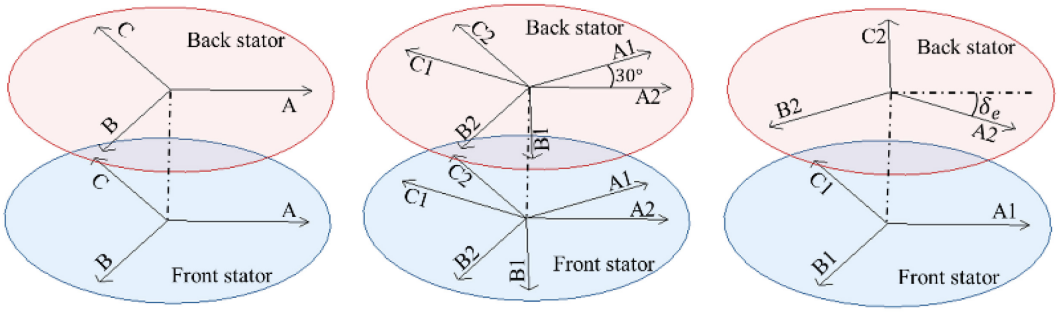

(a) (b) (c)

Fig. R.4 Diagramme des phases des deux disques du stator : (a) triphasé (b) double-triphasé avec structure symétrique (c) double-triphasé avec structure asymétrique.

L'analyse présentée dans le tableau R.1 permet d'en déduire que la structure symétrique et la structure asymétrique offrent des performances similaires avec néanmoins un léger avantage à la structure symétrique pour les caractéristiques mécaniques externes mais en requérant un niveau de tension un peu plus élevé. Cependant, la configuration du bobinage de la structure symétrique est plus complexe à réaliser en raison de la nécessité de réaliser de nombreuses connexions électriques notamment entre les deux stators.

Tableau R.1 Comparaison des performances des DS-HSDR-TFPMSMs

Paramètres	Structure asymétrique	Structure symétrique
Valeur efficace de la FEM	79.5V	82.4V
THD% de la FEM arrière	8.4%	11.1%
Amplitude Crete-crete du couple de détente	1052mN·m	979mN·m
Couple nominal	17,2Nm	
Ondulation du couple	7.77%	7.39%
Courant nominal	12.5A	12A

Il manque dans le comparatif symétrique/asymétrique le calcul des efforts axiaux au désavantage de la structure asymétrique.

R.4.2 Méthode d'analyse électromagnétique basée sur la transformation de Schwarz-Christoffel

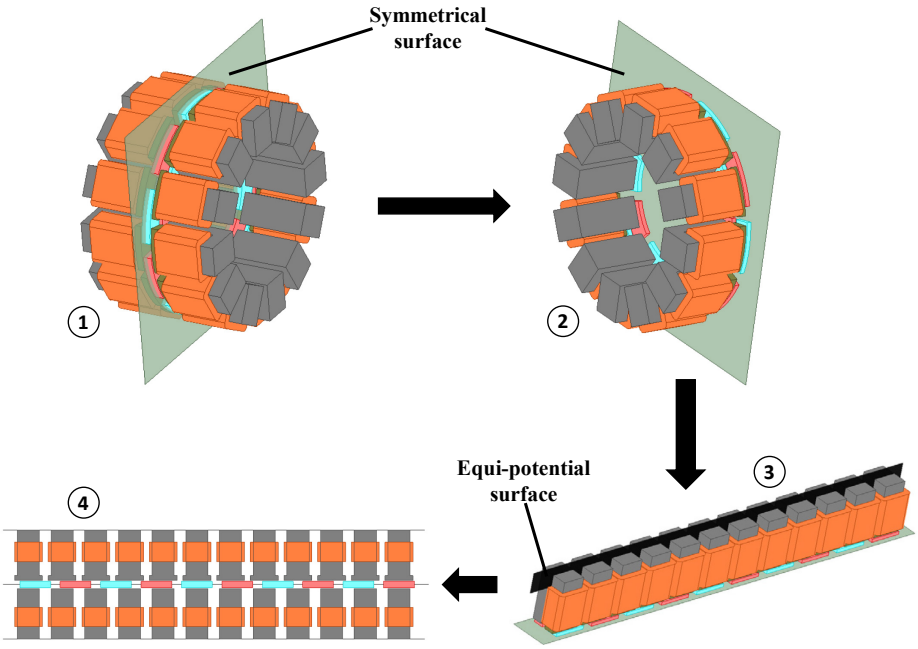

Fig. R.5 Transformation équivalente bidimensionnelle du DS-HSDR-TFPMSM

Le DS-HSDR-TFPMSM possède une structure axisymétrique (comme illustré à la Fig. R.5①), et la direction du champ magnétique dans le noyau du stator est perpendiculaire à sa section tout au long du processus. Cette caractéristique permet de choisir la position centrale du noyau du stator comme plan équipotentiel (comme illustré à la Fig. R.5③).

Pour analyser le champ électromagnétique de la DS-HSDR-TFPMSM dans le plan de coordonnées bidimensionnel, le modèle équivalent bidimensionnel obtenu dans la Fig. R.5 est transformé en un modèle analytique à plan complexe dans la Fig. R.6.

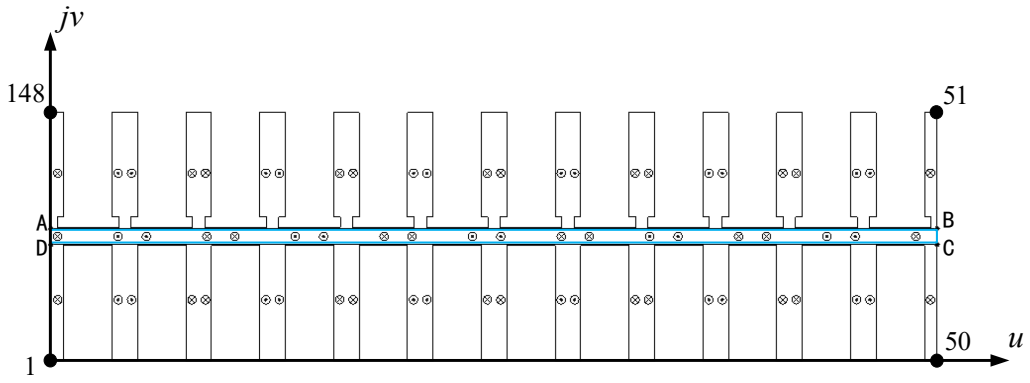

Fig. R.6 Modèle analytique en plan complexe du DS-HSDR-TFPMSM (plan w)

En utilisant la fonction de transformation de Schwarz-Christoffel f_s^{-1} , les sources d'excitation (y compris les courants d'armature et les aimants permanents) dans le *plan w* et les points à résoudre (situés sur les lignes auxiliaires AB, BC, CD et DA) peuvent être cartographiés dans la région rectangulaire du *plan z*, comme illustré dans la Fig. R.7. Enfin, le champ magnétique dans le domaine rectangulaire peut être déterminé en appliquant l'équation de Poisson. Pour refléter les conditions limites périodiques de la machine tournante, le domaine de solution rectangulaire du DS-HSDR-TFPMSM dans le *plan* z est mis en correspondance avec le domaine de solution circulaire dans le *plan* g. En fin de compte, l'équation de Hague permet de calculer le champ électromagnétique dans le domaine de solution circulaire à l'aide de l'équation de Hague[170] .

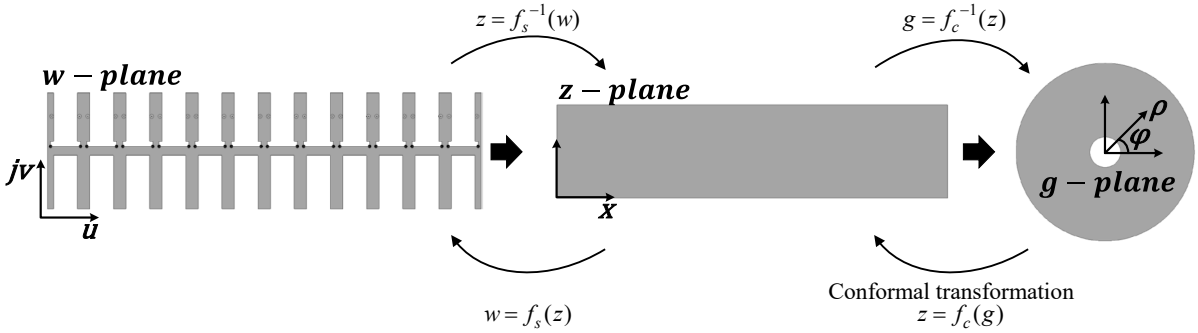

Fig. R.7 Procédure simplifiée du modèle analytique à plan complexe

La distribution de la densité de flux de l'entrefer le long de la ligne auxiliaire AB est présentée dans la Fig. R.8 comparée aux résultats obtenus par la méthode des éléments finis. On constate que les résultats obtenus par les deux méthodes sont cohérents. Cette cohérence est la preuve de la précision de la méthode de transformation de Schwarz-Christoffel.

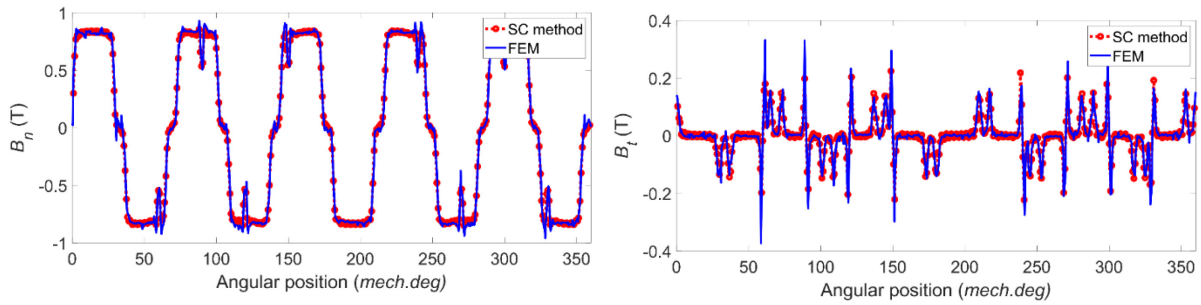

(a) Densité de flux normal (b) Densité de flux tangentiel

Fig. R.8 Comparaison de la densité de flux de l'entrefer obtenue par la méthode analytique basée sur le SC et la FEM

R.4.3 Conception optimale d'une machine basée sur un réseau neuronal BP et un algorithme d'optimisation par essaimage de particules multi-objectif

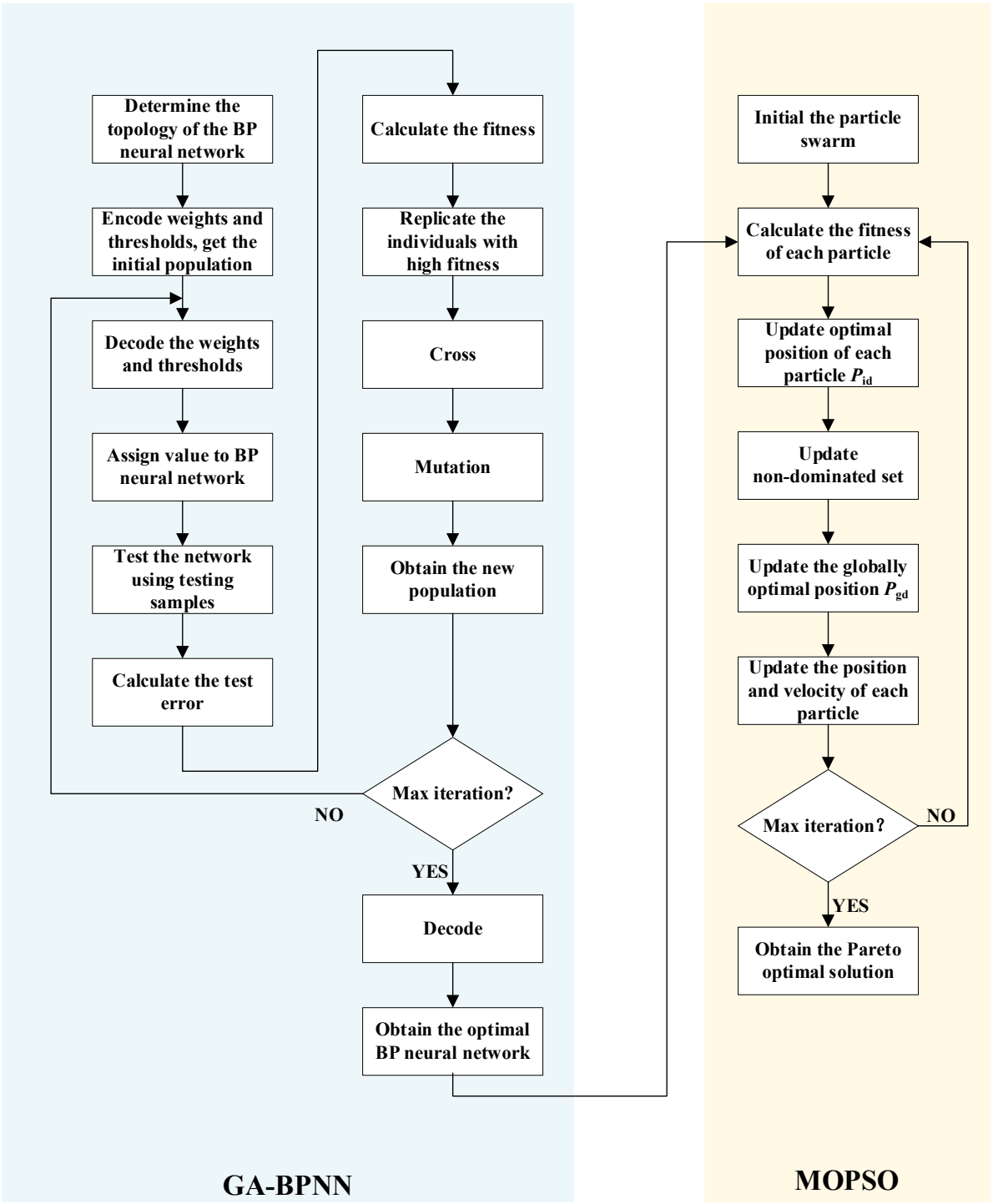

Fig. R.9 Organigramme de la nouvelle méthode d'optimisation de la conception

La méthode d'optimisation basée sur GA-BPNN et MOPSO est proposée, comme l'illustre l'organigramme de l'algorithme présenté dans la Fig. R.9. On peut voir que MOPSO est la partie principale de la méthode d'optimisation proposée, tandis que GA-BPNN sert de modèle de substitution intégré à MOPSO en tant que fonction objectif. GA-BPNN est utilisé pour calculer la valeur d'aptitude des particules de la population. La procédure détaillée d'adoption de la méthode d'optimisation proposée est la suivante :

(1) La méthode du plan d'expérience orthogonal est utilisée pour obtenir l'espace d'entraînement pour la construction du réseau neuronal BP, et les valeurs de l'objectif d'optimisation correspondant à chaque groupe de variables d'optimisation dans l'espace d'entraînement sont calculées.

(2) Le GA-BPNN est formé sur la base de l'espace d'entraînement, de manière à réaliser l'ajustement de la fonction par laquelle la relation entre les variables d'optimisation et l'objectif d'optimisation peut être prédite.

(3) La solution optimale de Pareto du problème de conception optimale est obtenue par l'algorithme MOPSO. La solution optimale de Pareto est en fait un ensemble de solutions non dominées, de sorte que la meilleure solution de conception doit finalement être sélectionnée en fonction des exigences de conception spécifiques.

R.4.4 Méthodes FTC pour le PMSM double-triphasé

La méthode FTC monophasée en circuit ouvert basée sur la transformation découplée classique est étudiée. Les méthodes FTC basées sur le principe de MCL et MTOR sont proposées sous contrainte de l'amplitude de courant de phase en fonction de différents objectifs d'optimisation FTC. Les valeurs par unité du couple maximal et des pertes cuivre sur la base des résultats de calcul en utilisant la méthode FTC DETW sont comparées dans le Tableau R.2.

Tableau R.2 Comparaison des performances à l'aide de différentes méthodes FTC

	DETW	MCL	MTOR
Couple maximum	1	1.077	1.1
Pertes cuivre	1	0.714	0.912

On peut conclure que la performance de la méthode DETW FTC est la plus mauvaise parmi les méthodes proposées. L'amélioration limitée du couple maximal sous contrainte de courant de phase est obtenue sur la base des principes MCL et MTOR. En outre, les pertes cuivre en utilisant la méthode FTC basée sur le principe MCL sont réduites de 28,6 % par rapport à la méthode DETW, réduisant ainsi de manière significative la perte de puissance pendant le fonctionnement tolérant aux pannes du PMSM double-triphasé.

Les performances de couple délivré obtenues en utilisant la méthode FTC basée sur le principe de MCL et le principe de MTOR pour les DS-HSDR-TFPMSM triphasés doubles sont comparées dans le Tableau R.3. On peut conclure qu'une amélioration limitée du couple est obtenue en utilisant la méthode FTC MTOR sous la contrainte de l'amplitude du courant de phase. Par conséquent, la méthode FTC basée sur le principe du MCL est préférable pour les PMSM double-triphasés avec des points neutres doublement isolés.

Tableau R.3 Comparaison des caractéristiques de couple du DS-HSDR-TFPMSM double-triphasé dans des conditions de défaut

	Méthodes de la FTC	**Résultats de la simulation**		Valeur de référence théorique
		Couple moyen	Ondulation du couple	Couple moyen
Structure symétrique	MCL	8,42Nm	0.43%	8,42Nm
	MTOR	8,62Nm	0.35%	8,62Nm
Structure asymétrique	MCL	8,14Nm	0.42%	8.10Nm
	MTOR	8,35Nm	0.37%	8.30Nm

Comme une machine à flux axial caractérisée par un rotor sans noyau à disque léger, la DS-HSDR-TFPMSM est plus sensible à la contrainte mécanique. Afin d'éviter tout risque de NVH (bruit, vibration et dureté) inacceptable et de dommage mécanique de la machine dans des conditions normales et de défaillance, la contrainte des efforts axiaux sur le rotor doit être analysée et traitée comme un indicateur d'évaluation critique pour juger de la faisabilité de la machine proposée.

La forme d'onde de la force axiale du rotor des structures symétriques et asymétriques lorsque la machine fonctionne dans des conditions normales et de défaut d'une phase ouverte est illustrée à la figure. R.10. Il est assez clair que la structure symétrique ne subit pas de grande force axiale dans les 3 modes de fonctionnement (normal, en défaut sans configuration et en défaut avec configuration FTC). Il n'est pas le cas pour la structure asymétrique. Il est à rappeler ici que l'avantage de la structure asymétrique par rapport à celle asymétrique est de ne pas avoir les connexions électriques entre les deux stators.

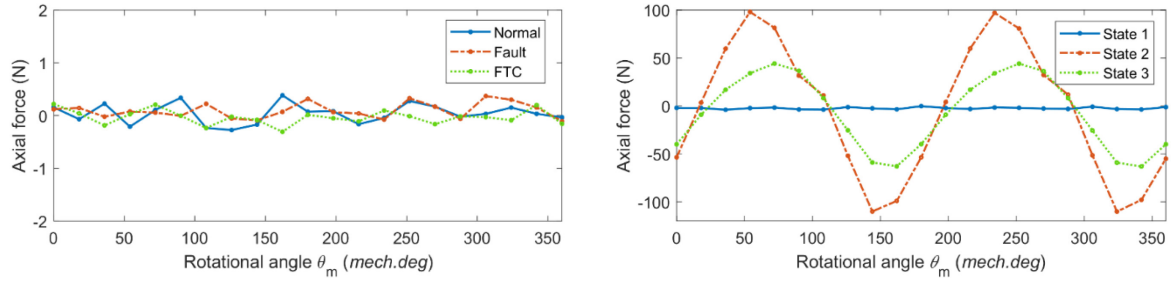

(a) Symmetrical structure (b) Asymmetrical structure

Fig. R.10 Forme d'onde de la force axiale du rotor dans le modèle sans décalage.

Les distributions synthétiques des forces axiales de la structure symétrique sont calculées au moment initial $\theta_m = 0°$ tandis que les distributions synthétiques des contraintes axiales sont calculées à $\theta_m = 294°$ pour la structure asymétrique. La figure. R.11 montre les distributions synthétiques des forces axiales sur la région intérieure des PM sous 3 états (normal, défaut et FTC) pour les deux versions, symétrique ou asymétrique. En outre, la comparaison de la valeur maximale de la force axiale entre la version sans décalage et celle avec décalage est donnée dans le Tableau R.4. On peut conclure que la contrainte axiale synthétique sur les MP de la structure asymétrique varie régulièrement le long de la direction circonférentielle et que la valeur de pointe de la force axiale du modèle avec décalage est beaucoup plus élevée que celle de la structure symétrique.

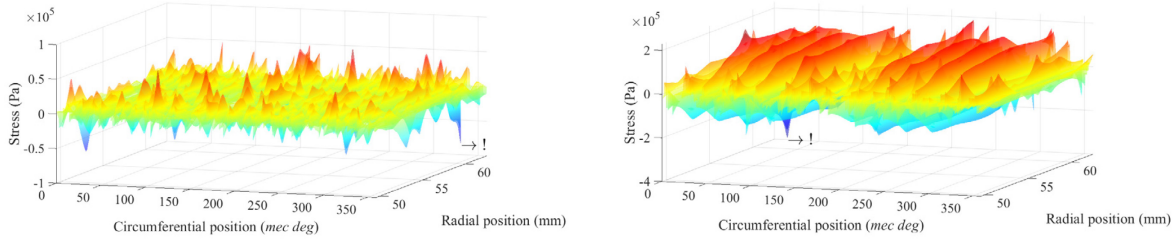

(a) (b)

Fig. R.11 Synthetic axial stress distribution on the inner PMs region under *stage 3*: (a) no shift model (b) shift model.

Tableau R.4 Comparaison de la valeur maximale de la force axiale (Unité : MPa)

		Symétrique	Asymétrique
Normal	PM extérieur	0.0758	-0.31
	PM intérieur	0.0663	-0.295
Défaut	PM extérieur	-0.0973	-0.377
	PM intérieur	-0.0803	-0.239
FTC	PM extérieur	0.0778	-0.288
	PM intérieur	-0.084	-0.349

Pour obtenir une excellente qualité du couple délivré dans des conditions de défaut, la méthode de contrôle des harmoniques de courants dans les repères tournants multiples (MRF) et la méthode de contrôle proportionnel-résonant (PR) sont proposées.

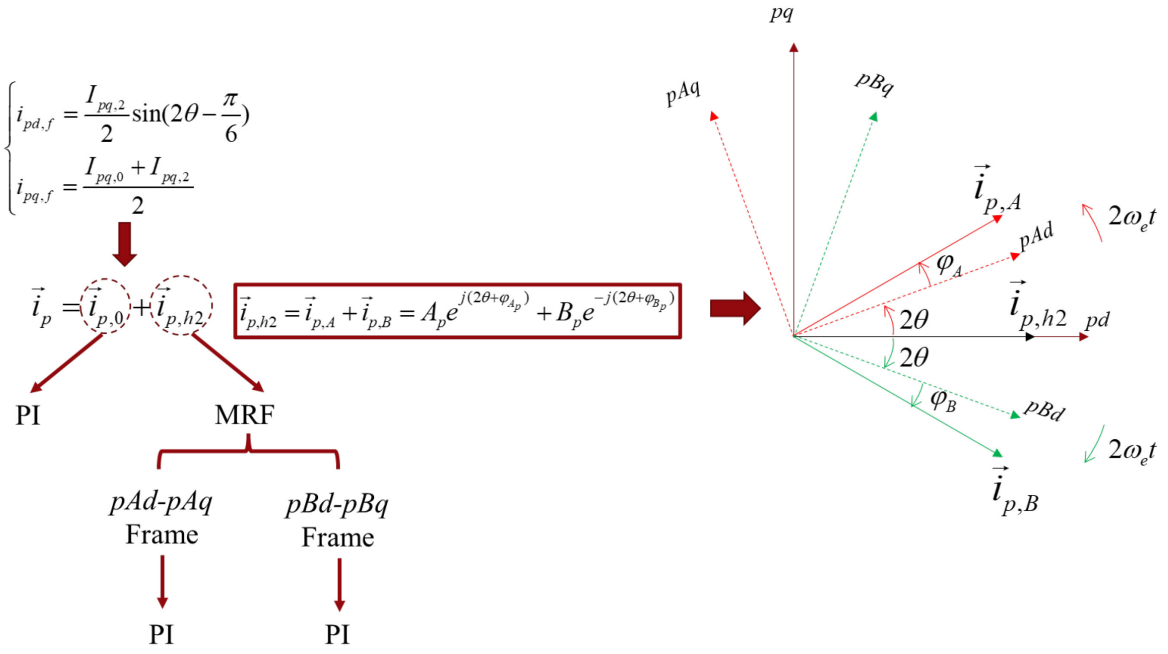

Fig. R.12 Schéma de la transformation MRF

Un schéma de la transformation MRF dans le repère *pd-pq* est présenté dans LaFig. R.12. La transformation du courant dans le cadre pd-pq est analysée. Tout d'abord, le courant dans le cadre *pd-pq* est exprimé sous une forme complexe $\vec{i}_p$ qui se compose du vecteur courant continu $\vec{i}_{p,0}$ et du vecteur courant de deuxième harmonique $\vec{i}_{p,\ h2}$. $\vec{i}_{p,\ 0}$ peut être contrôlé à l'aide d'un régulateur PI, tandis que $\vec{i}_{p,\ h2}$ est exprimé comme un combinaison du vecteur de courant $\vec{i}_{p,\ h2}$ tournant dans le sens positif avec deux fois la vitesse angulaire électrique et le vecteur de courant $\vec{i}_{p,\ A}$ tournant dans le sens négatif avec deux fois la vitesse angulaire électrique $\vec{i}_{p,\ B}$:

$$\vec{i}_{p,h2} = \vec{i}_{p,A} + \vec{i}_{p,B} = A_p e^{j(2\theta+\varphi_{A_p})} + B_p e^{-j(2\theta+\varphi_{B_p})} \tag{5-55}$$

où A_p et B_p représentent l'amplitude de $\vec{i}_{p,\ A}$ et $\vec{i}_{p,\ B}$, respectivement.

Ensuite, le vecteur de courant de séquence positive $\vec{i}_{p,A}$ est transformé dans le repère *pAd-pAq* tandis que le vecteur de courant de séquence positive $\vec{i}_{p,A}$ est transformé dans le repère *pBd-pBq*. Enfin, toutes les composantes du courant sont transformées en une valeur de courant continu qui peut être contrôlée à l'aide d'un régulateur PI.

Cependant, la partie contrôleur PI de la méthode de contrôle des harmoniques de courant basée sur le MRF nécessite un total de douze contrôleurs PI de courant, ce qui augmente considérablement par rapport à l'utilisation de quatre contrôleurs PI dans des conditions normales. Afin de réduire le nombre de contrôleurs de courant, la méthode de contrôle des harmoniques de courant basée sur PR est proposée pour contrôler la qualité spectrale.

Les formes d'ondes dynamiques du couple délivré selon quatre modes de fonctionnement en utilisant la méthode de contrôle des harmoniques de courant basée sur la MRF ou sur la PR sont calculées respectivement, comme indiqué dans la Fig. R.16.

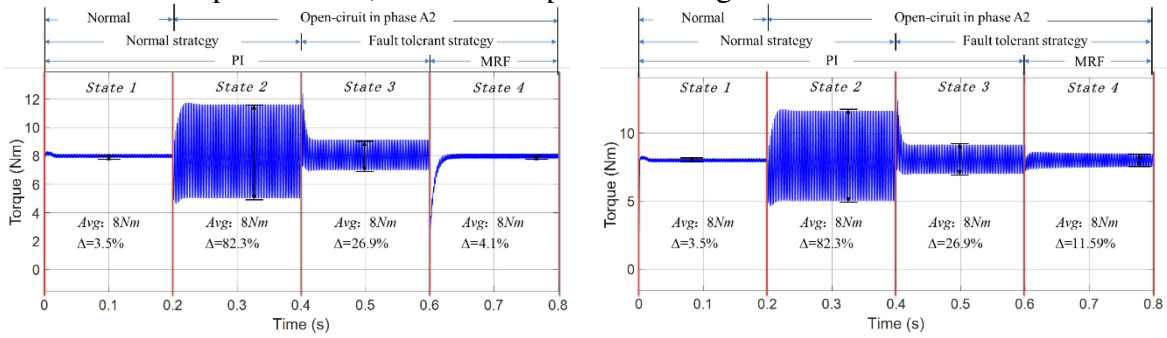

(a) Basé sur la MRF (b) Basé sur les Correcteurs résonants (PR)

Fig. R.13 Forme d'onde de couple pendant la procédure dynamique sous 3000r/min

On peut conclure que l'ondulation du couple délivré à haute vitesse obtenue par la méthode basée sur le PR est beaucoup plus élevée que celle de la méthode de contrôle des harmoniques de courant basée sur le MRF. Ce résultat confirme la validité de notre stratégie de contrôle qui est adapté à la machine électrique de continuer à fonctionner de manière stable en cas de défaut à haute vitesse.

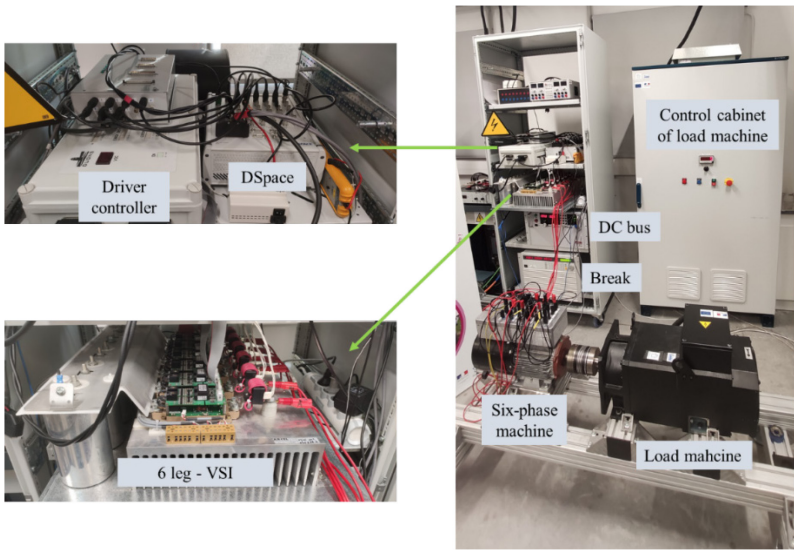

Fig. R. 14 Banc d'essai

Afin de vérifier l'efficacité de la méthode FTC monophasée en circuit ouvert basée sur la transformation normale découplée et la méthode de contrôle du courant harmonique de référence, une plate-forme expérimentale pour un PMSM triphasé double monté en surface est construite sur la base de dSPACE-MicroLabBox, comme le montre La Fig. R. 14. Les résultats expérimentaux démontrent l'efficacité de la méthode de contrôle tolérante aux pannes proposée.

R.4.5 Fabrication et expérimentation de prototypes

L'ensemble de la construction du DS-HSDR-TFPMSM est illustré à la Fig. R.16. Le disque du rotor, le rotor de frein, le codeur et deux roulements sont reliés par un arbre.

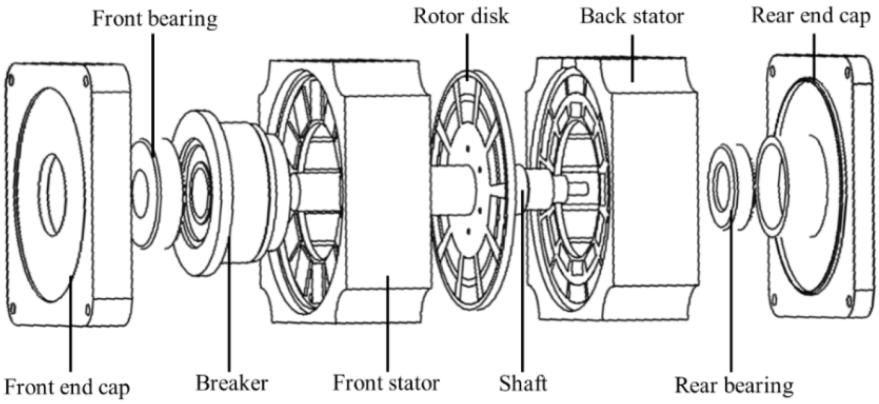

Fig. R.15 Vue éclatée de la structure globale du DS-HSDR-TFPMSM

Sur la base des résultats expérimentaux du prototype DS-HSDR-TFPMSM, un RPMSM commercialisé de même puissance est sélectionné pour une étude expérimentale comparative. LaFig. R.16 montre la comparaison de l'apparence des deux machines. Tableau R.5 donne également une comparaison des paramètres dimensionnels et de performance de base des deux machines. On constate que le prototype DS-HSDR-TFPMSM présente des avantages évidents, avec une réduction de 40,8 % de la longueur axiale et de 21,9 % du poids, et que son moment d'inertie est réduit de 54,2 %, ce qui lui confère de meilleures performances dynamiques.

Fig. R.16 Comparaison entre le prototype DS-HSDR-TFPMSM et le RPMSM commercialisé

Tableau R.5 Comparaison des performances et de la taille

	DS-HSDR-TFPMSM	RPMSM
Tension nominale	300V	336V
Courant nominal	12.5A	10.3A
Vitesse nominale	3000 tr/min	
Couple nominal	16,5 Nm	
Niveau d'isolation	F	
Méthode de refroidissement	Naturel	
Longueur axiale totale	190 mm	308 mm
Diamètre extérieur	190 mm	
Poids	22.8 Kg	28 Kg
Moment d'inertie	34,76 $Kgcm^2$	76 $Kgcm^2$

Tableau R.6 montre les paramètres caractéristiques du processus de démarrage. On peut conclure que le courant de démarrage de DS-HSDR-TFPM est considérablement réduit. Ainsi, la consommation d'énergie de DS-HSDR-TFPM est plus faible pendant le processus de démarrage, ce qui est crucial pour les robots industriels qui requièrent des démarrages fréquents des servomoteurs pendant le fonctionnement. Pendant le processus d'ajout de la pleine charge illustré à la Fig. R.17 DS-HSDR-TFPM a besoin de 1,2 seconde pour revenir à l'état d'équilibre et sa vitesse est tombée à 2993 tr/min au plus bas, tandis que le SPMSM a besoin de 1,5 seconde pour revenir à l'état d'équilibre et sa vitesse est tombée à 2972 tr/min au plus bas. En résumé, il est prouvé que les performances dynamiques de DS-HSDR-TFPM sont supérieures.

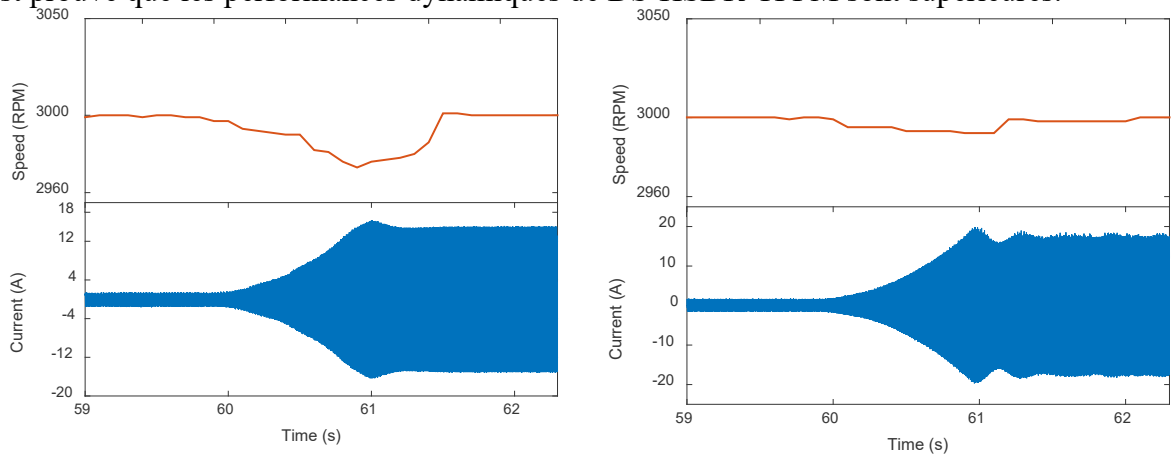

(a) RPMSM (b) DS-HSDR-TFPMSM

Fig. R.17 (Données expérimentales)Comparaison du processus dynamique en cas d'ajout de la charge nominale

Tableau R.6 Comparaison des caractéristiques de démarrage pendant le processus de démarrage

	instant initial	Courant de démarrage
RPMSM	1.1s	43.6A
DS-HSDR-TFPMSM	1.1s	25.3A

R.5 Conclusions générales et perspectives

Conclusions générales

Dans cette thèse, la conception, l'analyse et l'optimisation d'une machine synchrone à aimants permanents à flux transverse pour des applications robotiques industrielles sont étudiées, ainsi que ses conceptions multiphasées et les méthodes de contrôle FTC. Les principaux contenus de la recherche et les résultats obtenus sont les suivants.

(1) Une analyse comparative avec le RPMSM permet de conclure que le DS-HSDR-TFPMSM présente les avantages d'une structure compacte et d'un faible moment d'inertie, ce qui contribue à la miniaturisation et à la dynamique élevée des entraînements électriques utilisés dans les robots industriels. Deux types de DS-HSDR-TFPMSM à structure double-triphasée sont obtenus sur la base de la topologie à double disque du stator et de la combinaison 10 pôles/12 encoches du DS-HSDR-TFPMSM. Une étude comparative de l'ondulation du couple délivré des DS-HSDR-TFPM double-triphasés et triphasés est réalisée, et l'on peut conclure que les DS-HSDR-TFPM double-triphasés combinent l'avantage d'une faible ondulation du couple.

(2) La méthode de transformation de Schwarz-Christoffel est proposée pour analyser le champ électromagnétique du DS-HSDR-TFPMSM. La précision de la méthode de transformation de Schwarz-Christoffel est validée en comparant la distribution du champ magnétique de l'entrefer et les performances calculées avec la méthode des éléments finis. La comparaison de la consommation de ressources de calcul entre les deux méthodes révèle que la méthode de transformation de Schwarz-Christoffel permet d'économiser 90,9 % du temps de calcul et 88,4 % des ressources de calcul, ce qui prouve l'efficacité de la méthode de transformation de Schwarz-Christoffel.

(3) Le réseau neuronal BP est substitué à l'algorithme MOPSO pour obtenir la conception d'optimisation multi-objectifs du DS-HSDR-TFPMSM. La méthode d'optimisation proposée a été validée en comparant les résultats du calcul du couple de la solution optimale obtenue par la méthode des éléments finis avec les résultats de la conception initiale. Les résultats montrent que la valeur moyenne du couple délivré par le moteur passe de 17,26 Nm à 17,83 Nm et que l'ondulation du couple diminue de 9,05 % à 1,47 %, ce qui confirme l'efficacité de la méthode d'optimisation proposée. En outre, la précision du réseau neuronal BP est vérifiée en comparant les résultats de l'approximation de la solution optimale par le réseau neuronal BP avec les résultats obtenus par la méthode des éléments finis.

(4) La méthode FTC monophasée en circuit ouvert basée sur la transformation découplée normale est étudiée sur la base des principes MCL et MTOR. Les performances de la méthode FTC proposée sont comparées à celles de la méthode traditionnelle de tolérance aux pannes DETW, et l'on peut conclure que l'avantage de la méthode FTC basée sur le principe MCL est plus important, ce qui permet de réduire de manière significative les pertes de cuivre en cas de panne. Les méthodes de contrôle des harmoniques de courant de référence basées sur le MRF et le PR sont étudiées pour améliorer les performances de couple délivré par le PMSM double-triphasé dans des conditions de défaut à grande vitesse. En appliquant les deux méthodes de contrôle des harmoniques de courant susmentionnées à l'analyse de simulation du FTC dans des conditions de haute vitesse du DS-HSDR-TFPMSM double-triphasé, on conclut que la méthode basée sur le MRF se caractérise par un meilleur effet de suppression sur l'ondulation du couple. Enfin, la plate-forme expérimentale pour un PMSM double-triphasé monté en surface a été construite, puis l'efficacité des techniques FTC proposées a été vérifiée par des expériences.

(5) La fluctuation de la force axiale totale sur le rotor pour la version avec décalage entre les deux stators (la structure asymétrique) est beaucoup plus élevée que pour celle sans décalage (la structure symétrique), en particulier dans les conditions de fonctionnement avec un défaut de phase ouverte. Bien que la stratégie FTC puisse réduire considérablement la force axiale sur le rotor de la version avec décalage, son influence sur les vibrations et le bruit subsiste. En outre, la possibilité de rupture des PM de la version avec décalage est beaucoup plus élevée d'après les résultats de distribution des forces axiales obtenus. Étant donné que la contrainte axiale est l'indicateur crucial de la sécurité mécanique du DS-HSDR-TFPMSM proposé, la version sans décalage est le meilleur choix malgré les connexions électriques entre les deux stators existent.

(5) Les technologies de fabrication du prototype DS-HSDR-TFPMSM ont été étudiées et des recherches expérimentales ont été menées. Un RPMSM commercial de même puissance a été choisi pour une étude expérimentale comparative. Les résultats des comparaisons sur la taille et la performance dynamique démontrent la miniaturisation supérieure et la dynamique élevée du DS-HSDR-TFPMSM.

Les publications associées à cette thèse de doctorat sont répertoriées comme suit :

1) Articles dans des revues avec comité de lecture internationales:

- W. Zhang, Y. Xu and G. Zhou, "Research on a Novel Transverse Flux Permanent Magnet Motor With Hybrid Stator Core and Disk-Type Rotor for Industrial Robot Applications," in IEEE Transactions on Industrial Electronics, vol. 68, no. 11, pp. 11223-11233, Nov. 2021, doi: 10.1109/TIE.2020.3038060.
- W. Zhang, Y. Xu and M. Sun, "Design of a Novel Claw Pole Transverse Flux Permanent Magnet Motor Based on Hybrid Stator Core," in IEEE Transactions on Magnetics, vol. 57, no. 6, pp. 1-5, June 2021, Art no. 8104705, doi: 10.1109/TMAG.2021.3060748.

2) Conférences internationales avec actes :

- Zhang Wenjing, Xu Yanliang, Sun Mingxin. Cogging Torque Reduction for a Novel Disk Transverse Flux Permanent Magnet Motor[C]//2020 IEEE 19th Biennial Conference on Electromagnetic Field Computation (CEFC). IEEE, 2020: 1-4.
- Zhang Wenjing, Nguyen Ngac Ky, Semail Eric, Xu Yanliang. Axial Stress Analysis and Comparison of the Novel Dual 3-phase Axial Flux Permanent Magnet Machines [C]//2023 11th International Conference on Power Electronics and ECCE Asia (ICPE 2023-ECCE Asia). IEEE, 2023: 1-7.

3) Autre publication:

- W. Zhang, Y. Xu and S. Li, " Structure Principle and Optimization of a Novel Disk Transverse Flux Permanent Magnet Brushless Motor," in Transactions of China Electrotechnical Society, vol. 36, no. 14, pp. 2979-2988, July 2021.
- W. Zhang, Y. Xu, S. Wei and A Yu, " Design and Research of Axial Flux Permanent Magnet Motor Based on Soft Magnetic Composite Material-Si Steel Combined Core," in Proceedings of the Chinese Society of Electrical Engineering, vol. 41, no. 13, pp. 4656-4665, July 2021.

Perspectives

La thèse porte principalement sur la conception, l'analyse et l'optimisation d'une nouvelle structure de PMSM à flux transverse, ainsi que sur la technologie de commande tolérante aux pannes pour les PMSM double-triphasées . Bien que plusieurs résultats innovants aient été

obtenus, l’analyse peut être poursuivie et approfondie dans certains domaines et quelques défauts qui doivent être corrigés, comme indiqué ci-dessous.

(1) Le DS-HSDR-TFPMSM, en tant que PMSM à flux transverse, présente un grave problème de fuite magnétique qui, bien qu'il soit partiellement atténué par les pieds des pôles du stator du SMC, se traduit toujours par des facteurs de puissance machine plus faibles et des exigences de tension de bus plus élevées par rapport aux RPMSM traditionnels. Des recherches sont donc nécessaires pour explorer d'autres méthodes d'amélioration.

(2) La méthode analytique utilisée dans la thèse, basée sur la transformation de Schwarz-Christoffel, néglige la saturation non linéaire du matériau du noyau du stator dans le calcul du champ magnétique et des performances de la DS-HSDR-TFPMSM. Par conséquent, cette méthode n'est pas adaptée au calcul des paramètres de performance dans des conditions de surcharge, et des recherches supplémentaires sont nécessaires pour établir un modèle de calcul efficace tenant compte de la saturation non linéaire du matériau.

(3) La méthode MRF utilisée pour suivre le courant harmonique de référence requis par le contrôle tolérant aux pannes dans la thèse nécessite trop de contrôleurs PI de courant, ce qui augmente la complexité du système de contrôle. En outre, l'utilisation d'un grand nombre de LPF dans cette méthode crée une instabilité dans le système. Il est nécessaire de poursuivre l'exploration pour développer une méthode de contrôle de suivi du courant de référence harmonique avec moins de contrôleurs PI et sans LPF.

(4) Le concept de conception modulaire du disque statorique dans le DS-HSDR-TFPMSM offre l'avantage d'une maintenance aisée, facilitant la réparation et le remplacement d'un noyau d'induit statorique endommagé. Cependant, la méthode utilisée dans la thèse exige que l'ensemble du disque du stator soit collé après positionnement et fixation, ce qui a pour effet de solidifier tous les noyaux de l'armature du stator en une seule unité et de créer des difficultés pour l'entretien ultérieur.

Arts et Métiers Sciences et Technologies

Wenjing ZHANG

Design and Fault Tolerant Control of a Novel Multiphase Transverse Flux Permanent Magnet Synchronous Machine

HESAM UNIVERSITÉ

Résumé : La machine synchrone à aimant permanent à flux transverse combine les avantages d'une densité de couple intrinsèquement élevée, de la capacité à ajuster la charge électromagnétique de manière indépendante, d'une conception de structure flexible et d'une structure de bobinage simple, ce qui lui confère un potentiel important pour être utilisée comme servomoteur dans les applications de robots industriels afin de parvenir à la miniaturisation de son entraînement électrique. En outre, la structure d'enroulement multi-phases peut être utilisée dans une machine synchrone à aimant permanent à flux transverse pour obtenir l'avantage de la capacité de tolérance aux pannes, ce qui améliore encore la fiabilité fonctionnelle de l'entraînement électrique dans les robots industriels. Cependant, les recherches existantes sur les machines synchrones à aimant permanent à flux transverse et les recherches sur la tolérance aux pannes des machines multi-phases présentent encore des lacunes et des limites qui restreignent leur application dans le contexte de la thèse.

L'objectif principal de cette thèse de doctorat est de proposer une machine synchrone à aimant permanent à flux transverse de structure nouvelle pour améliorer les caractéristiques et les performances du robot industriel.

Tout d'abord, une machine synchrone à aimants permanents à flux transverse à topologie à un rotor central à aimants sans fer et deux stators externes avec un circuit magnétique statorique hybride comprenant tôle laminées et poudre de fer (DS-HSDR-TFPMSM) est proposée pour réaliser la miniaturisation et la dynamique élevée des entraînements électriques dans les robots industriels. Sa conception structurelle et électromagnétique est réalisée. Une étude de conception tolérante aux pannes basée sur la structure double-triphasée est ensuite réalisée selon deux approches pour le DS-HSDR-TFPMSM

Compte tenu de la structure tridimensionnelle complexe du DS-HSDR-TFPMSM, la méthode de calcul du champ magnétique de l'entrefer et les performances sont étudiées sur la base de la méthode de transformation de Schwarz-Christoffel. En outre, la conception de l'optimisation du DS-HSDR-TFPMSM est réalisée sur la base du réseau neuronal BP et de l'algorithme d'optimisation multi-objectifs afin d'améliorer ses performances en termes de couple.

Sur la base des conceptions accessibles de tolérance aux pannes de DS-HSDR-TFPMSM, la méthode de commande tolérante aux pannes pour la machine synchrone double-triphasée à aimant permanent est étudiée. Tout d'abord, une reconfiguration du courant de référence dans le repère découplé normal basé sur le principe des pertes cuivre minimales et de la plage de fonctionnement maximale du couple est proposée. Ensuite, la contrainte axiale sur le disque du rotor du DS-HSDR-TFPMSM triphasé double dans différents états est analysée. La force axiale synthétique et la distribution de la contrainte axiale sur le disque du rotor des deux types de DS-HSDR-TFPMSM double-triphasé sont comparées. Enfin, la méthode de contrôle tolérant aux pannes pour les machines électriques à aimant permanent triphasées fonctionnant à grande vitesse est étudiée, dans laquelle les composantes harmoniques du courant de référence sont suivies et contrôlées à grande vitesse en utilisant une méthode basée sur des repères tournants multiples et une autre méthode basée sur des contrôleurs résonants proportionnels. Enfin, les technologies de fabrication et les études expérimentales sont menées pour le prototype DS-HSDR-TFPMSM.

Mots clés : Machine synchrone à aimant permanent à flux transverse ; machine synchrone à aimant permanent triphasée double ; méthode de transformation de Schwarz-Christoffel ; optimisation de la conception de la machine électrique ; contrôle tolérant aux pannes.

Abstract: Transverse flux permanent magnet synchronous machine combines the advantages of intrinsically high torque density, the ability to adjust the electromagnetic load independently, flexible structure design, and simple winding structure, enabling it with significant potential for being used as a servo motor in industrial robot applications to achieve the miniaturization of its electric drive. In addition, multiphase winding structure can be used in transverse flux permanent magnet synchronous machine to obtain advantage of fault tolerant ability, which furtherly improves the functional reliability of the electric drive in industrial robots. However, there are still shortcomings and limitations among the existing research on transverse flux permanent magnet synchronous machine and the research on fault tolerance of multiphase machines, which limit their application in the context of the thesis

The main objective of this doctoral thesis is to propose a novel structure transverse flux permanent magnet synchronous machine to improve the characteristics and performances of the industrial robot.

Firstly, a dual-stator topology transverse flux permanent magnet synchronous machine combined with hybrid stator core and disk-type rotor (DS-HSDR-TFPMSM) is proposed to realize the miniaturization and high dynamics of the electric drives in industrial robots. Its structural and electromagnetic design is proceeded. A fault tolerant design study based on the dual three-phase structure is carried out for the proposed DS-HSDR-TFPMSM to improve its functional reliability.

Considering the complex three-dimensional structure of DS-HSDR-TFPMSM, the calculation method of air-gap magnetic field and performances are investigated based on the Schwarz-Christoffel transformation method. In addition, the optimization design of DS-HSDR-TFPMSM is conducted based on the BP neural network and multi-objective optimization algorithm to improve its torque performance.

Based on the accessible fault tolerant designs of DS-HSDR-TFPMSM, the fault tolerant control method for the dual three-phase permanent magnet synchronous machine is investigated. Firstly, the fault tolerant control method by reconfiguring the reference current in the normal decoupled frame based on the principle of minimum copper loss and maximum torque operation range is proposed. Then, the axial stress on the rotor disk of the dual three-phase DS-HSDR-TFPMSM under different states is analyzed. The synthetic axial force and the axial stress distribution on the rotor disk of the two kinds of dual three-phase DS-HSDR-TFPMSMs are compared. Finally, the fault tolerant control method for dual three-phase permanent magnet electric machine operating under high speed is investigated, in which the harmonic components of the reference current are tracked and controlled under high speed by using a multi-reference frame-based method and a proportional resonant controller-based method.

Eventually, the fabrication technologies and experimental studies are conducted for prototype DS-HSDR-TFPMSM.

Keywords: Transverse flux permanent magnet synchronous machine; dual three-phase permanent magnet synchronous machine; Schwarz-Christoffel transformation method; optimization design of electric machine; fault tolerant control.